Radio-frequency induced association of molecules in ^{87}Rb

Iurii Mordovin

Presented in fulfillment of the requirements
of the degree of Doctor of Philosophy

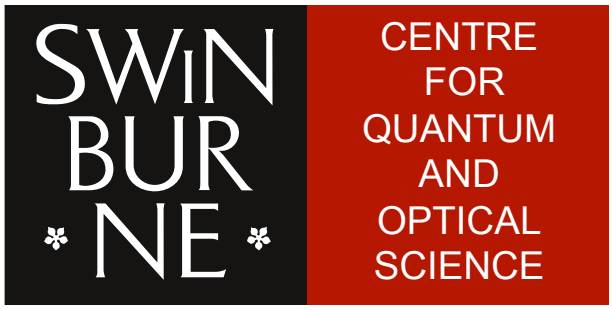

Centre for Quantum and Optical Science
Faculty of Science, Engineering and Technology
Swinburne University of Technology
Melbourne, Australia

March 18, 2015

Abstract

This thesis describes results of the experimental study on radio-frequency stimulated molecular associations in a ^{87}Rb Bose-Einstein condensate (BEC) without assistance of magnetic Feshbach resonances. This new method of molecular creation and the generation of associated rf-induced Feshbach resonances has been theoretically proposed in 2010; however, we are the first group who has demonstrated it experimentally.

In order to produce the atoms-molecule coupling the BEC was prepared in a coherent superposition of two states $|F = 1,\ m_F{=}{-}1\rangle$ and $|F = 2,\ m_F{=}1\rangle$ and then irradiated by a high power radio-frequency field for a certain time interval. During the search for the resonance many realizations of the experiment have been performed, varying the rf frequency with a fixed step (2 kHz). Sudden decrease of the number of atoms was used as an indication for the resonance location. The subsequent measurement of the increased two-body loss coefficient allowed us to assess the atoms-to-molecule conversion rate.

As high power radio-frequency radiation is needed for stimulated binding of the atoms, this thesis describes our method of generation of the rf fields with up to 6 G of amplitudes which can be easily reproduced and employed for rf induced molecular associations from other elements or in other experiments. The rf-induced atoms-molecule coupling can also be used as a tool for measurements of the Zeeman energy of the molecules with a kHz precision. This high accuracy has been achieved after the deep analysis of the coupling curves and the development of the theory describing the shapes of the atoms-molecule coupling. This thesis contains the experimental data for the Zeeman energies of five molecular states (F = 1, 2, 3), which have been measured in the range of DC-magnetic fields 0.15−3.3 G.

Acknowledgements

I want to express my sincere gratitude to everyone who helped me during the time of my PhD.

First of all, I want to thank my primary supervisor Prof. Andrei Sidorov, who was giving me excellent guidance and support during these years of the PhD research. His theoretical and experimental assistance was extremely valuable. The door to his office was always open for timely discussions of any contemporary issues.

It is hard to overestimate the contribution of Dr. Brenton Hall to the project. His bright ideas were often the keys for overcoming the challenges in the lab (such as the implementation of an rf transformer and an employment of the optical pumping laser to hide atoms on the reference frame in kinetics imaging mode). Brenton has also upgraded the Labview program which controls the experiment and done a lot for the automation of the experiment.

The next person I would like to thank is Prof. Russell McLean, who gave valuable support from the very beginning of my PhD (settling in Australia), through all the years of the research (as the acting director of our Centre he always supported my participation in the leading conferences) till the end of my project (by doing a fantastic job in the proof-reading of my thesis). I want to say a special thank you to all already mentioned people as well as Prof. Peter Hannaford for the assistance in the thesis writing, I appreciate your help very much.

I want to thank everyone who participated in our weekly meetings, especially my co-supervisor Dr. Alexander Akoulchine, as well as Dr. Mikhail Egorov, Dr. Valentin Ivannikov (predecessor students and co-creators of the experimental setup I was working on), Smitha Jose, Prince Surendran, Dr. Ivan Herrera, Alessandro Brolis and Yibo Wang. I

would like to thank Tatiana Tchernova for assistance with administrative paperwork and all members of the CQOS for creation of the atmosphere of a big family.

Next, I thank my dear friends who were mainly destracting me from the university business, which, however, only benefited in the outcomes of my research and taught how to find the balance between the work and the resting time. I'm very grateful to my dear parents and fiancee Sofia Golenkina for their infinite patience and great support during all these years. I would also like to thank Swinburne University of Technology for its amazing facilities and support for international students, especially the Learning and Academic Skills (LAS) Centre.

Declaration

The work presented in this thesis entitled "Radio-frequency induced association of molecules in ^{87}Rb" has been carried out in the Centre for Quantum and Optical Science (CQOS) at Swinburne University of Technology in Melbourne between April 2011 and November 2014. The thesis contains no material that has been accepted for the award of any other degree or diploma. To the best of my knowledge, the thesis contains no material previously published or written by another author, except where due reference is made in the text of the thesis.

Iurii Mordovin

Melbourne, Victoria, Australia

March 18, 2015

Table of Contents

Table of Contents vii

List of Figures xi

List of Tables xv

1 Introduction 1

1.1 Motivation . . . 1

1.2 Background . . . 2

1.3 Rf-induced molecular association . . . 5

1.4 Thesis outline . . . 7

2 Experimental setup 9

2.1 BEC production on an atom chip . . . 9

2.1.1 Mirror Magneto-Optical Trap (MMOT) . . . 9

2.1.2 CMMOT, optical pumping and rf-evaporation in the Z-wire MT . . . 11

2.2 Imaging system . . . 13

2.2.1 Absorption imaging . . . 13

2.2.2 Measurement of saturation intensity . . . 16

2.2.3 Kinetics mode imaging . . . 18

2.2.4 Size of the camera pixels in the object plane . . . 21

2.2.5 Problems with short time between two frames . . . 21

2.3 Experimental measurements of the trap frequencies . . . 22

2.4 Distance from the cloud to the chip wire, gravity sag 25
2.5 Two-component BEC 28
2.6 Adiabatic passage 29
2.7 Magnetic noise 32
2.8 Strong rf field generation 34
2.8.1 AC-current maximization and impedance matching 36
2.8.2 Rf transformer 40

3 Calibration of DC and AC magnetic fields 47
3.1 Shape and broadening effects of the microwave spectroscopy line 48
3.1.1 Spectral line of BEC in absence of gravity 49
3.1.2 Effect of gravity sag 51
3.1.3 Dipole oscillations during the microwave spectroscopy 56
3.1.4 Power broadening and magnetic noise 59
3.2 Microwave spectroscopy of the trapped Bose-Einstein condensate 62
3.3 AC magnetic field calibration 66
3.4 Conclusion 71

4 Radiofrequency atom-molecule coupling 73
4.1 Discovery of rf induced atom-molecule conversion without assistance of magnetic Feshbach resonance 74
4.1.1 Necessary conditions for the observation of the rf induced atom-molecule coupling 74
4.1.2 Experimental observation of rf induced molecular association . . . 77
4.1.3 Molecule formation rate 82
4.2 Shape of the atom loss curves 86
4.2.1 Theoretical shape of the resonances of rf-induced coupling to molecular states 86
4.2.2 Fitting of the experimental data for the rf induced atom losses . . 95
4.3 Zeeman dependence of molecular state energies 96

4.4 Dependence of the loss curve shape on rf field amplitude 101
4.5 Conclusion 106

5 Conclusions and outlook **107**

Bibliography **111**

A Elimination of parasitic resonances **125**

B Z-wire magnetic trap **131**

B.0.1 Magnetic field in the Z-wire magnetic trap 131
B.0.2 Analytical formulae for the frequencies of the Z-wire magnetic trap 137
B.0.3 Dipole oscillations of the atom cloud in the trap 138
B.0.4 Gravity sag in a harmonic magnetic trap 139

C Impedance matching and rf transformer operation **141**

C.0.5 Voltage and current amplitudes with a complex load 141
C.0.6 Measurement of the U-wire impedance 146
C.0.7 Rf transformer operation 147
C.0.8 Tuning the rf generation circuit to a certain frequency range 150

D Shape of the mw spectroscopy line **153**

D.0.9 Effect of gravity sag on the spectroscopy line 153
D.0.10 Uncertainty of magnetic field measurement 159
D.0.11 Step function and the mw spectroscopy fitting formulae 159

E Shape of the rf induced atom loss curve during molecule associations **163**

E.0.12 Two-body losses in a two-component BEC 163
E.0.13 Number of collisions between atoms in different states 166
E.0.14 Rf-induced atom loss curve fitting formulae 167
E.0.15 Measurement of the bound state energies at 0 G 169

List of Figures

1.1 Hyperfine structure of ^{87}Rb and six atomic spins combinations in molecules 5

1.2 Two theoretical predictions for the Zeeman energy of the molecular states . 6

2.1 Photographs of the atom chip 11

2.2 BEC transition during evaporative cooling 12

2.3 Schematic representation of the process of imaging 14

2.4 Experimental data for the measurement of the saturation intensity 16

2.5 Measured I_S decreases sensitivity of N to the imaging laser intensity 17

2.6 Comparison of the time diagrams of the full-frame and the kinetics modes . 19

2.7 Measurement of the camera pixel size in the object plane 20

2.8 Z-wire trap frequencies for different magnetic fields at the trap botton . . . 22

2.9 Experimental measurements of the frequencies of the Z-wire trap 24

2.10 Measurement of the distance from the cloud to the chip wire 26

2.11 Preparation of a two-component BEC by a two-photon transition 28

2.12 Adiabatic passage by the mw field 30

2.13 Experimental measurement of magnetic noise in the laboratory 33

2.14 Electrical scheme of decoupling the AC and DC currents 35

2.15 Equivalent circuit of the signal generation 36

2.16 Connection diagram for the measurement of the chip wire inductance 39

2.17 Experimental data of the measurement of the inductance of the chip wire . 40

2.18 Connection of the rf transformer in electrical circuits 41

2.19 Connection diagram for matching the chip-circuit to a chosen frequency . . 43

2.20 Signal amplitude versus frequency during matching impedance procedure . 44
2.21 Electric circuit of a current controlling switch 45

3.1 Energy diagram of the atoms during the mw spectroscopy 49
3.2 Mw spectral line of BEC in absence of gravity 50
3.3 Atoms in the shell are resonant at the same mw frequency 52
3.4 Theoretical mw spectral lines in the presence of gravity 53
3.5 Dependence of the mw spectral line on number of atoms in BEC 55
3.6 Effect of dipole oscillations on the spectral line 57
3.7 Contribution of different broadening into spectral lines 60
3.8 Time sequence of the mw spectroscopy experiment 62
3.9 Typical single-photon mw spectroscopy curves 63
3.10 The two-photon excitation, used for the AC magnetic field calibration . . . 66
3.11 Experimental data for two-photon Rabi flopping 67
3.12 Simultaneous imaging of atoms in different states during Rabi flopping . . . 68
3.13 Experiment data for the mw Rabi flopping 69

4.1 Dependence of theoretical rf induced γ_{12}^{rf} on the rf frequency 75
4.2 Simulation of the number of atoms evolution 76
4.3 Time sequence for the experiment of rf-induced molecular association 77
4.4 Search for an atom-molecule resonance for the bound state A 78
4.5 Shift of the rf induced loss resonance by the DC-magnetic field 80
4.6 Proof of the interspecies interaction origin of the atom losses 80
4.7 Rf induced loss curve for the molecule formation rate experiment 82
4.8 Experimental data for the measurement of two-body loss coefficients 83
4.9 Theoretical curves for the molecule formation rate 83
4.10 Atom loss curves for A and B molecular states 89
4.11 Effect of broadening factors on the molecular state A loss profiles 91
4.12 Typical rf induced loss curves of the bound state A 93
4.13 Typical rf induced loss curves of the bound state B 94

4.14 Comparison of the experimental data with theory [55] 97
4.15 Experimental data versus theory [55], subtracting the linear dependence . . 98
4.16 Calibration of the rf field amplitude 101
4.17 Loss curve dependence on the amplitude of the rf field 102
4.18 Dependence of loss coefficient on rf power 103
4.19 Shift of the DC magnetic field for different amplitudes of B_{rf} 103
4.20 Simultaneous detection of four molecular states 105

A.1 Loss resonance feature disappears after filtering of the rf signal 126
A.2 Spectra of the SRS345 generator signal at 23.077 MHz 128
A.3 Investigation of the sideband frequency shifts 129

B.1 Z-wire with infinite central wire and semi-finite ends 132
B.2 Magnetic fields, generated by different parts of the Z-wire 132

C.1 Lossless transmission line 141
C.2 Matching of an rf field source with a line terminated by a complex load . . 143

D.1 Coordinate system used for calculation of mw spectroscopy line shape . . . 154
D.2 Representation of areas in BEC, described by different functions in Eq. D.5 156
D.3 Dependence of Thomas-Fermi radius R_0 and the ratio $\frac{z_g}{R_0}$ on magnetic field 158
D.4 Graphic representation of the step function 160

List of Tables

2.1 Comparison of theoretical and experimental frequencies for the Z-wire trap 25

3.1 Extracted parameters from the best fit of the mw spectroscopy lines 65

4.1 Best fits parameters for rf-induced atom loss curves 95

4.2 Bound state energies at 0 G. 99

4.3 Comparison of predictions [54] and [55] with experiment 100

CHAPTER 1

Introduction

1.1 Motivation

A Bose-Einstein condensate (BEC) is another phase (state of matter like solid, liquid, gas or plasma) in which a large fraction of a bosonic ensemble settles in the lowest quantum state. In a typical experiment bosons (atoms with an integer spin) need to be sequentially cooled in a vacuum chamber by several techniques (laser cooling and trapping, evaporative cooling, sympathetic cooling) from room or higher temperatures (many hundreds of Kelvin) down to hundreds of nano-Kelvins above absolute zero where the atomic wavefunctions start to overlap and the bosons collapse into a single quantum state. All the bosons in a BEC behave as a single atom and it allows to observe quantum properties on a macroscopic scale. By imaging N atoms in a BEC with resonant or detuned laser light experimentalists can reconstruct the wave function of a single atom in the condensate as it is equivalent to making N images of the same atom in its original state. For this reason BEC is an ideal tool for testing laws of quantum mechanics and for simulation of more complex quantum systems.

After the first experimental demonstration of ^{87}Rb (Anderson et al. [1]), ^{7}Li (Bradley et al. [2]) and ^{23}Na (Davis et al. [3]) BECs in 1995 the major pathways and techniques were developed that has led to successful observation of BEC of most alkali atoms such as ^{39}K (Roati et al. [4]), ^{41}K (Modugno et al. [5]), ^{85}Rb (Roberts et al. [6]), ^{133}Cs (Weber et

al. [7]) as well as non-alkali species ^{1}H (Fried et al. [8]), metastable ^{4}He* (Robert et al. [9]), (Pereira Dos Santos et al. [10]), ^{52}Cr (Griesmaier et al. [11]), ^{174}Yb (Takasu et al. [12]), ^{84}Sr (Stellmer et al. [13]), ^{40}Ca (Kraft et al. [14]), ^{164}Dy (Lu et al. [15]), ^{168}Er (Aikawa et al. [16]) and diatomic molecules of fermionic ^{6}Li (Jochim et al. [17]), ^{40}K (Greiner et al. [18]). Nowadays ultracold molecules and tuning the interactions between the ultracold atoms arouse a lot of interest of experimentalists and theorists. Major cooling techniques tested on ultracold atoms can be extended to ultracold molecules which opens an opportunity for new experiments in chemistry and molecular physics. However, the direct cooling of molecules is not an easy task because of their complex quantum structure. For this reason another way of producing ultracold molecules is used by creating them from the ultracold atoms. Various pathways have been used for conversion of the ultracold atoms into ultracold molecules, such as photo-association or magnetic Feshbach resonances.

In this thesis we experimentally demonstrate a new way of rf-induced molecular association without assistance of magnetic Feshbach resonances, which gives certain advantages over the previously used methods such as very low heating (absence of spontaneous emission) and the ability to work at arbitrary magnetic fields.

1.2 Background

This section contains an overview of experimental and some theoretical works related to the creation and investigation of the properties of ultracold molecules.

In the first experiments cold molecules were made by a photoassociation method from laser cooled atoms of ^{85}Rb (Cline et al. [19], 1994) (experiment data was complemented in 2006 by Bergeman et al. [20]), ^{133}Cs (Fioretti et al. [21], 1998), (Takekoshi et al. [22], 1999), ^{39}K (Nikolov et al. [23], 1999), ^{87}Rb (Fioretti et al. [24], 2001). Later, the first ultracold molecules were created from BEC samples via Raman transitions: $^{87}Rb_2$ (Wynar et al. [25], 2000), (Verhaar et al. [26], 2001), starting an avalanche of publications about the new world of ultracold molecules. In an interesting realization the two-photon Raman photoassociation process was used for the creation of $^{87}Rb_2$ molecules in the two last bound states in an optical lattice with a single molecule per site (Rom et al. [27], 2004). Photoassociation was also used for production of polar RbCs molecules in their vibronic

ground state from laser cooled atoms (Sage et al. [28], 2005).

From 2002 magnetic Feshbach resonances (Chin et al. [29]) have become a workhorse for numerous experiments to generate ultracold molecules. The first experimental realizations of coherent mixtures of atoms and molecules in ^{85}Rb BEC created by the rapid scan of magnetic field across the magnetic Feshbach resonance, were reported (Donley et al. [30] and Kokkelmans et al. [31], 2002). The same technique was used for the measurement of the bound state energy of $^{85}Rb_2$ molecules (Claussen et al. [32], 2003). Another way of employing magnetic Feshbach resonances was experimentally demonstrated in 2003: an ultracold sample was held at a magnetic field near the Feshbach resonance on the positive scattering length side which enhanced three body collision rates and led to the creation of $^{6}Li_2$ molecules (Cubizolles et al. [33], Jochim et al. [34]). Other experiments involve the creation of $^{87}Rb_2$ molecules by sweeping over the magnetic Feshbach resonance with the subsequent conversion of molecules back into atoms and imaging by an absorption technique (Dürr et al. [35], 2004). The most recent experiment has been done in conjunction with a dark-state two-photon spectroscopy of ultracold molecules $^{87}Rb_2$ in an optical lattice, created from BEC by scanning through the resonance at 1007.4 G (Strauss et al. [36], 2010).

Utilization of magnetic Feshbach resonances was extended by the implementation of an rf field for the creation of ultracold molecules and precise measurements of their bound energies. The combination of magnetic Feshbach resonances and rf fields has led to reports of successful experimental observation of the molecules made from bosonic and fermionic, ultracold and quantum degenerate atomic samples: $^{40}K_2$ (Regal et al. [37], 2003), $^{6}Li_2$ (Chin et al. [38], 2005), $^{85}Rb_2$ (Thompson et al. [39], 2005), ^{85}Rb$-^{87}$Rb (Papp et al. [40], 2006) and ^{40}K$-^{87}$Rb (Ospelkaus et al. [41], 2006). Growing interest in rf-spectroscopy led to development of a number of theories about rf excitation rates and line shapes (Chin et al. [42], 2005) as well as the conversion efficiency as a function of different parameters (pulse duration, amplitude, field modulation frequency, temperature of the gas, Hanna et al. [43], 2007). Some experimental data about radio-frequency association of molecules near Feshbach resonances have been published together with analytic theories that describe the asymmetric shapes of the observed rf spectra for ^{40}K$-^{87}$Rb molecules (Klempt et

al. [44], 2008), ^{41}K−^{87}Rb (Weber et al. [45], 2008), $^{87}Rb_2$ (Kaufman et al. [46], 2009). Recently a new paper was published on the archive about the creation of $^{40}K_2$ molecules by sweeping over the magnetic Feshbach resonance and then using rf-spectroscopy to investigate bound-to-bound transitions as well as free atoms-to-bound state spectroscopy with $\Delta M = 0$ and $\Delta M \pm 1$ in the vicinity of the Feshbach resonance (Huang et al. [47], 2014).

Another type of experiment that is developing at present is the transfer of created weakly bound Feshbach molecules into more tightly bound states. Already experimentally demonstrated has been an optical method of transfer in $^{87}Rb_2$ (Winkler et al. [48], 2007), (Lang et al. [49], 2008) and on ^{40}K−^{87}Rb (Ospelkaus et al. [50], 2008) as well as the other method of radio-frequency adiabatic passage for $^{87}Rb_2$ (Lang et al. [51], 2008).

Nowadays rf-coupling is widely used in experiments with ultracold molecules and offers the highest precision for measurements of the bound energies. However, all rf-induced molecular associations so far have been restricted to being performed in the vicinity of magnetic Feshbach resonances (proximity of magnetic Feshbach resonance maximizes the coupling efficiency of the colliding atoms to the bound state, Beaufils et al. [52], 2010). In 2010 three theoretical papers were published about the employment of mw- (Papoular et al. [53]) or rf-driven (Tscherbul et al. [54]), (Hanna et al. [55]) molecular associations at arbitrary DC-magnetic field, regardless of the existence of magnetic Feshbach resonances. These ideas offer very promising opportunities for the rf-induced method to become a universal and widely used technique of molecular association and extend the number of ultracold molecules to be made from many different elements. Other proposals are concerned with using the rf field not just without, but instead of, the magnetic Feshbach resonances (Tscherbul et al. [54], 2010), (Avdeenkov et al. [56], 2012) to tune the interaction between the atoms in a similar way to optically induced Feshbach resonances (experimentally observed by Theis et al. [57], 2004 and Enomoto et al. [58], 2008). Alternatively, scattering lengths in multicomponent quantum gases might be tuned independently for every species by the employment of magnetic and radio-frequency fields (Zhang et al. [59], 2009). Other examples of the application of ultracold molecules include atomic scattering lengths measurements (theory has been tested on Cs_2 molecules, Lange et al. [60], 2009)

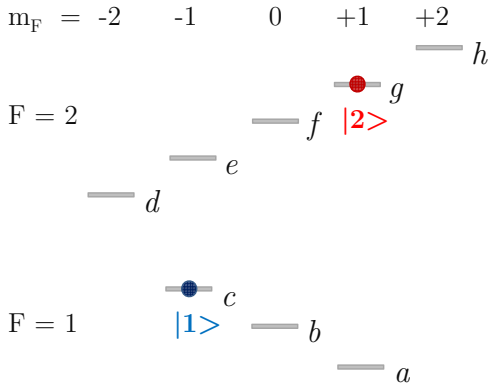

Δ m$_F$ = +1	Δ m$_F$ = −1
A (ch)	C (cf)
B (bg)	D (be)
E (af)	F (ad)

Figure 1.1: Zeeman splitting of the hyperfine structure of ^{87}Rb in magnetic field with letter notations for each level. The case of the mixture of atoms "c+g" in the entrance channel is of particular interest. With the selection rule for transitions $\Delta m_F = \pm 1$ rf-induced association leads to six possible molecular states, presented in the table.

and testing variations of the fundamental constants via precise measurements (accuracy $\sim$ 3 Hz) of mw-transitions in cold CH molecules (Truppe et al. [61], 2013).

1.3 Rf-induced molecular association

The main aim of the current experimental work is to observe for the first time rf-induced molecular association without the assistance of magnetic Feshbach resonances. The original inspiration has come from two novel theoretical papers by Tscherbul et al. [54] and Hanna et al. [55] published in 2010 where the authors used different approaches (the coupled channels method and the multichannel quantum defect method, respectively) and have come qualitatively to the same results. A quantitative analysis is presented in Section 4.3.

Figures 1.1 and 1.2 explain the principle of rf-induced molecular associations. The collision of two atoms in a BEC is a multi-channel process (i.e., multiple outcomes of the scattering) as atoms can undergo transitions to different internal states (Fig. 1.1) (this is the major loss mechanism of trapped atoms, Sec. 4 and 5 in Pethick an Smith [62]). The presence of the resonant radio-frequency radiation adds an additional output channel for the scattering process: the pair of atoms can emit a photon and become a molecule.

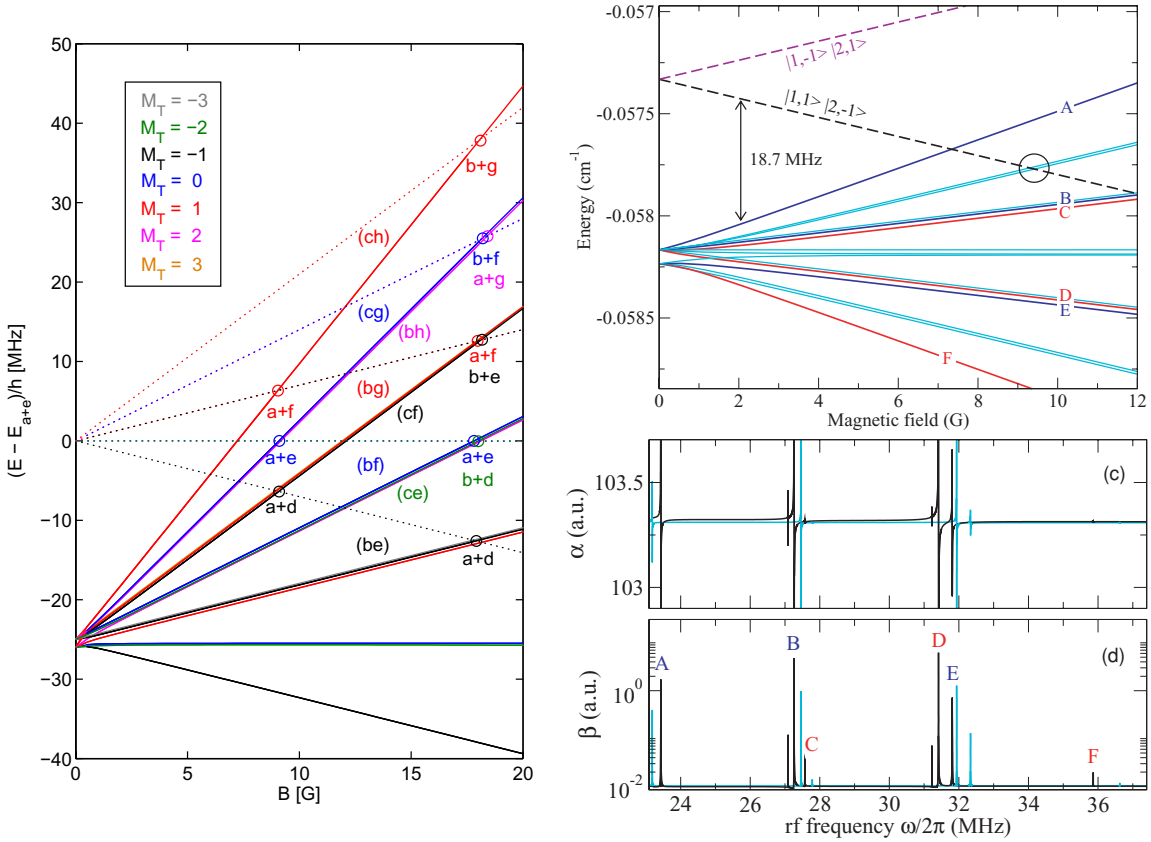

Figure 1.2: Adapted from [55] (left side) and [54] (right side). Comparison of theoretical predictions for the energies of molecular states with respect to magnetic field. On the left side the energies of pairs of colliding atoms are shown as dashed lines, labeled as a sum of the constituent states of atoms; energies of molecular states are labeled as small letters in brackets. On the right hand side the energies of pairs of free atoms are shown as dashed lines with solid lines representing the energies of the bound states. Capital letters represent the molecular states that can be achieved by rf-association. The relative and absolute strengths of the atoms-molecule coupling resonances have also been calculated for a 3.23 G trap.

The appeared photon has a momentum that leads to the selection rule for the transition $\Delta m_F = \pm 1$ (π-transitions with $\Delta m_F = 0$ are also possible but they are not of interest to us).

Each Zeeman level of the hyperfine splitting of ^{87}Rb atom is commonly described by a letter (Fig. 1.1). On the left side of Fig. 1.2 the authors show the energies of free atoms (a sum of two letters) and molecules (two letters in brackets) versus magnetic field for different combinations of constituent atoms. Atoms in initial states "c+g" are of particular interest because they are widely used in magnetic traps. The authors of [54] use different notations (right side of Fig. 1.2) which is explained in the table in Fig. 1.1. Energies of free atoms are shown as dashed lines in contrast with molecular states, drawn by solid colored lines with capital letters displaying the allowed transitions for the $|1,-1\rangle+|2,1\rangle$ (c+g) incoming channel. It is not easy to see because of the different units of energy but both theories predict energies of magnetic states around the same values. In [54] the authors have also calculated the exact energies of all molecular states for rf field amplitudes of 4 G and 10 G at 3.23 G of DC-magnetic field and given an assessment for the relative and absolute strengths of the resonances by calculating the imaginary part of the scattering length which is proportional to the two-body loss coefficient for the collisions of atoms in different initial states (bottom right part in Fig. 1.2).

1.4 Thesis outline

This thesis starts with an introduction that gives a historical overview on the experiments and theoretical work related to ultracold molecules. It also describes the direction of the development of methods for creation and analysis of ultracold molecules and highlights rf field spectroscopy as one of the most promising and accurate techniques.

The second chapter describes the experimental setup that is able to produce BEC of ^{87}Rb on the chip. It covers different stages of cooling of ^{87}Rb atoms in the high vacuum chamber and observation of the BEC transition by absorption imaging. Implementation of the new imaging camera, operating in kinetics mode, is a significant change in the experimental apparatus which is why it is given much attention in Section 2.2. Different auxiliary techniques such as creation of a two-component BEC, adiabatic passage, measurements of trapping frequencies that have been used in the main experiment are also

described in this chapter. The last section of the chapter is about the generation of strong rf fields, which are necessary for rf-induced molecular associations.

Chapter 3 describes the methods that have been used for measurements of DC and AC magnetic fields. Microwave spectroscopy, which employs transitions between Zeeman levels of the hyperfine structure, is a widely used technique for the precise measurement of the magnetic field. Analyzing the spectroscopy line shapes we have developed a theory that gives a better understanding about the process of the resonant mw-coupling and the broadening mechanisms which leads to smaller errors in magnetic field measurements. The second part of the chapter contains the description of the method for the calibration of the amplitude of the rf field. Theoretical predictions [54] and [55] for rf-induced molecular associations have been made for rf field magnitudes larger than 1 G. This necessitated us mastering high rf field generation as well as measurements of the radio-frequency field amplitude.

Chapter 4 is the main part of the thesis, containing all the important experimental results. It starts with the description of the experimental conditions for the first observation of rf-induced molecular association without the assistance of magnetic Feshbach resonances, followed by the analysis of the observed rate of molecular association. The shapes of the observed lines are analyzed in a similar way to the case of the mw-spectroscopy, leading to an unprecedented $\sim$2 kHz precision in measurements of the molecular state energies. In the last section of the chapter the experimental data for the energies of five molecular states at different magnetic fields is compared with theoretical predictions [55] and [54]. All the key ideas of the thesis are summarized in the conclusion, followed by the appendices which serve as a repository for comments and equation derivations.

CHAPTER 2

Experimental setup

This experimental setup was described in PhD theses of previous students in our group [63], [64], [65], [66]. The current chapter describes the every-day procedure of producing Bose-Einstein condensates with detailed focus on recent improvements in electronic circuitry for generating high power radio frequency electromagnetic fields on an atom chip [67].

Bose-Einstein condensation of dilute atomic gases occurs at extremely low temperatures (typically a few hundreds of nano-Kelvins). To isolate ^{87}Rb atoms from the room temperature environment they are trapped in magneto-optical or magnetic traps within an ultra-high vacuum chamber. Alkali atoms are in the first group of the periodical table of elements and are particularly attractive for laser cooling and trapping because they have only one electron outside a closed shell with strong $s - p$ optical transitions. ^{87}Rb is currently the most common element for BEC production because commercial laser systems with 780 nm wavelength are readily available.

2.1 BEC production on an atom chip

2.1.1 Mirror Magneto-Optical Trap (MMOT)

Each BEC production cycle starts with passing a current of 6.5 A for 10 s through a dispenser that can release rubidium atoms in a chemical reaction at high temperatures [68]. As the dispenser is not isotopically enriched the composition of the rubidium vapours is

determined solely by the natural abundances of the isotopes: 72% of ^{85}Rb and 28% of ^{87}Rb. Rubidium atoms are initially trapped in a mirror-magneto-optical trap (MMOT) which is created by a pair of water cooled quadrupole coils located outside of the vacuum chamber and four red-detuned laser beams. The trapping laser is locked to the transition $5^2S_{\frac{1}{2}}$(F=2) − $5^2P_{\frac{3}{2}}$(F′ =3) of ^{87}Rb , so automatically addresses only one isotope. Frequency locking is based on polarization spectroscopy with a double-pass acousto-optical modulator (AOM) that allows the detuning of trapping light to be changed without affecting its coupling to the fibre. The main MMOT laser beam passes through an additional single-pass AOM to set the total detuning from the resonance equal to $\Delta f_{MOT} = f_1$ - $2f_2$ = -18 MHz, [66], where f_1 and f_2 are the frequencies of the single- and double-pass AOMs, respectively. The total power of the trapping laser is chosen to be around 180−210 mW at the output of the optical fibre before the splitting into four beams to form a MMOT. Each trapping beam is mixed with repumper laser light tuned to the $5^2S_{\frac{1}{2}}$(F=1) to $5^2P_{\frac{3}{2}}$(F′=2) transition in order to pump atoms that have spontaneously decayed into the dark F=1 state. The fibre output of the repumper laser is typically 11.5 mW.

Rubidium atoms coming from the dispenser have an average temperature close to a thousand Kelvin. For this reason the dispenser is located below the chip edge which protects the growing cloud of cold ^{87}Rb from fast atoms coming directly from the dispenser (Fig. 2.1). The MMOT operates with large trapping beams diameters (∼45 mm) to yield a high capture velocity from the low energy tail of the room temperature Boltzmann distribution, aiming to trap atoms after contact with the walls of the chamber. The dispenser is operated in a cyclical fashion being turned on to rapidly raise the Rb vapour pressure within the UHV chamber, enhancing the MMOT loading rate to $R_{peak} \sim 5{\cdot}10^7$ atoms/second. When turned off the dispenser rapidly cools (<2 sec) and the background vapour pressure is reduced by two orders of magnitude allowing long lifetime magnetic trapping. While these two counter running requirements can be achieved by Zeeman slowers [69], chirp cooling methods [70], [71] or cold high flux atom sources [72], [73], this single vacuum system approach remains quite simple and in this setup robustly captures $5 \cdot 10^8$ atoms within 10 seconds of MMOT stage. All untrapped atoms are quickly removed from the vacuum chamber by a continuously working ion pump.

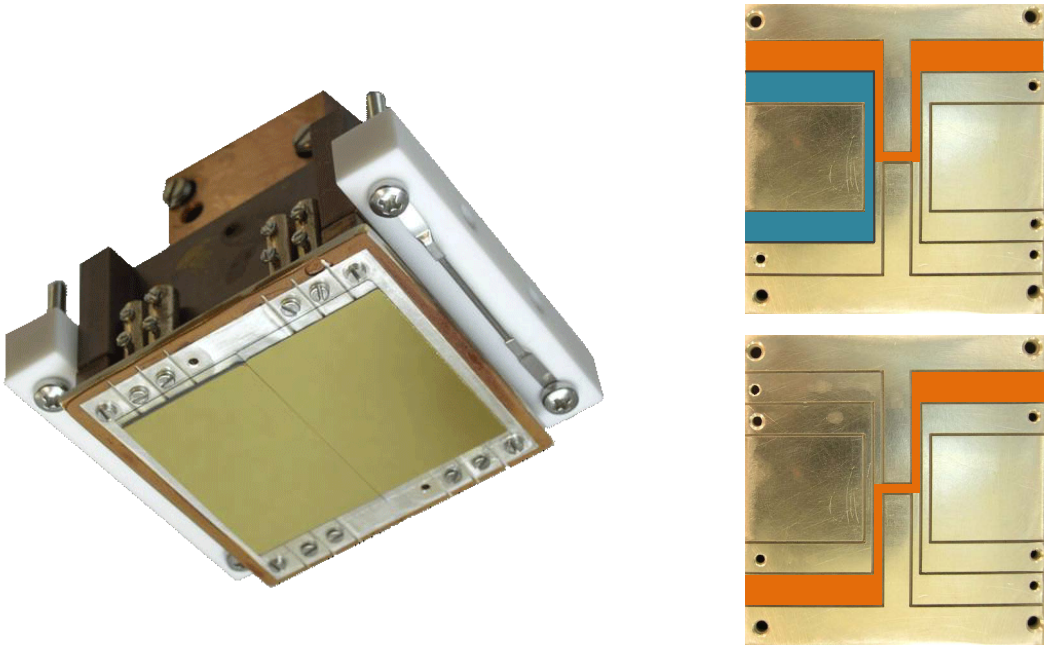

Figure 2.1: Left: the atom chip. Over the electric wires on the chip there is a substrate with a reflective gold coating used for MMOT creation. The silver wire on the white substrate is the rubidium dispenser. Right: wires on the chip. The End-wire (blue) is used for radio-frequency evaporative cooling. Magnetic traps are created by passing an electric current either through a U- (upper right figure) or a Z-wire (lower right figure) together with a homogeneous magnetic field B_{xLarge} directed horizontally and perpendicular to the central wire of the chip.

2.1.2 CMMOT, optical pumping and rf-evaporation in the Z-wire MT

The initial MMOT provides both cooling and trapping of the atoms from the vapors of Rb at the same time and at the end of this first stage atoms are transferred to the compressed MMOT (CMMOT). This process is realized by ramping down the current in the external quadrupole coils with the simultaneous creation of a quadrupole trap on the atom chip by ramping up the current through the U-wire (Fig. 2.1) and in the bias magnetic coils B_{xLarge}.

During the 50 ms CMMOT stage atoms are both radially compressed and translated to a position below the atom chip where they can be magnetically captured. To improve

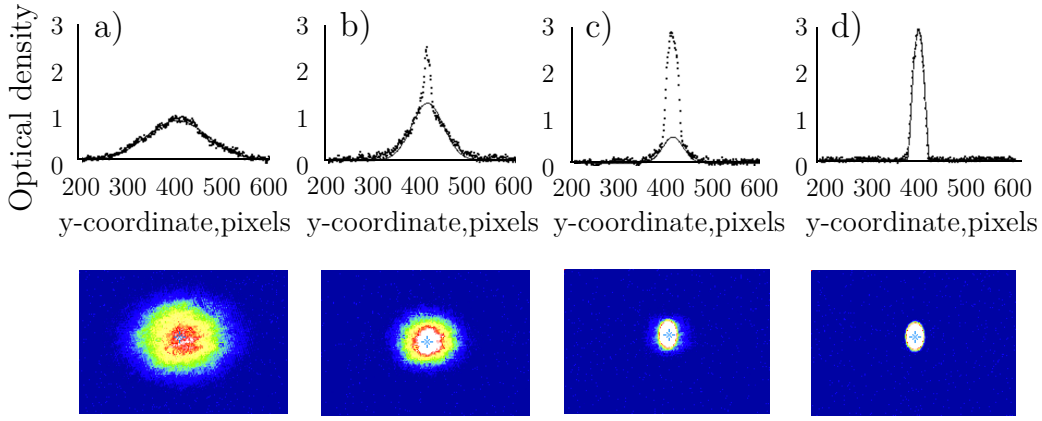

Figure 2.2: BEC transition during two stages of evaporative cooling. Bottom pictures are examples of absorption images (Section 2.2.1) and top pictures show their cross sections through the centres in the horizontal direction. (a) shows cold thermal atoms at the end of the first stage of evaporative cooling (22 MHz−650 kHz) in the trap with 0.7 G trap bottom. During the second evaporation at 3.23 G the radio-frequency is logarithmically swept from 2.4 MHz down to 2.29 MHz to end up with a cloud of a pure BEC (d). Pictures (b) and (c) show intermediate conditions with bimodal distribution of the cloud profiles for second evaporations 2.4 MHz−2.35 MHz and 2.4 MHz−2.295 MHz, respectively.

transfer to the magnetic trap a further 8 ms polarization gradient cooling (PGC) stage is applied in a reduced radial B-field gradient and increased laser detuning ~ -60 MHz. This lowers the cloud temperature with little reduction in the cloud density or movement of the cloud position.

In order to prepare BEC in the $F = 1, m_F = -1$ state Rb atoms need to be transferred into this state. Just after PGC the trapping light is turned off, followed by switching on σ^-- polarized optical pumping light ($5^2S_{\frac{1}{2}}$(F=2) to $5^2P_{\frac{3}{2}}$(F′=2)) with a small fraction of $\pi-$ polarized light, [65], [66]. The optical pumping beam and σ^-- polarized repump laser beam pump the atoms into the F=2, $m_F = -2$ state during 1.5 ms after PGC, followed by closing of the repump laser shutter. The optical pumping laser remains on for another 0.5 ms and pumps the atoms into $F = 1, m_F = -1$. Immediately after this, the currents through the Z-wire on the chip and the B_{xLarge} and B_{ySmall} coils are ramped up to create a pure magnetic trap (MT) of Ioffe-Pritchard design [74], [75]. To purify the atom cloud

in magnetic trap a 5 ms pulse of trapping light is applied to blow away atoms which had remained in the F=2 state. This yields a typical starting condition for forced rf-frequency evaporation of N = $(5 - 8)\cdot 10^7$ atoms.

A two-stage evaporation scheme is used to prepare a BEC in a magnetic trap with a trap bottom of 3.23 G. Two stages must be used as the radial trap frequency is inversely proportional to the minimum value of the magnetic field and this limits the maximum trap bottom of the trap during first evaporation. In the first stage lasting 13 s the rf is logarithmically swept from 22 MHz to 650 kHz while the MT is further tightened by reducing the Z wire current. Before the second evaporation sequence the trap bottom is ramped to its final value over 500 ms by applying a uniform field along the trap axis y. This procedure limits movement of the magnetic trap minimum and sloshing of the final cloud. The second rf evaporation runs over 4 s from 2.4 MHz to 2.29 MHz (Fig. 2.2).

2.2 Imaging system

One of the main reasons why Bose-Einstein condensates have become such popular quantum objects to study is the convenience of using optical wavelength light for imaging the wave function of BEC atoms. We use a cigar-shape magnetic trap in which the BEC has an ellipsoidal shape with a typical Thomas-Fermi radius [76] of ~ 5 μm in the radial direction and ~ 50 μm in the axial direction for a typical number of atoms $(1 - 3) \cdot 10^5$ in a magnetic trap with a trap bottom of 3.23 G. The conventional imaging technique is to use a laser light and observe either the fluorescence, absorption or phase contrast (dispersive imaging) [77]. In this experimental setup the BEC wave function is imaged by an absorption imaging technique after ballistic expansion with resonant laser light (Fig. 2.3).

2.2.1 Absorption imaging

Efficient direct imaging of the BEC which is initially prepared in the $|F = 1, m_F{=}-1\rangle$ state is not possible as the $5^2S_{\frac{1}{2}}$(F=1) manifold does not have cycling transitions. This necessitates the transfer of the atoms into the F = 2 hyperfine level prior to absorption imaging on the $5^2S_{\frac{1}{2}}$(F=2) $-$ $5^2P_{\frac{3}{2}}$(F′=3) cycling transition. Two different methods of

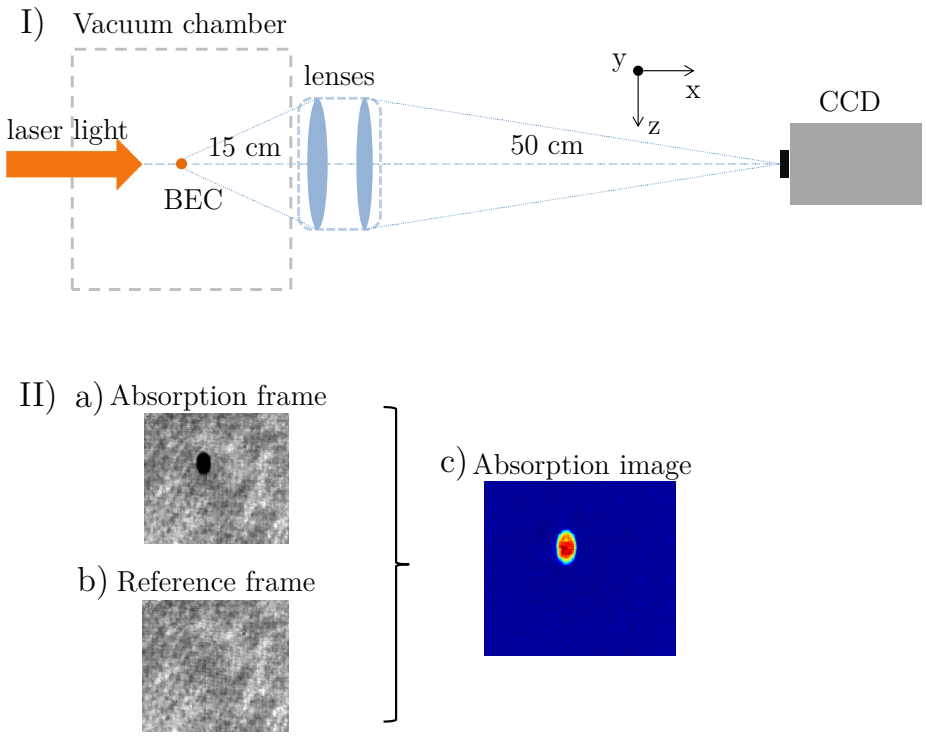

Figure 2.3: (I) Schematic representation of the imaging process: resonant laser light propagates through the cloud of atoms towards the CCD camera. The image of the cloud is magnified ~ 3 times with the lenses used in the setup [65]. (II) Two sequential frames (a) absorption and (b) reference are used to calculate the number of atoms in an absorption image (c).

transfer have been used in this apparatus: repumping with laser light and mw adiabatic passage. The first method consists of utilizing a repumper laser pulse of duration 2.6 ms (part of this time is used for the laser shutter to open) just before the application of the imaging 100 μs light pulse. It is crucial in this method to take an image just after the transfer of atoms as they start expanding due to recoil energy from absorption and spontaneous emission of photons. The second method employs mw adiabatic passage of atoms from the initial state $|1,-1\rangle$ into $|2,-2\rangle$ during relaxation of the magnetic fields forming the Z-wire trap (Section 2.6). As the mw adiabatic passage doesn't transfer sufficient momentum to heat up the cloud standard time of flight imaging can be used with typical fall times of 20 ms.

Resonant imaging is an inherently destructive process due to the momentum transferred to the BEC in the imaging direction and the diffusive heating arising from spontaneously emitted photons. An experimental cycle time of 65 s duration is achieved in the atom chip apparatus which is chosen to limit slow poisoning of the vacuum by rubidium vapour during daily operation. Typical BEC images are shown in Fig. 2.3 (II). Each frame is a 2D array of numbers which are proportional to the electric charge accumulated on each pixel that occurred during the photogeneration process. Thus the counts at each pixel are proportional to the number of impinging photons. The Princeton Instruments ProEM 512 CCD camera uses Peltier cooling to lower the sensors temperature down to $-20\ C$ and reduce thermal dark counts. Screening of the low ambient light levels present in the laboratory and mechanical shuttering of all laser beams is sufficient to eliminate the use of background frame images, so only an absorption frame (Fig. 2.3 II (a)) and a reference frame (Fig. 2.3 II (b)) are required.

Atoms present in the absorption frame reduce the intensity of the laser beam due to the processes of absorption and re-emission the photons out of the imaging beam. The 3D cloud is effectively projected onto the y-z plane as a shadow image (Fig. 2.3), from which the number of atoms can be calculated from the differential Beer-Lambert law [78]:

$$\frac{dI(x,y,z)}{dx} = -\sigma n(x,y,z) I(x,y,z) \tag{2.1}$$

where n is a number density that depends on x and σ is the absorption cross-section.

Integration of Eq. 2.1 over the probe propagation direction x (Fig 2.3 (I)) allows one to calculate the intensity reduction due to the whole cloud for each pixel of the CCD:

$$n_c(y,z) = \int n(x,y,z)dx = \frac{1}{\sigma} ln(\frac{I_0}{I}) \tag{2.2}$$

where $n_c(y,z)$ is the column density of the atoms in the absorption frame. Thus the total number of atoms imaged by the part of the probe beam falling on a single pixel is equal to

$$N_{pixel} \propto n_c(y,z) \cdot A \tag{2.3}$$

where A is the area of a pixel (in the case of a magnified cloud this quantity refers to the area of the pixel in the object plane). The sum over all the pixels in the frame gives the total number of atoms.

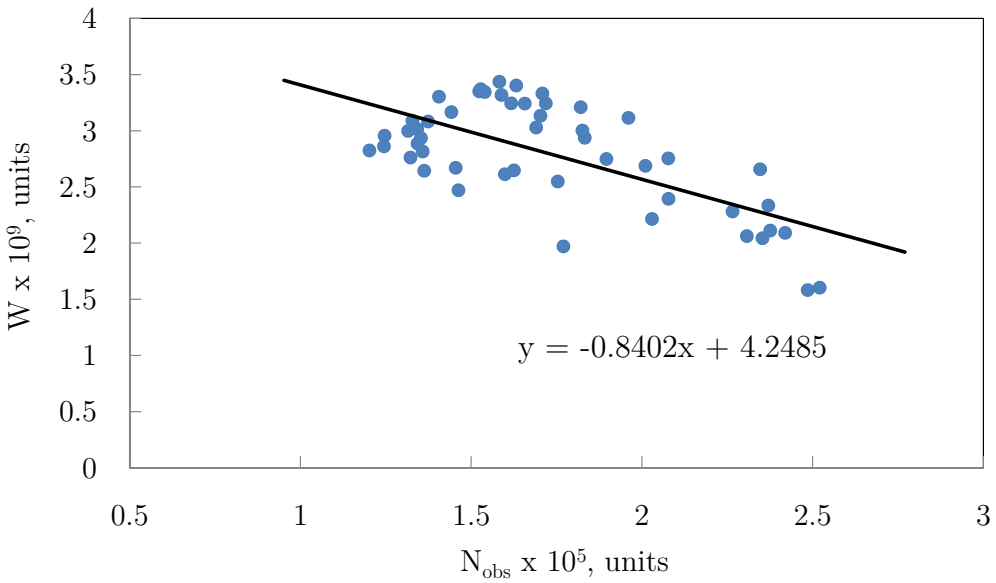

Figure 2.4: Measurement of I_S expressed in counts of the CCD camera. We make a series of images of low density thermal clouds with varying intensity of the probe beam. N_{obs} and W are defined in Eq. 2.6. The calibration yields $I_S = (8400 \pm 1300)$ counts.

2.2.2 Measurement of saturation intensity

Equations 2.1 and 2.2 can be rewritten to take into account the dependence of the absorption cross-section on intensity (saturation) and detuning of the imaging light [79], [65]:

$$\begin{aligned} \sigma &= \frac{\sigma_0}{1 + \frac{I}{I_S} + 4(\frac{\Delta}{\Gamma})^2}, \\ n_c(y,z) &= \frac{1}{\sigma_0}\left(\left[1 + 4(\frac{\Delta}{\Gamma})^2\right] ln\frac{I_0}{I} + \frac{I_0 - I}{I_S}\right) \end{aligned} \tag{2.4}$$

here Γ is the natural linewidth (for the D2 transition ^{87}Rb it is equal to $2\pi{\cdot}6.065(9)$ MHz), Δ is the detuning of the laser light from the resonance and σ_0 is the resonant cross-section for which the calculated value for the D2 transition of ^{87}Rb is equal to $2.9 \cdot 10^{-13} m^2$. The saturation intensity I_S can also be theoretically calculated and for a pure $\sigma+$ stretched transition is 1.67 $mW cm^{-2}$. However, this value is strongly dependent on the polarization of the imaging light; for instance linear polarization yields $I_S = 3.05\ mW cm^{-2}$ [80].

Imperfections of laser polarization affect the atom number calculation. Thus for a particular imaging setup (CCD camera, lens setup, imaging pulse length, detuning of the

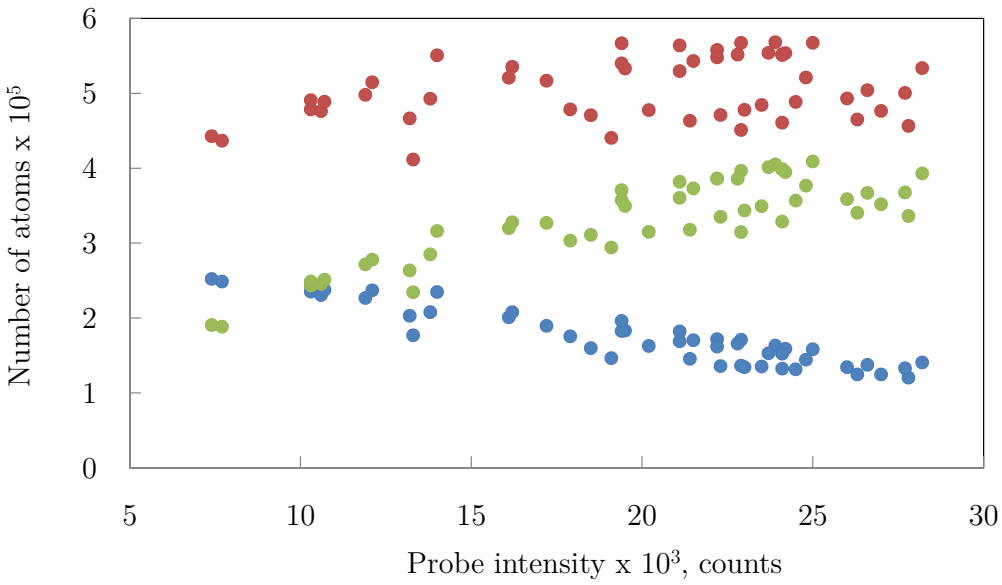

Figure 2.5: Dependence of N_{obs} (blue), $\frac{W}{I_S}$ (green) and total number of atoms N (red) on the probe beam intensity, expressed in CCD counts. Taking into account I_S significantly decreases the sensitivity of N to the imaging laser intensity and improves the precision of the atom number calculations.

probe beam) a measurement of the saturation intensity I_S expressed in CCD counts must be taken [65]. The number of counts in each pixel of the frame is designated as I_{abs} and I_{ref} for the absorption and reference frames, respectively, and they are proportional to the intensity of the probe light. Following from equations 2.2, 2.3 and 2.4 the total number of atoms can be calculated by summing over all pixels of the CCD chip:

$$N = \Sigma_{y,x} A \cdot n_c(y,z) = \frac{A}{\sigma_0}\Sigma_{y,x}\left((1+4(\frac{\Delta}{\Gamma})^2) ln\frac{I_{ref}}{I_{abs}}\right) + \frac{1}{I_S}\frac{A}{\sigma_0}\Sigma_{y,x}\left(I_{ref} - I_{abs}\right), \quad \text{or} \quad W(N_{obs}) = N \cdot I_S - N_{obs} \cdot I_S \tag{2.5}$$

with the designations:

$$N_{obs} = \frac{A}{\sigma_0}\Sigma_{y,x}\left(\left[1+4(\frac{\Delta}{\Gamma})^2\right] ln\frac{I_{ref}}{I_{abs}}\right), \quad W = \frac{A}{\sigma_0}\Sigma_{y,x}\left(I_{ref} - I_{abs}\right) \tag{2.6}$$

For large saturation intensities ($\frac{W}{I_S} \rightarrow 0$) the total number of atoms is equal to N_{obs}, whereas N_{obs} gives an underestimated number of atoms with the low probe intensities I_S, which can be corrected by the addition of $\frac{W}{I_S}$ (Fig. 2.5). Equation 2.5 is used to measure

the saturation intensity experimentally by taking a series of thermal cloud images with varying intensity of the probe laser. The laser intensity, expressed in CCD counts, is chosen to vary in the range 7400−28200 counts, averaged over all pixels in the reference frame. According to Eq. 2.5 with a constant total number of atoms N in the series the slope of the dependence $W(N_{obs})$ is equal to $-I_S$. After calculating W and N_{obs} for each image we measured $I_S = (8400 \pm 1300)$ counts for the Princeton Instruments ProEM 512 CCD (Fig. 2.4).

This experiment was made with low-density thermal clouds in order to avoid strong absorption saturation and with a large number of atoms to keep shot-to-shot atom number variations within 10%. To make clouds with these properties atoms in the MT were quickly cooled by one stage of evaporative cooling during 8 seconds with a logarithmic sweep of rf-frequency in the range 22 MHz − 1 MHz. The repumper laser was used to transfer atoms into the F=2 state before imaging after 20 ms time of flight.

In order to use I_S it is sufficient to know its value in units of CCD counts. A measured value of the saturation intensity significantly improves the accuracy of the atom number calculations. Figure 2.5 shows the dependence of N_{obs}, $\frac{W}{I_S}$ and total number of atoms N, calculated for the taken series from Eq. 2.5 with the known value of I_S. It is easy to see that the total number of atoms is almost constant with a standard deviation from the average of 8% while N_{obs} and W have notable dependencies on the probe intensity.

2.2.3 Kinetics mode imaging

The imaging setup of the experimental apparatus has been upgraded by the replacement of the "old" Princeton Instruments PI-MAX 1024 CCD camera with a new model Princeton Instruments ProEM 512. While the new camera has a smaller number of exposed pixels (512×520) the significant reduction in time between two sequential frames (400 μs versus 1 s) results in a much improved image: fringing due to image laser vibration is essentially eliminated. Kinetics mode operation [81] can be simply understood by considering the masked nature of the full CCD chip whose actual size is 512×1040 pixels. Only half of the chip can be exposed to light whereas the second half, which was masked during manufacture, can be used as storage. Transfer of charge from the exposed pixels into the

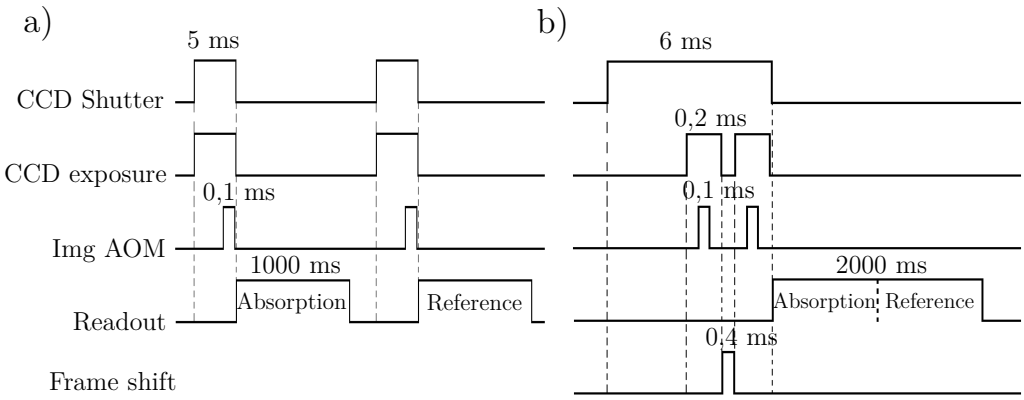

Figure 2.6: Imaging time diagrams for a) the full-frame mode and b) the kinetics mode. Kinetics mode's readout for both (absorption and reference) images starts after the second frame which significantly reduces the time interval between two sequential frames (400 μs instead of 1000 ms in the full frame mode).

storage pixels is a very fast process (0.6 μs per row), allowing the exposed pixel counts to be zeroed (cleaned) ready for a second light exposure. Readout of the entire 512 $\times$ 1024 chip is a slow process (t$\sim$2 s) which can only be made faster by reducing the area of interest in software or by changing the readout rate which increases readout noise. This timing sequence is shown in Fig. 2.6 (b) and can be compared with the old timing sequence used in Fig. 2.6 (a). An additional benefit of kinetics mode is the increased laser power stability between frames. This arises due to reduced thermal relaxation of the imaging laser AOM during switch off as this period is significantly less than in previous arrangements.

In kinetics mode, shutters of the CCD and imaging laser open only once. The first frame exposure starts after a 5 ms delay from the rising edge of the shutter signal to allow both shutters to fully open. The ProEM CCD does not require a clean frame before the absorption image as it is continuously cleaning pixel arrays in the absence of a trigger. The exposure time is just 200 μs and the imaging AOM signal is programmed to be in the middle of the exposure time (the exposure time is not important as long as it is longer then the imaging pulse because the amount of imaging light is determined by the AOM; however, it is kept reasonably short to reduce the noise from background light).

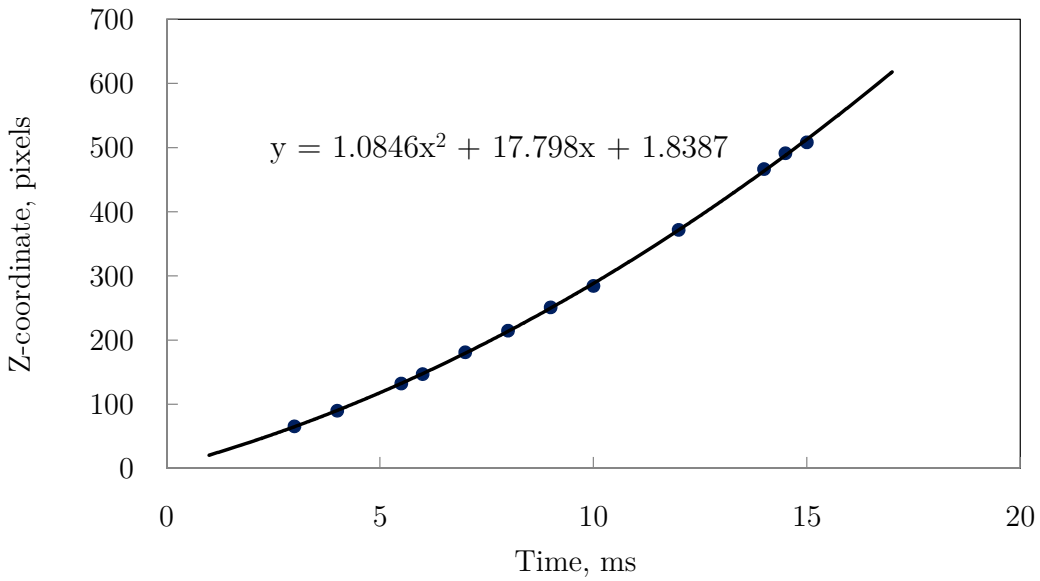

Figure 2.7: Measurement of the camera pixel size in the object plane by varying the free fall time of the cloud after switching off the magnetic trap. The experimental points (blue circles) are fitted by a second order polynomial function (solid line) to extract the pixel size from the known value of the free-fall acceleration g.

Immediately after the exposure time the whole first frame is shifted to the masked area of the chip. The speed of this shift can be selected in the camera software and a typical shift duration of the full frame is 400 μs. Background light as well as the imaging light that is not completely extinguished by the AOM result in a very small vertical count gradient in the second image as the CCD shutter is still open. Exposure of the second frame starts just after the shift of the first frame and the second 100 μs imaging laser pulse is send followed by closing the shutters. Readout of the full chip gives the number of counts in both frames. The total time of the imaging is almost the same for both modes (kinetics and the full frame mode in Fig. 2.6); however, the kinetics mode has the advantage of minimizing the time between the exposures of the first and the second frames.

2.2.4 Size of the camera pixels in the object plane

After installation of the new CCD we measured I_S in pixel counts (Fig. 2.4) and calibrated the pixel size by varying the ballistic fall time (Fig. 2.7). Every pixel of the CCD chip has dimensions 16μm $\times$ 16μm; however, the system of lenses magnifies the cloud by approximately three times. The CCD-pixels' size can be correlated with the area in the object plane by a simple measurement of the position of the cloud centre for different times during a free fall. In vacuum all bodies have the same acceleration of the free fall $g \sim 9.81$ ms^{-2} (in absence of other potentials than gravitational) so that the position of the cloud can be determined from the kinematic equation:

$$z(x) = \frac{g}{2}t^2 + v_0 t + z_0 \tag{2.7}$$

Fitting of the experimental points by a second order polynomial function gives the coefficient A in units of [pixel$\cdot$s^{-2}] in front of t^2. During the experiment, shown in Fig. 2.7 the initial position of the cloud is outside of the field of view of the CCD camera and the coordinate of the cloud centre is measured relative to the top line of the imaging frame (as well as the time is shown relative to the moment the cloud enters the field of view of the camera, which does not affect the the quadratic dependency and only changes the velocity at t = 0). If k is the real size of the pixel in the object plane then from Eq. 2.7 $kA = \frac{g}{2}$ from which $k = \frac{g}{2A} = 4.5\pm0.2$ [μm/pixel]. This measured pixel size agrees very well with the expected value, calculated from a rough estimation by dividing the physical dimension of the CCD pixel by the magnification of the lens setup: $16 \times \frac{150}{500} = 4.8$ μm.

2.2.5 Problems with short time between two frames

An additional technical issue of using the kinetics mode was the fact that during such a short shift time between two frames the atoms do not leave the field of view of the CCD camera. As a result the remnants of the exposed atomic cloud could be seen in the reference frame. 400 μs is too short period of time for the atoms to be blown away from the camera's field of view, so the only solution is to make them insensitive to the laser light. This can be achieved in several ways: detuning of the laser light, changing the magnetic field to shift the atoms' energy levels or transferring the atoms into $5^2S_{\frac{1}{2}}$(F=1)

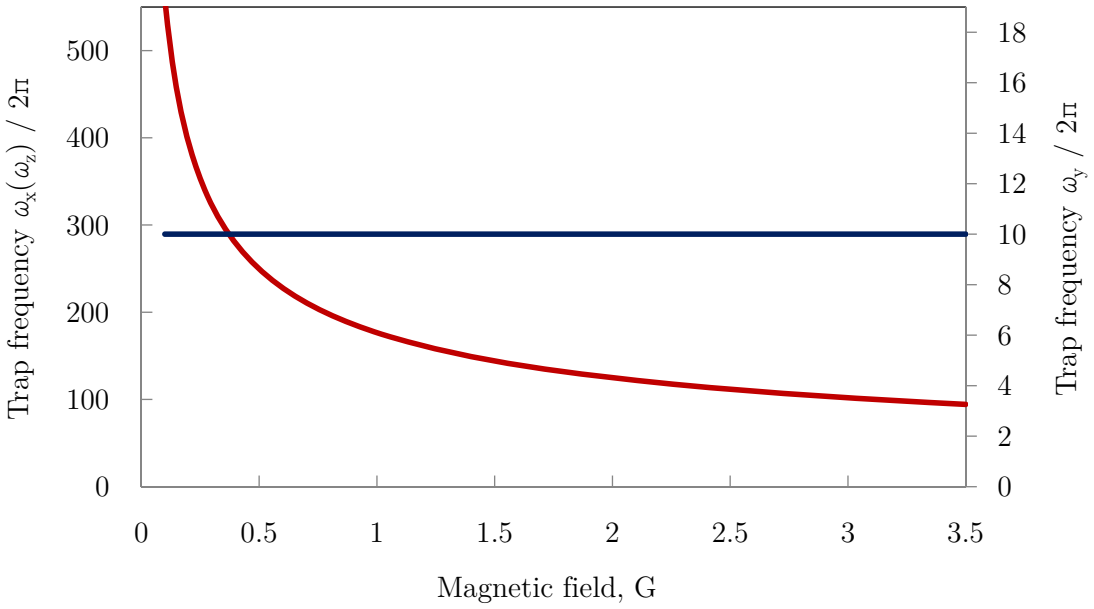

Figure 2.8: Dependence of the trapping frequencies of the Z-wire trap on the value of the magnetic field at the trap bottom, predicted from Eq. B.17. Blue line is the axial frequency, red is the radial one.

state. We chose the transfer method, for which during 400 μs of frame shift an optical pumping laser is also applied (not directed to the camera), which pumps all the atoms into the $5^2S_{\frac{1}{2}}$(F=1) state so they are no longer resonant with the imaging light.

2.3 Experimental measurements of the trap frequencies

The harmonic trapping potential determines the parabolic shape of the BEC cloud. Atoms in a BEC occupy some volume in which the magnetic field is not uniform. This means atoms in different parts of the cloud have a different response to microwave- and radio-frequency fields. For this reason properly characterized experiment conditions improve the understanding and interpretation of the experimental results. In the general case with the presence of anharmonicity in the trap the frequency of the dipole oscillations depends on its amplitude. This question was considered and analyzed in [65]. The main conclusions were that the dipole-oscillation method gives an overestimated value for the radial frequency

by $2\pi \times 0.019$ Hz and the correction for the axial frequency can be neglected.

To initiate dipole oscillations the position of the trap minimum is shifted and then returned back to the initial position after some time. The position of the atomic cloud centre is then registered after various holding times. The Z-wire trap is created by only three working units: current through the Z-wire on the chip, B_{xLarge} and B_{ySmall} coils. The vertical position of the BEC depends on the relation between the current through the central wire of the chip and B_{xLarge}. To push the atoms in the z (vertical) direction the current through the Z-wire is changed with a sinusoidal ramp by 0.5% for 3 ms and then returned to its initial value during the same ramp time. The horizontal position of the centre of the trap cannot be changed by homogeneous fields and is always in the middle of the central wire due to the symmetry. To make a horizontal displacement a magnetic field gradient in the y-direction needs to be applied. For this purpose one of the side-wires on the chip (perpendicular to the central wire) is employed (Fig. 2.1,the other side-wire is used as an rf antenna for evaporative cooling). Similarly to the vertical direction the current through the side-wire is sinusoidally ramped up to a few amperes during 30 ms and then switched off during the same time (time is chosen experimentally for good visibility of dipole oscillations).

During dipole oscillations atoms move in the trap for only a few microns, which is comparable with the resolution of our imaging system so there is little hope to be able to see this shift in-situ. For this reason the cloud is imaged after 20 ms of time of flight which converts the speed of the cloud during the dipole oscillations into its position Δz (Δy) on the imaging frame (explanation is in Appendix B.0.3) according to the equation:

$$\Delta z = 2v_0 t_0 = 2wz_0 t_0 \tag{2.8}$$

A large time of flight allows to measure small variations of the cloud positions in the trap. For instance with $z_0 = 1$ μm and a trap frequency $\omega_z = 2\pi \cdot 100$ Hz the maximum speed of the cloud is 0.63 μm/ms and total difference of z-position for 20 ms time of flight is 25 μm or 5.5 pixels.

In [65] trap frequencies were measured with a high precision for the trap with 3.23 G at the trap bottom. In the current work during experiments trap bottoms of the magnetic traps are varying in the range 0.15−3.23 G. For the analysis of the mw spectroscopy

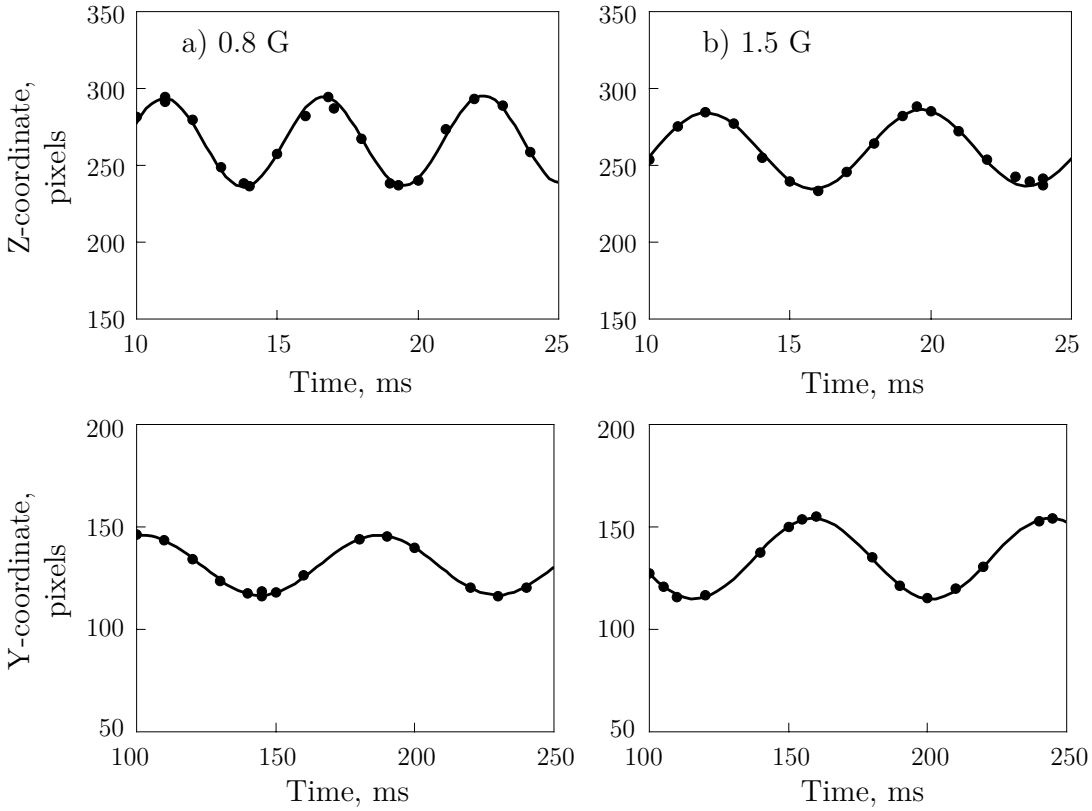

Figure 2.9: Experimental measurements of the trapping frequencies of the Z-wire magnetic trap via dipole oscillations. Top picture is for the radial frequency; bottom is for the axial one. a) 0.8 G at the trap bottom; b) 1.5 G at the trap bottom. Calculated frequencies are summarized in Table 2.1.

and rf induced atom loss curves we need to know the trap frequencies over the whole range; however, the measurements for each magnetic field would be too time consuming. Equation B.17 gives reasonable estimates for the trap properties at 3.23 G, so we rely on its predictions for traps with other trap bottoms. Figure 2.8 shows the trap frequencies dependence on the value of the local minimum of the magnetic field. To test these predictions the trap frequencies have been measured at two additional trap bottoms: 0.8 G and 1.5 G (Fig. 2.9). From a 2D image of the BEC there can only be extracted information about the cloud movement in two independent directions: vertical z and horizontal y; whereas the frequency ω_x can only be accessed from the theoretical modeling of the chip, such as Eq. B.17 in a rough approximation.

B, G	$\omega_z/2\pi$, Hz (radial)			$\omega_y/2\pi$, Hz (axial)		
	Exp.	Theory	Difference, %	Exp.	Theory	Difference, %
0.8	176.3±1.1	191.9	8.8%	11.74±0.05	10.04	14.5%
1.5	131.3±0.3	140.1	6.7%	11.73±0.02	10.04	14.4%
3.23	98.25±0.05	99.1	0.9%	11.507±0.007	10.04	12.8%

Table 2.1: Comparison of the theoretical values for the trapping frequencies of the Z-wire magnetic trap with experimental measurements via dipole oscillations for 0.8 G, 1.5 G and 3.23 G at the trap bottom.

The experimental data in Fig. 2.9 was fitted by sine functions to extract the frequencies of the dipole oscillations. The results are summarized in Table. 2.1. The analytical theory of Appendix B.0.1 produces predictions within the 10% for the actual radial frequency and underestimates the axial frequency by up to 15%. These deviations most likely come from the approximation of infinitely thin wires, ignoring the real rectangular cross section (1×0.5 mm^2) of the wires and proximity of the cloud location to the wires ($z_0 \sim 1.2$ mm for $B_0 = 0.8$ G). We did not know the exact value of the magnetic field gradient G and had to use estimated values for Eqs. B.17 for different trap bottoms. This most likely leads to the different sign of the deviations as the radial frequencies and the axial frequency has different scaling with G (Eqs. B.17). More precise numerical calculation of the frequencies and the effect of unharmonicity of the trap has been described in the thesis of the previous student [65].

It is also important to mention that the measured invariance of the axial frequency with respect to the magnetic field at trap bottom is described correctly so that the maximum relative deviation of the trap frequency ω_y is within 2%.

2.4 Distance from the cloud to the chip wire, gravity sag

Previously in Section 2.3, $z_0 \sim 1.23$ mm was used to calculate the trapping frequencies in Eq. B.17 and Table 2.1. To estimate this value a simple experiment has been performed with imaging the cloud of thermal atoms in situ, i.e., without time of flight. The

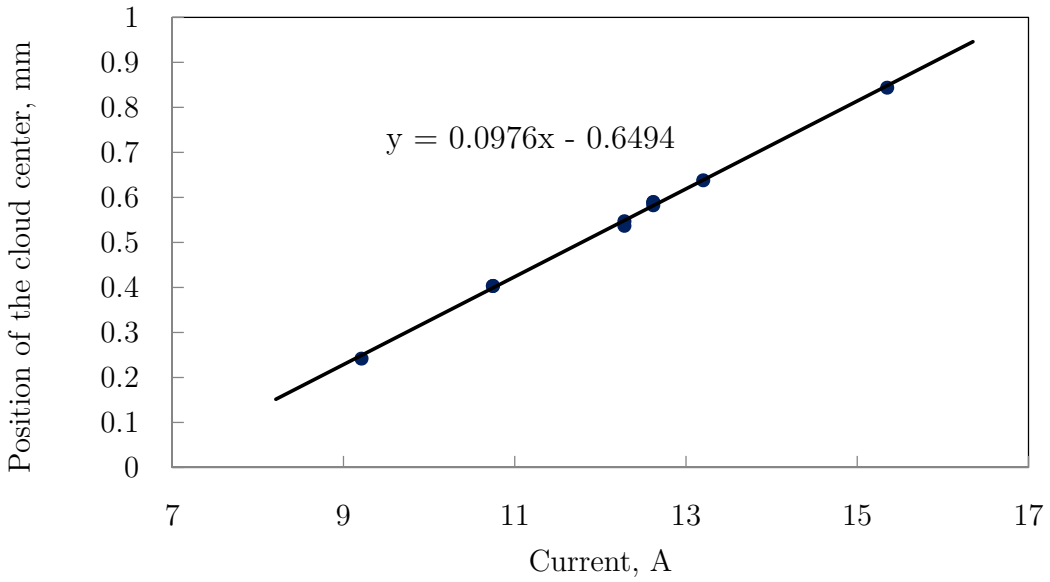

Figure 2.10: Measurement of the distance from the cloud to the current carrying central part of the Z-wire. We plot relative positions of the cloud centre, measured by in-situ imaging, for different values of the current through the chip wire.

experiment has been repeated with different currents through the Z-wire, monitoring the position of the cloud centre in the image. According to Eq. B.4 the position of the trap depends linearly on the current in the wire.

The experimental results are plotted in Fig. 2.10. The data is fitted very well with a straight line and from the slope it is calculated that for the usual conditions ($I = 12.62$ A) the BEC is located 1.23±0.02 mm below the central wire. The fitting line in the figure doesn't go through zero because the field of view of the CCD-camera is limited, so the position of the cloud was measured relative to the top line of the image. The vertical coordinate of the cloud centre in pixels was determined from gaussian fitting of the atoms in the trap and then converted into mm from the known pixel size.

In general the position of the BEC cloud is determined not only by the magnetic potential only but also by gravity. The gravitational potential energy decreases as atoms move lower i.e., further away from the chip surface. If the atom interactions with each other are not considered (they do not change the trap position), the total energy of an

atom is equal to (from Eqs. B.15, B.14 and B.17):

$$E = E^M + E^G = \mu_B \cdot g_F \cdot m_F \cdot |B| - mgz = \left[E_0 - \frac{m^2 g^2}{2\omega_z^2} - mgz_0\right] + \frac{m\omega_x^2 x^2}{2} + \frac{m\omega_y^2 y^2}{2} + \frac{m}{2}\omega_z^2\left(z - \left[z_0 + \frac{g}{\omega_z^2}\right]\right)^2 = E_1 + \frac{m\omega_x^2 x^2}{2} + \frac{m\omega_y^2 y^2}{2} + \frac{m\omega_z^2\left(z - \left[z_0 + z_g\right]\right)^2}{2} \tag{2.9}$$

where $E_0 = \mu_B \cdot g_F \cdot m_F \cdot B_0$ (Eq. B.20 in Appendix). The gravitational potential energy has a minus sign because the z-axis is directed vertically down. Comparing this result with Eq. B.17 the presence of gravity does not change the trapping frequencies but only shifts the centre of the trap down by the value z_g which is called the gravity sag.

$$z_g = \frac{g}{\omega_z^2} \tag{2.10}$$

Gravity sag is important because clouds of atoms with different magnetic moments (for example in two internal states) experience different trapping potentials that affects their shapes and positions. However, in the experiments in the current work we use atoms in two internal states, F=1, $m_F = -1$ and F=2, $m_F = +1$, with almost the same magnetic moments and assume a perfect overlap of the clouds. Due to gravity sag the magnetic field at the center of the cloud is different from the minimum of the Z-wire magnetic trap, so the atoms start to respond to a different resonant frequency as well as the magnetic field becoming less uniform along the finite size of the cloud. From Eq. B.14 the value of the magnetic field at the centre of the new trap position can be calculated as:

$$\left|B(0,0,z_g)\right| = B_0 + \frac{G^2}{2B_0} z_g^2 = B_0 + \frac{G^2}{2B_0} \frac{g^2}{G^4 \frac{\mu_B^2}{4m^2 B_0^2}} = B_0\left(1 + \frac{2m^2 g^2}{\mu_B^2 G^2}\right) \tag{2.11}$$

where $G = \dfrac{\mu_0 I}{2\pi z_0^2}$ is a gradient of the magnetic field in vertical direction in the vicinity of the minimum magnetic field value of the Z-wire trap B_0.

From Eq. 2.9 it follows that $z_g \sim 25$ μm for the 3.23 G magnetic trap. Gravity sag gives a correction to Eq. B.4 for the vertical position of the cloud in the trap. However, this modification is within 2% for the largest trap bottom in our experiments, 3.23 G, and even less for the smaller trap bottoms. The uncertainty of the described method of z_0 measurement is comparable with the calculated gravity sag, so 1.23±0.02 mm is a reliable

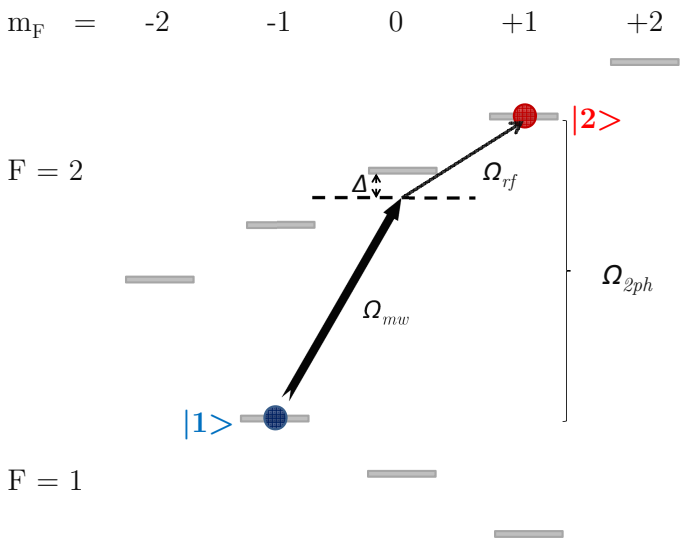

Figure 2.11: Preparation of a two-component BEC in states F=1, m_F=−1 and F=2, m_F=+1 by a two-photon (mw+rf) transition.

value for z_0. Equation 2.11 allows to calculate the magnetic field at the centre of the cloud which is called the trap bottom value in this thesis (the bottom of the whole trap at the location of the atoms) and is different from the minimum value of the magnetic field. The largest difference between these two values of magnetic field in our experiments reaches 40 mG at the 3.23 G trap.

2.5 Two-component BEC

We study the association of molecules initiated in collisions of ^{87}Rb atoms prepared in two different internal states. The molecule production rate increases with the atom density, so it is beneficial to employ ^{87}Rb Bose-Einstein condensates (rather than non-degenerate ultracold atoms) prepared in two hyperfine states (the two-component BEC) with moderate densities ($n_0 \sim 10^{14}\ cm^{-3}$) that can co-exist with lifetimes of several hundreds milliseconds. It is convenient to generate BECs of ^{87}Rb atoms in so-called stretched states - either F=1, m_F=−1 or F=2, m_F=+2. Atoms in these states can be held in magnetic traps for tens of seconds due to the absence of losses from two-body collisions. In our experiment the atoms in the F=1, m_F=−1 stretched state are used for the creation of the initial BEC

which then coupled with the second state F=2, m_F=+1 to create a superposition of states.

Standard tools for coupling hyperfine states in ultracold atoms are microwave and radio-frequency dipole transitions. For two chosen internal states the difference of the projection of the total angular momentum Δm_F is equal to 2, so the transfer of the atoms cannot be made with a one-photon transition. Instead a two-photon transition $|F = 1, m_F = -1\rangle \rightarrow |F = 2, m_F = +1\rangle$ is used with mw and rf radiation (Fig. 2.11). Measurements of the single-photon Rabi frequencies Ω_{mw} and Ω_{rf} have been described in the thesis [65]. The order of mw and rf couplings can be chosen arbitrarily ([64]) and we chose the mw coupling on the $|F = 1, m_F = -1\rangle \rightarrow |F = 2, m_F = 0\rangle$ transition and the rf coupling on the $|F = 2, m_F = 0\rangle \rightarrow |F = 2, m_F = +1\rangle$ transition. However, at low magnetic fields such as those we work with, the Zeeman splittings of the energy levels within a hyperfine state are almost the same, so the resonant rf pulse would populate all the Zeeman states, leading to poor transfer efficiency and a huge atom loss. To avoid this problem instead of the application of the resonant radiation both mw- and radio-frequencies are shifted by the same value Δ and applied at the same time. The appropriate choice of the detuning ($\Delta \gg \Omega_{mw}, \Omega_{rf}$) favours the direct transfer of atoms to the $|F = 2, m_F = 1\rangle$ state without populating the intermediate $|F = 2, m_F = 0\rangle$ or $|F = 1, m_F = 0\rangle$ states. Detuning from the intermediate state decreases the two-photon Rabi frequency Ω_{2ph} but should be chosen relatively high to avoid loss of atoms. In our typical experimental conditions (B_{dc} = 3.23 G) we use 988 kHz detuning with a two-photon Rabi frequency $\Omega_{2ph} = 2\pi\times1$ kHz.

2.6 Adiabatic passage

The imaging laser is locked to the cycling transition $5^2S_{\frac{1}{2}}$(F=2) − $5^2S_{\frac{3}{2}}$(F=3), so in order to image the atoms in the F=1 state they need to be transferred into the F=2 manifold first. Depending on the particular application, in our experiments two methods are used: by applying a repumper laser pulse just before the probe beam or by mw adiabatic transfer of the atoms into one of the Zeeman levels of F=2 prior to the imaging.

The repumping transfer method is used in the mw spectroscopy measurements (Section 3.2). Working in exactly the same way as during the MMOT stage of laser cooling (Section 2.1.1) the repumper laser effectively transfers all the atoms from $5^2S_{\frac{1}{2}}$(F=1,

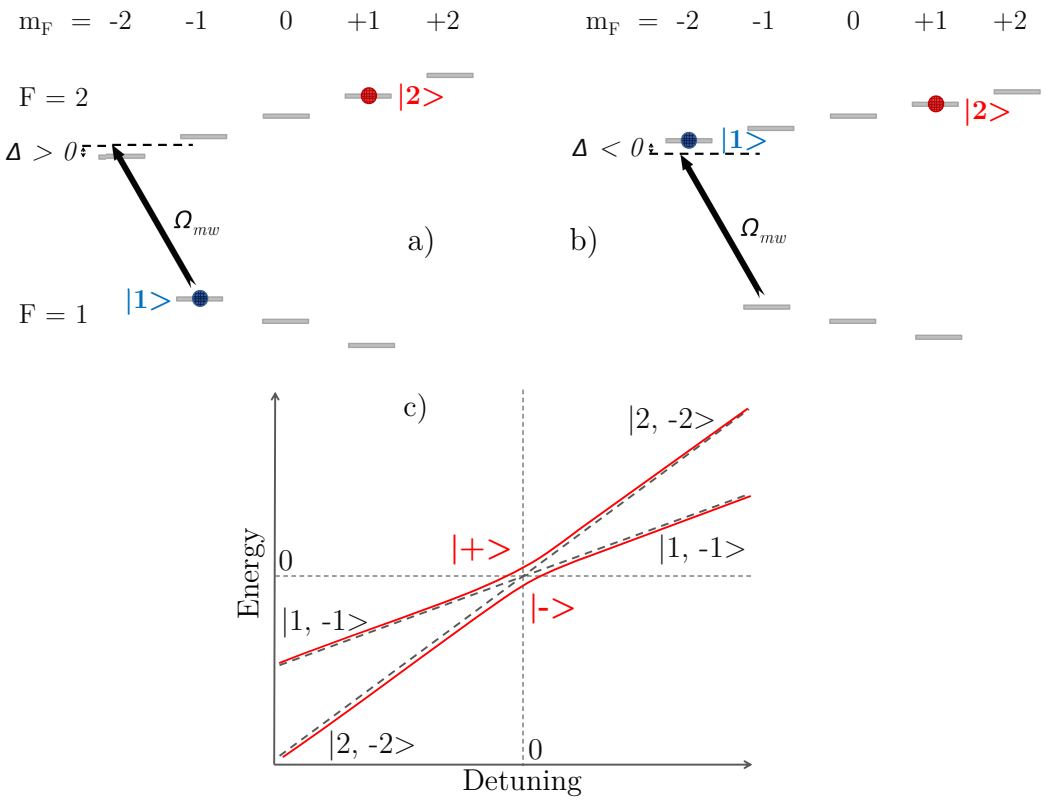

Figure 2.12: During adiabatic passage the mw frequency is kept constant with sweeping of the DC-magnetic field. In this process the detuning Δ changes from a positive value (a) through the resonance to a negative value (b). Atoms in the F=1, $m_F = -1$ state adiabatically follow the $|->$ dressed potential and undergo a transition into the F=2, m_F=−2 bare state (c).

m_F=−1) into $5^2P_{\frac{1}{2}}$(F=2) hyperfine levels. However, the population of a particular Zeeman state of the F = 2 manifold can not be controlled, so the atoms will be distributed among all Zeeman sublevels. Also with this method atoms in two states, F=1, m_F=−1 and F=2, m_F=+1, cannot be spatially separated in the image. The atoms remain in their initial states during time of flight and can't be separated by a Stern-Gerlach kick as the magnetic moments of the atoms in the two states are almost the same.

In the second method the atoms from the state F=1, m_F=−1 are transferred into one of the Zeeman sublevels of F=2 and a magnetic field gradient separates the two clouds with different moments during free fall of the atoms. By a one-photon resonant mw transition

(Fig. 2.12 (a)) atoms can be selectively transferred into m_F=−2, m_F=−1 or m_F=0 states of the F=2 level (selection rule is $\Delta m_F = 0, \pm 1$). In the current experimental setup we use the rapid adiabatic passage technique to transfer atoms into the F=2, m_F=−2 state.

There is an important difference between the adiabatic passage and the resonant transfer techniques. If radiation that is resonant to a particular splitting of the energy levels is applied, the atoms start oscillations at the Rabi frequency between the two states. In order to transfer 100% of the atoms into one of the states one needs to control very precisely the matching between the mw frequency, magnetic field and duration of the radiation pulse. During adiabatic transfer the microwave frequency is kept constant and the magnetic field is swept through the resonance from blue-detuned at the beginning to red-detuned at the end. This process is very robust and allows to transfer of up to 99% of the atoms into the desired state. Adiabatic following transfer is based on the adiabatic theorem [82], [83]. It has been well-known for many years and used for trapping atoms in time-orbiting potential (TOP) traps which was also used in the first experimental demonstration of BEC [1]. Adiabatic passage was implemented in our system by one of the previous students in our group, Russell Anderson, who also analyzed this process in his thesis [64].

The two-level crossing problem was solved in 1932 independently by four groups. The eigenstates of the time-dependent Hamiltonian are the so called dressed-states $|+>$ and $|->$. The intersection of two initial energy levels becomes an avoided crossing when the coupling is switched on. Figure 2.12 illustrates the process of adiabatic passage in our system. Atoms begin in the state $|->$ and during the adiabatic sweep of the magnetic field remain in the same state after crossing the resonance. But at negative detuning the state $|->$ corresponds to the F=2, $m_F = -2$ bare state i.e., in the initial basis atoms have made a transition into the other state.

In our system the sweep of the detuning is realized by a decrease of the magnetic field for a constant mw frequency which keeps the same value 6.831430031 GHz as during the two-photon transfer. After turning off all switches to release the BEC from the trap the currents through magnetic coils do not disappear instantly. For the largest coils B_{xlarge} the magnetic field takes about 10 ms to decay. However, this feature is used to perform the adiabatic passage. 6.6 ms after releasing atoms from the magnetic trap a mw pulse

is applied for 3 ms transferring all the atoms from F=1, $m_F = -1$ state into F=2, $m_F = -2$ one. Exact values of the mw frequency, the time between switching off trapping fields and the application of the mw pulse as well as the value of the additional magnetic field in the y-direction (generated by B_{yEarth} coils) are subjects for empirical optimization for different magnetic traps. In experiments with two-component BECs after the adiabatic passage a Stern-Gerlach kick is applied by passing current through the Z-wire on the chip for 0.5 ms producing a magnetic field gradient. Then the atoms continue to free fall and get spatially separated due to their different velocities at the end of the kick, so that on the image shadows of the two clouds can be seen. A typical distance between the two clouds during imaging is $\sim$700 μm.

2.7 Magnetic noise

The resonant magnetic dipole transition frequencies of atoms depend on the modulus of the total magnetic field. The Zeeman levels of the ground state split in accordance with the Breit-Rabi formula (Eq. 3.14). Magnetic noise plays an important role and affects the precision of the measurements of the resonant frequencies which couple different energy levels. In magnetic traps (Section 2.3) the total magnetic field is directed along the y-axis and in our experiments is in the range 0.14$-$3.30 G. The magnetic noise amplitude is of the order of a few mG so the fluctuations of the magnetic field along the x and z directions do not lead to a significant change of the modulus of the total magnetic field. However, the magnetic noise along the y-axis leads to a broadening of the transitions during measurements. For instance 1 mG noise amplitude leads to approximately 0.7 kHz uncertainty in the transition $|1,-1\rangle - |2,\ 0\rangle$.

Preliminary measurements of the magnetic noise led to a conclusion that the power supplies used in the experimental setup are the main sources of the field fluctuations both in the laboratory and inside the vacuum chamber. On the contrary, the magnetic coils which are used for generation of the magnetic field during the experiment produce a stable magnetic field with the variations of the current through the coils only in the fifth significant digit. To characterize the upper value of the background magnetic noise the magnetic field magnitude has been measured in the laboratory close to a working power

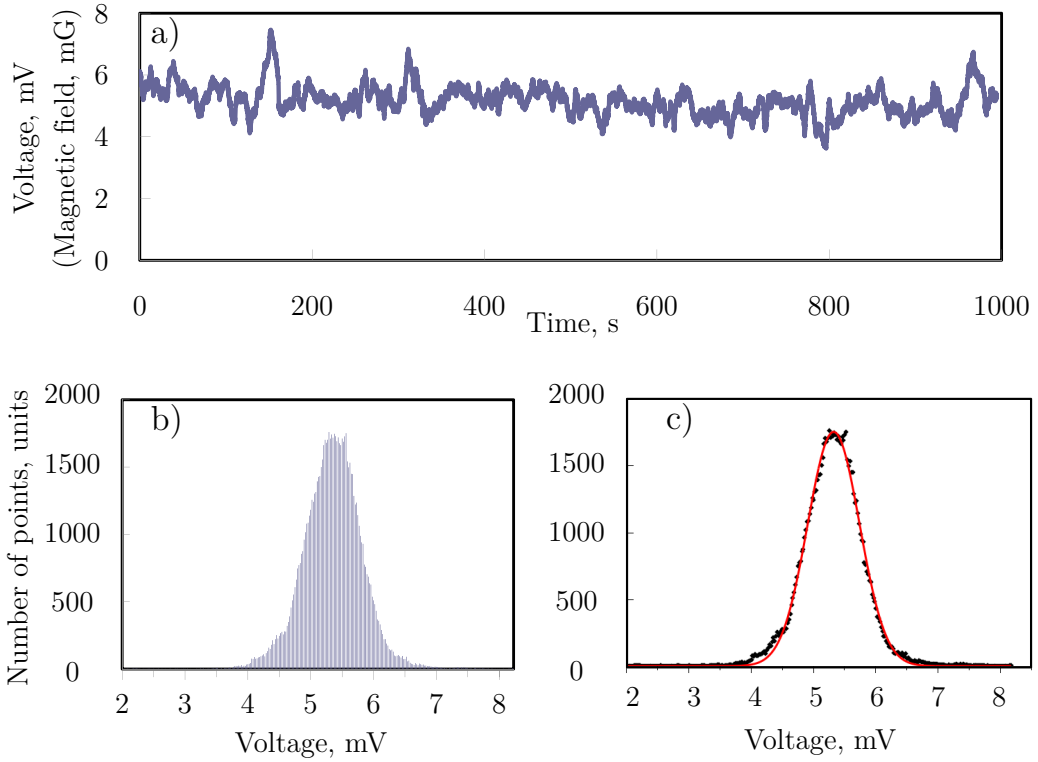

Figure 2.13: (a) Random fluctuations of the projection of the background magnetic field in a chosen direction, measured by the Stefan Mayer fluxgate magnetometer "Fluxmaster". Data is recorded with 16.5 Hz frequency and is expressed in volts that are proportional to the magnetic field. The histogram of the data (b) can be well approximated by a gaussian distribution (c) around the mean value 5.33 mV and RMS width 0.83 mV.

supply without running of the experimental apparatus. During the data taking procedure the "Fluxmaster" fluxgate magnetometer was recording the projection of the background magnetic field along a chosen direction every 60 ms (Fig 2.13 (a)). Integration time of the magnetometer is less than 1 ms and the sampling time was chosen to observe a field magnitude fluctuation and a drift during tens of minutes rather than to investigate the bandwidth of the magnetic noise. Analysis shows that the data can be approximated by a Gaussian distribution

$$f(x) = A \cdot e^{-\frac{(v-v_c)^2}{2\Delta^2}} \tag{2.12}$$

with the mean value $v_c = 5.33$ mV, and $\Delta = 0.83$ mV. During this experiment the DC offset produced by the Earth's magnetic field is mostly compensated by one of the B_y coils to enable use of the smallest fluxgate scale. The measured magnetic field is fluctuating with FWHM $= 2\sqrt{2\ln 2}\times 0.83 = 1.95$ mV (Fig 2.13 (c)), which leads to approximately 2 mG of FWHM uncertainty in the magnetic field according to the calibration of the magnetometer.

2.8 Strong rf field generation

Theoretical papers [54], [55] have predicted the appearance of Feshbach resonances in ^{87}Rb at large values of radio-frequency radiation ($B_{rf} \sim 4$ G). It is a challenging task to generate such strong rf fields that can force colliding atoms to form a molecule. In our experimental setup the BEC is trapped in a vicinity of the local minimum of the magnetic field at a distance ~ 1 mm from the current-carrying wire of the atom chip. In such a configuration the small distance to the wire is a big advantage as the magnetic field decays with an r^{-1} dependence from the wire or with an r^{-2} dependence from the antenna.

The first challenge was to realize passing DC and AC currents through the same wire at the same time. This was done by using an AC-DC decoupling scheme with two capacitors in the rf supply circuit to block the DC-current and two massive inductors in the DC circuit to block the AC current (Fig. 2.14). Theoretically, the described decoupling scheme should work perfectly but in practice some AC-current still leaked into the DC-switches. The problem was solved only by installing low-pass filters in every switch that is used during the application of the strong rf fields. The voltage on the gates of all the IGBTs

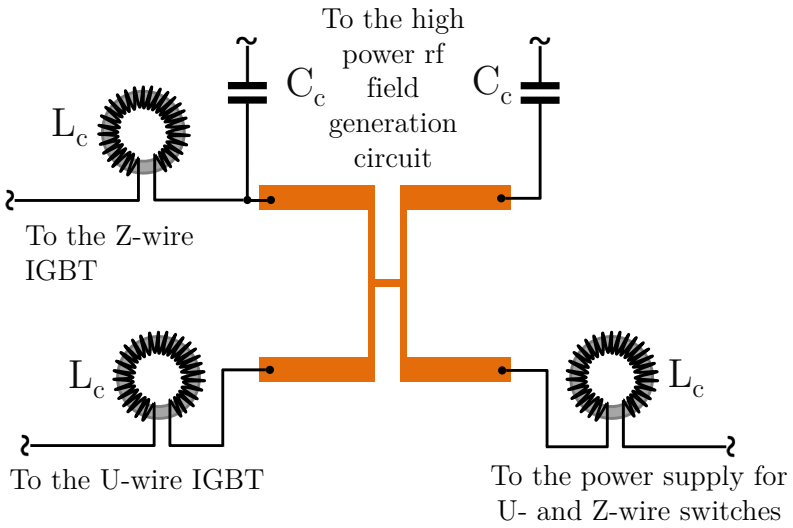

Figure 2.14: To pass AC and DC currents through the same wire we introduce capacitors C_C to block the DC current from coming into the high rf field generation circuit and inductors L_C to stop AC current from leaking to the switches controlling the magnetic trap fields.

inside the current controllers that must be off during the rf is set -10 Volts to isolate them completely.

After the rf field characterization (Section 3.3) it appeared that our strongest rf fields were more than order of magnitude lower than was necessary to satisfy the condition ($B_{rf} \sim 4$ G) of the theoretical predictions. The strength of the rf field was significantly increased via impedance matching between the rf amplifier and the load. However, even the theoretical maximum current still would not give sufficient rf power. The solution came with implementation of an rf transformer in the circuit in combination with impedance matching. Transformer theory and transmission line equations allowed us to understand and optimize the performance of the rf circuits and increased the strength of the rf field for different frequency tuned circuits. With these improvements we succeeded in generating of strong rf fields with an amplitude of up to 6 G.

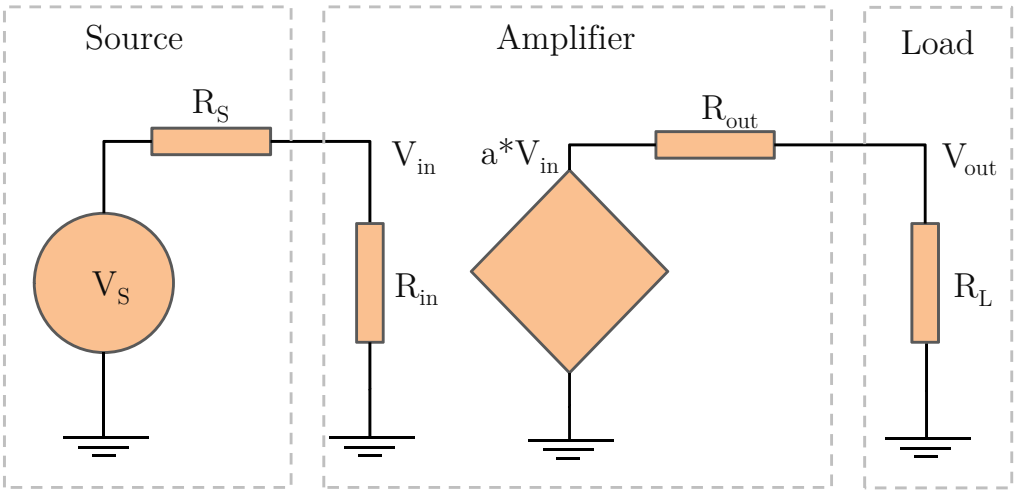

Figure 2.15: Equivalent circuit of impedance matching between an rf generator, an amplifier and a load, adapted from [84]. Impedances R_S, R_{in} and R_{out} are assumed to be purely resistive which corresponds to the specification of our signal generators SRS 345 and TTi TG4001 and power amplifiers OPHIR 5303055.

2.8.1 AC-current maximization and impedance matching

In our experimental setup we use SRS 345 and TTi TG 4001 function generators as a source of rf signal. The signal goes to a power amplifier first and then to a chip load circuit. To understand the processes that are going on in the circuits we consider that all the wires are short at first. Using the method of Thevenin and Mayer-Norton equivalents [84], [85], [86], [87], [88] each linear element of such a circuit can be drawn as a voltage source in series with a resistance, as shown on Fig. 2.15. All the elements in our circuit are linear as they do not change the frequency of the signal but only change its amplitude and phase. The power absorbed by the input resistor of the amplifier is

$$P_{in} = \frac{V_{in}^2}{R_{in}} = \frac{V_S^2 R_{in}}{(R_S + R_{in})^2} \tag{2.13}$$

where V_{in}^2 is the time-averaged voltage. The power transmitted to the load is

$$P_L = \frac{V_{out}^2}{R_L} = \frac{(\frac{aV_{in}R_L}{R_{out}+R_L})^2}{R_L} \tag{2.14}$$

and the power gain can be written

$$G_p = \frac{P_L}{P_{in}} = \frac{a^2 R_{in} R_L}{(R_{out} + R_L)^2} \tag{2.15}$$

where a is the amplifier voltage gain. The voltage gain can be obtained in a similar way:

$$G_v = \frac{a R_L}{(R_{out} + R_L)} \tag{2.16}$$

So G_v is proportional to G_p and for a matched circuit G_v can be calculated from the G_p given in the amplifier specification. From Fig. 2.15 additional information about the source can also be extracted. According to the specifications of the function generator SRS 345 the output impedance R_S is 50 Ω and the generator is designed to be used with a load of 50 Ω. From this it follows that when the source is set to generate a particular output voltage, V_S generates a constant doubled value of this voltage which is equally divided between R_S and the 50 Ω load. In the case when the load value is not 50 Ω but some R_{load} the output voltage will be equal to $\frac{R_{load}}{R_S+R_{load}} V_S$. According to Ampere's law the AC-magnetic field is proportional to the current through the atom chip wire, so our prime goal is the maximization of the current amplitude at the load (to be precise, at the end of the transmission line).

However, for frequencies of $\sim$ 20 MHz it becomes important to take into account the influence of connecting cables. At these frequencies BNC cables act as transmission lines and the signal reflection and line characteristic impedance should be taken into account. The propagation of a signal in transmission lines is analyzed in Appendix C.0.5, so that the voltage and current amplitudes at the load (Eq. C.12) are equal to

$$\begin{cases} |V_L| = \frac{|V_S|}{2}(1 + 2|\gamma| cos\phi + |\gamma|^2)^{\frac{1}{2}}, \\ |I_L| = \frac{|V_S|}{2Z_0}(1 - 2|\gamma| cos\phi + |\gamma|^2)^{\frac{1}{2}} \end{cases} \tag{2.17}$$

where $|V_S|$ is the amplitude of the generator signal in V_{pp} and $\gamma = |\gamma| e^{i\phi} = \frac{Z_L - Z_0}{Z_L + Z_0}$ is called the voltage reflection coefficient with the load impedance Z_L and Z_0 being the output impedance of the generator and the characteristic impedance of the transmission line, respectively.

The purpose of the impedance matching is minimization of the reflected power from the transmission line and the load, i.e., γ=0 or $Z_L = Z_0$. As follows from Eq. 2.17, in this case

the current amplitude is equal to $\frac{|V_S|}{2Z_0}$. However, it is easy to see that in the case $Z_L = 0$, $\gamma = -1$, $\phi = \pi$ and from Eq. 2.17 $|I_L| = |I_L|_{max} = \frac{|V_S|}{Z_0}$. So despite zero transferred power to the load, the current at the end of the transmission line has its maximum value. This is exactly what is wanted as B_{rf} is proportional to the current through the chip wire. It is interesting to note that in this case all the power is reflected back from the load and is in theory fully absorbed (instead of being reflected again) by the output resistor of the generator (or amplifier in our experiment) if R_S (R_{out}) is matched to the transmission line.

We use this type of connection in the rf driven evaporation circuit at the final stage of our BEC production by passing rf current through the end-wire (Fig. 2.1). The advantages of this setup are simplicity and a broad range of working frequencies (as we sweep the rf frequency during evaporation). The issue here is that our load at the end of the transmission line is not exactly just a short wire on a chip but a bundle of pins connected to the chip by a set of parallel wires $\sim$ 15 cm long. Ohmic resistance of such a load is negligible; however, its reactive part cannot be neglected. Thus it is a good approximation to consider that the rf evaporation circuit has a purely inductive load.

Instead of using the end-wire as in the evaporative cooling circuit to produce the high power rf field we exploit the U-wire on the chip because the central part of the U(Z)-wire is the closest to the atom cloud. DC currents in the U-wire are used for the compressed MMOT and in the Z-wire for the magnetic trapping. During the molecular association experiment a DC-current for trapping the atoms and an rf current are passed through the same wire at the same time. To decouple these two circuits two capacitors (one for the each side of the U-wire) are included in the rf supply circuit to block the DC-current and two massive inductors are placed in the DC-circuit to block AC-current.

To measure the impedance of the chip wire an oscilloscope is connected parallel to the load in the circuit in Fig. 2.16 for the purpose of measurement of the frequency dependence of the voltage at the end of the transmission line. The oscilloscope channel is set to 50 Ω input resistance to match the characteristic impedance of the BNC cable which connects the scope to the circuit and so that the signal on the scope is always equal to the voltage at the end of transmission line. However, the presence of the scope adds a 50 Ω resistor

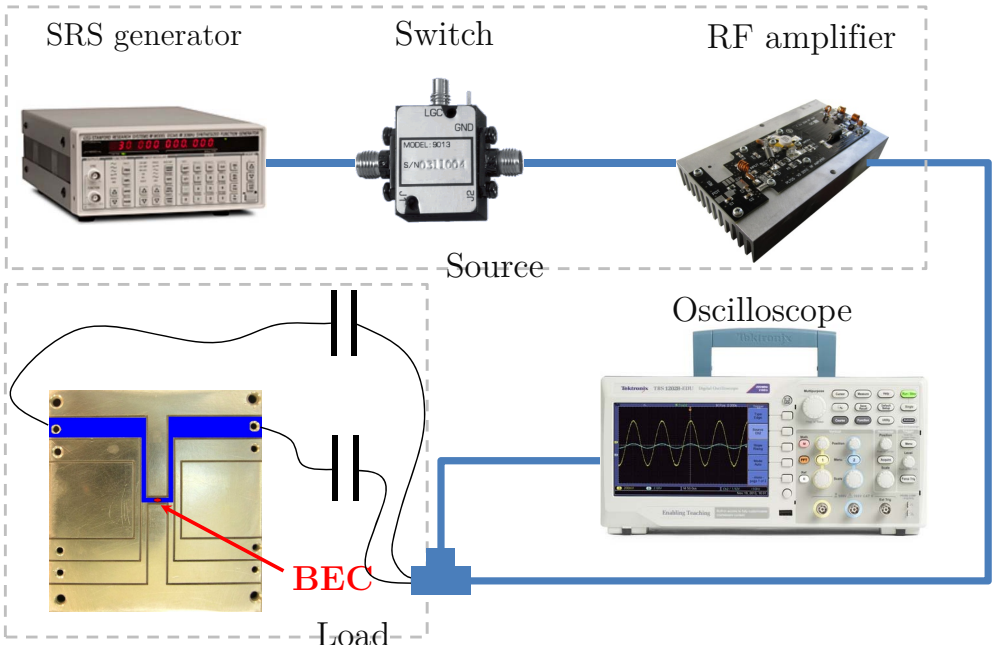

Figure 2.16: Rf generation circuit with a capacitor on each side of the chip wire to decouple the DC-current from the AC-circuit. The oscilloscope is connected parallel to the load for the measurement of the chip wire impedance.

in parallel with the initial load $iwL - \frac{1}{wC}i = iX$, so that $Z_L = \frac{Z_0 iX}{Z_0 + iX}$. Using Eq. 2.17 the expressions for the amplitudes of the voltage and current at the oscilloscope can be rewritten (Appendix C.0.6):

$$\begin{cases} |V_L| = \frac{|V_S|}{2}\sqrt{1 - \frac{Z_0^2}{Z_0^2+4X^2}}, \\ |I_L| = \frac{|V_S|}{2Z_0}\sqrt{1 + \frac{3Z_0^2}{Z_0^2+4X^2}} \end{cases} \tag{2.18}$$

In Fig. 2.17 the experimental data is fitted by Eq. 2.18. To obtain the experimental data the rf generator was set for an amplitude of 100 mV (for which $|V_S| = 200$ mV) and the amplitude of the signal on the oscilloscope was measured for different frequencies. The best fit with fixed $Z_0 = 50\ \Omega$ and $C = 0.5\ \mu$F gives the value $L \sim 0.4\ \mu$H. This corresponds to approximately 60 Ω for the total impedance of the chip circuit at 25 MHz.

The reactive inductive impedance $X = iwL$ can be compensated by introducing an additional capacitor in series with the chip wire. In this case the minimum circuit impedance is frequency dependent, so the capacitor value has to be tuned every time to have maxi-

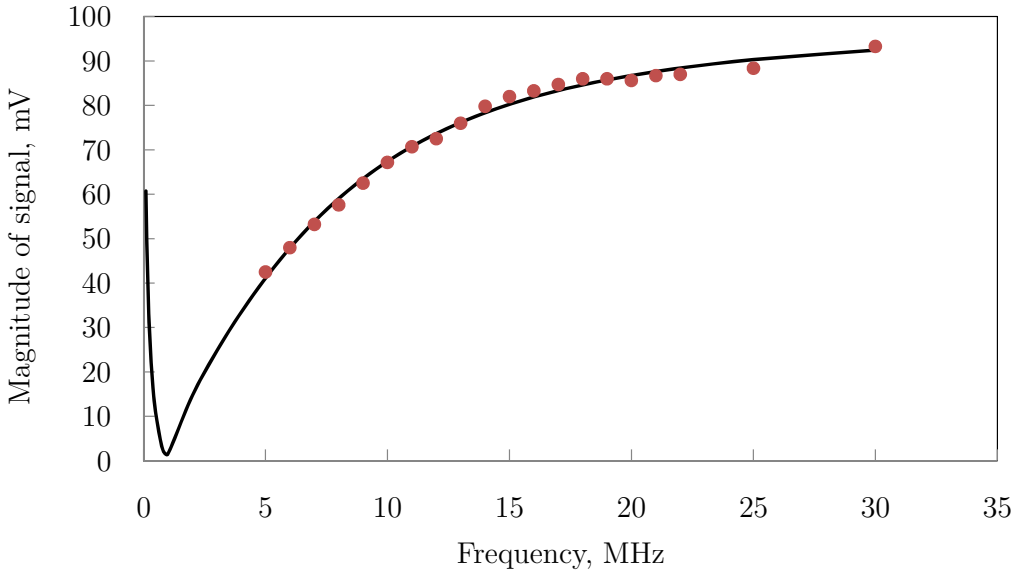

Figure 2.17: Measurement of the inductance of the chip wire. We measured the signal amplitude on an oscilloscope for the electric circuit shown in Fig. 2.16 for different frequencies while keeping a constant 100 mV output amplitude. Experimental data (dots) are fitted by the theory (solid line).

mum current at the desired frequency. With such a modification B_{rf} can be significantly increased but the circuit is not matched and in practice the reflected wave causes a lot of instabilities in the switches that are controlling currents in the magnetic coils during the experiment. To overcome this issue we install an rf transformer which helped to reach two goals at the same time: matching of the circuit impedance to minimize the reflected wave and increasing the current through the chip wire.

2.8.2 Rf transformer

An rf transformer is an ordinary transformer with a small number of turns in each winding. Rf transformers are usually used for matching transmission lines with different characteristic impedances (Fig. 2.18 (a)). According to the basic principles of transformer operation an oscillating voltage V_1 on the left (primary) windings of transformer creates a changing magnetic flux in its core which induces a periodic voltage V_2 in the secondary windings. In an ideal case (no wire resistance, no magnetic flux losses) it can be written $\frac{V_1}{V_2} = \frac{N_1}{N_2}$.

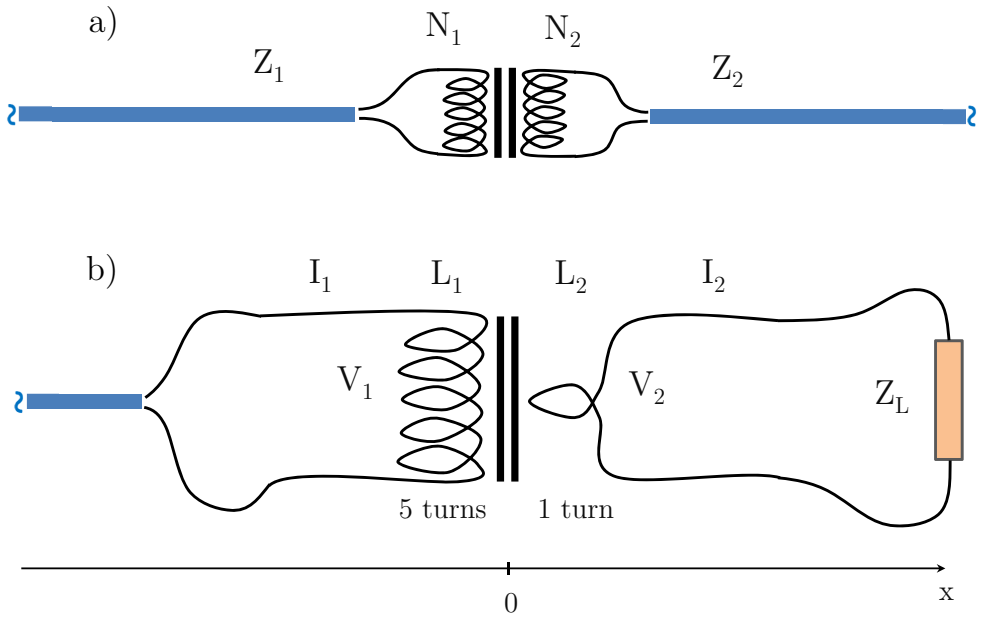

Figure 2.18: a) The rf transformer matches two lines with different characteristic impedances. b) In our setup the 5 turns of the rf transformer primary windings are connected to the end of transmission line whereas a single turn of the secondary windings goes to the chip circuit.

Also energy flows from the first transmission line into the second line with no losses, i.e., $V_1 I_1 = V_2 I_2$ for their apparent values of current and voltage. As a result the ratio of currents in the transformer windings is inversely proportional to the ratio of its turns $\frac{I_1}{I_2} = \frac{N_2}{N_1}$. Also, for the matched case (no reflected wave) it can be written that $Z_{1,2} = \frac{V_{1,2}}{I_{1,2}}$, so $\frac{Z_1}{Z_2} = (\frac{N_1}{N_2})^2$. According to Eq. 2.17, in the matched case $\gamma = 0$ from which the current amplitude is $|I_S| = \frac{|V_S|}{2Z_0}$. Comparing the amplitudes of the currents for matched cases with and without the rf transformer leads to:

$$\begin{aligned} |I_1| &= \frac{|V_1|}{2Z_1}, \\ |I_2| = \frac{|V_2|}{2Z_2} = \frac{|V_1|}{2Z_2}\frac{N_2}{N_1} &= \frac{|V_1|}{2Z_1}\frac{N_2}{N_1}\left(\frac{N_1}{N_2}\right)^2 = \frac{N_1}{N_2}|I_1| \end{aligned} \tag{2.19}$$

Thus Eq. 2.19 demonstrates that the decrease of resistance has a stronger effect than the drop of voltage and thus a step-down rf transformer helps to increase the current in the secondary circuit by a factor of $\frac{N_1}{N_2}$.

It is also interesting to compare the current amplitudes for the two cases: the matched case Eq. 2.19 with rf transformer and the mismatched case without transformer but connecting the same smaller impedance $Z_L = (\frac{N_2}{N_1})^2 Z_1$ as a load in the first line:

$$\gamma = \frac{(\frac{N_2}{N_1})^2 Z_1 - Z_1}{(\frac{N_2}{N_1})^2 Z_1 + Z_1} = \frac{N_2^2 - N_1^2}{N_2^2 + N_1^2} \tag{2.20}$$

This is a real negative number which means that $cos\phi$ = -1. Noting that $|\gamma| = \frac{N_1^2 - N_2^2}{N_2^2 + N_1^2}$ as $N_2 \leq N_1$, from Eq. 2.17 it follows that:

$$|I_L| = \frac{|V_1|}{2Z_1}(1 + |\gamma|) = \frac{|V_1|}{2Z_1}\left(\frac{2N_1^2}{N_1^2 + N_2^2}\right) \tag{2.21}$$

Comparing Eq. 2.19 with Eq. 2.21 gives:

$$\frac{|I_2|}{|I_L|} = \frac{N_1}{N_2}\left(\frac{N_1^2 + N_2^2}{2N_1^2}\right) = \frac{N_1^2 + N_2^2}{2N_1 N_2} > \frac{N_1}{2N_2} \tag{2.22}$$

In conclusion, the rf transformer gives an advantage in current amplitudes when the ratio of the number of turns in the windings is more than two.

In our experiment we use a commercial step-down rf transformer with 5 turns in the primary winding and a single turn in the secondary winding (Fig. 2.18 (b), there is no second transmission line but the load, ideally matched with the second transmission line, is equivalent to a direct connection of the load to the secondary windings of the transformer). In Appendix C.0.7 there is a brief theory of the rf transformer operation that supports Eq. 2.19 and leads to the conclusion that to achieve matching conditions the load impedance Z_L should satisfy:

$$\begin{cases} x = Re(Z_L) = \frac{L_2}{L_1} R_0 = \frac{N_2^2}{N_1^2} R_0, \\ y = Im(Z_L) = 0 \end{cases} \tag{2.23}$$

According to Section 2.8.1, from Fig. 2.17 the chip wire load behaves as an inductive impedance. Thus in order to satisfy conditions in Eq. 2.23 an additional capacitor C and resistor $R = \frac{N_2^2}{N_1^2} R_0$ should be introduced in the secondary circuit of the rf transformer (Fig. 2.19). Additional AC-DC decoupling capacitors C_C are used at both sides of the connection to the chip wire, similar to Fig. 2.16. By varying the capacitor C the total

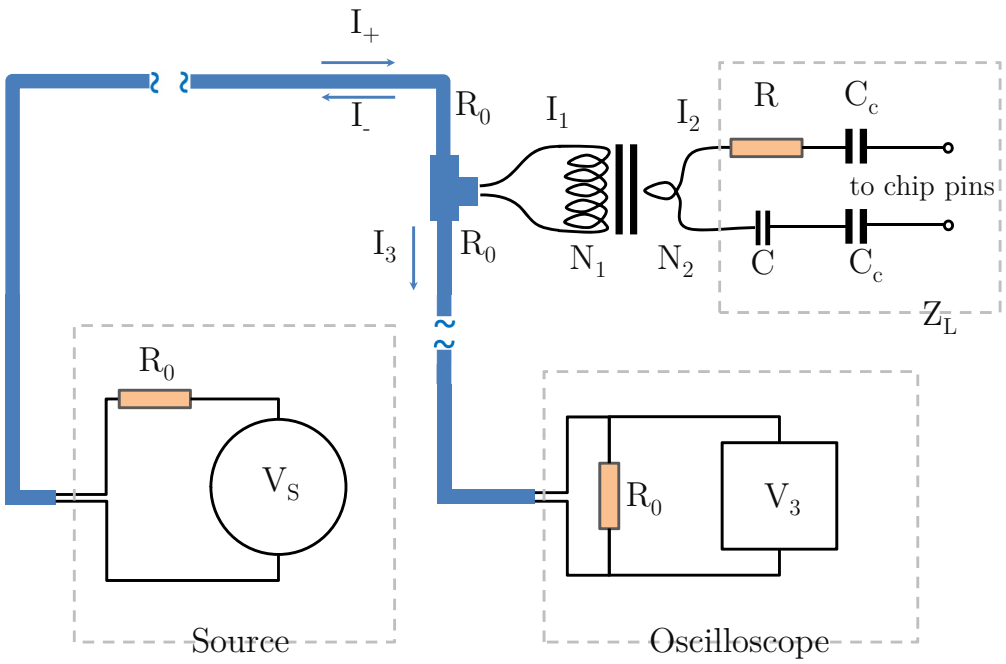

Figure 2.19: Scheme of connections for matching a chip-circuit to a chosen frequency by varying the capacitor C. We record the amplitude of the signal on an oscilloscope for a range of frequencies.

reactive part of the load is nullified: $(Lw - \frac{1}{wC_T}) = 0$, where C_T is the total capacitance of the three capacitors C, C_C and C_C in series.

From Eq. 2.23 it is clear that the load can only satisfy matching conditions for a specific frequency, so if we are interested in different frequencies we need to tune the circuit for each of them. We developed a simple method of tuning the circuit to have a matched load over a specific frequency range. Similar to the case of the previously described method of chip-wire inductance measurement (Fig. 2.16) a 50 Ω oscilloscope channel is connected parallel to the end of the transmission line (also parallel to the primary windings of our rf transformer (Fig 2.19)). For such a connection the theoretical dependence of the voltage on the oscilloscope for different frequencies is derived in Appendix C.0.8, which predicts:

$$|V_{scope}| = \frac{|V_s|}{2}\sqrt{\frac{(2L_0N_1^2\omega x)^2 + (2L_0N_1^2\omega y)^2}{(xR_0 - 2L_0N_1^2\omega y)^2 + (yR_0 + 2L_0N_1^2\omega x + L_0N_2^2\omega R_0)^2}} \tag{2.24}$$

where L_0 is the inductance of a single turn of rf transformer windings, $\omega = 2\pi f$ is the rf angular frequency and x and y denote the real and imaginary part of the impedance Z_L,

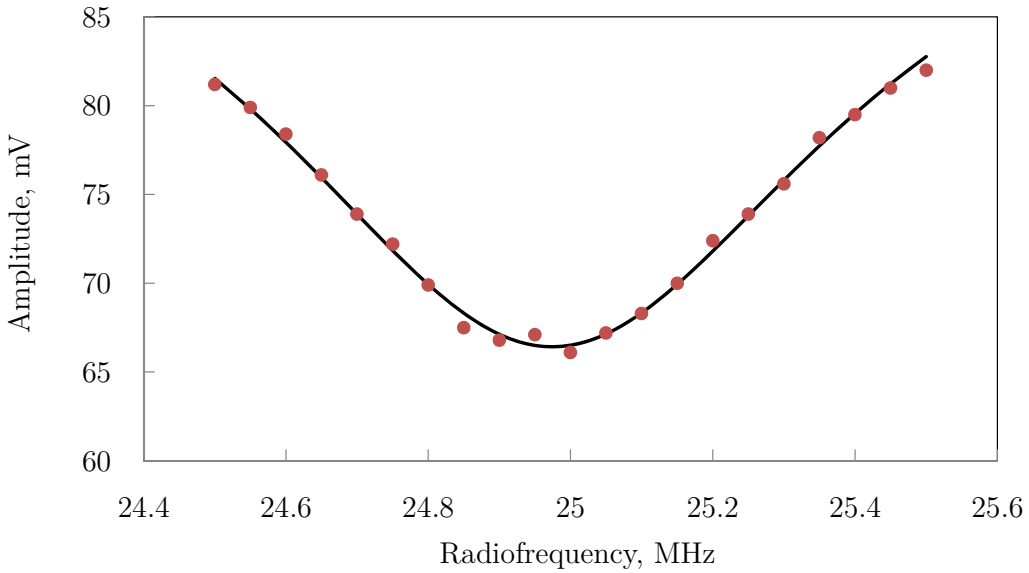

Figure 2.20: Example of a typical signal on the oscilloscope for a connection as in Fig. 2.19. Points are the experimental data and the line is the theoretical fit using Eq. 2.24.

respectively.

The oscilloscope signal amplitude is recorded with a 50 kHz frequency step for 100 mV of the signal amplitude on the generator (in this case $|V_S| = 200$ mV) and then Eq. 2.24 is used to fit the measured points with the known values of $L_0 = 2$ μH, $N_1 = 5$, $N_2 = 1$, $R_0 = 50$ Ω and free parameters V_S, x, L, C_T ($y = Lw - \frac{1}{C_T w}$). Figure 2.20 shows the dependence of the oscilloscope voltage on frequency for the chip-circuit tuned to 25 MHz. The signal amplitude stays equal to $\frac{|V_S|}{2}$ for all the frequencies except in the vicinity of the resonance, where it has a minimum that is equal to $\frac{|V_S|}{3}$ for the matched case (Eq. C.46). This behaviour is caused by the dominance of the reactive part of Z_L away from resonance, so that the total impedance becomes greater than the 50 Ω of the oscilloscope channel. This frequency selectivity acts as an additional filter in our experiment that blocks all other rf harmonics; however, it has the drawback of the need to change the capacitor for almost every experimental point during the molecule association measurements.

The shape of the curve can be changed by varying the capacitor C to shift the resonant frequency and the resistor R for the voltage amplitude at the minimum (they both are

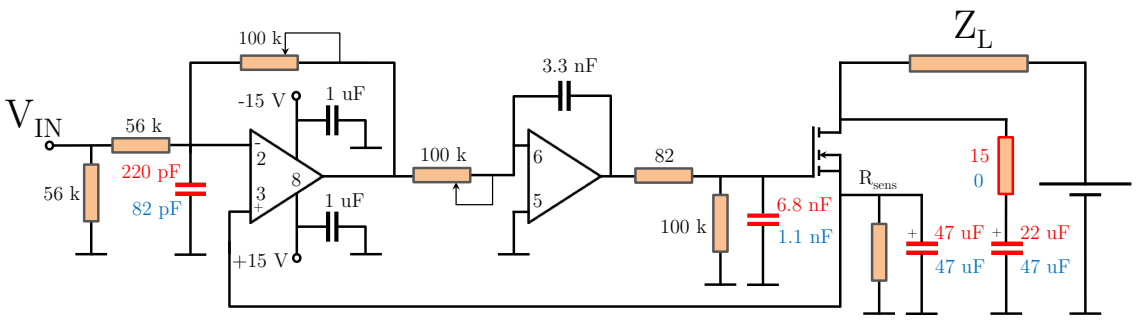

Figure 2.21: Electric circuit of a current controlling switch that we use in our experiments. Red elements were implemented to ground high frequency noise. Blue values are for Z-wire switch and red ones are for B_{xLarge} coils controller.

parts of the Z_L in Fig. 2.19). The best fit for a particular set of C and R, shown in Fig. 2.20, gives the following parameters: $|V_S| = 195$ mV, $x = 2.13\ \Omega$, $L = 0.46\ \mu$H, $C_T = 88$ pF, which is in good agreement with the previously measured $L = 0.4\ \mu$H and nominal value of 80 pF for the soldered set of capacitors (100 pF in series with 1 μF, in series with 1 μF, in series with 270 pF being in parallel with 82 pF).

The matched load minimizes the rf noise in our system associated with the reflected wave. However, to be able to perform the experiments with such high power radio-frequency it was also necessary to add low-pass filters into our home-made current controllers. Figure 2.21 shows the electrical circuit that is used to stabilize the current through the load Z_L which can be a magnetic coil or a chip wire. The values of the filtering capacitors were chosen experimentally as a compromise between filtering quality and the switching speed of the controllers.

CHAPTER 3

Calibration of DC and AC magnetic fields

In order to compare the experimental data with theoretical predictions all the experimental conditions should be accurately characterized, they include the amplitude and the resonant frequency of the rf field which is applied for the association of ultracold molecules and the DC magnetic field at which the trapped atoms are held during molecule association. Measurements of resonant radiofrequencies are described in Chapter 4. The following chapter describes how the DC magnetic field has been measured by employing a microwave spectroscopy technique in which atoms in the initial $|F = 1, m_F{=}{-1}\rangle$ state are coupled to the state $|F = 2, m_F{=}0\rangle$ (σ^+ transition) and monitoring the dependence of atom transfer on the mw frequency. From the resonant mw frequencies the magnetic field values are calculated by using the inverse Breit-Rabi formula, [89]. It is important to perform the mw spectroscopy with the rf field switched on as high rf power affects our atom chip circuitry and leads to a systematic shift of the magnetic trap bottom. The second part of the chapter describes the in-situ method of measurement of the amplitude of the AC magnetic field in the frequency range $23 - 31$ MHz by using the two-photon resonant microwave/radio-frequency excitations and known relations between the two-photon Rabi frequency and the single-photon mw and rf Rabi frequencies.

3.1 Shape and broadening effects of the microwave spectroscopy line

There are a number of factors that contribute to the spectral profile of Bose-condensed atoms. In this section we investigate how the shape of mw spectroscopy resonance curves of the trapped condensed atoms are affected by atomic interactions, gravity, induced dipole oscillations and power broadening. At equilibrium the total energy of interacting condensed atoms in a trap comprises three components: magnetic, mean field and gravitational interactions. In the current section more complex assumptions are successively added into the initial model. It starts with the consideration of only magnetic and mean field energies in the model followed by adding gravity, dipole sloshing of the condensate in the trap and then power broadening in the atom-radio-frequency-field interactions. During experiments the mw pulse duration (3 ms) is kept long compared to the period of the mw Rabi flopping (224 μs) and under this condition the anticipated lineshape has a Lorentzian profile due to power broadening [64]. However, experiments show coupling profiles that are much broader than the 4.5 kHz mw Rabi frequency with significant asymmetric deviations from the Lorentzian shape. By taking into account the finite size of the BEC cloud (atoms cover a certain volume in space so that different parts of the BEC experience a different magnetic field) and induced dipole oscillations our theory can explain the observed asymmetry. Fitting of all experimental mw spectroscopy data with the convolution of the asymmetric BEC profile and the Lorentzian accounts for differences in magnetic field experienced by different parts of the BEC cloud.

Broadening mechanisms of the rf spectroscopy profile during stimulated molecule association are similar to the case of mw spectroscopy so the results of the coupling profile analysis are also used in the next section. As a result fitting of the data with our theory significantly increases the accuracy of the measurements of DC magnetic fields and the corresponding radiofrequencies.

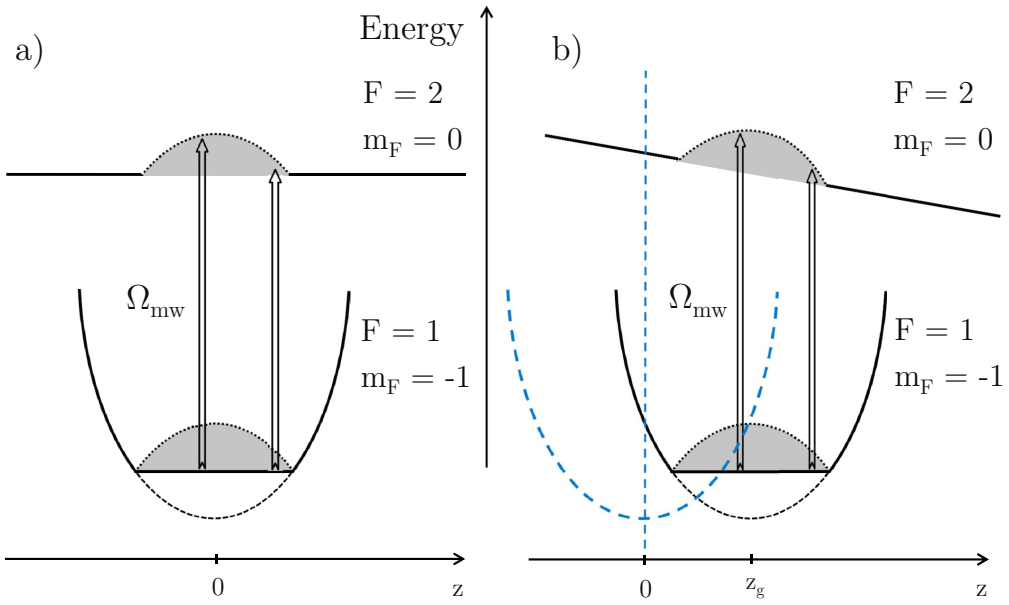

Figure 3.1: Solid black lines show total energy of BEC atoms of the trapped $|F = 1, m_F =$ -1$\rangle$ and untrapped $|F = 2, m_F = 0\rangle$ states. Arrows represent resonant mw coupling with the Rabi frequency Ω_{mw} (a) in absence of gravity and (b) in the gravitational field. Blue dashed lines represent the magnetic trapping potential and grey areas reflect the effect of non-uniform atomic interactions. The gravitational acceleration is aligned with the z axis.

3.1.1 Spectral line of BEC in absence of gravity

In the initial approximation gravity is neglected and the magnetic harmonic potential is considered to be symmetric in all directions. In the Thomas-Fermi approximation [76] the chemical potential of the trapped condensed atoms is determined by the fact that repulsive atomic interactions compensate the magnetic trapping potential (Fig. 3.1).

A resonant mw field turns on the coupling of the atoms from the magnetically trappable state $|1, -1\rangle$ to $|2, 0\rangle$. In Fig. 3.1 (a) the dashed line represents the energy of atoms in the magnetic potential and the dotted line with the grey area is the energy of the repulsive forces between atoms in the BEC. The total energy of the atoms is shown by the black solid line. The modulus of the total magnetic field is equal to $|B_0| + \frac{M}{\mu_B}\omega^2 r^2$ (Eqs. B.14 and B.17 with the substitution $r = \sqrt{x'^2 + y'^2 + (z - z_0)^2}$) and thus the magnetic energy

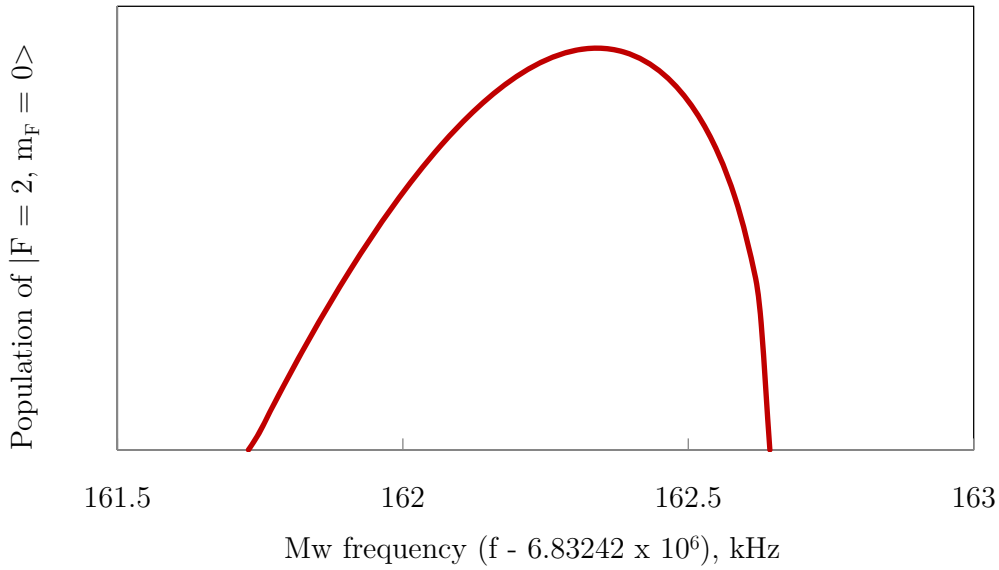

Figure 3.2: Mw spectral line of BEC with repulsive interactions in the absence of gravity, described by Eq. 3.4 with parameters: N = 2·10^5, $\omega_{x,z} = 2\pi\cdot 102$ Hz, $\omega_y = 2\pi\cdot 11.5$ Hz, R_0 = 4.7 μm, B_0=3 G, f_m = 162.64 kHz. The atoms are located near the local minimum of magnetic field which leads to relatively narrow coupling profiles.

is isotropic and depends only on the displacement r from the equilibrium position. B_0 is the magnetic field at the origin $r = 0$ and μ_B is the Bohr magneton. The magnetic energy is equal to:

$$E_B = m_F g_F \mu_B B = m_F g_F \mu_B (|B_0| + \frac{M}{\mu_B}\omega^2 r^2) \tag{3.1}$$

Interactions between the atoms in the same and in different internal states are almost the same, as they depend on the scattering lengths which have very close values around 100·a_0 [90]. Then the energies of the two states and the energy of the mw transition can be expressed as:

$$\begin{cases} E_{-1} = m_F g_F \mu_B (|B_0| + \frac{M}{\mu_B}\omega^2 r^2) + \chi n(r,\phi,\theta), \\ E_0 = E_{HF} + \chi n(r,\phi,\theta) \end{cases} \Rightarrow$$
$$E_{mw} = hf = E_{HF} - m_F g_F \mu_B (|B_0| + \frac{M}{\mu_B}\omega^2 r^2) = h(f_m - T^2 r^2) \tag{3.2}$$

where the $\chi n(r,\phi,\theta)$ term is the energy of the atomic interactions, $\chi = \frac{4\pi\hbar^2 a_{bd}}{m}$ with a_{bd} being the s-wave scattering length for collisions of two states b and d, $n(r,\phi,\theta)$ is the

number density, E_{HF} is the hyperfine splitting in ^{87}Rb and we have used substitutions $T = \sqrt{\frac{m_F g_F M}{\hbar}\omega^2} = \sqrt{\frac{M\omega^2}{2h}}$ and $f_m = \frac{1}{h}(E_{HF} - g_F\mu|B_0|)$. From Eq. 3.2 it follows that atoms in a spherical shell with radius r are resonant at the same mw frequency. With R_0 being the Thomas-Fermi radius of the BEC [76] the resonant transition frequency f decreases from f_m to $f_m - T^2R_0^2$ as r increases in the range $[0,\ R_0]$ (Fig. 3.1 (a)) and the number of resonant atoms in the shell is equal to:

$$dN(r) = n_0(1 - \frac{r^2}{R_0^2})4\pi r^2 dr \tag{3.3}$$

where n_0 is the peak number density. The number of resonant atoms can also be expressed as a function of the mw frequency:

$$dN(f) = \frac{2\pi n_0}{R_0^2 T^2}\frac{\sqrt{f_m - f}}{T}\left(R_0^2 - \left(\sqrt{\frac{f_m - f}{T}}\right)^2\right)df \tag{3.4}$$

It is reasonable to expect that the number of atoms that have been transferred to the $|2,\ 0\rangle$ state during the mw pulse is proportional to the total number of atoms that are resonant to this transition. Thus Eq. 3.4 describes the relative number of atoms transferred into the $m_F = 0$ state or the spectral line which is shown in Fig. 3.2.

3.1.2 Effect of gravity sag

In the general case the trap frequencies ω_x, ω_y and ω_z are different for the x', y' and z' directions. However, it is much easier to do the math in a spherically symmetrical trap. Through the coordinate transformations the results of the previous Section 3.1.1 can be generalized:

$$\begin{cases} x = x'\frac{\omega_x}{\omega}, \\ y = y'\frac{\omega_y}{\omega}, \\ z = z'\frac{\omega_z}{\omega} \end{cases} \tag{3.5}$$

where $\omega = (\omega_x\omega_y\omega_z)^{\frac{1}{3}}$ is the geometrical mean frequency of the trap.

In the presence of a gravitational field the center of the cloud is shifted from the minimum of the magnetic field vertically down to the value z_g. In the Thomas-Fermi approximation [76] all trapped atoms within the cloud have the same energy, so that the

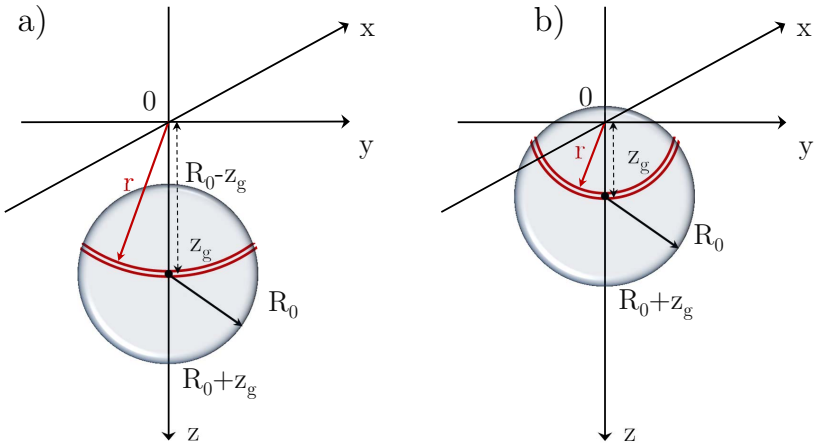

Figure 3.3: A general case with arbitrary trap frequencies can be simplified by choosing a new coordinate system (Eq. 3.5) so that the trap becomes spherically symmetric and as a consequence the BEC cloud has a spherical shape. According to Eq. D.3 the resonant mw frequency is the same for all the atoms in the BEC that are forming a semi-shell of radius r (red radius-vector in the figure; atoms in the shell are shown located between two red circular arcs). (a) represents the case $z_g \geq R_0$ so that $r \in [R_0 - z_g,\ R_0 + z_g]$. (b) represents the case $z_g < R_0$, where $r \in [0,\ R_0 + z_g]$.

repulsive forces between atoms compensate the magnetic trapping potential and gravity (Fig. 3.1 (b)). Similar to the previous case in Section 3.1.1 the difference of the total energies of the atoms in the two states in the new coordinate system, Eq. 3.5, depends only on the modulus of r (Eq. D.3 in Appendix D.0.9). Then by evaluating the integral in spherical coordinates the number of resonant atoms dN can be expressed as a function of r (Eq. D.10), which can be rewritten as a function of the mw frequency f:

$$\begin{cases} dN = \Phi_1(f) = \frac{1}{\chi} M\omega^2 \frac{\pi}{T^2} \frac{1}{8 z_g} \left(R_0^2 - (\frac{\sqrt{f_m - f}}{T} - z_g)^2 \right)^2 df, \\ \qquad\qquad f \ \in \ [f_m - (R_0 + z_g)^2 T^2,\ f_m - (R_0 - z_g)^2 T^2] \\ dN = \Phi_2(f) = \frac{1}{\chi} M\omega^2 \frac{\pi}{T^2} \frac{\sqrt{f_m - f}}{T} \left(R_0^2 - z_g^2 - (\frac{\sqrt{f_m - f}}{T})^2 \right) df, \\ \qquad\qquad f \ \in \ [f_m - (R_0 - z_g)^2 T^2,\ f_m] \end{cases} \tag{3.6}$$

In the current approximation it is assumed atoms in the BEC keep the Thomas-Fermi profile during the mw spectroscopy with a constant radius R_0 (this is only approximately

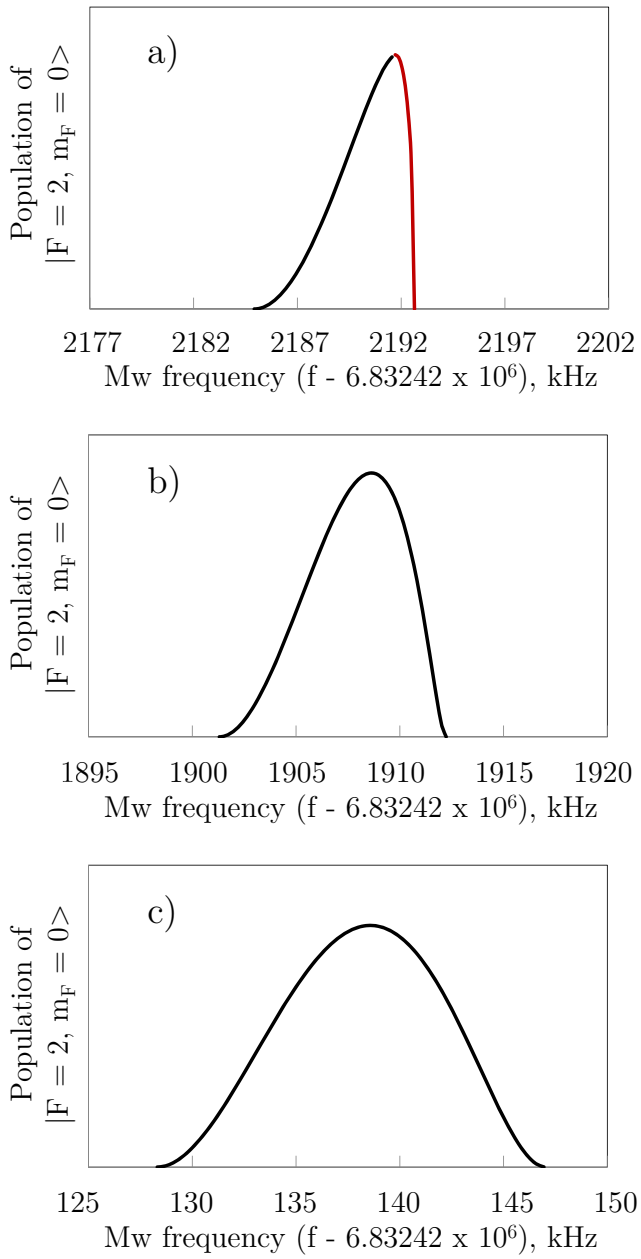

Figure 3.4: Theoretical mw spectral lines in the presence of gravity (Eq. 3.6). The contribution of functions Φ_1 and Φ_2 are shown by black and red lines at different magnetic fields ($\omega_y = 2\pi{\cdot}11.5$ Hz and N = $2{\cdot}10^5$ for all cases): (a) 0.1 G ($\omega_{x,z} = 2\pi{\cdot}560$ Hz, $R_0 = 1.7$ μm, $z_g = 0.8$ μm, $f_m = 2192.64$ kHz); (b) 0.5 G ($\omega_{x,z} = 2\pi{\cdot}250$ Hz, $R_0 = 2.7$ μm, $z_g = 4.0$ μm, $f_m = 1920.64$ kHz); (c) 3 G ($\omega_{x,z} = 2\pi{\cdot}102$ Hz, $R_0 = 4.7$ μm, $z_g = 24.1$ μm, $f_m = 162.64$ kHz). The vertical axes have been rescaled for better representation.

valid as after being transferred to the $|2,0\rangle$ state the atoms start to fall under gravity).

It follows from Eq. 3.6 that in the general case profile of the coupling frequencies is described by two functions: when $z_g \geq R_0$, r belongs to the interval $[R_0 - z_g,\ R_0 + z_g]$ whereas for $z_g < R_0$, $r \in [0,\ R_0 + z_g]$ (Fig. 3.3). The corresponding mw frequencies can be calculated from Eq. D.3 as $f = f_m - r^2T^2$. Thus for $z_g \geq R_0$, f changes within the interval $[f_m - (R_0 + z_g)^2T^2,\ f_m - (R_0 - z_g)^2T^2]$ and the entire profile is described by the function Φ_1 in Eq. 3.6, whereas the $z_g < R_0$ case corresponds to $f \in [f_m - (R_0 + z_g)^2T^2,\ f_m]$ and both functions Φ_1 and Φ_2 play a role. Equation 3.6 becomes identical to Eq. 3.4 in the limit $z_g \to 0$.

To visualize Eq. 3.6 the theoretical spectral lines for mw spectroscopy are plotted for three values of the magnetic field in Fig. 3.4. An approximate linear splitting of 700 kHz/G is used for the Zeeman levels in the magnetic field for estimating f_m, from which the parameters ω and z_g are calculated using equations B.17 and B.20 as well as the Thomas-Fermi radius R_0 for $2 \cdot 10^5$ atoms. The magnetic field directly affects only the position of the resonance through f_m, rather than its shape which depends on the trap frequencies. However, during the experiment the current through the Z-wire and the B_{xLarge} field in the last magnetic trap are rarely modified so that the trap frequencies change as shown in Fig. 2.8. It becomes clear from Fig. 3.4 that the spectral line shape changes with magnetic field: it is narrower and more asymmetric for smaller fields.

Atoms in the BEC cloud cover a range of magnetic fields which from Eq. 3.6 correspond to the resonant mw frequencies $[f_m - (R_0 + z_g)^2T^2,\ f_m - (R_0 - z_g)^2T^2]$ ($[f_m - (R_0 + z_g)^2T^2,\ f_m]$ in the case $z_g < R_0$), where the frequency f_m is determined by the local minimum value of the magnetic field B_0. The size of the cloud R_0 depends on the total atom number and so do the lowest $f_{min} = f_m$ - $\frac{M\omega^2(z_g+R_0)^2}{2h}$ and the highest $f_{max} = f_m$ - $\frac{M\omega^2(z_g-R_0)^2}{2h}$ frequencies which adds noise to the resonance coupling shape (Fig. 3.5). However, the frequency

$$f_0 = f_m - \frac{M\omega^2 z_g^2}{2h} \tag{3.7}$$

which corresponds to atoms in the centre of the trap (and hence in the centre of the cloud) is independent of shot-to-shot atom number fluctuations during the mw spectroscopy experiment and can be extracted with a high precision. From the Breit-Rabi formula we

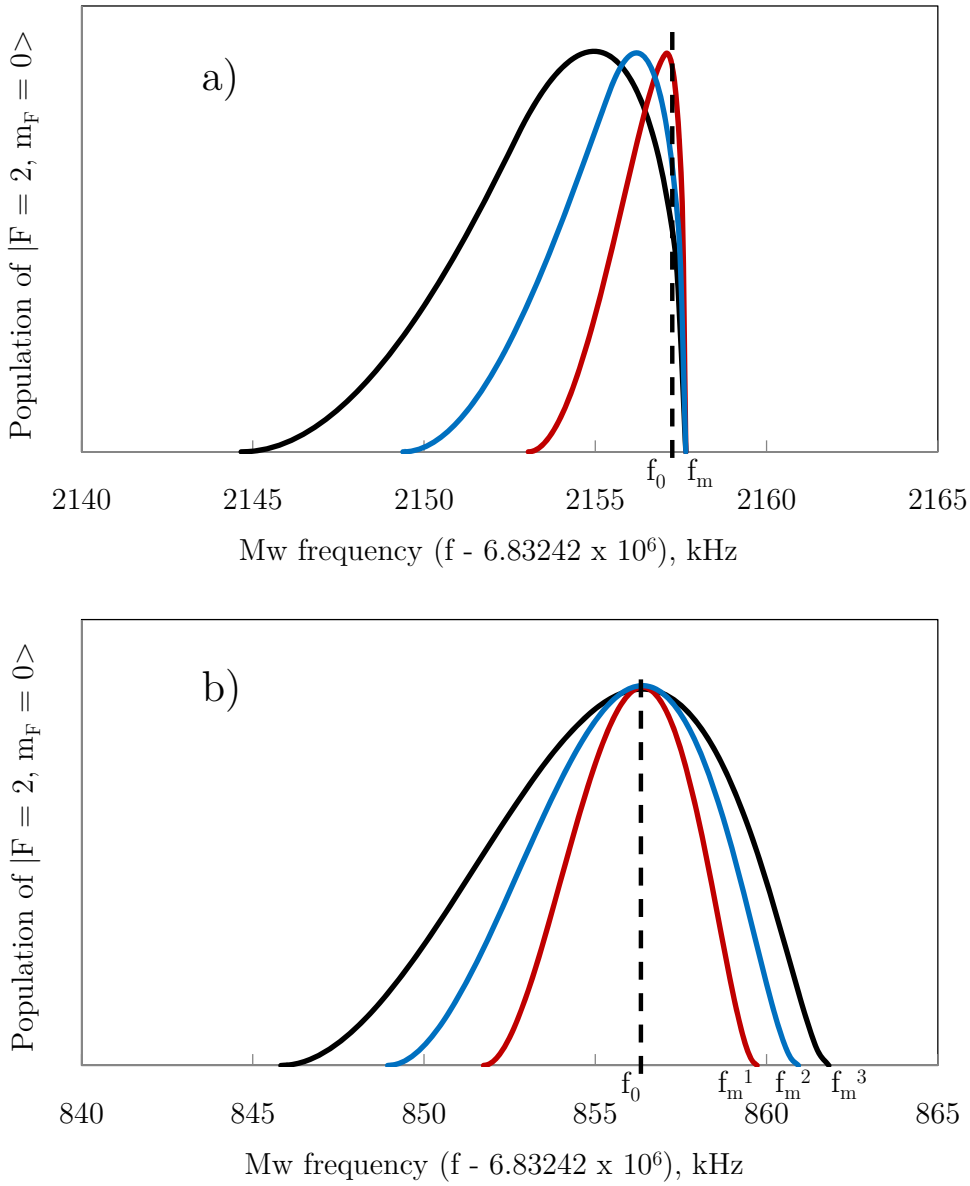

Figure 3.5: Dependence of the mw spectral line on the number of atoms in a BEC. (a) Coupling profiles at 0.15 G trap share the same frequency f_m with separate peaks in each case of R_0 equal to 1 μm (red line, N = 3.2·10^4), 1.5 μm (blue line, N = 2.4·10^5) and 2.0 μm (black line, N = 10^6). (b) Coupling profiles at 2 G trap for different atom numbers in the BEC spectral lines broaden and shrink, maintaining the same peak frequency. Red, blue and black lines correspond to R_0 equal to 2 μm (N = 2.1·10^4), 3 μm (N = 1.6·10^5) and 4 μm (N = 6.6·10^5), respectively. Black dashed line shows the frequency f_0 in both cases.

calculate the value of the magnetic field B_{bottom} corresponding to the frequency f_0 and then correlate it with the radio-frequency that is resonant with atoms in the centre of the BEC during the molecule association experiment.

It is interesting to note that the frequency f_0 corresponds to the maximum of the function $\Phi_1(f)$ in Eq. 3.6 (Eq. D.14 in Appendix D.0.9).

3.1.3 Dipole oscillations during the microwave spectroscopy

In order to measure the value of the magnetic field during the formation of molecules the mw spectroscopy is performed after applying the rf field for the same holding time as in the atom-molecule coupling experiment (usually 420 ms) before the mw pulse and keeping the rf field on during the pulse as well (Fig. 3.8). It was noticed that the shot-to-shot position of the clouds varies slightly in the imaging frames. This means that the BEC clouds are experiencing dipole oscillations in the trap, induced by shaking of the trap at the moment of turning on the high power rf field.

Equation 3.6 predicts the spectral profiles shown in Fig. 3.4 in the approximation of a non-moving cloud in the trap and weak coupling (the atoms feel only the resonant frequencies). The next improvement to the model is the derivation of the spectral profile for an oscillating cloud in the trap.

As described in Appendix B.0.1 the Z-wire magnetic trap is generated by only three units: B_{yEarth} magnetic coils, Z-wire current and B_{xLarge} coils. The sudden application of a strong rf field leads to small changes in the DC currents through the switches. Due to its design the centre of the magnetic trap is always located under the centre of the Z-wire and can not be shifted in the x or y direction by currents in these three units. As a result, the trap minimum is shifted along the z coordinate leading to dipole oscillations along this direction (it is confirmed by the observation of the fluctuations in only the vertical position of the cloud during the mw spectroscopy measurement). Thus, the vertical coordinate of the atomic cloud becomes a function of time $z_g(t)=z_g^0 + d \cdot cos(\omega t)$, which shifts the peak frequency and broadens the resonance (Fig. 3.6). For any time t Eq. 3.6 determines the number of atoms that are resonant with different frequencies during time dt. The average number of atoms that are resonant for different frequencies during one period of dipole

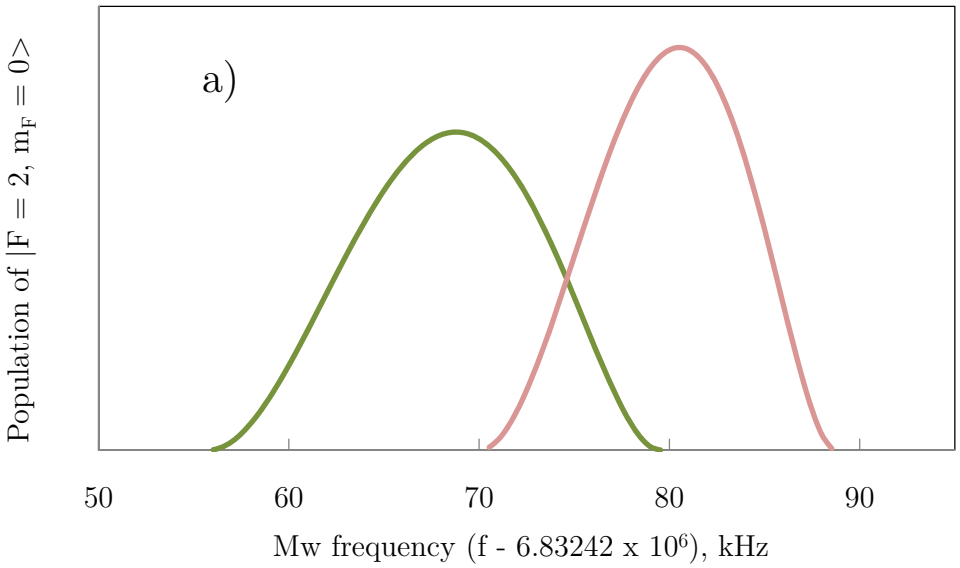

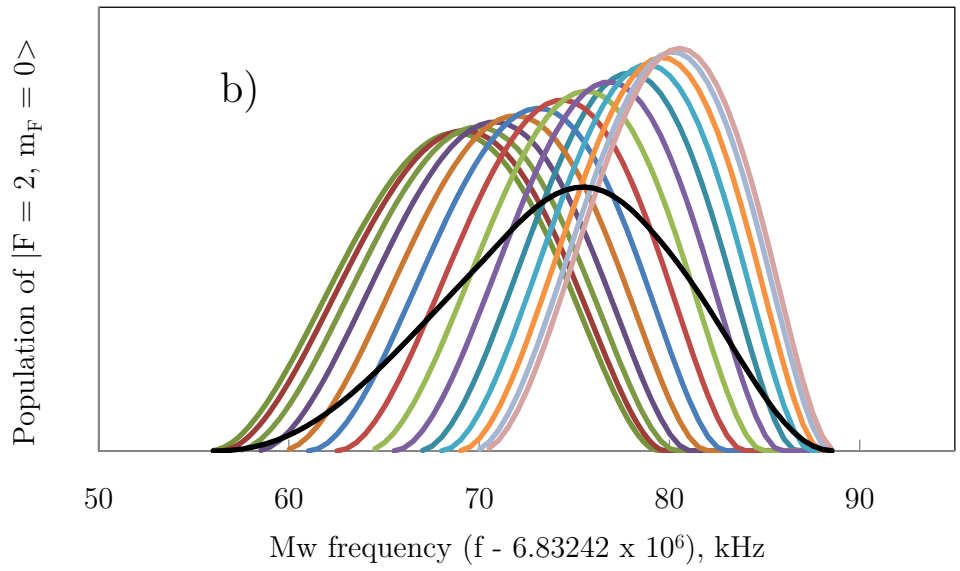

Figure 3.6: Spectral mw profiles that are given by Eq. 3.6 for simulating experimental conditions with $B_0 = 3.06$ G; $\omega_{x,z} = 2\pi{\cdot}101$ Hz; $\omega_y = 2\pi{\cdot}11.5$ Hz; $N = 2{\cdot}10^5$; $R_0 = 5$ μm; $z_g^0 = 25$ μm; $d = 3$ μm. The mw frequency is shown relative to 6.832419968 GHz which corresponds to a splitting of 3.23 G. (a) Demonstration that larger z_g (green solid line) corresponds to a broader profile with a lower peak frequency. (b) Black line represents an average of the coloured lines during one period of collective oscillation, visualizing the manual integration of Eq. 3.8.

oscillations T_{do} can be calculated by substituting $z_g(t)$ into Eq. 3.6 and integrating over time:

$$\begin{cases} dN = \frac{1}{8}\frac{2\pi h}{T_{do}\chi}df \int_t \frac{\left(R_0^2 - (\frac{\sqrt{f_m - f}}{T} - |z_g^0 + d\cdot cos(\omega t)|)^2\right)^2}{|z_g^0 + d\cdot cos(\omega t)|}dt, \\ \qquad\qquad f \in [f_m - (R_0 + z_g(t))^2T^2,\ f_m - (R_0 - z_g(t))^2T^2] \\ dN = \frac{2\pi h}{T_{do}\chi}df \int_t \frac{\sqrt{f_m - f}}{T}\left(R_0^2 - (z_g^0 + d\cdot cos(\omega t))^2 - (\frac{\sqrt{f_m - f}}{T})^2\right)dt, \\ \qquad\qquad f \in [f_m - (R_0 - z_g(t))^2T^2,\ f_m] \end{cases} \tag{3.8}$$

For frequencies f in the range $[(f_m - (R_0 - |z_g(t)|)^2T^2)_{min},\ (f_m - (R_0 - |z_g(t)|)^2T^2)_{max}]$ the average number of resonant atoms is the sum of both functions.

Due to the parasitic nature of the cloud movements in the trap it is reasonable to assume a random phase of the oscillations during the start of the mw pulse after the holding time. This means that the expected shape of the coupling curve is described by the average number of atoms, i.e. by Eq. 3.8. Figure 3.6 (b) helps to understand this fact, visualizing the position of the resonant coupling curve after equal time intervals during the dipole oscillations of the cloud in the trap. A short mw pulse duration compared to the period of the cloud oscillations would show a coupling curve with large fluctuations from the average. As is easily seen from Fig. 3.6 (b) on the sides of the profile it is possible to observe a maximum coupling strength or zero response, whereas at the centre some portion of the atoms is always in resonance but can significantly vary shot-to-shot. Longer mw pulses make the curves smoother as the number of atoms is integrated and so partly averaged during the pulse. In our experiments it was empirically found that 3 ms pulses give good results for mw spectroscopies over the whole range of the trap frequencies.

Unfortunately, direct integration of Eq. 3.8 is not possible as the function under the integration should be zero outside the range of frequencies $[f_m$ - $\frac{M\omega^2(z_g(t)+R_0)^2}{2h},\ f_{max}]$, i.e., multiplied by the gate-function which is also time-dependent. As a solution we use an approximate numerical averaging method by dividing the period of oscillation T_{do} into M time intervals and assuming that the function under the integral is time independent during $\Delta t = \frac{T_{do}}{M}$ with $z_g = z_g(t + \frac{\Delta t}{2})$. Visualization of this method is shown in Fig. 3.6. Part (a) shows resonant curves for the minimum (pink) and the maximum (green) values of z_g. During sloshing the position of the cloud in the trap is changing and so does its

spectral response. Figure 3.6 (b) shows resonant curves at different times (with a fixed time step) during the dipole oscillation and the black line is the sum of all coloured curves divided by M. It is interesting to note that time averaging increases the asymmetry of the resonant coupling curve as well as its width, and the density of lines is lower at the centre which makes perfect sense as during dipole oscillations the cloud slows down at larger deflection from the centre and so spends more time there.

3.1.4 Power broadening and magnetic noise

The effect of power broadening is also needed to be taken into account, i.e., during the coupling of the atoms with the strong rf field the line width of the transition becomes broader. Due to this effect the atoms become sensitive to a range of frequencies with a spectral profile described by a Lorentzian function [64]:

$$dN = \frac{dN_0 \Delta^2}{4(f - f_c)^2 + \Delta^2} \tag{3.9}$$

where dN_0 is the peak number of coupled atoms, f_c is the resonant frequency and Δ specifies the full width at half maximum (FWHM) of the resonance. This power broadening leads to an additional broadening of the BEC spectral lines in Eq. 3.8. Every group of atoms dN in Eq. 3.8 now has a spectral line in the shape of Eq. 3.9 instead of responding only to a resonant mw frequency.

The presence of the magnetic noise also leads to additional broadening of spectral lines described by a gaussian distribution function. Parameters f_m, ω and hence T, z_g and R_0 in Eq. 3.6 depend on the magnetic field; however, small variations of the magnetic field effectively do not change the shape of the spectral line leading only to a shift of the peak frequency. According to Section 2.7 the fluctuating background magnetic fields add some uncertainty to the magnetic field generated by the controlling switches. The position of the spectral line in Eq. 3.6 is determined by the frequency $f_m = \nu_{HF} - \frac{\mu_B m_F g_F}{h} B_0$ which has a linear dependence on the magnetic field. Thus a gaussian spread of the magnetic field leads to gaussian broadening of the resonance lines for every dN in Eq. 3.8

$$dN = dN_0 \cdot e^{-\frac{(f-f_c)^2}{2\Delta^2}} \tag{3.10}$$

To combine independent broadening effects a convolution of all three effects needs to

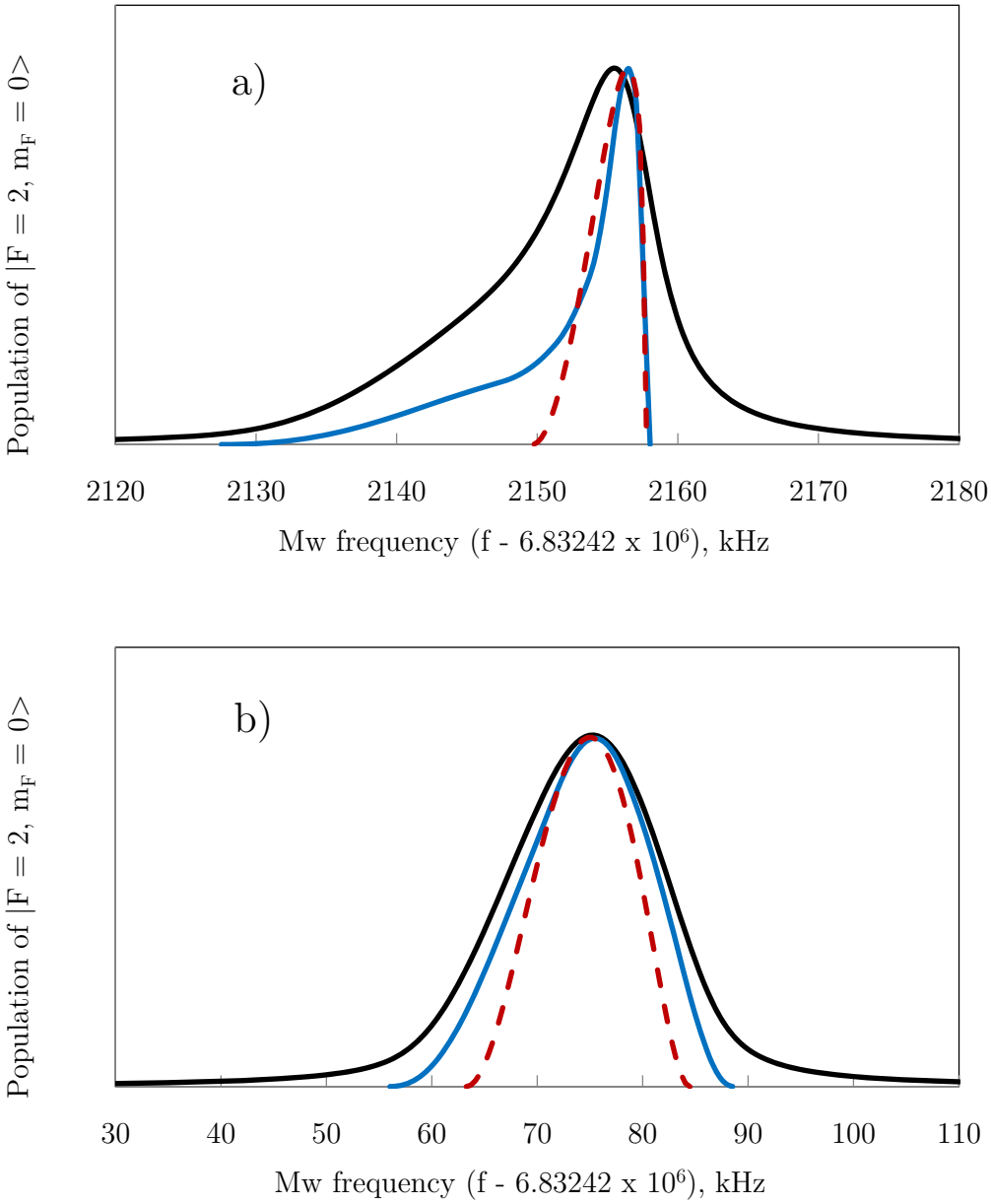

Figure 3.7: Contribution of different factors that determine the broadening of spectral lines for (a) 0.15 G, (b) 3 G at the centre of the trap. The red dashed line represents the initial shape, described by equation 3.6. The blue line shows broadening due to dipole oscillations, Eq. 3.8, with $d = 3$ μm in both cases. The black line demonstrates addition of the Lorentzian broadening with $\Delta = 2\pi{\cdot}5$ kHz.

be done using Eqs. 3.8, 3.9 and 3.10. A Voigt function is a convolution of gaussian and Lorentzian functions and is commonly used in many branches of spectroscopy. Thus the convolution of Eq. 3.8 with a Voigt function is a mathematically identical task which includes all the discussed broadening effects. However, this leads to a large complication of the fitting process and instead of that we simplify the model by keeping only the two strongest broadening effects. From Section 2.7 the measured FWHM of the magnetic noise is 2 mG, which corresponds to 1.4 kHz of the gaussian broadening width. At the same time the expected width of the power broadening is the value of the one-photon mw Rabi frequency (4.5 kHz). Thus, power broadening dominates over the magnetic noise effect and this is convoluted with the BEC profiles (Eq. 3.8), whose width is larger than 5 kHz even for the smallest magnetic fields used in our experiments (Fig. 3.4).

To combine the broadening due to the finite BEC size, the dipole oscillations and the power broadening the usual convolution function is employed

$$dN = \int g(\nu)h(f-\nu)d\nu \tag{3.11}$$

where $g(\nu)$ is described by Eq. 3.8 and $h(f-\nu)$ is Eq. 3.9. It is reasonable to assume that during the mw spectroscopy the number of atoms that have been transferred into the F=2, m_F=0 state is proportional to the number of atoms that are resonant at this frequency:

$$\begin{cases} dN = Adf \int_\nu \int_t \dfrac{\left(R_0^2 - (\frac{\sqrt{f_m-\nu}}{T} - |z_g^0 + d\cdot cos(\omega t)|)^2\right)^2}{|z_g^0 + d\cdot cos(\omega t)|\left(4(f-\nu)^2+\Delta^2\right)} dt d\nu, \\ \qquad\qquad f \in [f_m - (R_0 + z_g^0(t))^2T^2,\ f_m - (R_0 - z_g^0(t))^2T^2] \\ dN = 8Adf \int_\nu \int_t \dfrac{\sqrt{f_m-f}}{T} \dfrac{\left(R_0^2 - (z_g^0 + d\cdot cos(\omega t))^2 - (\frac{\sqrt{f_m-\nu}}{T})^2\right)}{4(f-\nu)^2+\Delta^2} dt d\nu, \\ \qquad\qquad f \in [f_m - (R_0 - z_g^0(t))^2T^2,\ f_m] \end{cases} \tag{3.12}$$

Equation 3.12 represents the final expressions that are used for fitting of the mw spectral lines. We simplify it by using the numerical averaging as described in Section 3.1.3. We also combine the piecewise defined function in Eq. 3.12 into one by multiplying the two parts of the equation by an analytical expression of the normalized step function (Eqs. D.17 and D.18 in Appendix D.0.11).

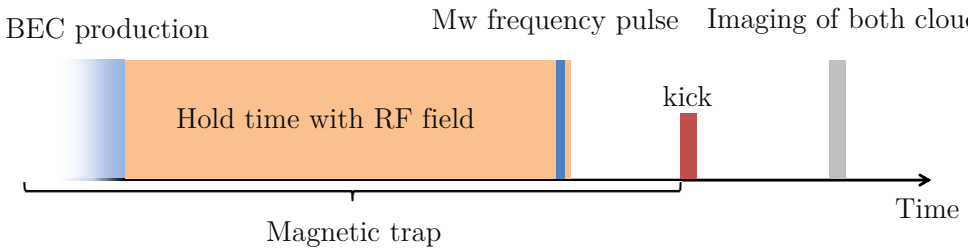

Figure 3.8: Time sequence of the mw spectroscopy experiment.

3.2 Microwave spectroscopy of the trapped Bose-Einstein condensate

In the presence of a magnetic field the magnetic states of an alkali atom split in accordance with the Breit-Rabi formula [89]. In addition to the Rabi flopping measurements described in Section 3.3 we perform a direct mw spectroscopy by tuning the mw frequency into resonance and measuring the dependence of the fraction of transferred atoms on the mw frequency. This is a common and accurate method of the magnetic field calibration.

The mw spectroscopy experiment starts with the production of a BEC in state $|1\rangle = |1,\ -1\rangle$ (Fig. 3.8). Powerful rf radiation slightly changes the values of the DC currents through all working switches and modifies the magnetic field in the trap centre. That is why it is important to perform the mw spectroscopy in the presence of the rf field. The atoms are coupled from the initial state $|1\rangle$ into the magnetic field insensitive state $|2,\ 0\rangle$ by applying a mw pulse of 3 ms duration. The pulse duration is long compared to the inverse of the mw Rabi frequency, so the probability of finding atoms in a particular internal state changes multiple times and averages out [64]. Atoms in the state $|2,\ 0\rangle$ are not trapped and fall from the trap under gravity. 10 ms after the mw pulse the magnetic trap is switched off followed by 11 ms of free fall of the atoms. Atoms in the $|2,\ 0\rangle$ state are constantly outcoupling from the magnetic trap during the mw pulse, so they appear as a stripe on the imaging frame similar to the atom laser experiments [91], [92]. In order to simultaneously image both atom states on a single CCD image the atoms remaining in state $|1\rangle$ are given a kick just after switching off the magnetic trap by ramping the Z-wire current to 30 A

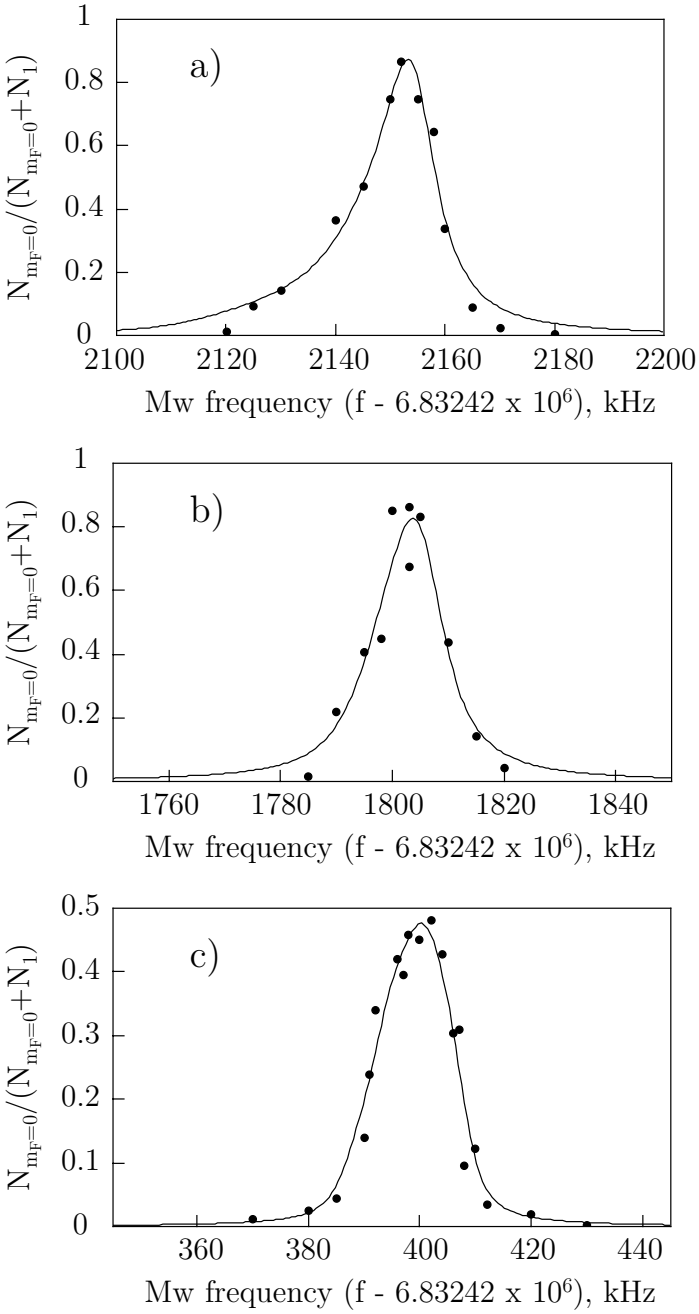

Figure 3.9: Typical single-photon mw spectroscopy curves that are used for measurements of DC magnetic fields of (a) 0.15 G, (b) 0.66 G and (c) 2.66 G. During the measurements a varying mw frequency is applied by the generator Agilent Technologies E8257D with 3 dBm amplitude.

for 0.6 ms. Before the imaging (Section 2.2.1) a repumper laser pulse of 2.6 ms duration is applied that is locked on the transition $5^2S_{\frac{1}{2}}$(F=1) − $5^2P_{\frac{3}{2}}$(F=2) to transfer all the atoms from F=1 into F=2 (Section 2.1.1). The population of each magnetic state is then evaluated from the absorption image. Examples of the mw spectroscopy lines are shown in Fig. 3.9, where each point represents a single run of experiment for a particular value of the mw frequency. Plotting the ratio $\frac{N_{m_F=0}}{N_1+N_{m_F=0}}$ versus the mw frequency value helps to reduce the noise associated with fluctuations of the atom number in the BEC.

In order to fit the mw spectroscopy experiment data with Eq. 3.12 the parameters ω, T, z_g^0 and R_0 are first calculated for the approximate value of the magnetic field. Then the first iteration of the fitting is performed with A, d, f_m and Δ being free parameters. Then the values of all fixed parameters are recalculated in accordance with the refined minimum value of the magnetic field extracted from the Breit-Rabi formula and the known frequency f_m and the second iteration of fitting is performed. Usually after two iterations the process converges and the third repetition does not lead to any difference in frequency f_m. Then the parameters of the best fit are used to calculate the magnetic field at the centre of the trap by calculating the frequency

$$f_0 = f_m - T^2(z_g^0)^2 \tag{3.13}$$

with high accuracy (uncertainty is $\sim$ 2 kHz which is only a fraction of a percent), which is put in the Breit-Rabi formula to calculate the magnetic field in the centre of the trap B_{bottom}.

The Breit-Rabi formula [89] gives the Zeeman energies of atoms in intermediate magnetic fields for the ground state of alkali atoms with J = $\frac{1}{2}$:

$$\begin{gathered}\nu_{F,m_F} = -\frac{\nu_{HF}}{2(2I+1)} + \frac{g_I\mu_B m_F B}{h} + sign(F-I)\frac{\nu_{HF}}{2}\sqrt{1+m_F\frac{4x}{2I+1}+x^2}, \\ x = \frac{(g_J-g_I)\mu_B}{h\nu_{HF}}B\end{gathered} \tag{3.14}$$

Here $g_I = -0.995141 \times 10^{-3}$, $g_J = 2.002331$, $\mu_B = 9.274009 \times 10^{-24}\frac{J}{T}$, h is Planck's constant $6.626069 \times 10^{-34} J \cdot s$ and $\nu_{HF} = 6\ 834\ 682\ 610.9$ Hz for ^{87}Rb [79]. For ^{87}Rb the nuclear spin I = $\frac{3}{2}$, so in Eq. 3.14 it is a plus sign for F=1 and a minus sign for F=2. In order to calculate the energy difference (in frequency units) of the corresponding magnetic

Parameter	3.9 (a)	3.9 (b)	3.9 (c)
N, atoms	$2{\cdot}10^5$	$2{\cdot}10^5$	$2{\cdot}10^5$
$\omega_y/2\pi$, Hz	11.5	11.5	11.5
$\omega_{x,z}/2\pi$, Hz	454.3 $\pm$1.1	218.1 $\pm$0.4	108.244 $\pm$0.012
R_0, μm	1.908 $\pm$0.003	2.964 $\pm$0.003	4.5125 $\pm$0.0003
z_g^0, μm	1.211 $\pm$0.006	5.26 $\pm$0.02	21.337 $\pm$0.005
d, μm	5.1 $\pm$0.7	2.0 $\pm$1.8	2.9 $\pm$0.3
Δ, kHz	10.2 $\pm$1.8	10 $\pm$3	4.0 $\pm$0.5
f_m, kHz	2156.6 $\pm$ 0.5	1808.2 $\pm$ 1.7	420.3 $\pm$ 0.4
f_0, kHz	2155.3 $\pm$ 0.5	1802.6 $\pm$ 1.7	397.9 $\pm$ 0.4
B_{bottom}, G	0.1528 $\pm$ 0.0007	0.655 $\pm$ 0.002	2.6600 $\pm$ 0.0006
χ^2/doF	$4.0{\cdot}10^{-3}$	$7.5{\cdot}10^{-3}$	$1.5{\cdot}10^{-3}$

Table 3.1: Parameters of the best fitting for the data shown in Fig. 3.9. Red font is used to distinguish fixed parameters during data fitting. The mw frequency is relative to 6.832 419 968 GHz which corresponds to the level splitting at 3.23 G. Calculation of B uncertainty is described in Appendix D.0.10.

states $|1,-1\rangle$ and $|2,0\rangle$ Eq. 3.14 can be rewritten as:

$$f = \frac{g_I \mu_B B}{h} + \frac{\nu_{HF}}{2}\sqrt{1-x+x^2} + \frac{\nu_{HF}}{2}\sqrt{1+x^2} \tag{3.15}$$

Table 3.1 summarises the parameters that have been taken from the best fitting curves of the data, shown in Fig. 3.9. The Lorentz width Δ is of the order of $3-10$ kHz for all experimental data, which is comparable with the measured one-photon Rabi flopping frequency 4.5 kHz.

In conclusion, the developed theory explains the observed asymmetries of the spectroscopy lines for the experiments with almost pure BECs and accounts for the non-uniform magnetic field, experienced by the different parts of the BEC cloud. The employment of the described fitting procedure for the mw spectroscopy allows us to determine the value of the magnetic field in the centre of the trap with 1 mG precision or with a relative error of less than 1%. It is important to note that taking into account the dipole oscillations of

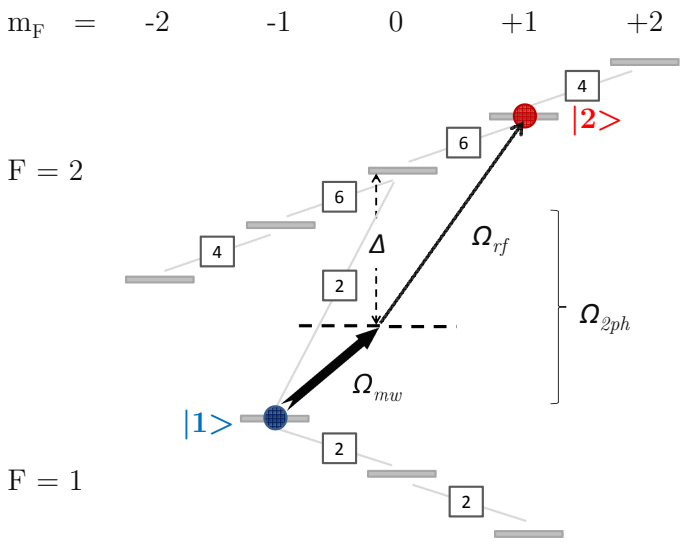

Figure 3.10: Relative coupling strength of magnetic dipole transitions in the ground state $5^2S_{\frac{1}{2}}$ of ^{87}Rb (adapted from [64]) and the two-photon excitation used for the AC magnetic field calibration. We measure the frequency of Rabi flopping for large detunings $\Delta \sim 2\pi \cdot 25$ MHz.

the cloud is a crucial step in the model because predicted in Section 3.1.2 widths of the resonances are significantly narrower than those measured experimentally. After convolution with the power broadening this effect leads to an overestimation of the Lorentzian width during the fitting procedure and makes the theoretical spectroscopy line symmetric. From the other hand, excluding the power broadening effect from the model leads to an inflation of the dipole oscillations amplitude, while the theoretical curve shows in general a good matching with the experimental points.

3.3 AC magnetic field calibration

The first attempt to calibrate the AC magnetic field was to measure the AC current through a test resistance that had been inserted into the rf circuit and then to calculate the rf field amplitude knowing the geometry of the chip and the distance from the cloud to the chip surface. However, this appeared to be not a very reliable approach as firstly, the signal was noisy and it was hard to get consistent results, and secondly, the oscilloscope

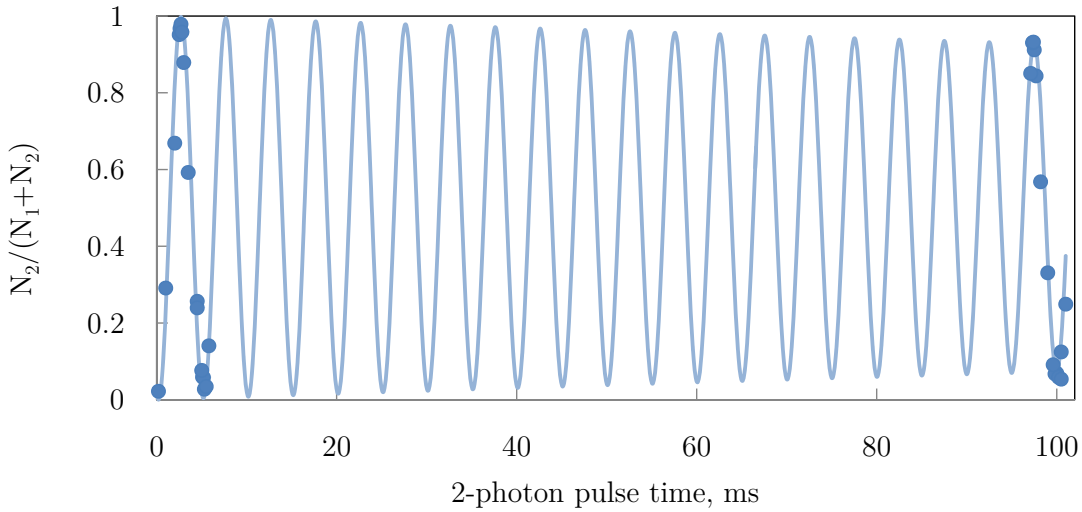

Figure 3.11: Two-photon Rabi flopping that is used for the AC magnetic field measurement. The transfer is realized by employing an rf field of 25.71 MHz with amplitude 1 V (pp) on the generator SRS DS345 and a mw frequency 6.808973380 GHz with amplitude 3 dBm on the generator Agilent Technologies E8257D.

input has a frequency dependent impedance in the MHz range. When connected to the characterizing circuit the scope changes the impedance matching conditions and affects the measured rf current.

We instead use a very elegant in-situ approach for the rf field characterization by a precise measurement of the two-photon (mw+rf) Rabi flopping frequency between two magnetically trappable states $|1\rangle = |F = 1,\ m_F = \text{-}1\rangle$ and $|2\rangle = |F = 2,\ m_F = +1\rangle$ (Fig. 3.10), which is proportional to B_{rf}. Additional advantages of this technique are that it doesn't rely on measurement of the distance to the atoms from the chip-wire and this method also automatically measures the component of the AC rf field perpendicular to the quantization axis in the magnetic trap. The difference of m_F is equal to 2 and thus this magnetic dipole transition can be realized only by a two-photon process. In order to measure the amplitude of the rf field at a particular frequency the mw frequency is adjusted to make the sum of the mw and rf frequencies equal to the $|1\rangle - |2\rangle$ transition frequency for a particular DC magnetic field.

The two-photon Rabi frequency is determined by the values of the rf Rabi frequency

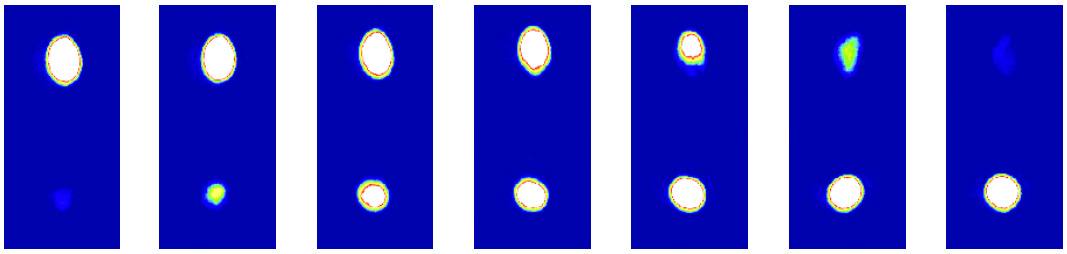

Figure 3.12: Experimental images of the simultaneous imaging of atoms in different states after adiabatic passage and a Stern-Gerlach kick. The two-photon pulse duration was varying to show the transfer of atoms from state $|1\rangle$ to state $|2\rangle$.

Ω_{rf} and the mw Rabi frequency Ω_{mw} as well as by the detuning Δ from the intermediate state F = 2, $m_F = 0$ (Fig. 3.10). The AC magnetic field amplitude can be evaluated by measuring Ω_{2ph} and Ω_{mw} (in a separate measurement of the σ^+ transition $|1\rangle - |F = 2, m_F = 0\rangle$). An additional factor that affects the frequency of the measured Rabi oscillations is the strength of the transitions. According to the Clebsch-Gordan coefficients in Fig. 3.10 the measured Rabi frequencies of the mw and the rf floppings from Figs. 3.11 and 3.13 are: $\Omega_{mw}^{exp} = \sqrt{2}\Omega_{mw}$ and $\Omega_{rf}^{exp} = \sqrt{6}\Omega_{rf}$, from which:

$$\begin{gathered}
\Omega_{2ph}^{exp} = \frac{2\pi}{T_{2ph}^{exp}}, \quad \Omega_{mw}^{exp} = \frac{2\pi}{T_{mw}^{exp}}, \\
\Omega_{2ph}^{exp} = \frac{\Omega_{rf}^{exp}\Omega_{mw}^{exp}}{2\Delta} = \frac{\sqrt{6}\Omega_{rf}\Omega_{mw}^{exp}}{2\Delta} \Rightarrow \Omega_{rf} = \sqrt{\frac{2}{3}}\frac{\Omega_{2ph}^{exp}\Delta}{\Omega_{mw}^{exp}}, \\
\Omega_{rf} = \frac{\mu_0 g_F B_{rf}}{2\hbar} \Rightarrow B_{rf} = \sqrt{\frac{2}{3}}\frac{2\hbar}{\mu_0 g_F}\frac{\Omega_{2ph}^{exp}\Delta}{\Omega_{mw}^{exp}}
\end{gathered} \tag{3.16}$$

The actual calibration procedure starts with the production of an almost pure BEC in the state $|1\rangle$. After that the mw and rf fields are simultaneously applied in a pulse of variable duration. In order to measure the amplitude of the specific radio-frequency corresponding to a particular molecular resonance the mw frequency needs to be adjusted to tune into the two-photon resonance. Immediately after the mw+rf pulse the atoms are released from the trap by switching off all magnetic coils and the Z-wire current. The pop-

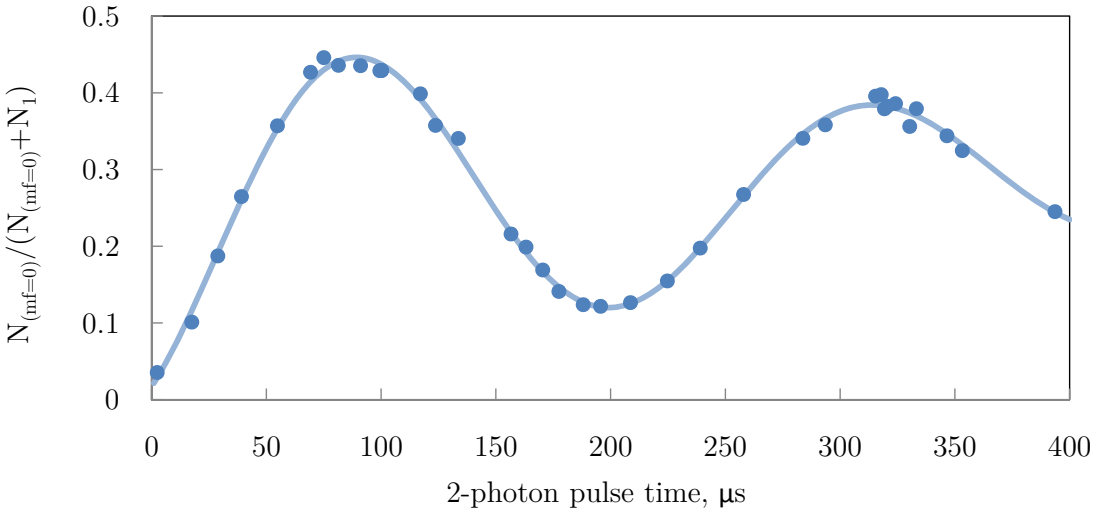

Figure 3.13: Rabi flopping in the atomic system $|1\rangle = |F = 1, m_F = -1\rangle - |F = 2, m_F = 0\rangle$ excited by resonant microwave radiation. For this particular experiment a mw frequency of 6.834097000 GHz with 3 dBm of amplitude on the generator Agilent Technologies E8257D was used.

ulations of both atomic states are measured in one experimental realization. To separate atoms in different states the atoms from $|1\rangle$ are transferred to the state $|F = 2, m_F = -2\rangle$ by adiabatic passage (Section 2.6) over 8.2 ms and then a short 0.3 ms Stern-Gerlach kick is applied by ramping the current through the Z-wire up to 30 A. In the magnetic field gradient atoms in the state $|F = 2, m_F = -2\rangle$ are attracted to the chip whereas atoms in the state $|2\rangle$ are pushed away. The difference in velocities of two atoms obtained during the kick provides the spatial separation after a subsequent 12.3 ms of free fall (Eq. B.19).

The imaging procedure is described in Section 2.2.1. Two separate clouds on the CCD image represent the populations of the two initial states $|1\rangle$ and $|2\rangle$ [90]. For different durations of the mw+rf pulse the oscillation of the atoms between the two states can be seen (Fig. 3.12). Typical Rabi flopping data is shown in Fig. 3.11 with the ratio $\frac{N_2}{N_1+N_2}$ being a measurable parameter and plotted as a function of evolution time. The observed oscillations correspond to $f_{mw}^{2ph} = 6.808973380$ GHz and $f_{rf} = 25.71$ MHz. The experimental data are fitted by a decaying sinusoidal function $\frac{1}{2}(1+e^{-\frac{t}{\nu}}sin(\omega_{2ph}t+\phi))$ to extract the period $T_{2ph} = (4.989\pm0.005)$ ms, the two-photon Rabi frequency $\Omega_{2ph} = \frac{2\pi}{T_{2ph}}$

= $2\pi\cdot(200.4\pm0.2)$ Hz and the decay time $\nu \sim 0.6$ s. We assume that the oscillation decay is caused mainly by the instability of the magnetic field during the experiment.

Ω_{mw} is measured in a separate experiment by applying a resonant mw field pulse of variable duration for the transition $|1\rangle = |F = 1, m_F = \text{-}1\rangle - |F = 2, m_F = 0\rangle$ and observing the Rabi flopping (Fig. 3.13). The experimental data is fitted by the function $Ae^{-\frac{t}{\nu}} sin(\omega_{mw}t + \phi) + B + k \times t$ to extract the period $T_{mw} = (223.8\pm1.4)$ μs, the mw Rabi frequency $\Omega_{mw} = 2\pi\cdot(4.47\pm0.03)$ kHz and the decay time ~ 350 μs. Atoms in the state $|F = 2, m_F = 0\rangle$ are not trapped in our system as the experiment is performed in the magnetic trap. The observed short decay time of the mw one-photon Rabi flopping can be explained by the fact that the atoms in the $|F = 2, m_F = 0\rangle$ state become off-resonant with the applied mw frequency as they fall from the trap centre under the gravity. Inhomogeneity of the magnetic field along the BEC cloud leads to a decrease of the fringe contrast: a fixed mw frequency is only resonant with part of the cloud whereas for the two-photon transition case this effect is not noticeable as states $|1\rangle$ and $|2\rangle$ have the same linear Zeeman splitting in the magnetic field.

In order to calculate Ω_{rf} from Eq. 3.16 it is assumed that the strength of the mw field is the same for the described two-photon and one-photon transitions. Indeed, the mw-amplifier which is used in the experiment is broadband and for the total mw-frequency of about 6.34 GHz the change of 30 MHz is only a fraction of a percent variation. During tuning of the one-photon mw Rabi flopping the resonant value of the frequency f^0_{mw} is found to be 6.834097000 GHz which allows to calculate the detuning $\Delta = f^0_{mw}$ - f^{2ph}_{mw} = 25.12362 MHz from the intermediate level $|F = 2, m_F = 0\rangle$ in this particular measurement. Now all the parameters in Eq. 3.16 are known to calculate the rf Rabi frequency $\Omega_{rf} = 2\pi\times(2.25\pm0.02)$ MHz. From this the component of the rf field perpendicular to the quantization axis of the magnetic trap B_{rf} is equal to 2.62 ± 0.02 G. In our experimental system we have already applied to the atoms rf magnetic fields as high as 6 G; however, we have the capability to increase this further.

3.4 Conclusion

This chapter describes the methods of calibration of the AC and DC magnetic fields. For the experiments of rf-induced molecular association it is important to know the amplitude of the rf-magnetic field for the characterization of the experimental conditions. The usual method of DC field measurement through resonant transitions between Zeeman levels has been enhanced by our theory of the mw spectroscopy line which significantly increases the precision of the technique.

CHAPTER 4

Radiofrequency atom-molecule coupling

This chapter describes the experimental observations of an rf induced association of molecules from pairs of ^{87}Rb atoms prepared in different internal states $|1\rangle = |1, -1\rangle$ and $|2\rangle = |2, 1\rangle$. During the collision of two atoms powerful resonant rf radiation stimulates the coherent emission of an rf-photon leading to the formation of a molecule in a highly excited state (the last bound state in our case). The rf recoil is very small and a molecule in a positive magnetic state would remain trapped in the magnetic trap if there are no collisions. The molecule is located in an atomic cloud and quickly relaxes to a lower quantum state during the collision with a third atom. This quenching leads to an increase of kinetic energies of the molecule and the third atom resulting in the loss of all three particles from the trap. The detection of the atom loss is widely exploited in the location of magnetic Feshbach resonances [29], [93] and is adopted in our investigation.

During the application of a powerful rf radiation the bare state notation for two states $|1\rangle$ and $|2\rangle$ is not entirely valid as the BEC can be better described in the dressed states basis. The BEC of the three-level F = 1 system in rf-dressed potentials has been analyzed by White et al. in [94]. In particular, one of conclusions is that bare state $|1\rangle$ undergoes an adiabatic transformation into $|-\rangle$ state for positive large values of detuning from the resonance (in our experiment the detuning $\Delta \sim 25$ MHz). The trapping potential for the $|-\rangle$ state remains the same as for undressed state $|1\rangle$ in the vicinity of the trap centre, with the same trapping frequencies. Due to symmetry it is reasonable to assume similar

conclusions for initial state $|2\rangle$.

The chapter starts with the description of two-body losses affecting the population of state $|2\rangle$ in a two component BEC in the absence and presence of radio-frequency coupling of atoms to molecules. In order to choose appropriate experimental conditions (such as rf amplitude, coupling time, frequency step) the predictions of [54] have been used to plot the decay of the atom number in state $|2\rangle$. Section 4.1.2 contains a description of the experimental sequence and the first observations of the atom-molecule resonances, proves that the found resonances are generated by the atom-molecule conversion and provides an estimation of the molecular formation rate. Section 4.2 describes the theory about the interaction of atoms in a BEC with an rf field which explains the shape of the resonances in different molecular bands and various effects responsible for the broadening of the spectroscopy lines and used in the fitting of the experimental data. Section 4.3 contains all the main experimental results of the Zeeman dependence of the energy of five molecular bands with the molecular hyperfine numbers F = 3, 2 and 1 along with the dependence of the resonance strength and position on rf amplitude.

4.1 Discovery of rf induced atom-molecule conversion without assistance of magnetic Feshbach resonance

4.1.1 Necessary conditions for the observation of the rf induced atom-molecule coupling

An increase of the atom losses due to molecule association is the usual technique for the location of the Feshbach resonances. Atoms in a BEC collide with each other at a very high rate. These atomic collisions can be elastic (participate in thermalization processes) and inelastic (lead to atom losses). In two-component BECs (Section 2.5) losses of atoms due to inelastic collisions are described by the two-body loss coefficients γ_{11}, γ_{12}, γ_{22} and the three-body coefficients γ_{111}, γ_{222}, etc (due to almost the same values of magnetic moments of atoms in states $|1\rangle$ and $|2\rangle$ the two BEC clouds have good overlapping with each other). Usually BECs are dilute (n $\sim 10^{20}$ m^{-3}) and three-body collisions can be neglected.

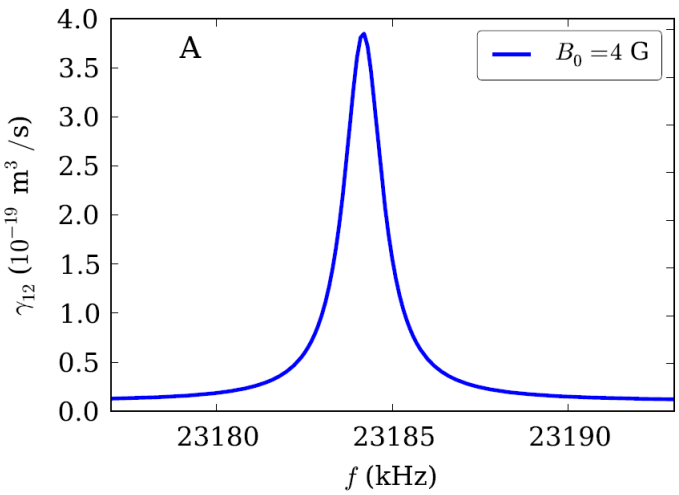

Figure 4.1: The dependence of rf induced two-body loss coefficient γ_{12}^{rf} on the rf frequency, calculated for the molecular state A for 3.23 G of DC magnetic field and the amplitude of the rf field of 4 G [95]. The resonant frequency is 23.184 Mhz with the FWHM $\sim$ 1.5 kHz.

A resonant radio-frequency field couples the energy levels of the two scattering atoms in different states with the energy of a weakly bound Feshbach molecule. This induces the molecule association process via stimulated emission of an rf-photon and the atoms in the bound state do not respond to the imaging laser, indicating the loss of both atoms from the BEC. Meanwhile, the molecules in the low magnetic field-seeking states may remain trapped. The created molecules are in a high vibrational state and may emit a photon spontaneously or due to an inelastic collision with a third atom ([96], [97]) or even have more than one inelastic collision [98], leading to the loss of more than two initial atoms from the trap. The uneven initial splitting of the atoms with 80% in state $|1\rangle$ mostly shields the atoms in state $|2\rangle$ from secondary losses associated with collisions with molecules. Thus the vibrational quenching of molecules leads to a negligible loss of atoms in state $|1\rangle$ and in the current approximation it is assumed that the atom number in state $|2\rangle$ is only affected by the two-body loss mechanism.

A simple theory of two-body losses (described in Appendix E.0.12) has been used to select the appropriate experimental conditions for the observation of the rf-induced molecular association. The number of atoms N_2 in state $|2\rangle$ evolve in accordance with the

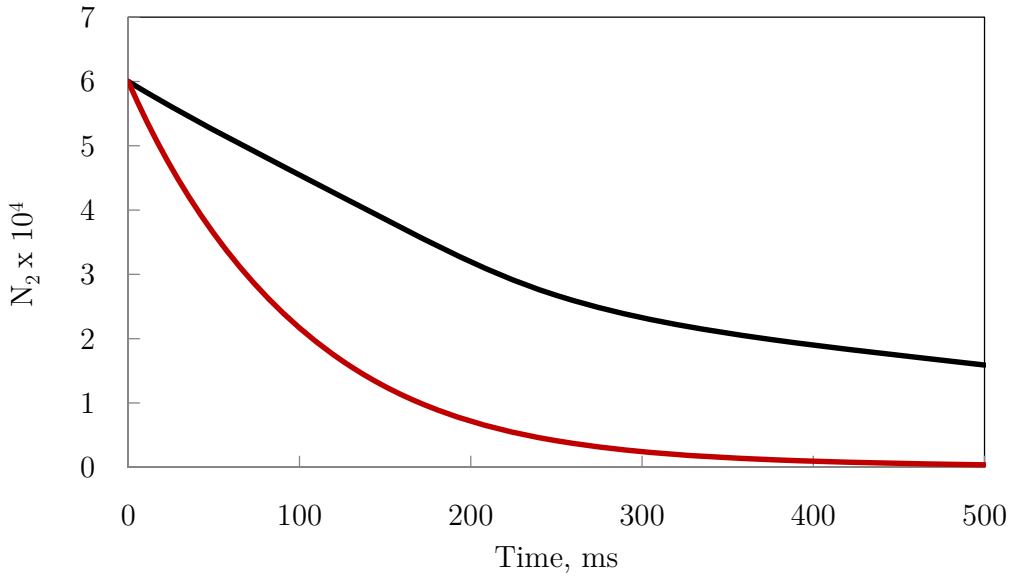

Figure 4.2: Simulation of the time evolution of the number of atoms N_2 without (the black line, $\gamma_{12}^0 = 1.51(18)\cdot10^{-20}\ m^3s^{-1}$) and with (the red line, $\gamma_{12} = 10^{-19}\ m^3s^{-1}$) the resonant rf field for 60 000 initial atoms and a constant number density of the cloud of atoms in the $|1\rangle$ state $n_{10} = 1.5\cdot10^{20}\ m^{-3}$. From this graph the time interval 100−400 ms has been chosen as the optimal rf coupling time.

equation (Eq. E.10)

$$\frac{dN_2}{dt} = -\frac{15\gamma_{22}N_2^2}{14\pi R_\rho^2 R_z(t)} - \frac{\gamma_{12}n_{10}}{7}\left(5 - \frac{R_z^2(t)}{R_{z0}^2}\right)N_2 \tag{4.1}$$

where n_{10} is the number density of the bigger cloud (state $|1\rangle$) with the radial and axial radii R_ρ and R_{z0} accordingly; $R_z(t)$ is the oscillating axial radius of the atomic cloud in state $|2\rangle$.

The two-body loss coefficients for ^{87}Rb atoms in states $|1\rangle$ and $|2\rangle$, γ_{22}^0=8.1(3)·$10^{-20}\ m^3s^{-1}$ and $\gamma_{12}^0 = 1.51(18)\cdot10^{-20}\ m^3s^{-1}$, have been measured in our group [65] at the magnetic field of 3.23 G. The resonant rf field generates additional inter-state losses γ_{12}^{rf}:

$$\gamma_{12} = \gamma_{12}^0 + \gamma_{12}^{rf} \tag{4.2}$$

Tscherbul [54], [95] has predicted $\gamma_{12}^{rf} \sim 3.9\cdot10^{-19}\ m^3s^{-1}$ for the resonant rf field of 4 G (Fig. 4.1) which is more than an order of magnitude larger than γ_{12}^0. In order to find experimental conditions that are sufficient for observation of the predicted effect, all the

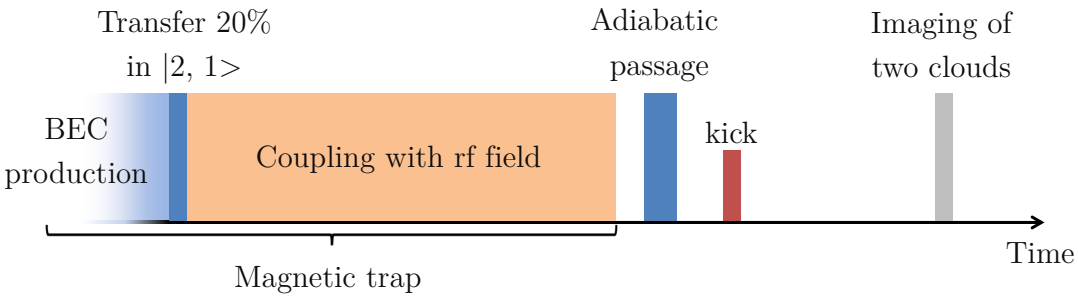

Figure 4.3: Time sequence of the experiment for observation of rf-induced molecular association. The time during the rf-coupling has varied during the experiments: it was set to 250 ms during the initial search for the atom-molecule coupling and 420 ms for most of the experiments in Sections 4.2.2 and 4.3.

parameters in Eq. 4.1 have been calculated from the Thomas-Fermi approximation formulae [76] and the experimentally measured trapping frequencies (Section 2.3). For $3{\cdot}10^5$ atoms in the BEC it has been calculated $R_\rho = 5.1$ μm, $R_{z0} = 44.9$ μm, $n_{10} = 1.5{\cdot}10^{20}$ m^{-3} from Eq. E.3 and the period of the collective oscillation ~ 330 ms at 3.23 G [65]. Figure 4.2 shows the time evolution of the number of atoms N_2 with ($\gamma_{12} = 10^{-19}$ $m^3 s^{-1}$) and without ($\gamma_{12}^0 = 1.51{\cdot}10^{-20}$ $m^3 s^{-1}$) a resonant rf field as numerical solutions of Eq. 4.1. The difference in the number of atoms for the two cases (vertical distance between the two curves) is significant in a range 100−400 ms, which is why this interval of evolution time has been chosen as optimal. A 2 kHz step has been selected as a reasonable variation of the radio-frequency during the search for the resonance to be able to resolve the narrow resonance, as shown in Fig. 4.1. Two theoretical predictions: 23.027 MHz [55] and 23.184 MHz [54] have defined the range of frequencies 22.5−23.5 MHz as our region of search for one of the strongest predicted resonances A (Fig. 1.2).

4.1.2 Experimental observation of rf induced molecular association

To maximize the molecule formation rate during collisions of atoms in different states, the initial splitting of the atoms should be even. However, in an experiment the shot-to-shot atom variation can be significant (up to 20% during an hour) and losses associated with Feshbach molecules may be hidden under this noise or it can lead to chasing fictive

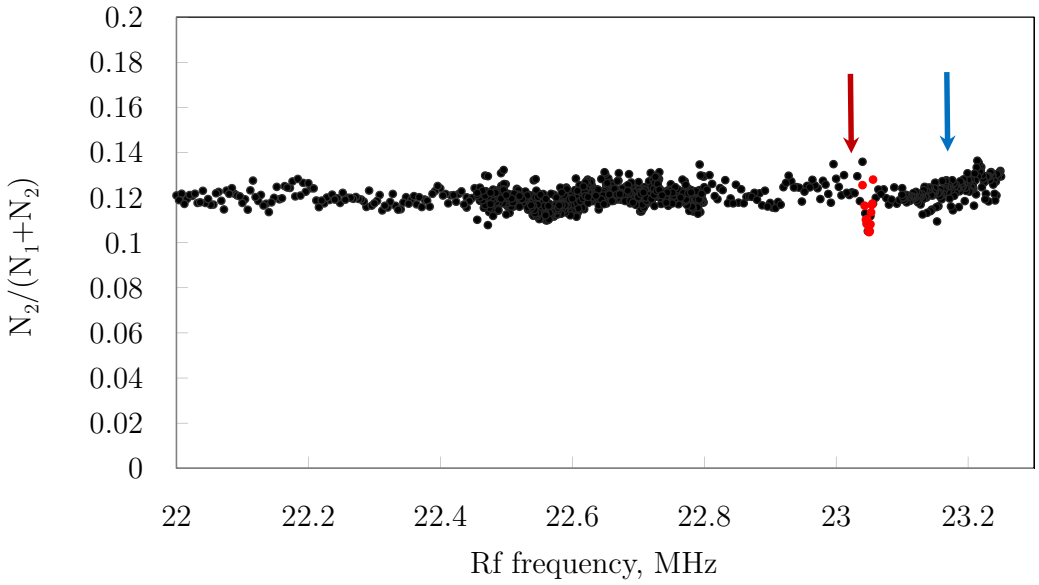

Figure 4.4: Search for an elusive atom-molecule resonance for the bound state A (shown as light red) at a DC magnetic field of 3.23 G and an rf amplitude of 4 G. The rf frequency step was 0.2 kHz in the ranges 22.5−22.8 MHz, 23.05−23.25 MHz and 2 kHz everywhere else. The rf coupling time was 250 ms. Blue and red arrows show the predictions of [54] and [55] for the magnetic field of 3.23 G.

artifacts. That is why the transfer of a smaller fraction of atoms (20%) into state $|2\rangle$ is not only helpful for the shielding of atoms from secondary losses (4.1.1) but also effective in identifying the molecule association losses of atoms by the measurement of the ratio of the atom number in the second state to the total number of atoms.

For the initial splitting of the BEC during a two-photon transition the fraction of transferred atoms depends only on the time of the pulse and doesn't depend on the total number of atoms in the BEC. The number of formed molecules depends on the initial number of atoms ($dN = g \cdot N_1^0 \cdot N_2^0$, where g is the molecule association factor) and in the absence of other losses the total number of atoms after the evolution time with the rf-coupling N_T^t is equal to $N_T^0 - 2dN$, from which:

$$\frac{N_2^t}{N_T^t} = \frac{N_2^0 - dN}{N_T^0 - 2dN} \approx \left(\frac{N_2^0}{N_T^0} - \frac{dN}{N_T^0}\right)\left(1 + 2\frac{dN}{N_T^0}\right) \approx \frac{N_2^0}{N_T^0} - \frac{dN}{N_T^0} = \frac{N_2^0}{N_T^0} - \frac{g \cdot N_1^0 N_2^0}{N_T^0} \tag{4.3}$$

Thus the expected off-resonance ratio is a constant regardless of shot-to-shot fluctuations

of the total number of atoms and molecule association would lead to a sudden drop in the atom number in state $|2\rangle$ and hence in the normalized atom number $\frac{N_2^t}{N_T^t}$. In the experiment there are additional non-negligible losses of the atoms in state $|2\rangle$; however taking this into account doesn't change the previous argumentation and only decreases the expected off-resonant value of the ration of the number of atoms after the rf-coupling time.

The timeline of the experimental sequence is shown at Fig. 4.3. A cloud of $(2-3)\cdot 10^5$ ^{87}Rb atoms in an almost pure BEC is obtained after the final stage of the rf-evaporation (Section 2.1.2) in state $|1\rangle$, F = 1, $m_F = -1$, 20 % of which is then transferred to state $|2\rangle$ (Section 2.5). Straight after the transfer high power rf radiation of ~ 4 G amplitude is applied to the Z-wire on the atom chip (Section 2.8), stimulating the molecule associations while both BEC components are held for 250 ms (420 ms in latter experiments). Then the rf field and the magnetic trap are turned off and the atoms start fall under the gravity. During the fall the state $|1\rangle$ component is transferred into the other hyperfine state $|2,-2\rangle$ via the adiabatic passage sequence (Section 2.6). After that the DC current through the Z-wire is quickly ramped up for 0.3 ms to create a kick to spatially separate states $|2\rangle = |2,1\rangle$ and $|2,-2\rangle$ in free fall due to their different magnetic moments (the Stern-Gerlach kick), followed by the application of a probe laser and collection of images of both clouds in the same frame of the CCD camera (Section 2.2.1). At the end of the experiment cycle the atom numbers in the two states N_1 and N_2 are counted in order to plot the variable $\frac{N_2}{N_1+N_2}$ versus the rf frequency. Then the rf frequency is changed by a certain step (0.2 − 2 kHz in different frequency ranges) and the sequence is repeated again.

Figure 4.4 illustrates the experimental outcomes of the search for the atom-molecule resonance A. For the magnetic field of 3.23 G two different types of simulations ([55] and [54]) have predicted two different locations of the resonance, 23.027 MHz and 23.184 MHz, respectively. The experiment has revealed the resonance at 23.05 MHz with the relative population of state $|2\rangle$ decreasing from 12% down to 10% after 250 ms of rf coupling time whereas Tscherbul's prediction [54] of the rf induced two-body coefficient would lead to a relative population decrease of $\sim 2\%$ for the resonance (Fig. 4.2).

After observation of the effect it was necessary to run tests to ensure that the increase

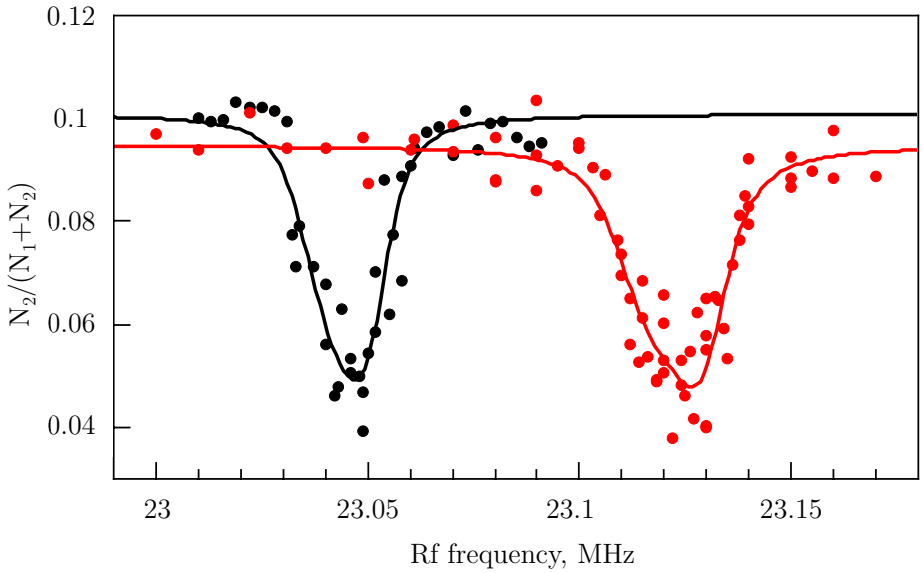

Figure 4.5: Shift of the rf induced molecular association resonance due to a decrease of the magnetic field from 3.23 G (black) to 3.12 G (red). The solid lines are the fits with our model (Section 4.2).

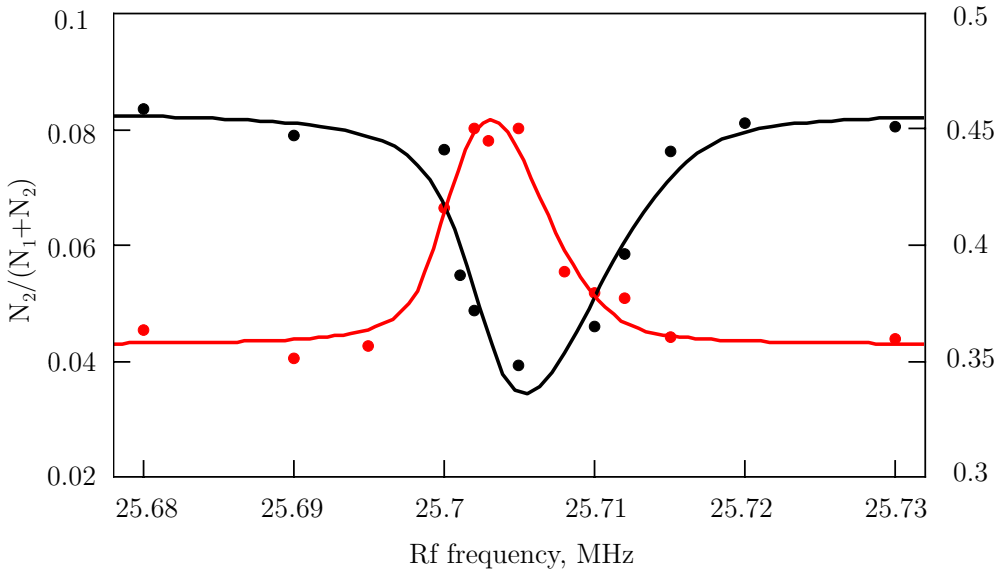

Figure 4.6: Proof of the interspecies interaction origin of the atom losses. The black dots and the fitted curve correspond to an initial splitting of the BEC with 20% in state $|2\rangle$ and 80% in state $|1\rangle$; the red dots and the fitted curve correspond to the opposite initial splitting (secondary axis on right side). The experiment is performed for the bound state B at 0.8 G trap bottom.

of losses is driven by the rf field induced molecular association. According to [54] and [55] the resonant frequency of the bound state A becomes larger for lower bias magnetic fields. The experiment was repeated with a smaller magnetic field at the trap bottom of 3.12 G and an increased holding time of 420 ms to make the resonance more pronounced (this holding time has become a standard for the subsequent measurements) (Fig. 4.5). In accordance with expectations the resonance shifted to a higher frequency of 23.12 MHz which proved that the observed resonance corresponds to coupling to the molecular state A. The size of the frequency shift was not analyzed during the check; however later on the dependence of the resonant frequency on magnetic field was measured over the range from 3.23 G down to the lowest reachable field $\sim$ 0.15 G in our magnetic trap (Section 4.3).

The second test aimed to show that the observed increase in atom losses is associated with collisions of atoms in different internal states. The experiment was performed with rf-induced association to the molecular state B at 0.8 G trap bottom. After location of the resonant frequency (black dots with the fitted curve in Fig. 4.6) by the sequence shown in Fig. 4.3, the full experiment was repeated with the opposite initial splitting of the BEC, leaving only 20% of atoms in state $|1\rangle$ and transferring 80% of atoms to state $|2\rangle$. Figure 4.6 demonstrates an increase of the ratio $\frac{N_2}{N_1+N_2}$ (red dots with the fitted curve) at the resonant frequency due to a decrease of the number of atoms N_1 in state $|1\rangle$. The population of component $|2\rangle$ decreases due to two body collisions with each other and the relatively large γ_{22} coefficient. Whereas the atoms in state $|1\rangle$ are lost predominantly due to interspecies inelastic collisions (neglecting three-body collision losses in the approximation of dilute BEC clouds). As a result, after 420 ms of the holding time the off-resonance fraction of the atoms in state $|2\rangle$ decreases from the initial 80% down to only $\sim$ 35% but at the resonance the atoms in state $|1\rangle$ are lost faster in the process of molecular association and at the end of the rf coupling time the proportion of the atoms in state $|2\rangle$ becomes 45%. This proves that the atoms in both states $|1\rangle$ and $|2\rangle$ experience increased losses at the observed resonances due to the interspecies interactions that are induced by the rf field. The positions of the resonances do not coincide perfectly with each other; however this is related to technical imperfections during the experiment, leading to a slight drift of the magnetic field at the bottom of the magnetic trap, and does not affect the main conclusions from the experiment.

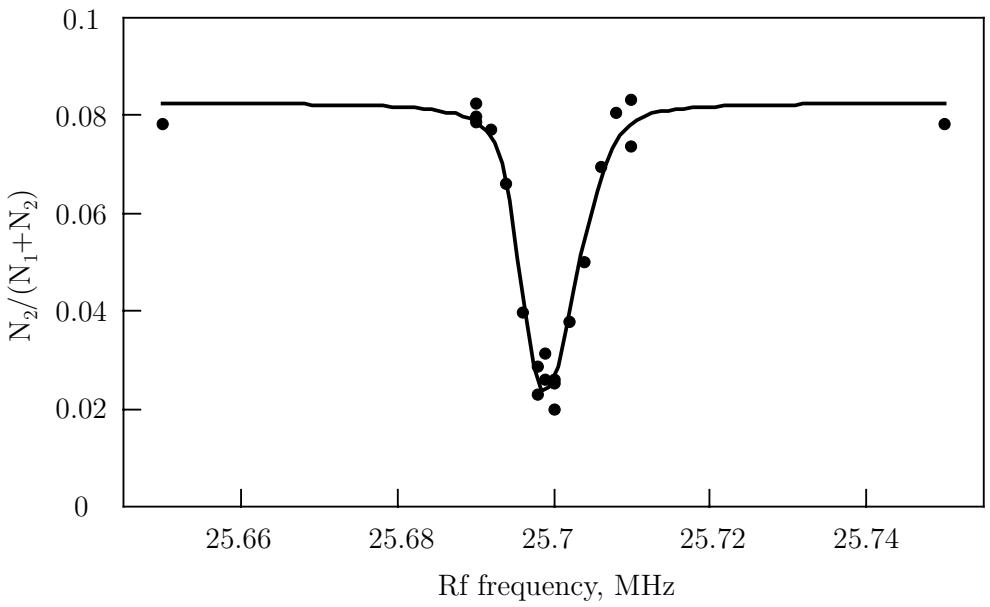

Figure 4.7: Measurement of the resonance-coupling curve to determine resonant and off-resonant frequencies for a molecule formation rate experiment.

4.1.3 Molecule formation rate

In accordance with the theoretical predictions for the loss coefficient γ_{12}^{rf} (Fig. 4.1) the anticipated atom number in state $|2\rangle$ should drop down to 2% of the total number of atoms after 250 ms holding time (Fig. 4.2). However, the experiment showed a barely visible decrease (change from 12% to 10%) of the normalized number of atoms in state $|2\rangle$ (Fig. 4.4) which means that the loss coefficient γ_{12}^{rf} could have been overestimated by the theorists [54]. We performed an experiment to measure the loss coefficient of the rf-stimulated molecule association by varying the holding time while applying the resonant rf-radiation and recording the atom losses.

The central idea of the experiment is to compare the atom losses with and without the resonant rf field. In addition a set of data was also collected for the off-resonant rf field. The experiment was run with $\sim 3{\cdot}10^5$ atoms of the almost pure BEC, produced in the trap with 0.8 G at the bottom. At this magnetic field the initial splitting with 23% of the atoms in state $|2\rangle$ leads to 10% of the relative population of component 2 after the holding time of 420 ms.

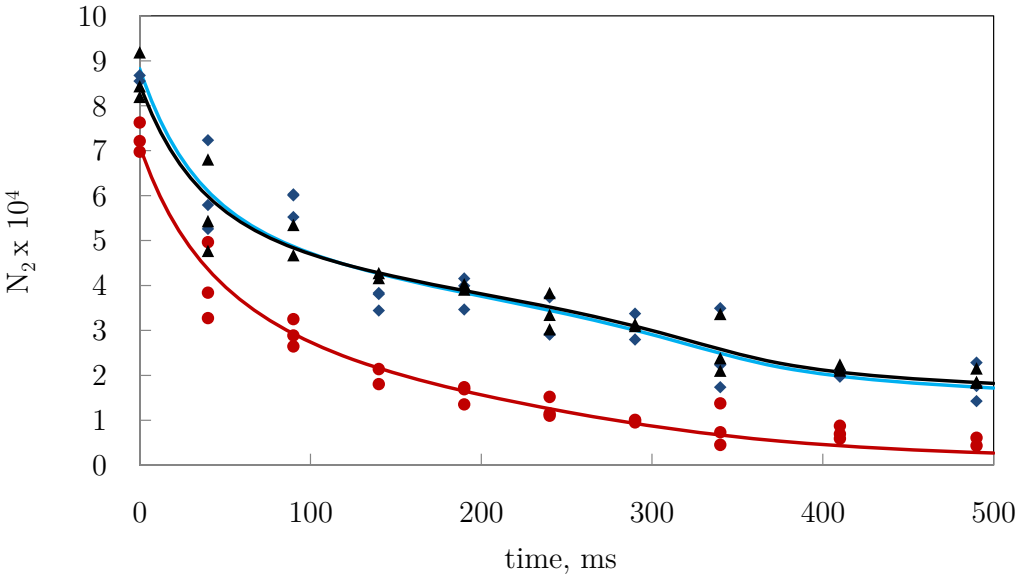

Figure 4.8: Experimental data for the measurement of two-body loss coefficients. Red circles correspond to the points with the resonant rf field; blue diamonds are for the case without rf-radiation; black triangles correspond to the off-resonant rf field set of data. Solid lines represent the fits with Eq. E.11.

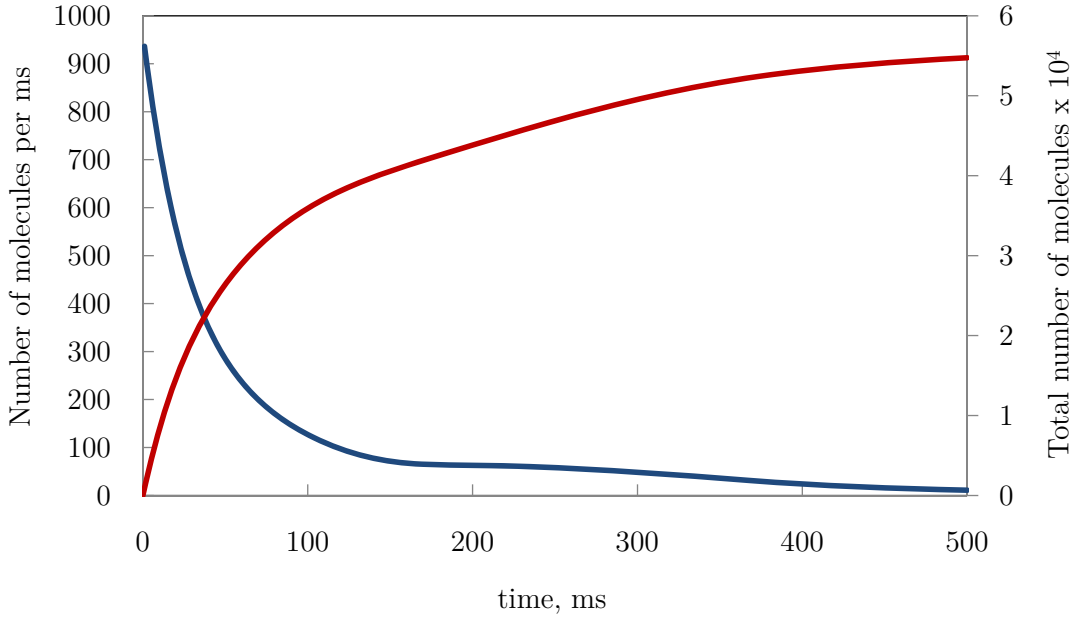

Figure 4.9: Theoretical curves generated using Eq. E.11 for the molecule formation rate per ms (blue line) and the total number of molecules (red curve) with respect to the coupling time for 70 000 initial atoms in state $|2\rangle$.

The time sequence of the atom loss measurement was the same as in Fig. 4.3 with the only difference being a variable rf coupling time. To decrease the effect of a systematic atom number drift with time three sets of measurements were taken for every coupling time. Each set consisted of an experimental sequence with the resonant rf-frequency (25.70 MHz), followed by an experimental run with the off-resonant rf field (25.75 MHz) and the same rf-amplitude and then a third sequence with the same holding time without the application of the rf field. The resonant and the off-resonant frequencies had been determined from the atom loss curve, measured prior to the experiment (Fig. 4.7). The experiment data is shown in Fig. 4.8 with circle, diamond and triangle points designating the cases of holding atoms with the resonant rf field, without the rf radiation and with the off-resonant rf field, respectively. It is clear that the that experimental points for the off-resonant case are very close to those without rf field which indicates that the non-resonant powerful rf radiation does not change the experimental conditions.

Our simple atom loss theory, described in Section E.0.12, was used to fit the experimental data points (Fig. 4.8) and extract the loss coefficients. During the fitting procedure the parameters n_{10}, R_{z0} and R_ρ from Eq. E.11 were calculated from the Thomas-Fermi approximation [76] for the average number of atoms N_1 and the trap frequencies were taken from table 2.1. The loss coefficient γ_{22} was set to the value $8.1(3)\cdot 10^{-20} m^3 s^{-1}$ measured by M. Egorov [65], [90]. The parameters R_{zmin}, ω_{co} and the initial phase φ_0 have been set free during the fitting but restricted to be the same for all three cases of the application of the rf field whereas the loss coefficients γ_{12} and the initial number of atoms N_2 have been determined from the best fits. For the trap bottom field of 0.8 G the fitting converges to the loss coefficients $0.42(14)\cdot 10^{-20} m^3 s^{-1}$ for the case without the rf field, $0.3(1)\cdot 10^{-20} m^3 s^{-1}$ for the off-resonant rf field and $3.6(2)\cdot 10^{-20} m^3 s^{-1}$ for the resonant rf field with amplitude of 2.23(2) G. The measured value of γ_{12}^0 without the rf field at 0.8 G is different from the previously measured $1.51(18)\cdot 10^{-20} m^3 s^{-1}$ at 3.23 G [90] and $7.80(19)\cdot 10^{-20} m^3 s^{-1}$ at 8.32 G [99]. However, this dependence of γ_{12}^0 on the magnetic field is in qualitative agreement with the theoretical model [100], which predicts a local minimum in the loss coefficient in the vicinity of 2 G. Another reason may be the dependence of the loss coefficient γ_{22} on the magnetic field: it has not been measured in the current experiment but set as a fixed parameter due to its slow dependence on

the magnetic field (previously measured values are $8.1(3)\cdot10^{-20}m^3s^{-1}$ at 3.23 G [90] and $7.80(19)\cdot10^{-20}m^3s^{-1}$ at 8.32 G [99]).

The experimentally measured value of the loss coefficient $\gamma_{12}^{rf} = 3.2(2)\cdot10^{-20}m^3s^{-1}$ is lower than the theoretical estimation $\gamma_{12}^{rf} \sim 4\cdot10^{-19}m^3s^{-1}$ (Fig. 4.1 shows the theoretical prediction for the resonance A which should have a comparable strength to the resonance B (Fig. 1.2)). However, the theoretical prediction was made for a different value of the magnetic field of 3.23 G and a higher amplitude of the rf field of 4 G (in our experiment B = 0.8 G and $B_{rf} = 2.2$ G). The experimentally measured value of the loss coefficient was also affected by different broadening mechanisms (Section 4.2) which are not included in the simple theory for two-body losses (Section E.0.12). Other parameters extracted from the fitting of the experimental data include the period of the collective oscillations ω_{co}, which has been estimated as $\sim$ 360 ms, in a good agreement with the period of collective oscillations 330 ms measured in the 3.23 G trap [90]. The initial phase φ_0 is measured to be close to π which makes perfect physical sense as straight after the splitting the smaller cloud starts to squeeze down to the smallest radius (fitting gives the value $R_{z0\ min}=\frac{R_{z0}}{3}$).

After the measurement of the loss coefficients the theory in Section E.0.12 was used to calculate of the total number of created molecules and the molecule formation rate (Fig. 4.9). The number of molecules produced within one time step (1 ms in our simulations) is calculated as the difference in the number of atoms calculated from Eq. E.11 with $\gamma_{12}= \gamma_{12}^0$ and $\gamma_{12}= \gamma_{12}^0+\gamma_{12}^{rf}$. As follows from Fig. 4.9 the initial molecule association rate almost reaches 1000 molecules/ms; however it quickly goes down due to the loss of atoms in state $|2\rangle$. For evolution times of 150−250 ms the rate is almost constant, where the drop of the molecule formation speed is compensated by the squeezing of the smaller cloud, increasing its density (half a period of the collective oscillations).

4.2 Shape of the atom loss curves

4.2.1 Theoretical shape of the resonances of rf-induced coupling to molecular states

The theory [54] predicted a Lorentzian dependence of the two-body loss coefficient (Fig. 4.1) and the first experimental data appears to show a symmetrical shape of the loss resonances. However, later it was noticed that the resonances have slightly asymmetrical shapes: in Fig. 4.6 it is clear that the left slopes of both curves are steeper than the right ones. We associate these asymmetric shapes of the loss curves with the finite size of the BEC and the small amplitude dipole oscillations of the cloud in the magnetic trap, so that the atoms at different parts of the BEC experience different magnetic field and hence are resonant at different radio-frequencies. A way of taking these effects into account is similar to the one that was described in Section 3.1 for the mw spectra. To explain the shape of the resonances it is assumed that during the rf coupling time the two clouds have perfect overlap with each other, i.e., the less dense component $|2\rangle$ is diluted within the cloud with the higher density in state $|1\rangle$ or $n_2 = n_1$. Variations of the scattering lengths a_{11}, a_{22} and a_{12} do not exceed 5% [90] and in the following it is assumed that they are equal (the collective oscillations are also not taken into account).

In a three-dimensional harmonic trap the total energy of the atoms is the sum of the magnetic, the mean field and the gravitational energies. In the Thomas-Fermi approximation the repulsive mean field interactions compensate the trapping potential so that the total energy of the condensed atoms is the same (Fig. 3.1 (b)). Here, we consider transitions to the weakly-bound molecular states with a large separation of bound atoms and assume that the molecular state energy can be approximated as the sum of the energies of the two unbound atoms $E^{F=1}_{m_F^1} + E^{F=2}_{m_F^2}$ minus the bound state energy C. Calculations of the transition frequencies are easier in the rescaled system of coordinates where the trap

is spherically symmetric (Eq. 3.5) (the origin is at the minimum of the magnetic field):

$$\begin{cases} E^0 = E^{F=1}_{-1} + E^{F=2}_{+1}, \\ E^b = E^{F=1}_{m^1_F} + E^{F=2}_{m^2_F} - C \end{cases} <=>$$

$$\begin{cases} E^0 = \mu_B(-1)(-g_f)B_0 + \frac{M\omega^2(x^2+y^2+z^2)}{2} - Mg\frac{\omega}{\omega_z}z + \chi n(x,y,z) + \\ \qquad \mu_B(+1)(g_f)B_0 + \frac{M\omega^2(x^2+y^2+z^2)}{2} - Mg\frac{\omega}{\omega_z}z + \chi n(x,y,z), \\ E^b = \mu_B(m^1_F)(-g_f)B_0 + (-m^1_F)\frac{M\omega^2(x^2+y^2+z^2)}{2} - Mg\frac{\omega}{\omega_z}z + \chi n(x,y,z) + \\ \qquad \mu_B(m^2_F)(g_f)B_0 + (m^2_F)\frac{M\omega^2(x^2+y^2+z^2)}{2} - Mg\frac{\omega}{\omega_z}z + \chi n(x,y,z) - C \end{cases} \tag{4.4}$$

where $g_f = g_f^{F=2} = \frac{1}{2}$ ($g_f^{F=1} = -g_f^{F=2}$) and it is also assumed that the colliding atoms are located close to each other (have the same coordinates).

The experimental setup is designed to look for σ^+ and σ^- transitions with the rf field polarized orthogonally to the local magnetic field direction. The selection rule for the change of the total projection of the magnetic moment of two atoms $\Delta m_F = \pm 1$ dictates that at least one of the colliding atoms should flip its spin while forming the molecule. All possible combinations of m^1_F and m^2_F in Eq. 4.4 for the molecules that can be written for the initial states $|1,-1\rangle + |2,+1\rangle$ are:

$$\begin{aligned} A:&\ |1,-1\rangle + |2,+2\rangle, \\ B:&\ |1,\ \ 0\rangle + |2,+1\rangle, \\ C:&\ |1,-1\rangle + |2,\ \ 0\rangle, \\ D:&\ |1,\ \ 0\rangle + |2,-1\rangle, \\ E:&\ |1,+1\rangle + |2,\ \ 0\rangle, \\ F:&\ |1,+1\rangle + |2,-2\rangle, \end{aligned} \tag{4.5}$$

Assuming that the mean field energy of the atoms is the same for different states the resonant frequency is defined by the magnetic field energy and C (in general C can be different for each path in Eq. 4.5). From which the resonant frequencies are equal to:

$$hf = C + k\left(\mu_B g_f B_0 + \frac{M\omega^2 r^2}{2}\right) \tag{4.6}$$

where $r = \sqrt{\frac{2}{kM\omega^2}\left(hf - C - k\mu_B g_f B_0\right)}$ and $k = 2 + m^1_F - m^2_F$ depends on the particular combination of the initial and final m_F-quantum numbers for the projection of the total

magnetic moment of both atoms in Eq. 4.5 and is equal to −1 (A), +1 (B and C), +3 (D) and +5 (F). From Eq. 4.6 it follows that the resonant frequency depends only on the distance from the origin. Thus all atoms in states $|1\rangle$ and $|2\rangle$ that collide with each other in a shell with radius r from the minimum of the magnetic field are resonant at the same rf frequency.

In the case of induced molecular association the coupling to a molecular state is proportional to the number of collisions between the atoms in different internal states as this is a two-particle process (unlike the mw spectroscopy case where the number of transferred atoms is proportional to the number of atoms that are resonant at a particular mw frequency). As noticed before the current approximation considers that the two clouds overlap perfectly, so that the difference in the number of atoms in each state is accounted for by the different number densities. The number of collisions per unit time in a small volume is proportional to the densities of atoms in both states at that point in space. The total number of formed molecules is then proportional to the integral along the volume occupied by the shell in the BEC cloud:

$$dN \sim \iint_{\phi\theta} n_1(r,\theta) n_2(r,\theta) r^2 sin\theta dr d\theta d\phi \tag{4.7}$$

Similarly to the mw spectroscopy case in Section 3.1.2 the solution of this integral (Appendix E.0.13) is the piecewise defined function (the illustration of two cases is shown in Fig. 3.3):

$$\begin{cases} dN(r) \sim \pi r^2 \dfrac{M^2\omega^4}{\chi^2} dr \left[\left(R_0^2 - z_g^2 - r^2 \right)^2 + \dfrac{4 z_g^2 r^2}{3} \right], \ r \in [0,\ R_0 - z_g] \\ dN(r) \sim \dfrac{\pi M^2 \omega^4 r}{12 \chi^2 z_g} (R_0^2 - (r - z_g)^2)^3 dr, \ r \in [R_0 - z_g, R_0 + z_g] \end{cases} \tag{4.8}$$

The dependence of the number of created molecules on the initial splitting of the BEC is contained in the coefficient $= \dfrac{n_2}{n_1}$. In this model it is assumed that the Thomas-Fermi radius R_0 of the BEC in state $|1\rangle$ does not change with time and that the process of losing atoms from state $|2\rangle$ is slow so that they keep the Thomas-Fermi profile with the same radius R_0 but smaller number density. Equation 4.8 shows the number of collisions between atoms in different states as a function of r. The number of atoms that are lost from state $|2\rangle$ due to the creation of molecules is proportional to the total number of

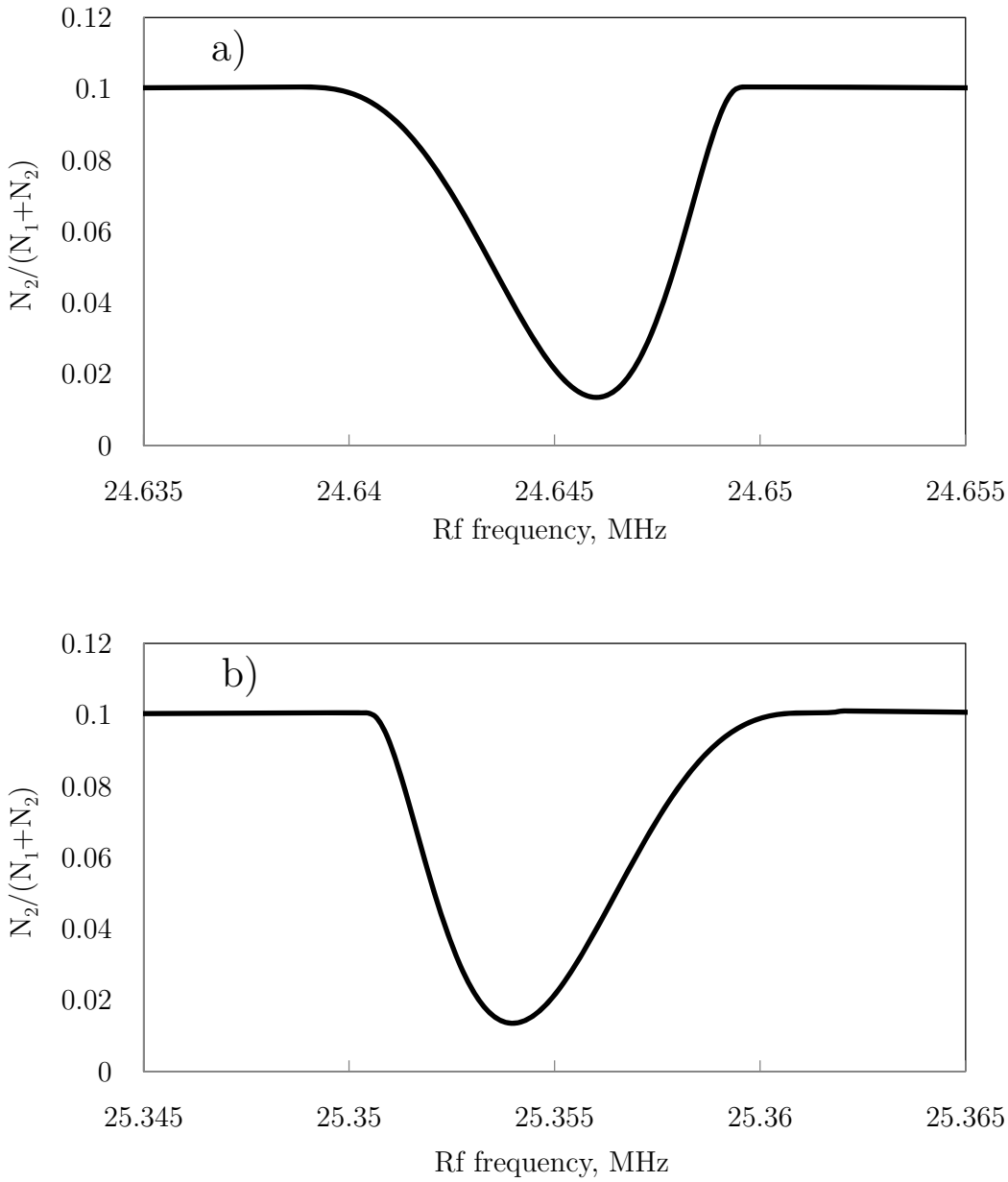

Figure 4.10: Loss curves for (a) A and (b) B molecular states (Eq. 4.5), calculated from Eqs. 4.9 and 4.11 (inserted into Eq. 4.3) for a 1 G trap. Calculation parameters are: N = $2{\cdot}10^5$, $\omega = 2\pi{\cdot}250$ Hz, $R_0 = 2.7$ μm, $z_g = 4$ μm, $y_0 = 0.1$ (the off-resonant ratio of the atom splitting), $f_m^{(a)} = 24.65$ MHz, $f_m^{(b)} = 25.35$ MHz. An appropriate strength of the resonances (the depth) is selected for the best display.

collisions per unit time. Equation 4.8 can be rewritten as a function of the resonant rf frequency f with the substitution from Eq. 4.6. The molecular state A case (Eq. 4.5) is different from the other molecular states because the parameter k is negative which leads to a decrease of the frequency f with increasing value of r:

$$\begin{cases} dN(f) \sim \dfrac{\pi h M\omega^2}{12\chi^2 z_g}\left[R_0^2-\left(\frac{\sqrt{f_m-f}}{T}-z_g\right)^2\right]^3 df, \\ \qquad\qquad f\in[f_m-T^2(R_0+z_g)^2,\ f_m-T^2(R_0-z_g)^2], \\ dN(f) \sim \dfrac{\pi h M\omega^2}{\chi^2 T}\sqrt{f_m-f}\left[\left(R_0^2-z_g^2-\frac{\sqrt{(f_m-f)^2}}{T^2}\right)^2+\frac{4z_g^2}{3T^2}\sqrt{(f_m-f)^2}\right]df, \\ \qquad\qquad f\in[f_m-T^2(R_0-z_g)^2,\ f_m] \end{cases} \tag{4.9}$$

where $f_m=\dfrac{C+k\mu_B g_f B_0}{h}$ and $T=\sqrt{\dfrac{|k|M\omega^2}{2h}}$ and from Eq. 4.6:

$$f=f_m+\frac{k}{|k|}T^2r^2;\quad r=\frac{1}{T}\sqrt{\frac{(f-f_m)|k|}{k}};\quad rdr=\frac{|k|}{k}\frac{df}{2T^2} \tag{4.10}$$

For all positive k (the molecular states B, C, D and F) Eq. 4.8 becomes:

$$\begin{cases} dN(f) \sim \dfrac{\pi h M\omega^2}{\chi^2 T}\sqrt{f-f_m}\left[\left(R_0^2-z_g^2-\frac{\sqrt{(f-f_m)^2}}{T^2}\right)^2+\frac{4z_g^2}{3T^2}\sqrt{(f-f_m)^2}\right]df, \\ \qquad\qquad f\in[f_m,\ f_m+T^2(R_0-z_g)^2] \\ dN(f) \sim \dfrac{\pi h M\omega^2}{12k\chi^2 z_g}\left[R_0^2-\left(\frac{\sqrt{f-f_m}}{T}-z_g\right)^2\right]^3 df, \\ \qquad\qquad f\in[f_m+T^2(R_0-z_g)^2,\ f_m+T^2(R_0+z_g)^2] \end{cases} \tag{4.11}$$

As in the case of the mw spectroscopy (Section 3.1.3) the current model for a resonant rf profile can be extended by including the dipole oscillation of the cloud and power broadening. As before the core idea is that the range of resonant frequencies varies as the cloud oscillates in the trap, so that the vertical coordinate of its centre depends on time as $z_g(t)=z_g^0+d\cdot cos(\omega_{do}t)$ (Fig. 3.6). The average number of atoms that are resonant at the different frequencies (B, C, D, E, F in Eq. 4.5) over one period of oscillations T_{do} can

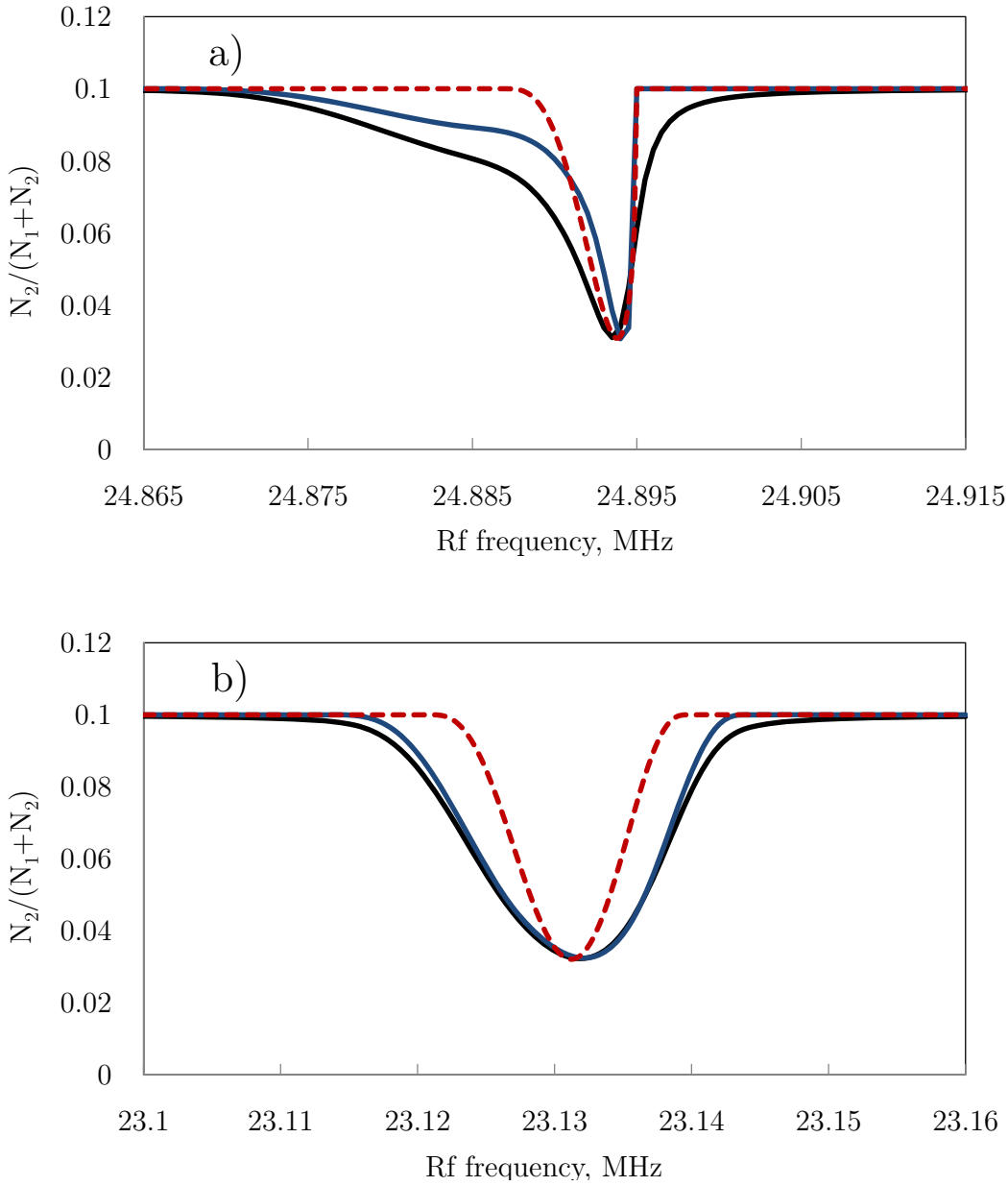

Figure 4.11: Contribution of different factors to the shape of the A molecular state loss profiles, calculated for a (a) 0.15 G trap, (b) 3 G trap. The red dashed line shows the initial shape defined by gravity and the atomic interactions (Eq. 4.9). The blue line represents the broadening effect due to dipole oscillations with $d = 3$ μm in both cases. The black line demonstrates the addition of Lorentzian broadening with $\Delta = 2$ kHz.

be calculated from the integral:

$$\begin{cases} dN(f) \sim \dfrac{\pi h M\omega^2}{\chi^2 T_{do}} df \displaystyle\int_t^{\frac{\sqrt{f-f_m}}{T}} \left[(R_0^2 - z_g^2(t) - \frac{|f-f_m|}{T^2})^2 + \frac{4z_g^2(t)}{3T^2}|f-f_m|\right] dt, \\ \qquad\qquad f \in [f_m,\ f_m + T^2(R_0 - |z_g(t)|)^2] \\ dN(f) \sim \dfrac{\pi h M\omega^2}{12k\chi^2 T_{do}} df \displaystyle\int_t \frac{\left[R_0^2 - \left(\frac{\sqrt{f-f_m}}{T} - |z_g(t)|\right)^2\right]^3}{|z_g(t)|} dt, \\ \qquad\qquad f \in [f_m + T^2(R_0 - |z_g(t)|)^2,\ f_m + T^2(R_0 + |z_g(t)|)^2] \end{cases} \tag{4.12}$$

For rf frequencies f in the range $[(f_m + (R_0 - |z_g(t)|)^2 T^2)_{min},\ (f_m + (R_0 - |z_g(t)|)^2 T^2)_{max}]$ the sum of both functions should be used in the calculation of the average number of resonant atoms. A similar equation can be written for curve A in Eq. 4.5. In the experiments the two-component BEC are exposed to the rf field for times that is much longer than the period of dipole oscillations, which justifies the usage of Eq. 4.12.

Power broadening also plays an important role as in the case of mw spectroscopy. To account for this effect the function in Eq. 4.12 $g(f)$ is convoluted with a Lorentzian $h(f)$:

$$dN \sim \int g(\nu) h(f-\nu) d\nu \quad =>$$

$$\begin{cases} dN(f) \sim A df \displaystyle\int_\nu \int_t^{\frac{\sqrt{\nu-f_m}}{T}} \frac{\left[(R_0^2 - z_g^2(t) - \frac{|\nu-f_m|}{T^2})^2 + \frac{4z_g^2(t)}{3T^2}|\nu-f_m|\right]}{4(f-\nu)^2 + \Delta^2} dt d\nu, \\ \qquad\qquad f \in [f_m,\ f_m + T^2(R_0 - |z_g(t)|)^2] \\ dN(f) \sim \dfrac{A}{12k} df \displaystyle\int_\nu \int_t \frac{\left[R_0^2 - \left(\frac{\sqrt{\nu-f_m}}{T} - |z_g(t)|\right)^2\right]^3}{|z_g(t)|(4(f-\nu)^2 + \Delta^2)} dt d\nu, \\ \qquad\qquad f \in [f_m + T^2(R_0 - |z_g(t)|)^2,\ f_m + T^2(R_0 + |z_g(t)|)^2] \end{cases} \tag{4.13}$$

In order to fit the experimental data with Eq. 4.13 a numerical integration method is used. The period of the collective oscillations is divided into M equal time intervals so that for each of them Eq. 4.9 or Eq. 4.11 can be used by setting $z_g = z_g^0 + d \cdot cos(\omega_{do} \frac{T_0}{M}(m + \frac{1}{2}))$. Then the integral on frequency in Eq. 4.13 is converted into the sum of N Lorentzian functions with modulated amplitudes and different central frequencies. In the final fitting formula there are M×N summands (Appendix E.0.14).

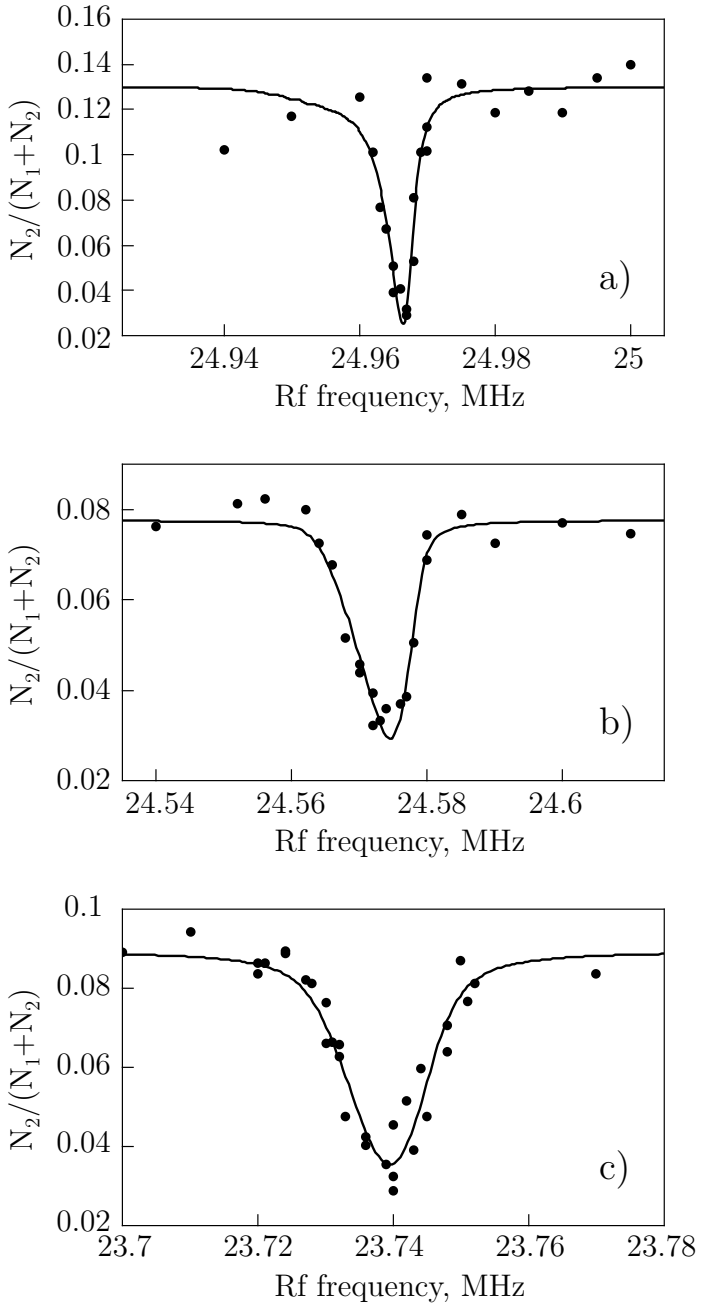

Figure 4.12: Typical rf induced loss curves used for measurements of the energy of the bound state A for (a) 0.16 G, (b) 0.96 G and (c) 2.19 G at the centre of the magnetic traps. Corresponding values of the magnetic fields are calculated from subsequent measurements of the mw spectroscopies.

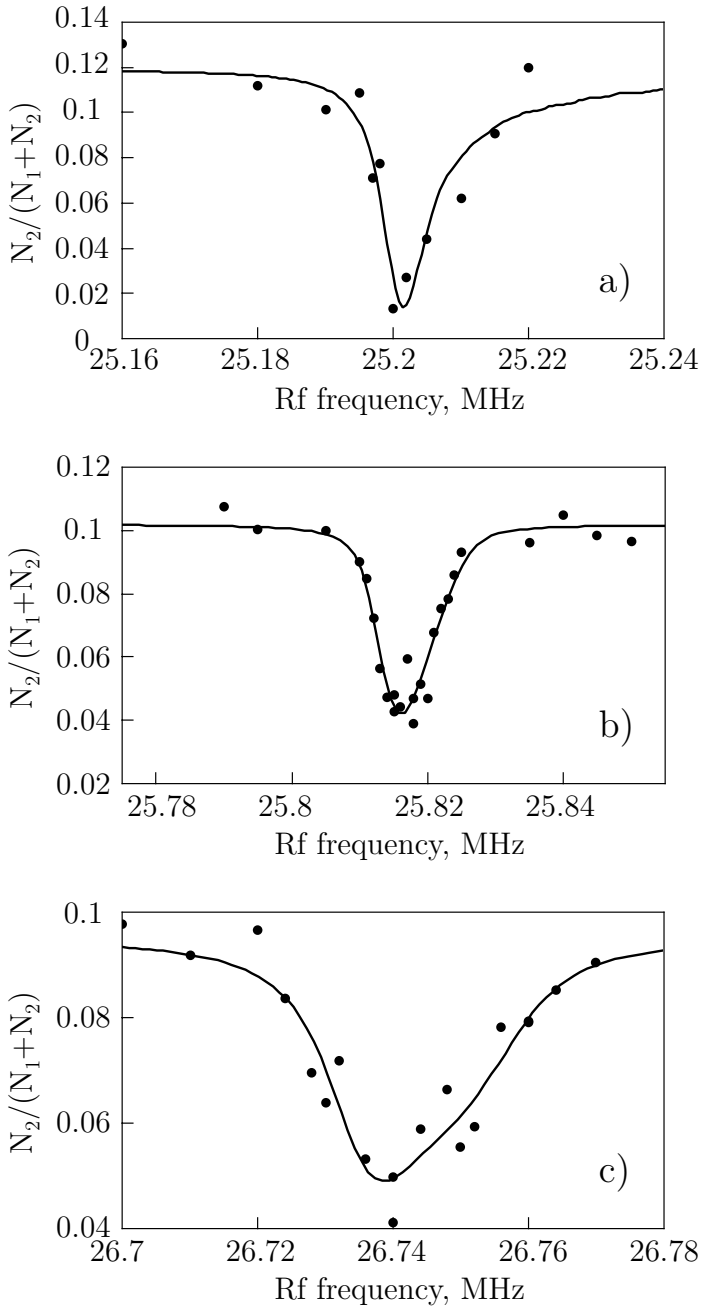

Figure 4.13: Typical rf induced loss curves used for measurements of the energy of the bound state B for (a) 0.21 G, (b) 1 G and (c) 2.26 G at the centre of the magnetic traps. Molecular states B, C, D, E and F have opposite asymmetries for the loss curves compared to case A in accordance with the developed theory in Section 4.2 (Fig. 4.10).

Resonance	Parameter	(a)	(b)	(c)
A (Fig. 4.12)	d_{mw}, μm	6 ±2	2.5 ±1.5	3.0±1.3
	d, μm	3.2 ±1.1	1.9 ±0.3	2.0 ±0.7
	Δ, kHz	2.7 ±0.7	2.0 ±1.1	7 ±2
	f_m, MHz	24.9676 ± 0.0002	24.5809 ± 0.0004	23.7569 ± 0.0004
	f_0, MHz	24.967 ± 0.003	24.573 ± 0.003	23.738 ± 0.002
	χ^2/doF	$1.4{\cdot}10^{-4}$	$1.5{\cdot}10^{-5}$	$3.0{\cdot}10^{-5}$
B (Fig. 4.13)	d_{mw}, μm	6 ±3	2.0 ±0.7	3.6 ±0.8
	d, μm	8 ±2	1.7 ±0.3	5.0 ±0.8
	Δ, kHz	6.0 ±1.7	3.4 ±1.1	13 ±4
	f_m, MHz	25.1996 ± 0.0007	25.8090 ± 0.0003	26.725 ± 0.001
	f_0, MHz	25.199 ± 0.002	25.8005 ± 0.0013	26.706 ± 0.002
	χ^2/doF	$1.8{\cdot}10^{-4}$	$2.8{\cdot}10^{-5}$	$3.2{\cdot}10^{-5}$

Table 4.1: Parameters of atom-molecule coupling extracted form the fitting of the radio-frequency resonances in Fig. 4.12 (molecular state A) and Fig. 4.13 (molecular state B) for different values of the magnetic field. This includes the amplitude of the induced dipole oscillations d (compared with d_{mw}, extracted from the fits of the corresponding mw spectroscopies), the power broadening width Δ, the frequency at the local minimum of magnetic field f_m and the frequency, resonant with the atoms at the centre of the trap f_0.

4.2.2 Fitting of the experimental data for the rf induced atom losses

As in the case of the mw spectroscopy the parameters z_g^0, T and R_0 are functions of ω and are calculated from Eqs. 2.10, 4.10 and the Thomas-Fermi approximation [76] where the value of ω is taken from the magnetic field, extracted from the corresponding measurement of the mw spectroscopy. Fitting of the experimental data with Eq. 4.13 is performed with the free parameters A, d, f_m and Δ serving to extract a precise value of the frequency:

$$f_0 = f_m + \frac{k}{|k|} T^2 (z_g^0)^2 \tag{4.14}$$

which corresponds to atoms in the centre of the cloud.

It was described in Section 4.2 that the resonance loss curves A from Eq. 4.5 have

opposite asymmetry compared to the curves of the other molecular states B, C, D, E and F. Figure 4.10 shows the difference of the theoretical loss curves for bound states A and B. The experimental data fully confirm the predicted asymmetries (Figs. 4.12 and 4.13, where each point represents a single run of experiment for a particular value of the radio-frequency) as well as for the other molecular states C, D and E.

As in the mw spectroscopy case the total width of the resonances is determined by the atomic interactions (which determine the shape of the BEC), dipole oscillations of the cloud and power broadening effects. At lower magnetic fields the trapping frequencies become larger which leads to a compression of the cloud. This effect narrows the resonances; however a big cloud sloshing can become a dominant broadening factor and cause significant distortion of the loss curves. Table 4.1 summarizes the information that is typically extracted from fits to the loss curves. Another measurement of the mw spectroscopy is performed straight after each measurement of the rf-induced molecular association. The parameter d_{mw}, extracted from the mw spectroscopy fits, is also shown in table 4.1 to demonstrate that fits from mw spectroscopy and the rf loss curves are consistent with each other as the main cause of the cloud sloshing in both cases is the rf-induced shift of the DC-current in the Z-wire.

4.3 Zeeman dependence of molecular state energies

The curve for the resonant rf induced molecular association allows to measure the energy (relative to the energy of two free atoms in states $|1\rangle$ and $|2\rangle$) of the molecular state at arbitrary magnetic field B_{bottom}. This DC magnetic field corresponds to the centre of the trap and is determined from the subsequent measurement of the mw spectroscopy. A series of these two measurements was repeated for different traps, mapping the dependence of the relative bound state energy on magnetic field over the range 0.15 G$-$3.3 G. During the rf transition the projection of the total angular momentum of one atom (or both atoms) changes to another value. As a result, the molecular magnetic moment is different from the total magnetic moment of two initial atoms and the resonant values of the atom-molecule transition frequency depends upon the magnetic field. We measured this dependence for five molecular states A, B, C, D and E (Fig. 4.14).

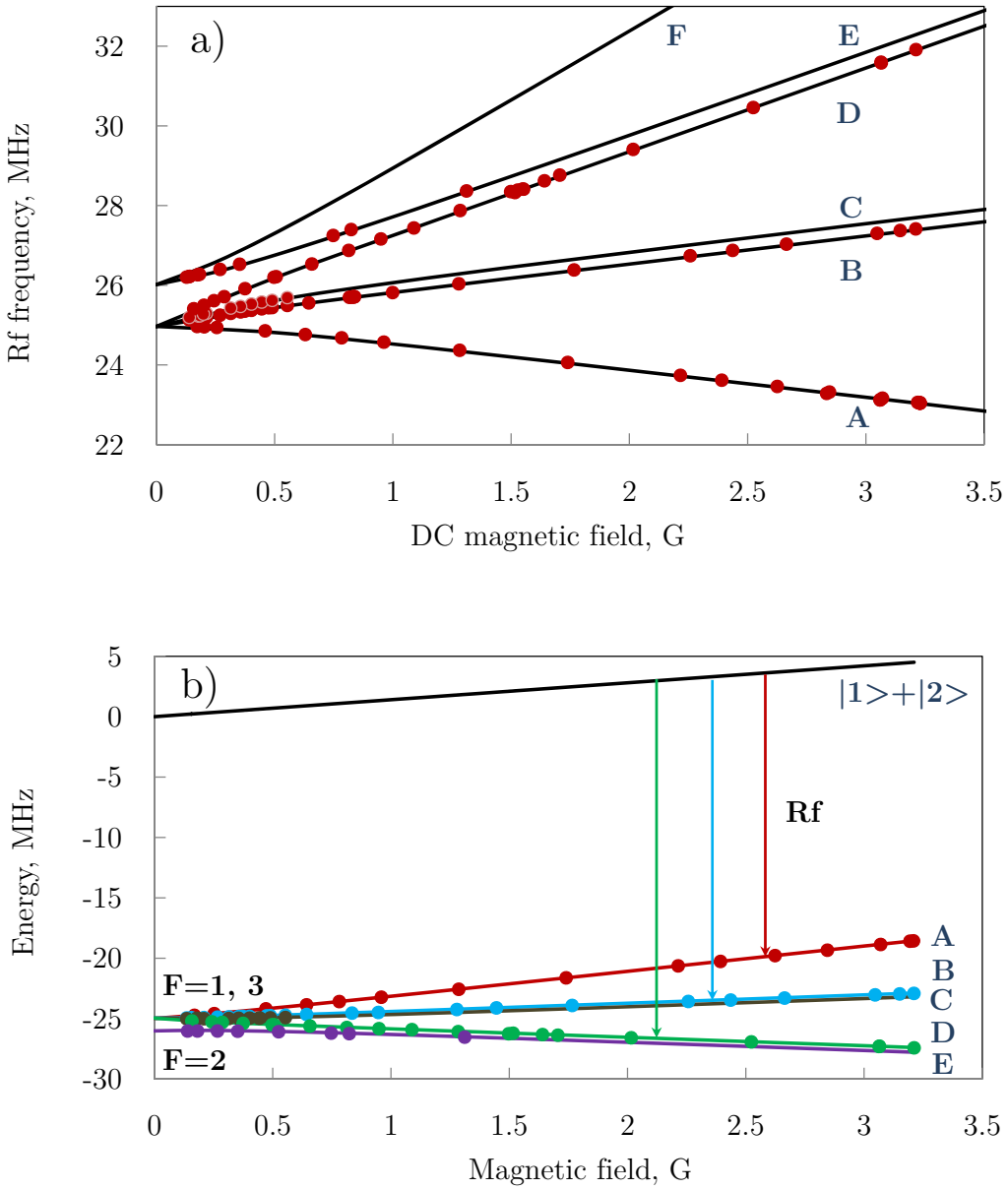

Figure 4.14: (a) Zeeman dependence of the resonant frequencies f_0 for molecular states A, B, C, D, E and F. The manifold F was not detected in our experiments. (b) The energy of the bound states is evaluated from (a) by deducting the energy of the colliding atomic pair from the corresponding transition energy. Solid lines show the theoretical predictions of [55] and the points are the experimental data. Labels F = 1, 2 and 3 show the different hyperfine states of the molecules.

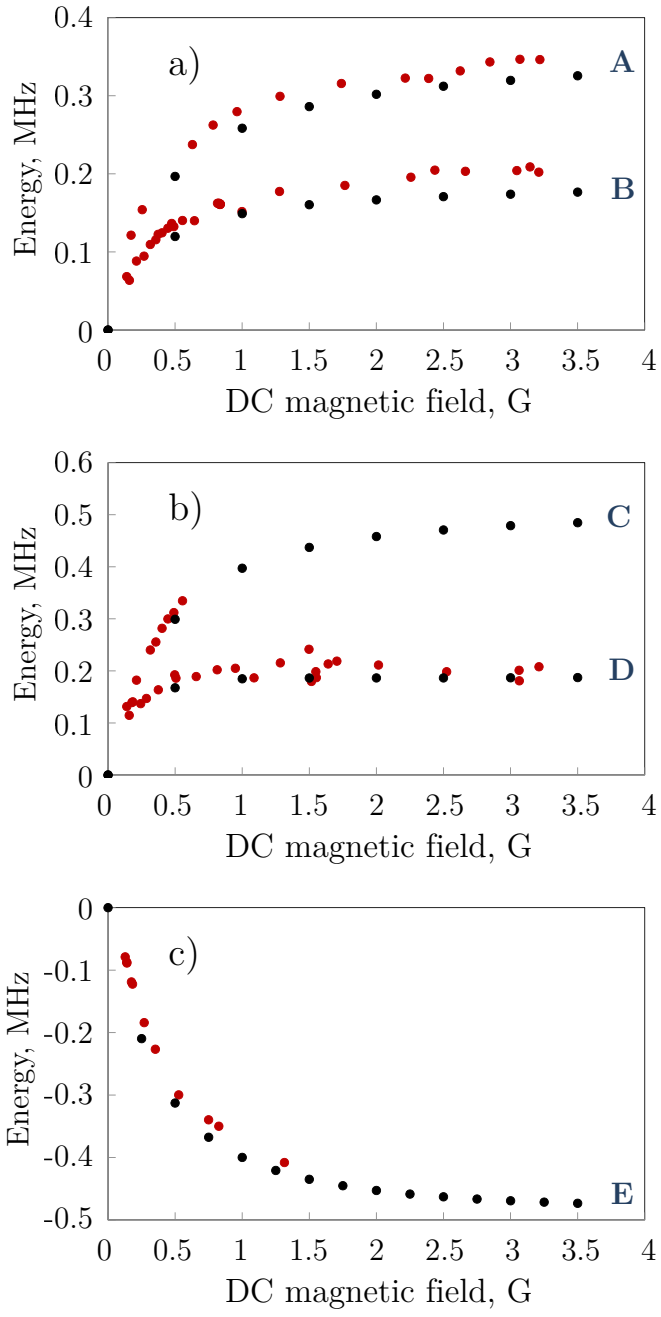

Figure 4.15: Comparison of experimental data with theory [55] after subtracting the linear asymptotical slopes originating from the theoretical zero magnetic field energies of the bound states: 24.96609 MHz for molecular states A, B (a), C, D (b) and 26.01606 MHz for state E (c). Experimental data and theory are shown as red and black points, respectively. It is easy to see that the experimental points have a vertical shift from the theory.

Molecular state	Energy, MHz (0 G)	Error, kHz
A	24.9852	1.9
B	24.9829	1.9
C	24.976	3
D	24.981	3
E	26.055	5

Table 4.2: Measurements of the energies of the molecular states at zero magnetic field. The experimental data is matched with the theoretical points by varying their vertical position.

At low magnetic field the Z-wire magnetic trap has a tighter confinement in the radial direction and the larger atom number density increases the rate of two-body collisions, which lowers the required rf power for locating the loss resonances. That is why it is convenient to use low field traps (around 0.5 G) during the search for the first resonance that belongs to a new molecular curve. To observe the weak resonances C and E it was necessary to additionally increase the atom collision rate by a tighter confinement. In the experiments it was realized by reducing the Z-wire current which simultaneously increases the radial trapping frequency and brings the centre of the trap closer to the chip surface, enhancing the amplitude of the rf field. On the other hand, an increased rate of collisions is a limiting factor for the holding time and as a result 200 ms rf pulses were used for the lower Z-wire current instead of 420 ms as for the measurements of the energies of the A, B and D molecular states. The measurements of all data, shown in Fig. 4.14, were a very time consuming routine - it took almost seven months of continuous experiment running.

The solid lines in Fig. 4.14 are the theoretical predictions that were provided to us in a private communication by the courtesy of the authors [55]. The theory predicts that the molecular energies of weakly bound atoms asymptotically approach linear dependencies at higher magnetic fields with slopes of 0.7 MHz/G (approximately), multiplied by the coefficient k from Eq. 4.6. The error bars for the measured resonant frequencies are only a few kHz (Table 4.1) and in Fig. 4.14 they are within the size of the points. Figure 4.15 displays the same molecular curves with the linear slopes subtracted, revealing the dif-

	Theory for 3.23 G		Experiment	
Resonance	f, MHz [54]	f, MHz [55]	f, MHz	Magnetic field
A	23.184	23.027	23.0592(8)	3.2200(2)
B	27.459	27.402	27.419(2)	3.2129(14)
C	27.785	27.710	-	-
D	31.935	31.936	31.921(3)	3.2137(9)
E	32.335	32.328	-	-
F	36.625	36.668	-	-

Table 4.3: Comparison of two predictions [54] and [55] for the locations of the rf-induced molecular association resonances at 3.23 G with the experimentally measured frequencies. Predicted values from both theories are in a reasonable qualitative agreement with the experiment. Matching new experimental data points within their small error-bars can lead to a better accuracy in determination of the parameters used in the theories.

ference between the experimental data and the theoretical curves [55]. It is easy to see there is a systematic shift between the experimental data and the theoretical points. By varying the origins of the theoretical points (doing a vertical parallel translation of the whole curves) it is possible to combine the theory with the experimental data and thus extract values of the bound states' energies at zero magnetic field. To have a quantitative measure of the matching process the theoretical points are fitted by an analytical function (Appendix E.0.15) and then the same function is used to fit the experimental data with the vertical position as the only free parameter. Estimations of the bound state energies at zero magnetic field are shown in the Table 4.2.

In the paper [54] the calculated energies of the molecular states have also been presented (Fig. 1.2); however detailed information about it is out of our reach. In a private communication [95] through the courtesy of the authors we were provided with the pictures of their predictions for the location and strength of the resonances (Fig. 4.1) at 3.23 G for 4 G of B_{rf} amplitude. Table 4.3 summarizes information on the comparison of the predictions in [54] with [55] with the experimental data points for 3.23 G.

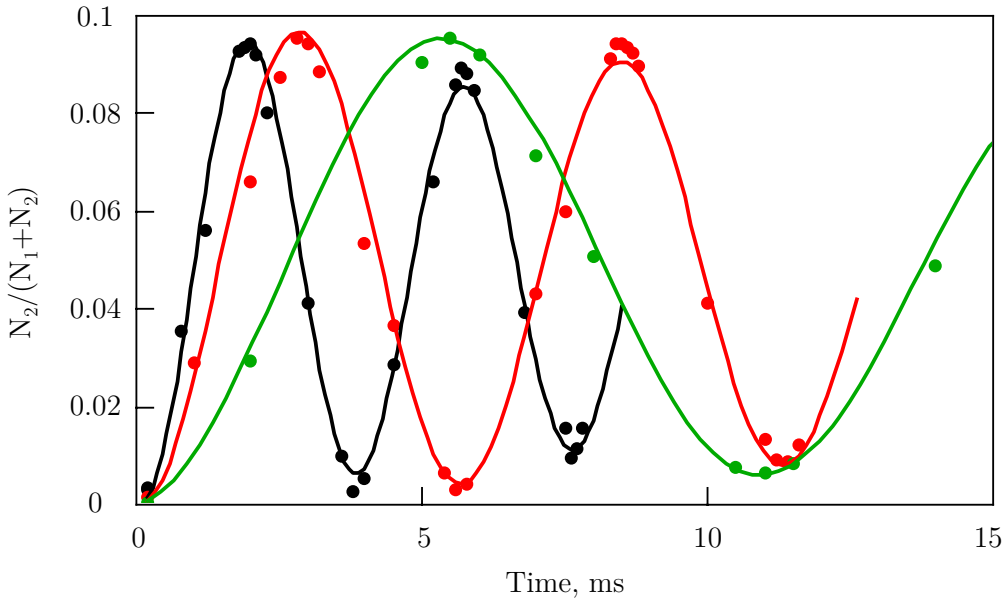

Figure 4.16: Measurement of the amplitude of the rf field by two-photon Rabi oscillations (Section 3.3). Points and lines of different colors correspond to different amplitudes of the rf field: (3.43±0.02) G (black, 1.5 V (pp) on the SRS345 function generator); (2.31±0.02) G (red, 1 V (pp)); (1.18±0.02) G (green, 0.5 V (pp)).

4.4 Dependence of the loss curve shape on rf field amplitude

In [54] it is stated that the position of the resonance depends on the power of the applied radio-frequency radiation and that the shift of the resonant frequency should be proportional to the rf field magnitude squared. In order to check this relation a series of four loss curve measurements were made with different amplitudes of B_{rf}: 3.43 G, 2.31 G, 1.18 G and 0.59 G for the molecular state B at the magnetic field of 0.82 G for the trap bottom (Fig. 4.17 (a)). The rf field amplitude was accurately measured (Fig. 4.16) by the method described in Section 3.3.

The experiment shows that the resonance frequency shifts to lower values with increasing rf amplitude (Fig. 4.17 (a)); however, the corresponding mw spectroscopy lines also undergo a shift, which can be caused by a change of the magnetic field in the centre of the trap due to leaking of the AC-current into DC-magnetic field controllers or by an rf

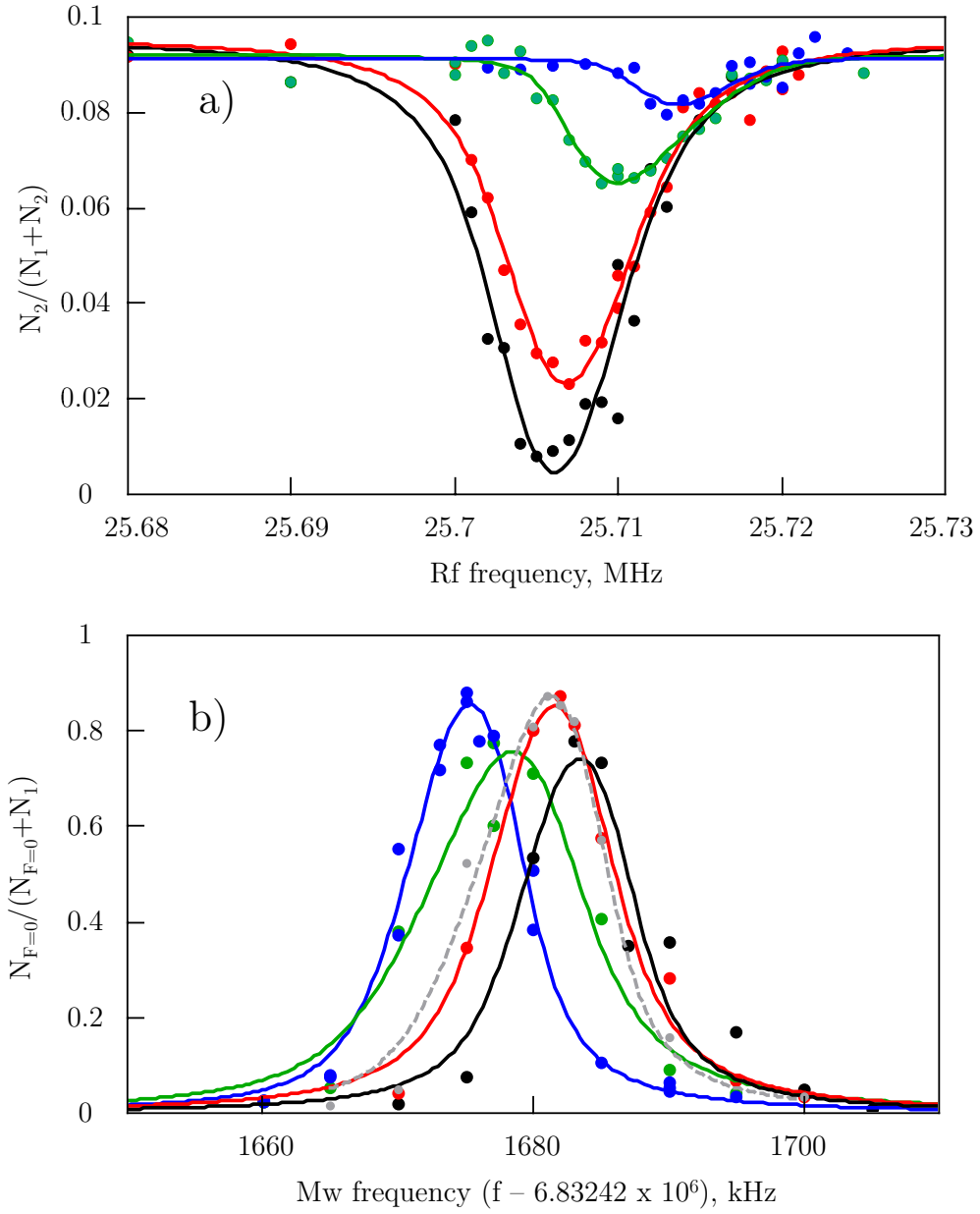

Figure 4.17: (a) Rf induced atom-molecule resonances for different rf field amplitudes for the molecular state B at the magnetic field of 0.82 G. Solid lines show fits of the data according to Eq. 4.13. Black, red, green and blue curves correspond to 3.4 G, 2.3 G, 1.2 G and 0.6 G (Fig. 4.16). (b) Mw spectroscopy profiles measured simultaneously for the same conditions. The grey dashed line shows the shift of the mw spectroscopy profile due to the change of electric current in the B_y coils.

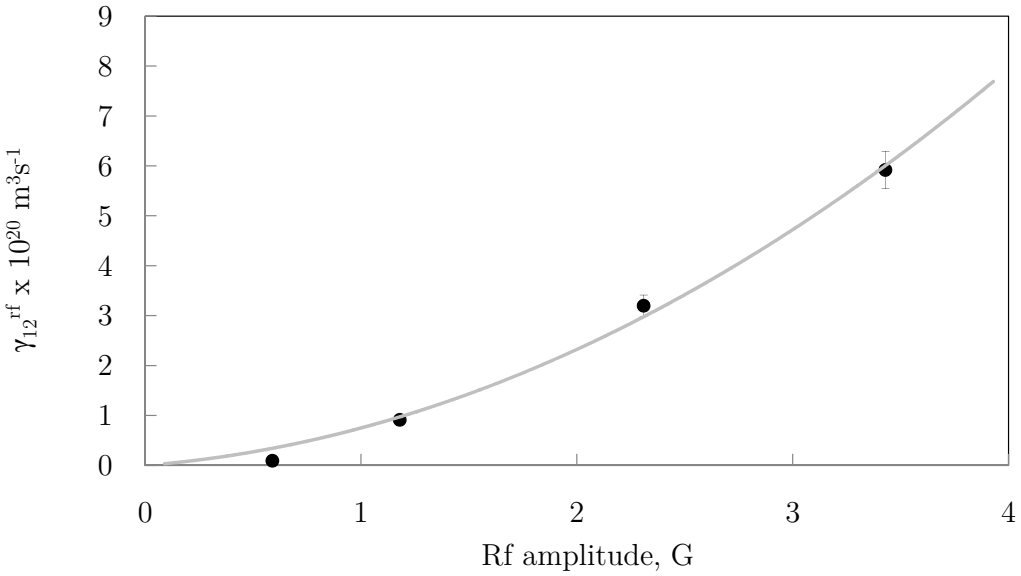

Figure 4.18: Dependence of the loss coefficient γ_{12}^{rf} on rf power. Experimental points are fitted by a second-order polynomial function in accordance with the predictions [54].

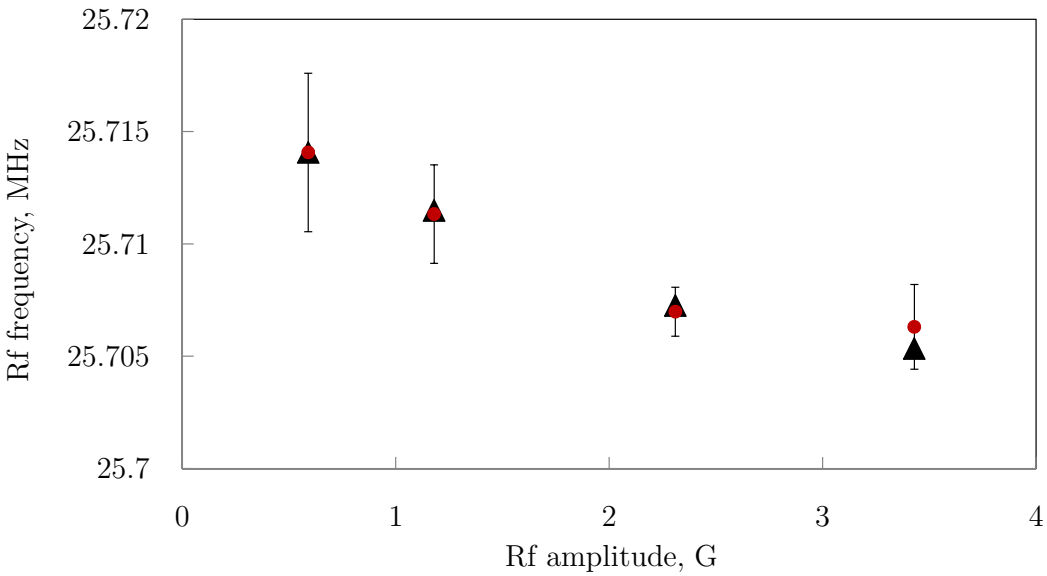

Figure 4.19: Red circles show the resonance frequencies with error bars for different amplitudes of the rf field from Fig. 4.17 (a). Black triangles show the anticipated position of the resonances due to the shift of the DC-magnetic field from Fig. 4.17 (b).

field shift of the atom energy levels (Fig. 4.17 (b)). To distinguish between these two effects, variations of the monitor voltages of the current controllers were recorded during the mw spectroscopy measurement with the rf field amplitude of 3.4 G. A subsequent mw spectroscopy measurement was performed without rf field and applying a current through the B_y coils corresponding to the particular value of the monitor voltage on the controller changed due to the presence of the strong rf field (Fig. 4.17 (b), grey dashed line). Comparing the solid black and dashed grey lines in Fig. 4.17 (b) indicates that the shift of the mw spectroscopy lines is mainly caused by the modified DC-magnetic field at the trap bottom (currents in two other working switches, controlling the Z-wire current and B_{xLarge} coils, were not changed in the second experiment which may explain the fact that positions of the two spectroscopy lines do not coincide exactly). Fig. 4.19 compares the observed shift of the rf frequency with the shift due to the variation of the DC-magnetic field, calculated from the mw spectroscopy profiles. We report that within the accuracy of our method we did not observe any measurable shifts of the resonant radio-frequency with increasing the rf amplitude by more than five times. This insensitivity of the resonance position on B_{rf} appears to be very convenient in measurements of the energies of the molecular states versus magnetic field (Section 4.3). If it were not the case, every point in Fig. 4.14 would need to be measured with precisely controlled amplitude of the rf magnetic field and this would dramatically slow the data gathering process.

At the same time the width and the strength of the resonances have increased significantly with the increase of amplitude (Fig. 4.17 (a)). According to the predictions of [54] the loss coefficient should be proportional to B_{rf}^2. Figure 4.18 demonstrates the dependence of the loss coefficient γ_{12}^{rf} on the amplitude of the rf field. A second-order polynomial function gives a reasonable fit to the experimental data; however, the number of collected points is not enough to demonstrate a clear dependence behaviour.

In [54] the authors also have made a prediction regarding the relative strength of the resonances (Fig. 1.2). The quantitative comparison for molecular state A is discussed in Sections E.0.12 and 4.1.3 revealing a theoretical overestimation of the loss coefficient (the two-body losses theory in Section E.0.12 is rather simple and a more extensive theory may be needed, which would account for the inhomogeneous magnetic field within the

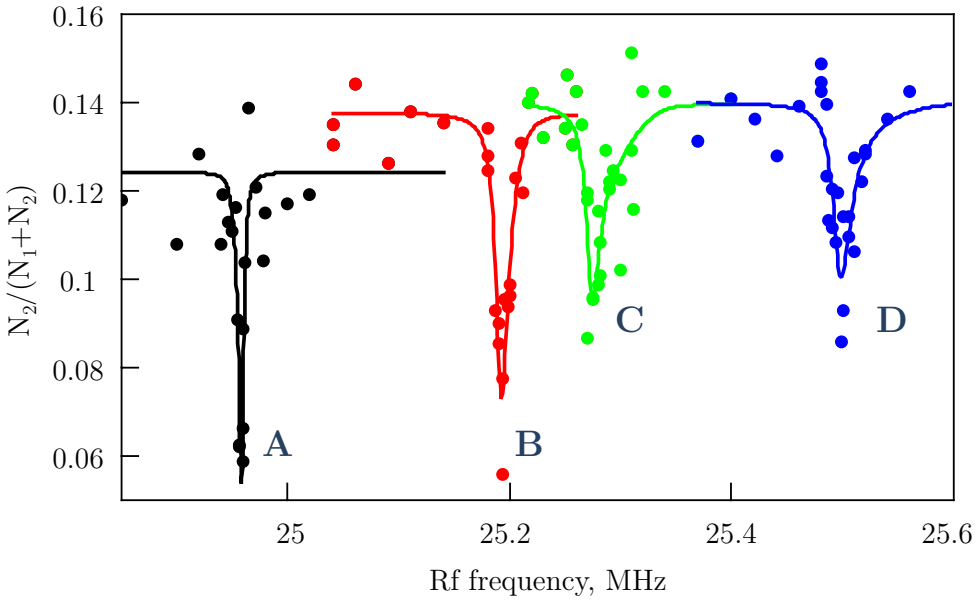

Figure 4.20: Simultaneous detection of the molecular states A (black), B (red), C (green) and D (blue) at the magnetic field of 0.2 G showing the relative strength of the resonance coupling.

cloud size as in Sections 3.1 and 4.2). At the same time the qualitative estimations [54] for the strongest and weakest resonances are correct. Five out of a total of six rf-induced resonances have been successfully observed in our experiments. Resonance couplings to molecular states A, B and D are the strongest, coupling to the bound state E is weaker, with molecular state C being the weakest of the observed resonances. Bound state F has not yet been found despite its coupling strength predicted to be equal to C, according to [54]. The relative strength of the resonances is noticed to be different at different DC-fields; at low values of magnetic field the resonances become almost equally strong. Figure 4.20 shows measurements of the four molecular resonances A, B, C and D in the same experiment in a 0.2 G trap. During the experiment the radio-frequency was changed in a random order within the range 24.8−25.6 MHz. It is easy to see that the four resonant frequencies lead to similar losses of atoms although the resonance A has a noticeably opposite asymmetry shape compared to the other three loss curves.

4.5 Conclusion

This chapter describes the first experimental observation of rf-induced coupling of atoms from the initial $|1,-1\rangle$ and $|2,1\rangle$ states to the molecular bound states of Rb_2, far away from any magnetic Feshbach resonance. The recorded data has the fundamental importance of confirming the predictions of the theoretical models [54] and [55], so they can be used to predict new phenomena. Some parameters used in these theories may also be refined by fitting our new data. Observation of the rf coupling to five different molecular states demonstrates that the rf-induced method offers the flexibility to select the internal state of the created molecules. Introduction of the theory, describing the shape of the rf-induced loss curves, gives a better understanding of the interactions between the rf field and atoms in the BEC which significantly improves the precision of the measured resonant frequencies and as a result the energies of the molecular states. The new data have also led to a measurement of the bound state energies at zero magnetic field with only a few kHz error.

CHAPTER 5

Conclusions and outlook

This thesis describes the experimental observation of molecular association through the application of a powerful resonant radio-frequency field to a two-component ^{87}Rb Bose-Einstein condensate. In addition to magnetic Feshbach resonance and photoassociation methods (Chapter 1) the rf-induced technique can be used as another method for molecular association at any magnetic field.

Chapter 2 contains a description of the experimental apparatus for the production of a ^{87}Rb BEC on an atom chip. The main focus of this chapter is on resolving the technical challenge of generating a high power rf field. Experimental apparatus with atom chips appears to be the best candidate for this kind of task as the ultracold samples in these systems are situated near the electrical wires. High rf fields with amplitudes up to 6 G have been generated with our atom chip and they can also be used in all sorts of other experiments (such as the creation of a double well potential). The amplitude of the rf radiation can be increased more by increasing the current through the chip wire or by simply bringing the trap closer to the chip surface ([101], [102], [67]).

In the current work every measured energy of the bound state is related to the corresponding accurately characterized magnetic field. High precision measurements have been achieved by introducing a theoretical description in Chapter 3 that describes the shapes of the mw and rf spectroscopy lines and accounts for the specific effects of our experimental conditions (gravity sag, inhomogeneity of the magnetic field along the cloud,

dipole oscillations of the cloud in the trap, etc). In contrast with the previous numerical models for the ultracold (non-degenerate) atom samples [42], [43], [44], [45] our theory offers a simple analytic approach, based on the Thomas-Fermi approximation for the pure BEC clouds. The shapes of both the mw and the rf couplings have been fitted using the new model significantly improving the accuracy of the measurements of both the bound state energy and the corresponding value of the magnetic field. The developed theory can also be easily adapted for the case of optically trapped BECs. Chapter 3 also includes a description of our method for the measurement of the rf field amplitude.

The main outcome of the current work is the experimental demonstration of rf-induced molecular association without assistance of a magnetic Feshbach resonance, as described in Chapter 4. This effect was predicted theoretically by two groups [54] and [55] in 2010 and since that time it has not yet been confirmed experimentally. In recent years many publications have reported the observation of rf-induced atom-molecule coupling in the vicinity of magnetic Feshbach resonances [37], [38], [39], [40], [41], [44], [45], [46], [47] where the rf field was mostly used for precise measurements of the bound energies. Now we have demonstrated for the first time the possibility to perform atoms-to-molecules rf-spectroscopy at any magnetic field, independent of the existence of a magnetic Feshbach resonance. As a molecule association technique the rf-stimulating method has the advantage of selection of a specific internal state of the created molecule, unlike the usual magnetic Feshbach resonances. This was demonstrated in the current work by the successful addressing of five different molecular states.

Using the rf field induced atoms-to-molecules couplings the energies of the five bound states were measured over a range of magnetic fields from 0.17 to 3.3 G. This experimental data was collected for the purpose of comparison with the theories in [55] and [54]. Both theoretical predictions were close to the observed positions of the resonances which proves the validity of these theoretical methods of caculations. Some parameters in the theoretical models can also be tuned to achieve better concordance with the new experimental data, such as the energies of the bound states at zero magnetic field. We use a very simple approach of parallel shifting of the theoretical points and extracting the corrections for these energies. The dependence of the atoms-to-molecules rf spectroscopy line on the amplitude

of the rf field has also been measured and compared with the theoretical predictions.

The observed rf field molecule association has many future applications. First of all, it can be used for creation of the ultracold molecules at any magnetic field and any mixtures of atoms (bosonic or fermionic) with precise measurements of the bound energies. The rf field coupling also allows to address a specific molecular state which can be useful in the study of molecule-molecule interactions (in combination with the trapping of the molecules). In experiments of this type molecules are usually held in optical lattices which brings the idea for a future realization of an experimental setup, combining optical traps with an atom chip.

The coupling to the bound state also changes the scattering length, the parameter responsible for interactions between colliding atoms. According to predictions [56] this may allow one to use mw- or rf-induced Feshbach resonances instead of magnetic Feshbach resonances and to extend interaction tuning techniques to many other elements. So far, optical Feshbach resonances have been proposed in [103] and experimentally demonstrated in [57], [58], [104]. However, they suffer from unavoidable losses due to spontaneous emission processes which according to [56] should not be a problem for mw- or rf-induced Feshbach resonances. Other theoretical work [59] foresees the future application of rf stimulated Feshbach resonances for precise control over the interactions between different species in multicomponent gases.

Bibliography

[1] M. H. Anderson, J. R. Ensher, M. R. Matthews, C. E. Wieman, and E. A. Cornell. Observation of Bose-Einstein condensation in a dilute atomic vapor. *Science*, 1995. (Cited on pages 1 and 31.)

[2] C. C. Bradley, C. A. Sackett, J. J. Tollett, and R. G. Hulet. Evidence of Bose-Einstein condensation in an atomic gas with attractive interactions. *Phys. Rev. Lett.*, 75:1687–1690, 1995. (Cited on page 1.)

[3] K. B. Davis, M. O. Mewes, M. R. Andrews, N. J. van Druten, D. S. Durfee, D. M. Kurn, and W. Ketterle. Bose-Einstein condensation in a gas of sodium atoms. *Phys. Rev. Lett.*, 75:3969–3973, 1995. (Cited on page 1.)

[4] G. Roati, M. Zaccanti, C. D'Errico, J. Catani, M. Modugno, A. Simoni, M. Inguscio, and G. Modugno. ^{39}K Bose-Einstein condensate with tunable interactions. *Phys. Rev. Lett.*, 99:010403, 2007. (Cited on page 1.)

[5] G. Modugno, G. Ferrari, G. Roati, R.J. Brecha, A. Simoni, and M. Inguscio. Bose-Einstein condensation of potassium atoms by sympathetic cooling. *Science*, 294(5545):1320–1322, 2001. (Cited on page 1.)

[6] J. L. Roberts, N. R. Claussen, S. L. Cornish, E. A. Donley, E. A. Cornell, and C. E. Wieman. Controlled collapse of a Bose-Einstein condensate. *Phys. Rev. Lett.*, 86:4211–4214, 2001. (Cited on page 1.)

[7] Tino Weber, Jens Herbig, Michael Mark, Hanns-Christoph Nägerl, and Rudolf Grimm. Bose-Einstein condensation of cesium. *Science*, 299(5604):232–235, 2003. (Cited on page 2.)

[8] Dale G. Fried, Thomas C. Killian, Lorenz Willmann, David Landhuis, Stephen C. Moss, Daniel Kleppner, and Thomas J. Greytak. Bose-Einstein condensation of atomic hydrogen. *Phys. Rev. Lett.*, 81:3811–3814, 1998. (Cited on page 2.)

[9] Alice Robert, Olivier Sirjean, Antoine Browaeys, Julie Poupard, S. Nowak, Denis Boiron, Christoph I. Westbrook, and Alain Aspect. A Bose-Einstein condensate of metastable atoms. *Science*, 292(5516):461–464, 2001. (Cited on page 2.)

[10] F. Pereira Dos Santos, J. Léonard, Junmin Wang, C. J. Barrelet, F. Perales, E. Rasel, C. S. Unnikrishnan, M. Leduc, and C. Cohen-Tannoudji. Bose-Einstein condensation of metastable helium. *Phys. Rev. Lett.*, 86:3459–3462, 2001. (Cited on page 2.)

[11] Axel Griesmaier, Jörg Werner, Sven Hensler, Jürgen Stuhler, and Tilman Pfau. Bose-Einstein condensation of chromium. *Phys. Rev. Lett.*, 94:160401, 2005. (Cited on page 2.)

[12] Yosuke Takasu, Kenichi Maki, Kaduki Komori, Tetsushi Takano, Kazuhito Honda, Mitsutaka Kumakura, Tsutomu Yabuzaki, and Yoshiro Takahashi. Spin-singlet Bose-Einstein condensation of two-electron atoms. *Phys. Rev. Lett.*, 91:040404, 2003. (Cited on page 2.)

[13] Simon Stellmer, Meng Khoon Tey, Bo Huang, Rudolf Grimm, and Florian Schreck. Bose-Einstein condensation of strontium. *Phys. Rev. Lett.*, 103:200401, 2009. (Cited on page 2.)

[14] Sebastian Kraft, Felix Vogt, Oliver Appel, Fritz Riehle, and Uwe Sterr. Bose-Einstein condensation of alkaline earth atoms: ^{40}Ca. *Phys. Rev. Lett.*, 103:130401, 2009. (Cited on page 2.)

[15] Mingwu Lu, Nathaniel Q. Burdick, Seo Ho Youn, and Benjamin L. Lev. Strongly dipolar Bose-Einstein condensate of dysprosium. *Phys. Rev. Lett.*, 107:190401, 2011. (Cited on page 2.)

[16] K. Aikawa, A. Frisch, M. Mark, S. Baier, A. Rietzler, R. Grimm, and F. Ferlaino. Bose-Einstein condensation of Erbium. *Phys. Rev. Lett.*, 108:210401, 2012. (Cited on page 2.)

[17] S. Jochim, M. Bartenstein, A. Altmeyer, G. Hendl, S. Riedl, C. Chin, J. H. Denschlag, and R Grimm. Bose-Einstein condensation of molecules. *Science*, 302(5653):2101–2103, 2003. (Cited on page 2.)

[18] Markus Greiner, Cindy A. Regal, and Deborah S. Jin. Emergence of a molecular Bose-Einstein condensate from a Fermi gas. *Nature*, 426(6966):537–540, 2003. (Cited on page 2.)

[19] R. A. Cline, J. D. Miller, and D. J. Heinzen. Study of Rb_2 long-range states by high-resolution photoassociation spectroscopy. *Phys. Rev. Lett.*, 73:632–635, 1994. (Cited on page 2.)

[20] T. Bergeman, J. Qi, D. Wang, Y. Huang, H.K. Pechkis, E.E. Eyler, P.L. Gould, W.C. Stwalley, R.A. Cline, J.D. Miller, et al. Photoassociation of ^{85}Rb atoms into 0_u^+ states near the 5s + 5p atomic limits. *Journal of Physics B: Atomic, Molecular and Optical Physics*, 39(19):S813, 2006. (Cited on page 2.)

[21] A. Fioretti, D. Comparat, A. Crubellier, O. Dulieu, F. Masnou-Seeuws, and P. Pillet. Formation of cold Cs_2 molecules through photoassociation. *Phys. Rev. Lett.*, 80:4402–4405, 1998. (Cited on page 2.)

[22] T. Takekoshi, B. M. Patterson, and R. J. Knize. Observation of cold ground-state cesium molecules produced in a magneto-optical trap. *Phys. Rev. A*, 59:R5–R7, 1999. (Cited on page 2.)

[23] A. N. Nikolov, E. E. Eyler, X. T. Wang, J. Li, H. Wang, W. C. Stwalley, and P. L. Gould. Observation of ultracold ground-state potassium molecules. *Phys. Rev. Lett.*, 82:703–706, 1999. (Cited on page 2.)

[24] A. Fioretti, C. Amiot, C.M. Dion, O. Dulieu, M. Mazzoni, G. Smirne, and C. Gabbanini. Cold rubidium molecule formation through photoassociation: A spectroscopic study of the 0_g long-range state of $^{87}Rb_2$. *The European Physical Journal D - Atomic, Molecular, Optical and Plasma Physics*, 15(2):189–198, 2001. (Cited on page 2.)

[25] Roahn Wynar, R. S. Freeland, D. J. Han, C. Ryu, and D. J. Heinzen. Molecules in a Bose-Einstein condensate. *Science*, 287(5455):1016–1019, 2000. (Cited on page 2.)

[26] B.J. Verhaar, Servaas Kokkelmans, Eric van Kempen, R.S. Freeland, Roahn Wynar, D. Comparat, C. Ryu, and D.J. Heinzen. Spectroscopy of the highest Rb_2 bound states with 10 khz precision. In *APS Division of Atomic, Molecular and Optical Physics Meeting Abstracts*, volume 1, page 4002, 2001. (Cited on page 2.)

[27] Tim Rom, Thorsten Best, Olaf Mandel, Artur Widera, Markus Greiner, Theodor W. Hänsch, and Immanuel Bloch. State selective production of molecules in optical lattices. *Phys. Rev. Lett.*, 93:073002, 2004. (Cited on page 2.)

[28] Jeremy M. Sage, Sunil Sainis, Thomas Bergeman, and David DeMille. Optical production of ultracold polar molecules. *Phys. Rev. Lett.*, 94:203001, 2005. (Cited on page 3.)

[29] Cheng Chin, Rudolf Grimm, Paul Julienne, and Eite Tiesinga. *Reviews of Modern Physics*. (Cited on pages 3 and 73.)

[30] Elizabeth A. Donley, Neil R. Claussen, Sarah T. Thompson, and Carl E. Wieman. Atom–molecule coherence in a Bose–Einstein condensate. *Nature*, 417(6888):529–533, 2002. (Cited on page 3.)

[31] S. J. J. M. F. Kokkelmans and M. J. Holland. Ramsey fringes in a Bose-Einstein condensate between atoms and molecules. *Phys. Rev. Lett.*, 89:180401, 2002. (Cited on page 3.)

[32] N. R. Claussen, S. J. J. M. F. Kokkelmans, S. T. Thompson, E. A. Donley, E. Hodby, and C. E. Wieman. Very-high-precision bound-state spectroscopy near a ^{85}Rb Feshbach resonance. *Phys. Rev. A*, 67:060701, 2003. (Cited on page 3.)

[33] J. Cubizolles, T. Bourdel, S. J. J. M. F. Kokkelmans, G. V. Shlyapnikov, and C. Salomon. Production of long-lived ultracold Li_2 molecules from a Fermi gas. *Phys. Rev. Lett.*, 91:240401, 2003. (Cited on page 3.)

[34] S. Jochim, M. Bartenstein, A. Altmeyer, G. Hendl, C. Chin, J. Hecker Denschlag, and R. Grimm. Pure gas of optically trapped molecules created from Fermionic atoms. *Phys. Rev. Lett.*, 91:240402, 2003. (Cited on page 3.)

[35] Stephan Dürr, Thomas Volz, Andreas Marte, and Gerhard Rempe. Observation of molecules produced from a Bose-Einstein condensate. *Phys. Rev. Lett.*, 92:020406, 2004. (Cited on page 3.)

[36] C. Strauss, T. Takekoshi, F. Lang, K. Winkler, R. Grimm, J. Hecker Denschlag, and E. Tiemann. Hyperfine, rotational, and vibrational structure of the $a^3\Sigma_u^+$ state of $^{87}Rb_2$. *Phys. Rev. A*, 82:052514, 2010. (Cited on page 3.)

[37] Cindy A. Regal, Christopher Ticknor, John L. Bohn, and Deborah S. Jin. Creation of ultracold molecules from a Fermi gas of atoms. *Nature*, 424(6944):47–50, 2003. (Cited on pages 3 and 108.)

[38] C. Chin, M. Bartenstein, A. Altmeyer, S. Riedl, S. Jochim, J. Hecker Denschlag, and R. Grimm. Observation of the pairing gap in a strongly interacting Fermi gas. *Science*, 305(5687):1128–1130, 2004. (Cited on pages 3 and 108.)

[39] S. T. Thompson, E. Hodby, and C. E. Wieman. Ultracold molecule production via a resonant oscillating magnetic field. *Phys. Rev. Lett.*, 95:190404, 2005. (Cited on pages 3 and 108.)

[40] S. B. Papp and C. E. Wieman. Observation of heteronuclear Feshbach molecules from a ^{85}Rb–^{87}Rb gas. *Phys. Rev. Lett.*, 97:180404, 2006. (Cited on pages 3 and 108.)

[41] C. Ospelkaus, S. Ospelkaus, L. Humbert, P. Ernst, K. Sengstock, and K. Bongs. Ultracold heteronuclear molecules in a 3D optical lattice. *Phys. Rev. Lett.*, 97:120402, 2006. (Cited on pages 3 and 108.)

[42] Cheng Chin and Paul S. Julienne. Radio-frequency transitions on weakly bound ultracold molecules. *Phys. Rev. A*, 71:012713, 2005. (Cited on pages 3 and 108.)

[43] Thomas M. Hanna, Thorsten Köhler, and Keith Burnett. Association of molecules using a resonantly modulated magnetic field. *Phys. Rev. A*, 75:013606, 2007. (Cited on pages 3 and 108.)

[44] C. Klempt, T. Henninger, O. Topic, M. Scherer, L. Kattner, E. Tiemann, W. Ertmer, and J. J. Arlt. Radio-frequency association of heteronuclear Feshbach molecules. *Phys. Rev. A*, 78:061602, 2008. (Cited on pages 4 and 108.)

[45] C. Weber, G. Barontini, J. Catani, G. Thalhammer, M. Inguscio, and F. Minardi. Association of ultracold double-species bosonic molecules. *Phys. Rev. A*, 78:061601, 2008. (Cited on pages 4 and 108.)

[46] A. M. Kaufman, R. P. Anderson, Thomas M. Hanna, E. Tiesinga, P. S. Julienne, and D. S. Hall. Radio-frequency dressing of multiple Feshbach resonances. *Phys. Rev. A*, 80:050701, 2009. (Cited on pages 4 and 108.)

[47] Lianghui Huang, Pengjun Wang, B.P. Ruzic, Zhengkun Fu, Zengming Meng, Peng Peng, J.L. Bohn, and Jing Zhang. Radio-frequency manipulation of Fano-Feshbach resonances in an ultracold Fermi gas of ^{40}K. *arXiv preprint arXiv:1407.0431*, 2014. (Cited on pages 4 and 108.)

[48] K. Winkler, F. Lang, G. Thalhammer, P. v. d. Straten, R. Grimm, and J. Hecker Denschlag. Coherent optical transfer of Feshbach molecules to a lower vibrational state. *Phys. Rev. Lett.*, 98:043201, 2007. (Cited on page 4.)

[49] F. Lang, K. Winkler, C. Strauss, R. Grimm, and J. Hecker Denschlag. Ultracold triplet molecules in the rovibrational ground state. *Phys. Rev. Lett.*, 101:133005, 2008. (Cited on page 4.)

[50] S. Ospelkaus, A. PeEr, K-K Ni, J.J. Zirbel, B. Neyenhuis, S. Kotochigova, P.S. Julienne, J. Ye, and D.S. Jin. Efficient state transfer in an ultracold dense gas of heteronuclear molecules. *Nature Physics*, 4(8):622–626, 2008. (Cited on page 4.)

[51] F. Lang, P. vd Straten, B. Brandstätter, G. Thalhammer, K. Winkler, P.S. Julienne, R. Grimm, and J. Hecker Denschlag. Cruising through molecular bound-state manifolds with radiofrequency. *Nature Physics*, 4(3):223–226, 2008. (Cited on page 4.)

[52] Q. Beaufils, A. Crubellier, T. Zanon, B. Laburthe-Tolra, E. Marchal, L. Vernac, and O. Gorceix. Radio-frequency association of molecules: an assisted Feshbach resonance. *The European Physical Journal D*, 56(1):99–104, 2010. (Cited on page 4.)

[53] D. J. Papoular, G. V. Shlyapnikov, and J. Dalibard. Microwave-induced Fano-Feshbach resonances. *Phys. Rev. A*, 81:041603, 2010. (Cited on page 4.)

[54] T. V. Tscherbul, T. Calarco, I. Lesanovsky, R. V. Krems, A. Dalgarno, and J. Schmiedmayer. Rf-field induced Feshbach resonances. *Phys. Rev. A*, 81:050701, 2010. (Cited on pages xv, 4, 5, 6, 7, 8, 34, 74, 76, 77, 78, 79, 81, 82, 86, 100, 101, 103, 104, 105, 106, 108, and 127.)

[55] Thomas M Hanna, Eite Tiesinga, and Paul S Julienne. Creation and manipulation of Feshbach resonances with radiofrequency radiation. *New Journal of Physics*, 12(8):083031, 2010. (Cited on pages xiii, xv, 4, 5, 6, 8, 34, 77, 78, 79, 81, 97, 98, 99, 100, 106, 108, and 169.)

[56] Alexander V. Avdeenkov. Dipolar collisions of ultracold polar molecules in a microwave field. *Phys. Rev. A*, 86:022707, 2012. (Cited on pages 4 and 109.)

[57] M. Theis, G. Thalhammer, K. Winkler, M. Hellwig, G. Ruff, R. Grimm, and J. Hecker Denschlag. Tuning the scattering length with an optically induced Feshbach resonance. *Phys. Rev. Lett.*, 93:123001, 2004. (Cited on pages 4 and 109.)

[58] K. Enomoto, K. Kasa, M. Kitagawa, and Y. Takahashi. Optical Feshbach resonance using the intercombination transition. *Phys. Rev. Lett.*, 101:203201, 2008. (Cited on pages 4 and 109.)

[59] Peng Zhang, Pascal Naidon, and Masahito Ueda. Independent control of scattering lengths in multicomponent quantum gases. *Phys. Rev. Lett.*, 103:133202, 2009. (Cited on pages 4 and 109.)

[60] A. D. Lange, K. Pilch, A. Prantner, F. Ferlaino, B. Engeser, H.-C. Nägerl, R. Grimm, and C. Chin. Determination of atomic scattering lengths from measurements of molecular binding energies near Feshbach resonances. *Phys. Rev. A*, 79:013622, 2009. (Cited on page 4.)

[61] S. Truppe, R.J. Hendricks, S.K. Tokunaga, H.J. Lewandowski, M.G. Kozlov, C. Henkel, E.A. Hinds, and M.R. Tarbutt. A search for varying fundamental con-

stants using Hertz-level frequency measurements of cold CH molecules. *Nature communications*, 4, 2013. (Cited on page 5.)

[62] C.J. Pethick and H. Smith. *Bose-Einstein condensation in dilute gases*. Cambridge University Press, 2008. (Cited on page 5.)

[63] S. Whitlock. *Bose-Einstein condensates on a magnetic film atom chip*. PhD thesis, Swinburne University of Technology, Melbourne, Australia, 2007. (Cited on page 9.)

[64] R.P. Anderson. *Non-equilibrium dynamics and relative phase evolution of two-component Bose-Einstein condensates*. PhD thesis, Swinburne University of Technology, Melbourne, Australia, 2009. (Cited on pages 9, 29, 31, 48, 59, 62, and 66.)

[65] Mikhail Egorov. *Coherence and collective oscillations of a two-component Bose-Einstein condensate*. PhD thesis, Swinburne University of Technology, Melbourne, Australia, 2012. (Cited on pages 9, 12, 14, 16, 17, 22, 23, 25, 29, 76, 77, 84, 125, and 163.)

[66] Valentin Ivannikov. *Analysis of a trapped atom clock with losses*. PhD thesis, Swinburne University of Technology, Melbourne, Australia, 2013. (Cited on pages 9, 10, and 12.)

[67] József Fortágh and Claus Zimmermann. Magnetic microtraps for ultracold atoms. *Rev. Mod. Phys.*, 79:235–289, 2007. (Cited on pages 9 and 107.)

[68] Stephen J. Hellier. *Alkali metal vapor generator*. Number 4195891. April 1980. (Cited on page 9.)

[69] William D. Phillips and Harold Metcalf. Laser deceleration of an atomic beam. *Phys. Rev. Lett.*, 48:596–599, 1982. (Cited on page 10.)

[70] V.I. Balykin, V.S. Letokhov, and V.I. Mushin. Observation of the cooling of free sodium atoms in a resonance laser field with a scanning frequency. *Jetp Letters*, 29(10):560–564, 1979. (Cited on page 10.)

[71] J.V. Prodan and W.D. Phillips. Chirping the light - fantastic- recent NBS atom cooling experiments. *Progress in quantum electronics*, 8(3-4):231–235, 1984. (Cited on page 10.)

[72] Christopher Slowe, Laurent Vernac, and Lene Vestergaard Hau. High flux source of cold rubidium atoms. *Review of Scientific Instruments*, 76(10), 2005. (Cited on page 10.)

[73] S. E. Maxwell, N. Brahms, R. deCarvalho, D. R. Glenn, J. S. Helton, S. V. Nguyen, D. Patterson, J. Petricka, D. DeMille, and J. M. Doyle. High-flux beam source for cold, slow atoms or molecules. *Phys. Rev. Lett.*, 95:173201, 2005. (Cited on page 10.)

[74] David E. Pritchard. Cooling neutral atoms in a magnetic trap for precision spectroscopy. *Phys. Rev. Lett.*, 51:1336–1339, 1983. (Cited on page 12.)

[75] Y. V. Gott, M. S. Ioffe, and V. G. Telkovskii. *Nucl. Fusion Supplement*, 3:1045, 1962. (Cited on page 12.)

[76] Franco Dalfovo, Stefano Giorgini, Lev P. Pitaevskii, and Sandro Stringari. Theory of Bose-Einstein condensation in trapped gases. *Rev. Mod. Phys.*, 71:463–512, 1999. (Cited on pages 13, 49, 51, 77, 84, 95, 154, and 163.)

[77] D.S. Durfee W. Ketterle and D.M. Stamper-Kurn. Making, probing and understanding Bose-Einstein condensates. *Varenna lecture notes*, 1999. (Cited on page 13.)

[78] August Beer. Bestimmung der absorption des rothen lichts in farbigen flssigkeiten (determination of the absorption of red light in colored liquids). *Annalen der Physik und Chemie*, 86:78, 1852. (Cited on page 15.)

[79] D. A. Steck. Rubidium 87 D line data. 2003. (Cited on pages 16, 64, and 137.)

[80] G. Reinaudi, T. Lahaye, Z. Wang, and D. Guéry-Odelin. Strong saturation absorption imaging of dense clouds of ultracold atoms. *Opt. Lett.*, 32(21):3143–3145. (Cited on page 16.)

[81] Princeton Instruments. Kinetics readout for fast temporal studies. (Cited on page 18.)

[82] Tosio Kato. On the adiabatic theorem of quantum mechanics. *Journal of the Physical Society of Japan*, 5(6):435–439, 1950. (Cited on page 31.)

[83] Kurt Otto Friedrichs. On the adiabatic theorem in quantum theory. part 1. *New York: Courant Institute of Mathematical Sciences, New York University*, 1955. (Cited on page 31.)

[84] Doug Stuetzle. Designing effective baseband circuits. *Microwaves and RF*, 2009. (Cited on page 36.)

[85] E. L. Norton. Technical report TM26-0-1860 - design of finite networks for uniform frequency characteristic. *Bell Laboratories*, 1926. (Cited on page 36.)

[86] H. F. Mayer. Ueber das ersatzschema der verstrkerrhre (on equivalent circuits for electronic amplifiers). *Telegraphen- und Fernsprech-Technik*, 15:335, 1926. (Cited on page 36.)

[87] L. Thvenin. Extension de la loi dohm aux circuits lectromoteurs complexes (extension of ohms law to complex electromotive circuits). *Annales Tlgraphiques*, 3e series 10:222, 1883. (Cited on page 36.)

[88] L. Thvenin. Sur un nouveau thorme d'lectricit dynamique (on a new theorem of dynamic electricity). *Comptes rendus hebdomadaires des sances de l'Acadmie des Sciences*, 97:159, 1883. (Cited on page 36.)

[89] G. Breit and I. I. Rabi. Measurement of nuclear spin. *Phys. Rev.*, 38:2082–2083, 1931. (Cited on pages 47, 62, and 64.)

[90] M. Egorov, B. Opanchuk, P. Drummond, B. V. Hall, P. Hannaford, and A. I. Sidorov. Measurement of a_{12}-wave scattering lengths in a two-component Bose-Einstein condensate. *Phys. Rev. A*, 87:053614, 2013. (Cited on pages 50, 69, 84, 85, 86, and 163.)

[91] Gary Taubes. First atom laser shoots pulses of coherent matter. *Science*, 275(5300):617–618, 1997. (Cited on page 62.)

[92] M.-O. Mewes, M. R. Andrews, D. M. Kurn, D. S. Durfee, C. G. Townsend, and W. Ketterle. Output coupler for Bose-Einstein condensed atoms. *Phys. Rev. Lett.*, 78:582–585, 1997. (Cited on page 62.)

[93] M. Erhard, H. Schmaljohann, J. Kronjäger, K. Bongs, and K. Sengstock. Measurement of a mixed-spin-channel Feshbach resonance in ^{87}Rb. *Phys. Rev. A*, 69:032705, 2004. (Cited on page 73.)

[94] M. White, H. Gao, M. Pasienski, and B. DeMarco. Bose-Einstein condensates in rf-dressed adiabatic potentials. *Phys. Rev. A*, 74:023616, 2006. (Cited on page 73.)

[95] T. V. Tscherbul. private communication, 2011. (Cited on pages 75, 76, and 100.)

[96] S. T. Thompson, E. Hodby, and C. E. Wieman. Spontaneous dissociation of ^{85}Rb Feshbach molecules. *Phys. Rev. Lett.*, 94:020401, 2005. (Cited on page 75.)

[97] Thorsten Köhler, Eite Tiesinga, and Paul S. Julienne. Spontaneous dissociation of long-range Feshbach molecules. *Phys. Rev. Lett.*, 94:020402, 2005. (Cited on page 75.)

[98] Tino Weber, Jens Herbig, Michael Mark, Hanns-Christoph Nägerl, and Rudolf Grimm. Three-body recombination at large scattering lengths in an ultracold atomic gas. *Phys. Rev. Lett.*, 91:123201, 2003. (Cited on page 75.)

[99] K. M. Mertes, J. W. Merrill, R. Carretero-González, D. J. Frantzeskakis, P. G. Kevrekidis, and D. S. Hall. Nonequilibrium dynamics and superfluid ring excitations in binary Bose-Einstein condensates. *Phys. Rev. Lett.*, 99:190402, 2007. (Cited on pages 84 and 85.)

[100] E. G. M. van Kempen, S. J. J. M. F. Kokkelmans, D. J. Heinzen, and B. J. Verhaar. Interisotope determination of ultracold rubidium interactions from three high-precision experiments. *Phys. Rev. Lett.*, 88:093201, 2002. (Cited on page 84.)

[101] J. Fortagh, A. Grossmann, C. Zimmermann, and T. W. Hänsch. Miniaturized wire trap for neutral atoms. *Phys. Rev. Lett.*, 81:5310–5313, 1998. (Cited on page 107.)

[102] A. Günther, M. Kemmler, S. Kraft, C. J. Vale, C. Zimmermann, and J. Fortágh. Combined chips for atom optics. *Phys. Rev. A*, 71:063619, 2005. (Cited on page 107.)

[103] P. O. Fedichev, Yu. Kagan, G. V. Shlyapnikov, and J. T. M. Walraven. Influence of nearly resonant light on the scattering length in low-temperature atomic gases. *Phys. Rev. Lett.*, 77:2913–2916, 1996. (Cited on page 109.)

[104] Gregor Thalhammer, Matthias Theis, Klaus Winkler, Rudolf Grimm, and Johannes Hecker Denschlag. Inducing an optical Feshbach resonance via stimulated raman coupling. *Phys. Rev. A*, 71:033403, 2005. (Cited on page 109.)

[105] J. Schmiedmayer J. Denschlag R. Folman, P. Kruger and C. Henkel. Microscopic atom optics: from wires to an atom chip. *Adv. At. Mol. Opt. Phys.*, 48:263356, 2002. (Cited on page 131.)

[106] József Fortágh and Claus Zimmermann. Magnetic microtraps for ultracold atoms. *Rev. Mod. Phys.*, 79:235–289, 2007. (Cited on page 131.)

[107] E.A. Hinds and Hughes I.G. Magnetic atom optics: mirrors, guides, traps, and chips for atoms. *Journal of Physics D: Applied Physics*, 32(18):R119, 1999. (Cited on page 131.)

[108] J. Reichel. Microchip traps and Bose-Einstein condensation. *Applied Physics B*, 74:469, 2002. (Cited on page 131.)

[109] W.C. Johnson. *Transmission lines and networks*. McGraw-Hill electrical and electronic engineering series. McGraw-Hill, 1950. (Cited on page 142.)

[110] R.F. Harrington. *Time-harmonic electromagnetic fields*. McGraw-Hill electrical and electronic engineering series. McGraw-Hill, 1961. (Cited on page 142.)

[111] Kirk T. McDonald. *Impedance Matching of Transmission Lines*. Princeton University, 2005. (Cited on pages 144, 147, and 148.)

[112] Matthew N. O. Sadiku. *Elements of Electromagnetics*. Oxford University Press, USA, 3rd edition, 2000. (Cited on page 144.)

[113] Thomas M. Hanna. private communication, 2012. (Cited on page 169.)

APPENDIX A

Elimination of parasitic resonances

There have been other attempts at the observation of rf stimulated molecular association in our group. The previous student, Mikhail Egorov, has observed increased losses of atoms in state $|2\rangle$ at 3.23 G and attributed them to atom-molecule coupling to the molecular states A, B and C. These observations and their analysis were described in the last chapter of his thesis [65]. In the original experiment the radio-frequency coupling field from the SRS345 (Stanford Research Systems 345) function generator was applied to a broadband rf amplifier (OPHIR 5303055), whose output was directly connected to one of the end-wires on the atom chip. The initial task of my PhD project was to reproduce these results, investigate the properties of the resonances and observe the rf induced molecule association to other molecular states.

Employing the same means of rf generation have led to the observation of a resonance atom loss curve (Fig. A.1 (a)). However, all attempts to reproduce the same resonance feature with other function generators (TTi TG4001, TTi TG1040) failed (it was necessary to use other function generators to search for the resonances to the molecular states D and E at 3.23 G trap bottom in the radio-frequency range $30-32$ MHz as the SRS345 generator has an upper frequency limit of 30 MHz in generating rf field). Doubts about the resonance origin arose even more after the resonance vanished during a repetition of the experiment with a $19.2-23.6$ MHz band-pass filter on the output of the SRS345 generator (Fig. A.1 (b)). After initial transfer of 99% of the atoms into state $|2\rangle$ the total

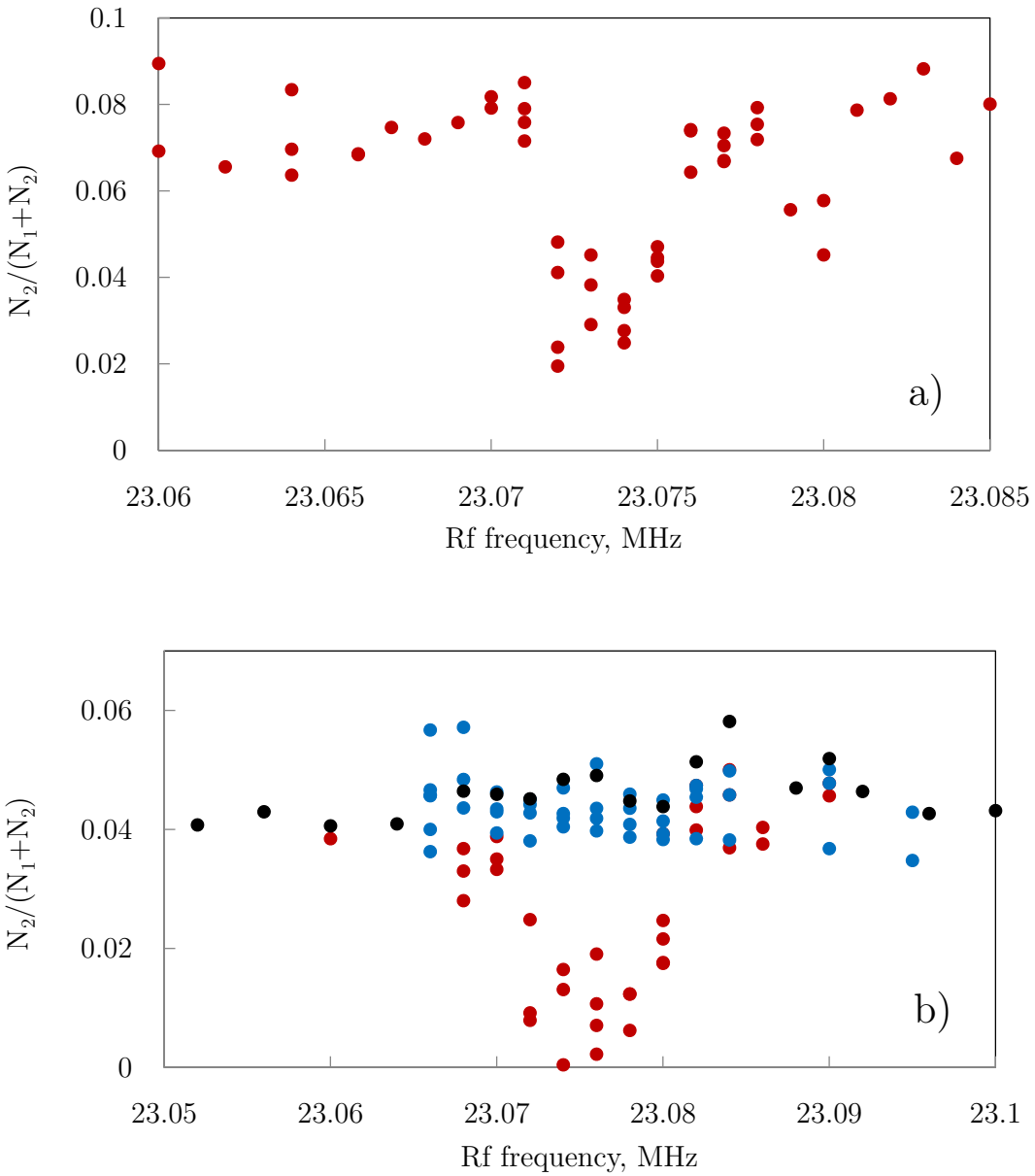

Figure A.1: (a) Rf induced loss resonance observed with the SRS345 generator. (b) Initially observed increase of atom loss resonance disappears after filtering of the rf signal: red dots correspond to the SRS345 generator; black dots correspond to the SRS345 generator plus band-pass filter; blue dots correspond to other generators (TTi TG4001, TTi TG1040).

number of atoms showed a similar resonance loss curve which confirmed that the rf field induces atom losses in state $|2\rangle$ directly and that it has little to do with coupling to the molecular state during interspecies collisions.

According to our further investigation of the SRS generator signal spectrum the cause of the atoms loss was a sideband ($\sim$ 2.3 MHz) which came from the generator and coupled atoms into other Zeeman sublevels. It appeared that the spectrum of the generator signal, shown in Fig. A.2, carries multiple sidebands. One of the sidebands with $\sim$ 60 dB attenuation is close to the one-photon transition frequency 2.3 MHz between the Zeeman levels for 3.23 G of the magnetic field. The sideband peak frequency shifts from 2.236 MHz to 2.398 MHz while the frequency of the signal changes from 23.070 MHz to 23.085 MHz (Fig. A.3).

These parasitic resonances demonstrated the necessity to use band-pass filters during the search for the new resonances and the need to critical tests of the observed features. Luckily, this all happened at the beginning of my PhD and we didn't waste too much time on chasing the false resonances. The search for rf induced molecular associations has been continued with the development of a method for the measurement of the rf field amplitude (Section 3.3). The maximum amplitude that we could generate at that time appeared to be less than 0.15 G which was more that an order of magnitude lower than in the theoretical prediction [54] (4 G and 10 G). This pointed out that the production of a high power rf field needed the introduction of big changes to the experimental setup (such as the rf transformer and matching the load with the transmission line, Section 2.8) and revealed that there was little hope to observe the rf induced atom-molecule coupling with the existing rf field generation circuit.

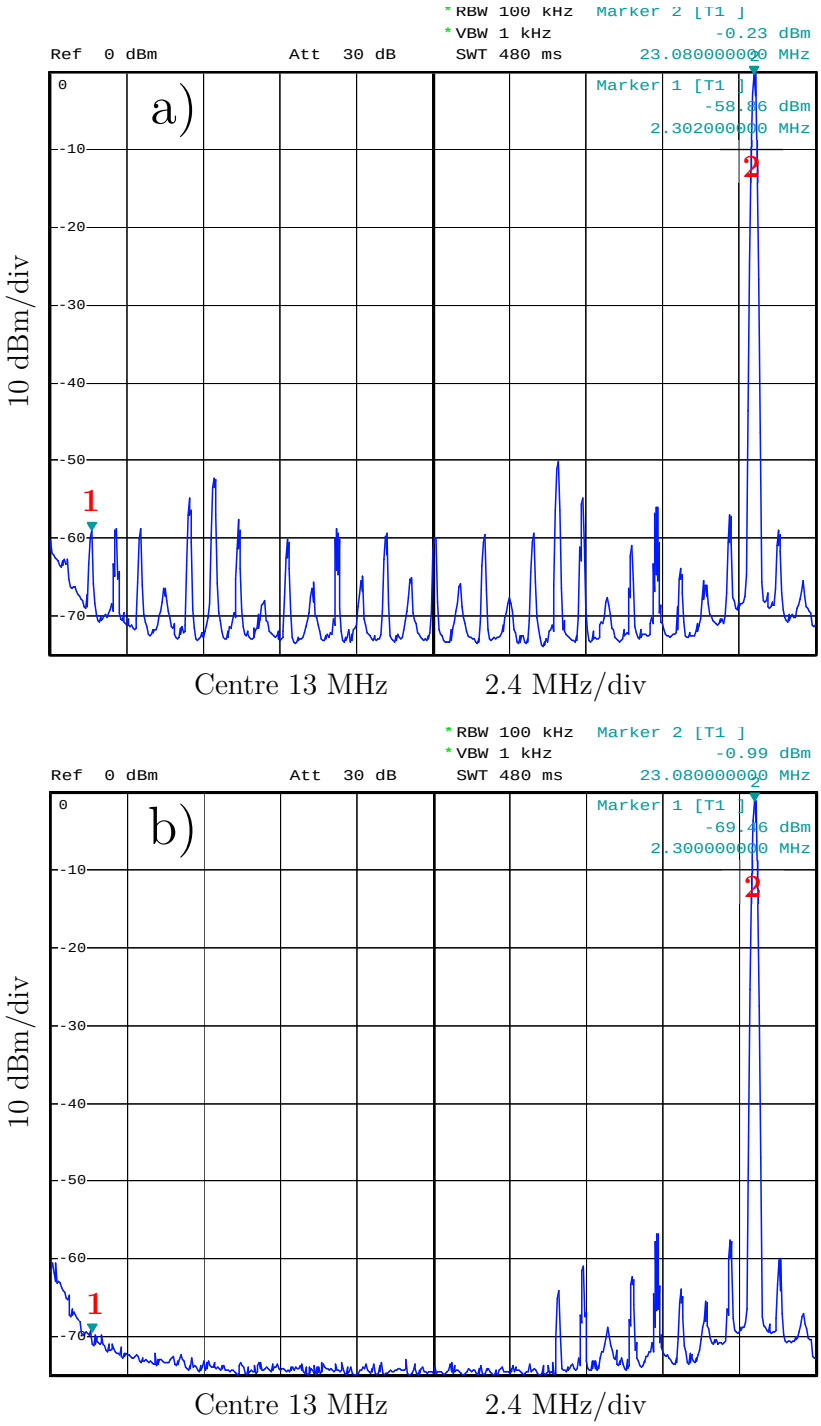

Figure A.2: Spectra of the SRS345 generator signal with settings 23.077 MHz frequency and 0 dBm amplitude: (a) the spectrum shows multiple sidebands with one being close to 2.3 MHz of ~ -60 dBm amplitude; (b) after connection of the band-pass filter to the generator output the 2.3 MHz sideband disappears.

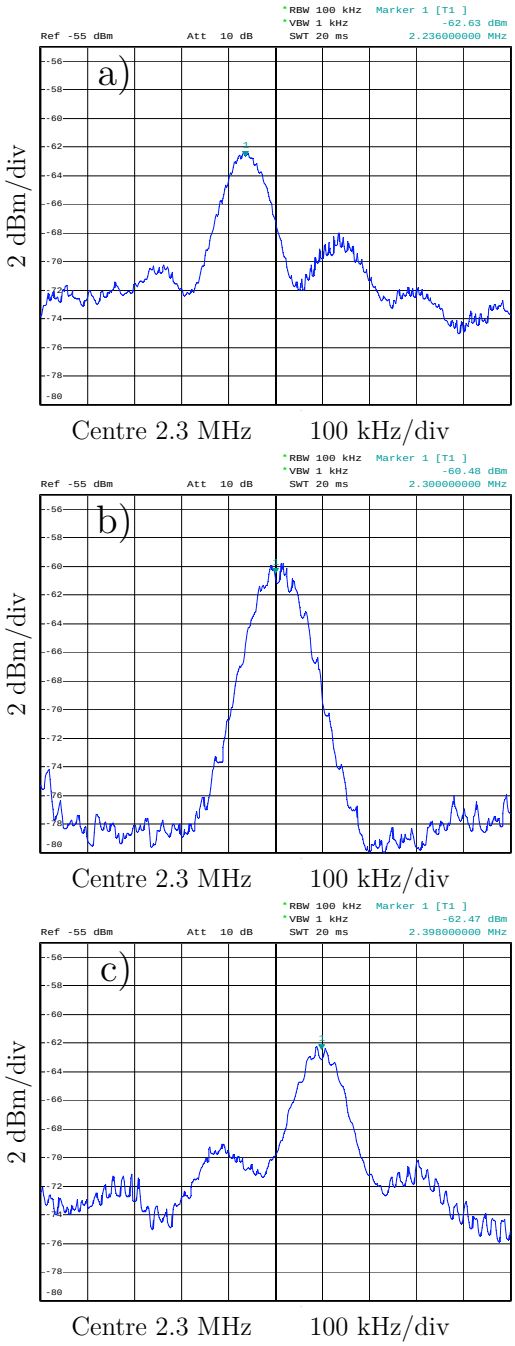

Figure A.3: Investigation of the 2.3 MHz sideband frequency shifts during variations of the SRS345 generator settings (0 dBm amplitude): (a) 23.070 MHz frequency corresponds to the sideband frequency peak at 2.236 MHz; (b) 23.077 MHz frequency corresponds to the sideband frequency peak at 2.300 MHz; (a) 23.085 MHz frequency corresponds to the sideband frequency peak at 2.398 MHz.

APPENDIX B

Z-wire magnetic trap

B.0.1 Magnetic field in the Z-wire magnetic trap

In order to describe the position of atom cloud the following coordinate system is used: the x-axis is horizontal and directed towards the CCD-camera; the y-axis is also horizontal and parallel to the middle section of the Z wire (Fig. B.1). High gradients of the magnetic field are created close to the chip surface by passing high currents through the Z- or U-wires (Fig. 2.1). These trap configurations are well known and the properties of magnetic potentials are discussed in a number of review papers [105], [106], [107], [108].

Usually it is useful to describe magnetic traps via the introduction of the trap frequencies along the different coordinate axes so that:

$$\omega_i = \sqrt{\frac{1}{m}\frac{d^2V}{dq_i^2}} \tag{B.1}$$

where q_i are the coordinates x, y and z and V is the trapping potential.

All experiments with BEC described in this thesis have been made in the Z-wire magnetic trap and it is important to know its properties. Magnetic fields of the trap can be approximately calculated in a simplification of the infinitely long central part and semi-infinite ends of the Z-wire. A current passing through the wires generats a concentric magnetic field perpendicular to the wires as shown in Fig. B.1. The magnitude of the magnetic field generated by a single wire is proportional to the current in the wire and inversely proportional to the distance from the centre of the wires r. It can be calculated

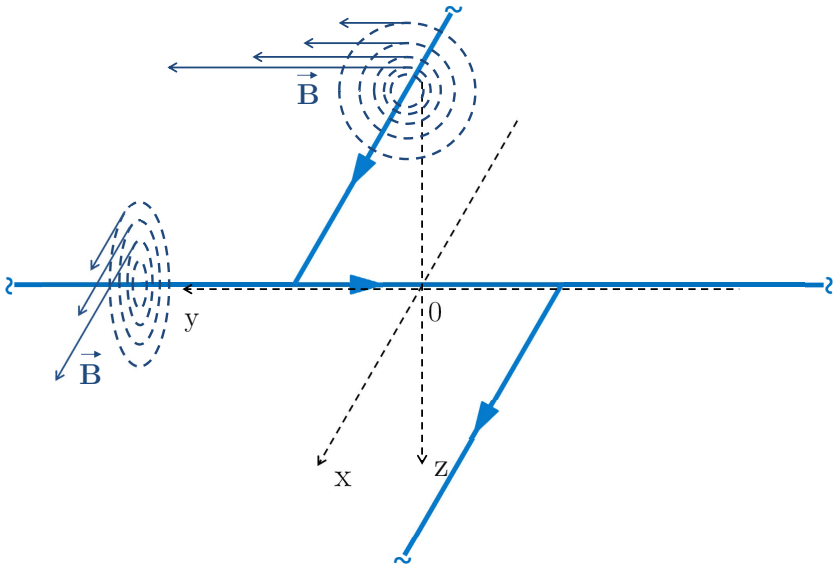

Figure B.1: Magnetic field generated by a Z-wire on a chip can be calculated in approximation of an infinite central wire and semi-finite ends with the same currents passing through all the wires.

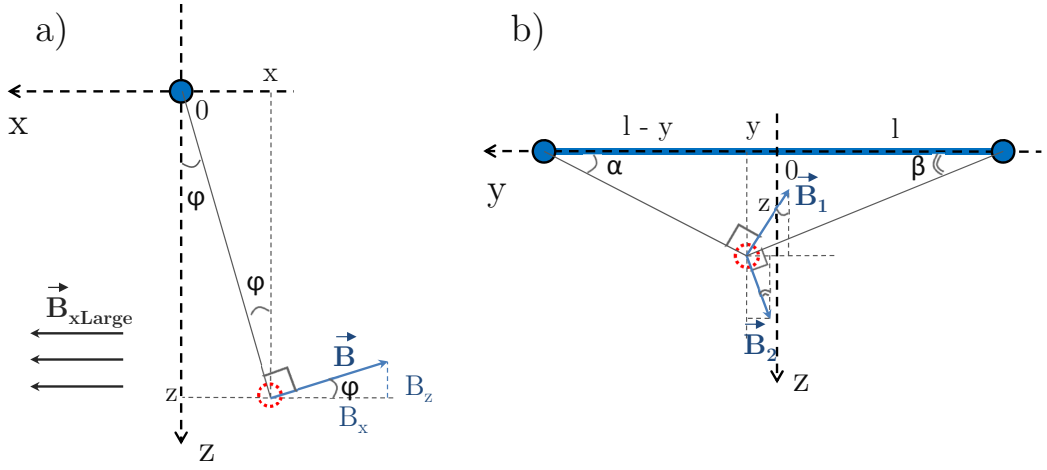

Figure B.2: (a) View from the right side in Fig. B.1. Blue circle is the central part of the wire with a current passing out from the plane of picture. To create a local minimum of magnetic field an additional external uniform magnetic field B_{xLarge} is applied along the x-axis. (b) View from the front in Fig. B.1. Magnetic field generated from side wires is lying in the $y-z$ plane.

in SI units as

$$|B| = \frac{\mu_0}{2\pi}\frac{I}{r} \tag{B.2}$$

On the points of the z-axis the magnetic field is horizontal and to create a local minimum of the magnetic field it is necessary to add a uniform field B_{xLarge} parallel to the x-axis (Fig. B.2 (a)). The vector sum of these two magnetic fields B^c (index c stands for central) has the following projections on the coordinate axis:

$$\begin{cases} B_x^c = B_{xLarge} - |B|cos\phi, \\ B_z^c = -|B|sin\phi \end{cases} <=> \begin{cases} B_x^c = B_{xLarge} - |B|\frac{z}{\sqrt{x^2+z^2}}, \\ B_z^c = -|B|\frac{(-x)}{\sqrt{x^2+z^2}} \end{cases} <=>$$
$$\begin{cases} B_x^c = B_{xLarge} - \frac{\mu_0}{2\pi}\frac{I}{\sqrt{x^2+z^2}}\frac{z}{\sqrt{x^2+z^2}}, \\ B_z^c = \frac{\mu_0}{2\pi}\frac{I}{\sqrt{x^2+z^2}}\frac{x}{\sqrt{x^2+z^2}} \end{cases} <=> \begin{cases} B_x^c = B_{xLarge} - \frac{\mu_0}{2\pi}\frac{I}{x^2+z^2}z, \\ B_z^c = \frac{\mu_0}{2\pi}\frac{I}{x^2+z^2}x \end{cases} \tag{B.3}$$

From which the coordinates of the minimum of $|B^c|$ are equal to

$$\begin{cases} B_x^c = 0, \\ B_z^c = 0 \end{cases} <=> \begin{cases} z_0 = \frac{\mu_0}{2\pi}\frac{I}{B_{xLarge}}, \\ x_0 = 0 \end{cases} \tag{B.4}$$

In typical experimental conditions the cloud of atoms is situated at $z_0 \sim 1.2$ mm from the central wire and the radial size of the cloud is of the order of 5 μm $<<$ z_0. For this reason in the vicinity of the trap minimum x $<<$ z $\approx$ z_0 and Eq. B.3 can be rewritten as:

$$G = \frac{\mu_0}{2\pi}\frac{I}{z_0^2} \quad => \quad \begin{cases} B_x^c = G(z_0 - z), \\ B_z^c = Gx \end{cases} \tag{B.5}$$

The magnitude of the magnetic field generated by a semi-infinite wire is equal to one half of the field of an infinite wire, described by Eq. B.2. The modulus of the magnetic field, generated by the ends of the Z-wire, depends on the x coordinate; however it can be considered constant in the approximation $x << l$. Thus the magnetic field from the two

ends of the Z-wire B^e (index e stands for end (Fig. B.2 (b))) is equal to:

$$\begin{cases} B_y^e = -|B_1|sin\alpha - |B_2|sin\beta, \\ B_z^e = -|B_1|cos\alpha + |B_2|cos\beta \end{cases} <=>$$

$$\begin{cases} B_y^e = -\frac{\mu_0}{4\pi}\frac{I}{\sqrt{(l-y)^2+z^2}}\frac{z}{\sqrt{(l-y)^2+z^2}} - \frac{\mu_0}{4\pi}\frac{I}{\sqrt{(l+y)^2+z^2}}\frac{z}{\sqrt{(l+y)^2+z^2}}, \\ B_z^e = -\frac{\mu_0}{4\pi}\frac{I}{\sqrt{(l-y)^2+z^2}}\frac{l-y}{\sqrt{(l-y)^2+z^2}} + \frac{\mu_0}{4\pi}\frac{I}{\sqrt{(l+y)^2+z^2}}\frac{l+y}{\sqrt{(l+y)^2+z^2}} \end{cases} <=>$$

$$\begin{cases} B_y^e = -\frac{\mu_0}{4\pi}Iz\left[\frac{1}{l^2-2yl+y^2+z^2} + \frac{1}{l^2+2yl+y^2+z^2}\right], \\ B_z^e = \frac{\mu_0}{4\pi}I\left[-\frac{l-y}{l^2-2yl+y^2+z^2} + \frac{l+y}{l^2+2yl+y^2+z^2}\right] \end{cases} <=>$$

$$\begin{cases} B_y^e = -\frac{\mu_0}{4\pi(l^2+z^2)}Iz\left[(1-\frac{2yl}{l^2+z^2}+\frac{y^2}{l^2+z^2})^{-1} + (1+\frac{2yl}{l^2+z^2}+\frac{y^2}{l^2+z^2})^{-1}\right], \\ B_z^e = \frac{\mu_0}{4\pi(l^2+z^2)}I\left[(y-l)(1-\frac{2yl}{l^2+z^2}+\frac{y^2}{l^2+z^2})^{-1} + (y+l)(1+\frac{2yl}{l^2+z^2}+\frac{y^2}{l^2+z^2})^{-1}\right] \end{cases} \tag{B.6}$$

As follows from symmetry at $y = 0$ the z-components of B_1 and B_2 (Fig. B.2 (b)) compensate each other, so the resulting magnetic field of the trap is directed along the y axis and is not zero for any positive z_0. For small deviations from the centre of the trap the x- and z-components of the magnetic field make little contribution to the total field, so that $B_x << B_y$, $B_z << B_y$ and thus:

$$|B| = \sqrt{B_x^2 + B_y^2 + B_z^2} \approx |B_y|\left(1 + \frac{B_x^2 + B_z^2}{2B_y^2}\right) \tag{B.7}$$

The last equation in Eq. B.6 can be expressed in the Taylor expansion around $z \approx z_0$, $y = 0$. As B_x and B_z are squared in Eq. B.7, in the expansion of B_y the second-order terms should also be kept:

$$\begin{aligned} B_y^e = -\frac{\mu_0}{4\pi(l^2+z^2)}Iz\Bigg[1 - \left(-\frac{2yl}{l^2+z^2}+\frac{y^2}{l^2+z^2}\right) + \left(\frac{y^2}{l^2+z^2}-\frac{2yl}{l^2+z^2}\right)^2 + ... \\ +1 - \left(\frac{2yl}{l^2+z^2}+\frac{y^2}{l^2+z^2}\right) + \left(\frac{2yl}{l^2+z^2}+\frac{y^2}{l^2+z^2}\right)^2 + ...\Bigg] \approx \\ -\frac{\mu_0}{4\pi(l^2+z^2)}Iz\Bigg[1 + \frac{2yl}{l^2+z^2} - \frac{y^2}{l^2+z^2} + \frac{y^4}{(l^2+z^2)^2} - \frac{4y^3l}{(l^2+z^2)^2} + \frac{4y^2l^2}{(l^2+z^2)^2} + \\ 1 - \frac{2yl}{l^2+z^2} - \frac{y^2}{l^2+z^2} + \frac{y^4}{(l^2+z^2)^2} + \frac{4y^3l}{(l^2+z^2)^2} + \frac{4y^2l^2}{(l^2+z^2)^2}\Bigg] = \\ -\frac{\mu_0}{4\pi(l^2+z^2)}Iz\left[2 - \frac{2y^2}{l^2+z^2} + \frac{2y^4}{(l^2+z^2)^2} + \frac{8y^2l^2}{(l^2+z^2)^2}\right] = \\ -\frac{\mu_0 Iz}{2\pi(l^2+z^2)}\left[1 + \frac{y^2(3l^2-z^2)}{(l^2+z^2)^2} + \frac{y^4}{(l^2+z^2)^2}\right] \approx -\frac{\mu_0 Iz_0}{2\pi(l^2+z_0^2)}\left[1 + \frac{y^2(3l^2-z_0^2)}{(l^2+z_0^2)^2}\right] \end{aligned} \tag{B.8}$$

And for the z-component:

$$B_z^e = \frac{\mu_0}{4\pi(l^2+z^2)} I \left[(y-l)\left(1-\left(-\frac{2yl}{l^2+z^2}+\frac{y^2}{l^2+z^2}\right)+...\right)+ \right.$$
$$\left.(y+l)\left(1-\left(\frac{2yl}{l^2+z^2}+\frac{y^2}{l^2+z^2}\right)+...\right)\right] \approx$$
$$\frac{\mu_0}{4\pi(l^2+z^2)} I \left[y-l+\frac{2y^2l}{l^2+z^2}-\frac{2yl^2}{l^2+z^2}-\frac{y^3}{l^2+z^2}+\frac{y^2l}{l^2+z^2}+ \right.$$
$$\left. y+l-\frac{2y^2l}{l^2+z^2}-\frac{2yl^2}{l^2+z^2}-\frac{y^3}{l^2+z^2}-\frac{y^2l}{l^2+z^2}\right] =$$
$$\frac{\mu_0}{4\pi(l^2+z^2)} I \left[2y-\frac{4yl^2}{l^2+z^2}-\frac{2y^3}{l^2+z^2}\right] \approx -\frac{\mu_0 I y}{2\pi(l^2+z_0^2)^2}\left[l^2-z_0^2\right] \tag{B.9}$$

So the expression for all three components of the total magnetic field in the Z-wire trap is:

$$\begin{cases} B_x = B_x^c + B_x^e, \\ B_y = B_y^c + B_y^e, \\ B_z = B_z^c + B_z^e \end{cases} <=> \begin{cases} B_x = G(z_0 - z), \\ B_y = -G_{out} z_0 \left[1 + \frac{y^2(3l^2-z_0^2)}{(l^2+z_0^2)^2}\right], \\ B_z = Gx - G_{out} y \frac{l^2-z_0^2}{l^2+z_0^2} \end{cases} \tag{B.10}$$
$$G_{out} = \frac{\mu_0 I}{2\pi(l^2+z_0^2)}$$

As follows from Eq. B.10 the magnetic field at the trap centre is approximately equal to $G_{out}z_0$. In order to be able to control this value we add an external uniform magnetic field B_{ySmall}, so that the lowest value of the magnitude of the magnetic field becomes $B_0 = G_{out}z_0 + B_{ySmall}$. From Eq. B.7 the magnitude of the total magnetic field can be written as a function of coordinates x, y and z.

$$|B| \approx |B_y| + \frac{1}{2|B_y|}\left(B_x^2 + B_z^2\right) \approx$$
$$B_0 + G_{out} z_0 \frac{3l^2-z_0^2}{(l^2+z_0^2)^2} y^2 + \frac{1}{2B_0}\left(G^2(z-z_0)^2 + (Gx - G_{out}\frac{l^2-z_0^2}{l^2+z_0^2}y)^2\right) =$$
$$B_0 + \frac{1}{2B_0}G^2(z-z_0)^2 +$$
$$\left[\frac{1}{2B_0}G^2x^2 - \frac{2G}{2B_0}G_{out}\frac{l^2-z_0^2}{l^2+z_0^2}xy + \left(G_{out}z_0\frac{3l^2-z_0^2}{(l^2+z_0^2)^2} + \frac{G_{out}^2}{2B_0}\frac{(l^2-z_0^2)^2}{(l^2+z_0^2)^2}\right)y^2\right] \tag{B.11}$$

For a fixed $|B|$ Eq. B.11 is an ellipsoid with the axes of symmetry x', y' and z where x' and y' are "old" axes x and y twisted at some angle α in the x-y plane. In the new

coordinates it can be written $x = x'cos\alpha$ - $y'sin\alpha$ and $y = x'sin\alpha + y'cos\alpha$, from which:

$$
\begin{aligned}
|B| \approx B_0 + \frac{G^2}{2B_0}(z-z_0)^2 + \frac{G^2}{2B_0}\Big(x'^2cos^2\alpha - 2x'y'cos\alpha sin\alpha + y'^2sin^2\alpha\Big) - \\
\frac{G}{B_0}G_{out}\frac{l^2-z_0^2}{l^2+z_0^2}\Big(x'^2cos\alpha sin\alpha - x'y'sin^2\alpha + x'y'cos^2\alpha - y'^2sin\alpha cos\alpha\Big) + \\
\left(G_{out}z_0\frac{3l^2-z_0^2}{(l^2+z_0^2)^2} + \frac{G_{out}^2}{2B_0}\frac{(l^2-z_0^2)^2}{(l^2+z_0^2)^2}\right)\Big(x'^2sin^2\alpha + 2x'y'sin\alpha cos\alpha + y'^2cos^2\alpha\Big) = \\
B_0 + \frac{G^2}{2B_0}(z-z_0)^2 + \Bigg[\frac{G^2}{2B_0}cos^2\alpha - \\
\frac{G}{B_0}G_{out}\frac{l^2-z_0^2}{l^2+z_0^2}cos\alpha sin\alpha + \left(G_{out}z_0\frac{3l^2-z_0^2}{(l^2+z_0^2)^2} + \frac{G_{out}^2}{2B_0}\frac{(l^2-z_0^2)^2}{(l^2+z_0^2)^2}\right)sin^2\alpha\Bigg]x'2 + \\
\Bigg[-\frac{2G^2}{2B_0}cos\alpha sin\alpha + \frac{G}{B_0}G_{out}\frac{l^2-z_0^2}{l^2+z_0^2}sin^2\alpha - \frac{G}{B_0}G_{out}\frac{l^2-z_0^2}{l^2+z_0^2}cos^2\alpha + \\
\left(G_{out}z_0\frac{3l^2-z_0^2}{(l^2+z_0^2)^2} + \frac{G_{out}^2}{2B_0}\frac{(l^2-z_0^2)^2}{(l^2+z_0^2)^2}\right)2cos\alpha sin\alpha\Bigg]x'y' + \Bigg[\frac{G^2}{2B_0}sin^2\alpha + \\
\frac{G}{B_0}G_{out}\frac{l^2-z_0^2}{l^2+z_0^2}cos\alpha sin\alpha + \left(G_{out}z_0\frac{3l^2-z_0^2}{(l^2+z_0^2)^2} + \frac{G_{out}^2}{2B_0}\frac{(l^2-z_0^2)^2}{(l^2+z_0^2)^2}\right)cos^2\alpha\Bigg]y'2
\end{aligned}
\tag{B.12}
$$

At the right angle α the cross-product term with $x'y'$ vanishes, resulting in:

$$
\begin{aligned}
&\frac{G^2}{2B_0}sin2\alpha + \frac{G}{B_0}G_{out}\frac{l^2-z_0^2}{l^2+z_0^2}cos2\alpha = \left(G_{out}z_0\frac{3l^2-z_0^2}{(l^2+z_0^2)^2} + \frac{G_{out}^2}{2B_0}\frac{(l^2-z_0^2)^2}{(l^2+z_0^2)^2}\right)sin2\alpha \\
&<=>\ tan2\alpha = \frac{\frac{G}{B_0}G_{out}\frac{l^2-z_0^2}{l^2+z_0^2}}{G_{out}z_0\frac{3l^2-z_0^2}{(l^2+z_0^2)^2} + \frac{G_{out}^2}{2B_0}\frac{(l^2-z_0^2)^2}{(l^2+z_0^2)^2} - \frac{G^2}{2B_0}} \approx -\frac{2G_{out}}{G}\frac{l^2-z_0^2}{l^2+z_0^2}
\end{aligned}
\tag{B.13}
$$

In typical experimental conditions with $B_0 = 3$ G a good estimate for the gradient of the magnetic field G is 190 G/cm, $z_0 \sim 0.12$ cm, $2l = 0.6353$ cm. From Eqs. B.5 and B.10 it follows that $\frac{G_{out}}{G} = \frac{z_0^2}{l^2+z_0^2} \approx \frac{1}{8}$. For these values Eq. B.13 gives $\alpha = -5.4°$ from the formula for precise value and $-5.3°$ from the approximate one. For such small angles $\alpha \approx sin\alpha \approx tan\alpha \approx -\frac{G_{out}}{G}\frac{l^2-z_0^2}{l^2+z_0^2}$ from Eq. B.13. Now Eq. B.12 can be rewritten with $cos\alpha$

$= 1$:

$$|B| \approx B_0 + \frac{G^2}{2B_0}(z-z_0)^2 + \left[\frac{G^2}{2B_0} + \frac{G_{out}^2}{B_0}\frac{(l^2-z_0^2)^2}{(l^2+z_0^2)^2} + \left(G_{out}z_0\frac{3l^2-z_0^2}{(l^2+z_0^2)^2} + \frac{G_{out}^2}{2B_0}\frac{(l^2-z_0^2)^2}{(l^2+z_0^2)^2}\right)\frac{G_{out}^2}{G^2}\frac{(l^2-z_0^2)^2}{(l^2+z_0^2)^2}\right]x'^2 + \left[\frac{G_{out}^2}{2B_0}\frac{(l^2-z_0^2)^2}{(l^2+z_0^2)^2} - \frac{G_{out}^2}{B_0}\frac{(l^2-z_0^2)^2}{(l^2+z_0^2)^2} + G_{out}z_0\frac{3l^2-z_0^2}{(l^2+z_0^2)^2} + \frac{G_{out}^2}{2B_0}\frac{(l^2-z_0^2)^2}{(l^2+z_0^2)^2}\right]y'^2 = \quad \text{(B.14)}$$
$$B_0 + \frac{G^2}{2B_0}(z-z_0)^2 + \left[\frac{G^2}{2B_0} + \frac{G_{out}^2}{B_0}\frac{(l^2-z_0^2)^2}{(l^2+z_0^2)^2} + \left(G_{out}z_0\frac{3l^2-z_0^2}{(l^2+z_0^2)^2} + \frac{G_{out}^2}{2B_0}\frac{(l^2-z_0^2)^2}{(l^2+z_0^2)^2}\right)\frac{G_{out}^2}{G^2}\frac{(l^2-z_0^2)^2}{(l^2+z_0^2)^2}\right]x'^2 + G_{out}z_0\frac{3l^2-z_0^2}{(l^2+z_0^2)^2}y'^2$$

B.0.2 Analytical formulae for the frequencies of the Z-wire magnetic trap

In the case of the linear Zeeman effect the energy of an atom in the magnetic field is

$$E^M = \mu_B\ g_F\ m_F\ |B| \quad \text{(B.15)}$$

where $\mu_B = 9.27400968(20)\cdot 10^{-24}\ J\cdot T^{-1}$ is the Bohr magneton, g_F is the hyperfine Lande-factor and m_F is the quantum number of the projection of the total angular momentum.

$$g_F \approx g_J\frac{F(F+1) - I(I+1) + J(J+1)}{2F(F+1)} \quad \text{(B.16)}$$

We work with ^{87}Rb atoms in the ground state $5^2S_{\frac{1}{2}}$, so $g_J = 2.002\ 331\ 13(20)$ [79]. For both internal states F = 1, $m_F = -1$ and F = 2, $m_F = +1$ the multiplication $g_F \cdot m_F \approx \frac{1}{2}$. Substituting $|B|$ from Eq. B.14 into Eq. B.15 allows to calculate the trap frequencies from Eq. B.1:

$$\omega_{x'} = \sqrt{\frac{\mu_B}{m}\left[\frac{G^2}{2B_0} + \left(\frac{G^2}{B_0} + G_{out}z_0\frac{3l^2-z_0^2}{(l^2+z_0^2)^2} + \frac{G_{out}^2}{2B_0}\frac{(l^2-z_0^2)^2}{(l^2+z_0^2)^2}\right)\frac{G_{out}^2}{G^2}\frac{(l^2-z_0^2)^2}{(l^2+z_0^2)^2}\right]}$$
$$\omega_{y'} = \sqrt{\frac{\mu_B G_{out}z_0}{m}\frac{(3l^2-z_0^2)}{(l^2+z_0^2)^2}} \quad \text{(B.17)}$$
$$\omega_z = G\sqrt{\frac{\mu_B}{2mB_0}}$$

In Eq. B.17 the second and third terms in square brackets for $\omega_{x'}$ make a very little contribution to the sum so $\omega_{x'} \approx \omega_z$.

B.0.3 Dipole oscillations of the atom cloud in the trap

During dipole oscillations the position of the cloud centre is a function of time. Variations in the cloud position at the moment of switching off the trapping fields cannot be registered by our imaging system (pixel size is 4.5 μm, Section 2.2.4); however the different initial speeds of the clouds result in measurable variations of the cloud centre coordinates during imaging. The following refers to the case of vertical dipole oscillations with the largest deviation from equilibrium denoted as $\pm z_0$. The potential energy of the displaced cloud converts to its initial speed $\pm v_0$ at the position z=0:

$$\begin{gathered}\frac{m\omega^2 z_0^2}{2} = \frac{m v_0^2}{2} \;<=>\; |v_0| = w z_0, \\ \begin{cases} z_1 = \frac{g}{2}t_0^2 - v_0 t_0 + z_0, \\ z_2 = \frac{g}{2}t_0^2 + v_0 t_0 + z_0 \end{cases} \qquad => \Delta z = z_2 - z_1 = 2 v_0 t_0 \end{gathered} \tag{B.18}$$

Thus after a time t_0 of free fall the initial difference in speed results in $2|v_0|t_0$ difference in the z-coordinate. Sometimes during free fall an additional kick is also applied (to separate the components with different magnetic moments). In this case the total time is the same $t_0 = t_0^{(1)} + t_0^{(2)}$, where $t_0^{(1)}$ is the time before the kick and $t_0^{(2)}$ is the time after the kick and before the imaging. A short kick does not change the position of the cloud, resulting in the speed change Δv_{kick}. This leads to a difference of the z-positions for two clouds with different initial speeds:

$$\begin{gathered} \begin{cases} z_1^{(1)} = \frac{g}{2}(t_0^{(1)})^2 - v_0 t_0^{(1)} + z_0, \\ z_2^{(1)} = \frac{g}{2}(t_0^{(1)})^2 + v_0 t_0^{(1)} + z_0 \end{cases} \\ \begin{cases} z_1^{(2)} = \frac{g}{2}(t_0^{(2)})^2 + (\Delta v_{kick} - v_0) t_0^{(2)} + z_1^{(1)}, \\ z_2^{(2)} = \frac{g}{2}(t_0^{(2)})^2 + (\Delta v_{kick} + v_0) t_0^{(2)} + z_2^{(1)} \end{cases} \\ \Delta z = z_2^{(2)} - z_1^{(2)} = 2 v_0 (t_0^{(1)} + t_0^{(2)}) = 2 v_0 t_0 \end{gathered} \tag{B.19}$$

The final result is the same as without a kick, Eq. B.18.

In Eq. B.19 it has been neglected the fact that Δv_{kick} depends on the distance from the chip, so that it should be slightly different for the two cases with different initial speeds. However, this is a reasonable approximation as the total distance from the chip is

~ 1.2 mm, whereas Δz before the kick is of the order of 10 μm so the correction is only a fraction of percent.

B.0.4 Gravity sag in a harmonic magnetic trap

The following considerations describe calculation steps in Eq. 2.9 of Section 2.4. In the magnetic trap gravity shifts the position of the cloud centre:

$$\begin{aligned}
E = E^M + E^G = \mu_B g_F m_F |B| - mgz \approx \\
E_0 + \frac{m\omega_x^2 x^2}{2} + \frac{m\omega_y^2 y^2}{2} + \frac{m\omega_z^2 (z-z_0)^2}{2} - mgz = \\
E_0 + \frac{m\omega_x^2 x^2}{2} + \frac{m\omega_y^2 y^2}{2} + \frac{m}{2}\left(\omega_z^2 (z-z_0)^2 - 2g(z-z_0)\right) - mgz_0 = \\
E_0 + \frac{m\omega_x^2 x^2}{2} + \frac{m\omega_y^2 y^2}{2} + \frac{m}{2}\left(\omega_z^2 (z-z_0)^2 - 2g(z-z_0) + \frac{g^2}{\omega_z^2}\right) - \frac{mg^2}{2\omega_z^2} - mgz_0 = \\
\left[E_0 - \frac{m^2 g^2}{2\omega_z^2} - mgz_0\right] + \frac{m\omega_x^2 x^2}{2} + \frac{m\omega_y^2 y^2}{2} + \frac{m}{2}\omega_z^2\left(z - \left[z_0 + \frac{g}{\omega_z^2}\right]\right)^2
\end{aligned} \tag{B.20}$$

APPENDIX C

Impedance matching and rf transformer operation

C.0.5 Voltage and current amplitudes with a complex load

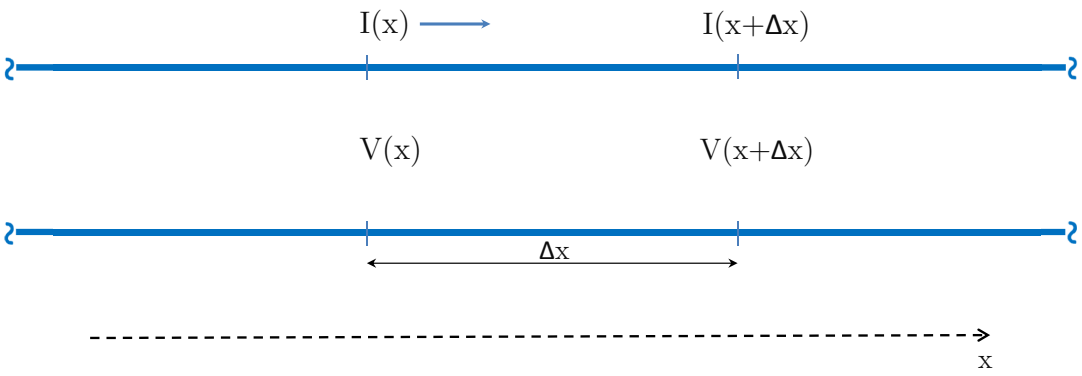

Figure C.1: Lossless transmission line formed by two parallel conductors.

Let us consider the rf field signal propagation in a transmission line formed by two parallel conductors (Fig. C.1). In the case of a short transmission line (any BNC cable in the experiment is just a few meters long) ohmic losses can be neglected. Then for the line segment Δx it can be written from Kirchhoff's law (or simply using the definition of the

inductance for the upper line):

$$V(x) - V(x + \Delta x) = L\Delta x \frac{\partial I}{\partial t} <=> -\frac{\Delta V}{\Delta x} = L\frac{\partial I}{\partial t} \tag{C.1}$$

where the inductance per unit length is labelled as L and C is the capacitance per unit length. At the same time the charge collected inside the upper line can be written:

$$Q = C\Delta x(V(x) - V(x + \Delta x)) = (I(x + \Delta x) - I(x))dt <=> C\frac{\Delta V}{dt} = -\frac{\Delta I}{\Delta x} \tag{C.2}$$

from which in the limit of $\Delta x \to 0$ one gets:

$$\begin{aligned} -\frac{\partial V}{\partial x} &= L\frac{\partial I}{\partial t}, \\ -\frac{\partial I}{\partial x} &= C\frac{\partial V}{\partial t} \end{aligned} \tag{C.3}$$

The functions $V(x,t)$ and $I(x,t)$ in Eq. C.3 can be separated by a second partial derivative and the result is called the Telegrapher's equations [109], [110]:

$$\begin{aligned} \frac{\partial^2 V}{\partial x^2} &= LC\frac{\partial^2 V}{\partial t^2}, \\ \frac{\partial^2 I}{\partial x^2} &= LC\frac{\partial^2 I}{\partial t^2} \end{aligned} \tag{C.4}$$

Any function of $(x \mp \frac{1}{\sqrt{LC}}t)$ is the solution for these equations but the most well-known results are $V = V_{\pm}e^{i(\omega t \mp kx)}$ and $I = I_{\pm}e^{i(\omega t \mp kx)}$ where $\frac{\omega}{k} = \frac{1}{\sqrt{LC}}$. The solution $V = V_{+}e^{i(\omega t - kx)}$ is the wave moving in the positive direction of the x-axis, i.e., towards the load. The second solution $V = V_{-}e^{i(\omega t + kx)}$ is the reflected wave moving into the opposite direction and $v = \frac{\omega}{k}$ is the phase velocity of both waves. $V_{\pm}$ are in general complex functions, so V_{-} includes also a possible phase shift due to reflection. Inserting these solutions into either of part of Eq. C.3 one can get:

$$V_{\pm} = I_{\pm}L(\pm\frac{\omega}{k}) = \pm I_{\pm}\sqrt{\frac{L}{C}} \tag{C.5}$$

The parameter $Z = \sqrt{\frac{L}{C}}$ is called the characteristic impedance of the transmission line and Eq. C.5 shows its physical meaning as a coefficient of proportionality between $V_{\pm}$ and $I_{\pm}$. In the experiment the chip wire is connected with an output 50 Ω impedance of the rf amplifier by using a BNC cable with a characteristic impedance of 50 Ω.

Whenever an incident wave in the transmission line with a characteristic impedance Z_1 comes to a junction with another impedance Z_2 (it can be anther transmission line or

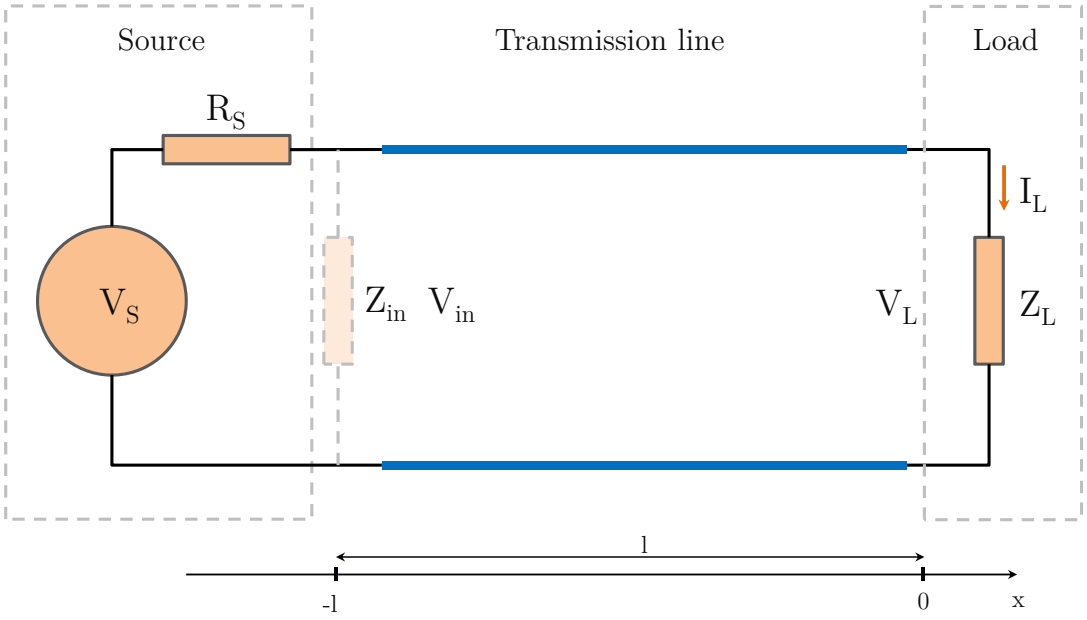

Figure C.2: Matching of an rf field source with a transmission line terminated by a complex load.

a load) it splits into reflected and transmitted waves. Labelling the voltage amplitudes of the incident and reflected waves as V_{1+} and V_{1-} and the amplitude of the transmitted wave as V_{2+}, at the junction point it can be written:

$$\begin{aligned} V_{2+} &= V_{1+} + V_{1-}, \\ I_{2+} &= I_{1+} + I_{1-} \end{aligned} \tag{C.6}$$

Replacing the voltages by currents (Eq. C.5), one gets the solution:

$$\begin{cases} I_{2+}Z_2 = I_{1+}Z_1 - I_{1-}Z_1, \\ I_{2+} = I_{1+} + I_{1-} \end{cases} \Rightarrow$$

$$\begin{cases} I_{1-} = \frac{Z_1 - Z_2}{Z_1 + Z_2} I_{1+}, \\ I_{2+} = \frac{2Z_1}{Z_1 + Z_2} I_{1+} \end{cases} \Leftrightarrow \begin{cases} V_{1-} = \frac{Z_2 - Z_1}{Z_1 + Z_2} V_{1+}, \\ V_{2+} = \frac{2Z_2}{Z_1 + Z_2} V_{1+} \end{cases} \tag{C.7}$$

Equation C.7 shows that reflection of the wave is always present when $Z_1 \neq Z_2$. The coefficient $\gamma = \frac{Z_2 - Z_1}{Z_1 + Z_2}$ is called a voltage reflection coefficient and the negative sign in it means that reflected wave has a π phase shift.

Let us deduce the input impedance of the circuit, shown in Fig. C.2, constructed by a lossless transmission line with length L, characteristic impedance Z_0 and complex load Z_L at the end of the line [111], [112]. At $x = 0$ it can be written:

$$\begin{gathered} Z_L = \frac{V_L}{I_L} = \frac{V_+ e^{i(\omega t - k\cdot 0)} + V_- e^{i(\omega t + k\cdot 0)}}{I_+ e^{i(\omega t - k\cdot 0)} + I_- e^{i(\omega t + k\cdot 0)}} => \\ Z_L = \frac{V_+ + V_-}{V_+ - V_-} Z_0 = \frac{1+\gamma}{1-\gamma} Z_0 \end{gathered} \tag{C.8}$$

Then at any point x one can write:

$$\begin{cases} V(x) = V_+ e^{i(\omega t - kx)} + V_- e^{i(\omega t + kx)}, \\ I(x) = I_+ e^{i(\omega t - kx)} + I_- e^{i(\omega t + kx)} \end{cases} <=>$$

$$\begin{cases} V(x) = V_+ e^{i(\omega t - kx)} + V_- e^{i(\omega t + kx)}, \\ I(x) = \frac{V_+}{Z_0} e^{i(\omega t - kx)} - \frac{V_-}{Z_0} e^{i(\omega t + kx)} \end{cases} <=> \tag{C.9}$$

$$\begin{cases} V(x) = V_+ e^{i\omega t}(e^{-ikx} + \gamma e^{ikx}), \\ I(x) = \frac{V_+}{Z_0} e^{i\omega t}(e^{-ikx} - \gamma e^{ikx}) \end{cases}$$

which gives the solution for $Z(x)$ and for $x = -l$ in particular:

$$\begin{gathered} Z(x) = Z_0 \left[\frac{1+\gamma e^{2ikx}}{1-\gamma e^{2ikx}}\right], \\ Z_{in}(-l) = \frac{V_{in}(-l)}{I_{in}(-l)} = Z_0 \left[\frac{1+\gamma e^{-2ikl}}{1-\gamma e^{-2ikl}}\right] \end{gathered} \tag{C.10}$$

As a consequence when the impedance is matched, i.e., $Z_L = Z_0 \Rightarrow \gamma = 0$ and $Z_{in} = Z_L$, the usual Ohm's law can be used to calculate the properties of the circuit just like there is no transmission line at all. Whereas in the mismatched case the amplitudes of the voltage and the current are not constant along the transmission line. Their values at a distance l from the load can be obtained from Eq. C.9 with $x = -l$:

$$\begin{cases} V(-l) = V_+ e^{i\omega t}(e^{ikl} + \gamma e^{-ikl}), \\ I(-l) = \frac{V_+}{Z_0} e^{i\omega t}(e^{ikl} - \gamma e^{-ikl}) \end{cases} \tag{C.11}$$

The reflection coefficient γ can be rewritten as $|\gamma| e^{i\phi}$ (after all, γ is just a complex

number), then the module of the amplitude at $x = -l$ is equal to:

$$\begin{cases} |V(-l)| = |V_+| \left[(e^{ikl} + |\gamma|e^{i\phi}e^{-ikl})(e^{-ikl} + |\gamma|e^{-i\phi}e^{ikl})\right]^{\frac{1}{2}}, \\ |I(-l)| = \frac{|V_+|}{Z_0} \left[(e^{ikl} - |\gamma|e^{i\phi}e^{-ikl})(e^{-ikl} - |\gamma|e^{-i\phi}e^{ikl})\right]^{\frac{1}{2}} \end{cases} =>$$
$$\begin{cases} |V(-l)| = |V_+| \left[(1 + 2|\gamma|cos(\phi - 2kl) + |\gamma|^2\right]^{\frac{1}{2}}, \\ |I(-l)| = \frac{|V_+|}{Z_0} \left[(1 - 2|\gamma|cos(\phi - 2kl) + |\gamma|^2\right]^{\frac{1}{2}} \end{cases} \tag{C.12}$$

Thus, the amplitude of the voltage and the current are changing periodically along the transmission line. Also from Eq. C.12 the maximum of the voltage amplitude corresponds to the minimum of the current amplitude. It can be easily explained by the fact that the impedance $Z(x)$ is also varying along the transmission line.

If for the circuit shown in Fig. C.2 the parameters $V_S = |V_S|e^{i\omega t}$, $R_S = Z_0$, Z_L, l are known, then the signal generator sees the transmission line with a load impedance as an equivalent Z_{in}:

$$I_S = \frac{|V_S|}{Z_{in} + R_S}e^{i\omega t} = \frac{|V_S|}{Z_{in} + Z_0}e^{i\omega t}, \qquad V_{in} = \frac{|V_S|Z_{in}}{Z_{in} + Z_0}e^{i\omega t} \tag{C.13}$$

Inserting the expression for Z_{in} from Eq. C.10 allows one to get:

$$V_{in} = \frac{|V_S|Z_0\left[\frac{1+\gamma e^{-2ikl}}{1-\gamma e^{-2ikl}}\right]}{Z_0\left[\frac{1+\gamma e^{-2ikl}}{1-\gamma e^{-2ikl}}\right] + Z_0}e^{i\omega t} = \frac{|V_S|Z_0\left(1+\gamma e^{-2ikl}\right)}{Z_0\left(1+\gamma e^{-2ikl}+1-\gamma e^{-2ikl}\right)}e^{i\omega t} = \frac{|V_S|}{2}\left(1+\gamma e^{-2ikl}\right)e^{i\omega t} \tag{C.14}$$

On the other hand the expression for V_{in} is known from Eq. C.11:

$$\begin{cases} V_{in} = \frac{|V_S|}{2}\left(1+\gamma e^{-2ikl}\right)e^{i\omega t}, \\ V_{in} = V_+e^{ikl}(1+\gamma e^{-2ikl})e^{i\omega t} \end{cases} =>$$
$$V_+ = \frac{|V_S|}{2}e^{-ikl} \tag{C.15}$$

Thus the voltage and the current of the load ($x = 0$) can be written (using Eq. C.9):

$$\begin{cases} V_L = \frac{|V_S|}{2}e^{-ikl}e^{i\omega t}(1+\gamma), \\ I_L = \frac{|V_S|}{2Z_0}e^{-ikl}e^{i\omega t}(1-\gamma) \end{cases} \tag{C.16}$$

Let us consider the case of a pure reactive impedance, i.e. $Z_L = iX$ where X is a real variable. Then for the reflection coefficient γ it follows:

$$\begin{gathered}\gamma = \frac{iX - Z_0}{iX + Z_0}, \\ |\gamma|^2 = \frac{(iX - Z_0)(-iX - Z_0)}{(iX + Z_0)(-iX + Z_0)} = \frac{(X^2 + Z_0^2)}{(X^2 + Z_0^2)} = 1\end{gathered} \tag{C.17}$$

As a result the module of γ is 1, or $\gamma = e^{i\phi_0}$:

$$\begin{cases} \gamma = \frac{iX - Z_0}{iX + Z_0} = \frac{X^2 - Z_0^2}{X^2 + Z_0^2} + \frac{2XZ_0}{X^2 + Z_0^2} i, \\ \gamma = cos\phi_0 + isin\phi_0 \end{cases} \quad => \tag{C.18}$$

$$cos\phi_0 = \frac{X^2 - Z_0^2}{X^2 + Z_0^2}$$

Then the amplitude of the voltage and current at the load can be expressed as (from Eq. 2.17):

$$\begin{cases} |V_L| = \frac{|V_S|}{2}(2 + 2cos\phi_0)^{\frac{1}{2}} = \frac{|V_S|}{2}\left[2 \cdot \frac{X^2 + Z_0^2 + X^2 - Z_0^2}{X^2 + Z_0^2}\right]^{\frac{1}{2}}, \\ |I_L| = \frac{|V_S|}{2Z_0}(2 - 2cos\phi_0)^{\frac{1}{2}} = \frac{|V_S|}{2Z_0}\left[2 \cdot \frac{X^2 + Z_0^2 - X^2 + Z_0^2}{X^2 + Z_0^2}\right]^{\frac{1}{2}} \end{cases} \quad <=>$$

$$\begin{cases} |V_L| = |V_S|\frac{|X|}{(X^2 + Z_0^2)^{\frac{1}{2}}}, \\ |I_L| = \frac{|V_S|}{Z_0}\frac{Z_0}{(X^2 + Z_0^2)^{\frac{1}{2}}} = \frac{|V_S|}{(X^2 + Z_0^2)^{\frac{1}{2}}} \end{cases} \tag{C.19}$$

As described in Section 2.8 two capacitors are used in our rf circuit to decouple the AC-circuit from the DC current (Fig. 2.16). To maximize the current amplitude through the load the impedance X should be small and for this reason a pair of 1 μF capacitors was chosen. For a series connection with a capacitor on each side of the U-wire, the total capacitance becomes 0.5 μF and for a frequency of 25 MHz the capacitive part of the impedance $X_C = -\frac{1}{\omega C}$ = -0.08 Ω << Z_0 = 50 Ω. From Eq. C.19 it follows that for a small reactive impedance of the load the amplitude of the current is $|I_L| = \frac{|V_S|}{Z_0}$; however, in the case of the considerable inductance of the chip wires the magnitude of the current is reduced.

C.0.6 Measurement of the U-wire impedance

For the measurement of the U-wire impedance an oscilloscope is connected parallel to the chip circuit (which consists of the U-wire and two 1 μF capacitors on each side of the

wire). The input impedance of the scope channel is set to $Z_0 = 50\ \Omega$ to be matched with the connecting BNC cable, which changes the load impedance of the total load from iX to Z_L:

$$\begin{gathered} Z_L = \frac{Z_0 iX}{Z_0 + iX}, \\ \gamma = \frac{Z_L - Z_0}{Z_L + Z_0} = \frac{\frac{Z_0 iX}{Z_0 + iX} - Z_0}{\frac{Z_0 iX}{Z_0 + iX} + Z_0} = \\ -\frac{Z_0^2}{2iXZ_0 + Z_0^2} = -\frac{Z_0}{2iX + Z_0}, => \\ |\gamma| = \frac{Z_0}{\sqrt{Z_0^2 + 4X^2}}, \\ \gamma = -\frac{Z_0}{Z_0^2 + 4X^2}(Z_0 - 2iX) = -\frac{Z_0^2}{Z_0^2 + 4X^2} + \frac{2iXZ_0}{Z_0^2 + 4X^2}, \\ cos\phi = \frac{Re(\gamma)}{|\gamma|} = -\frac{Z_0}{\sqrt{Z_0^2 + 4X^2}} \end{gathered} \tag{C.20}$$

From Eq. 2.17 the amplitudes of the voltage and current at the oscilloscope can be written:

$$\begin{cases} |V_L| = \frac{|V_S|}{2}\sqrt{1 - \frac{2Z_0^2}{Z_0^2+4X^2} + \frac{Z_0^2}{Z_0^2+4X^2}} = \frac{|V_S|}{2}\sqrt{1 - \frac{Z_0^2}{Z_0^2+4X^2}}, \\ |I_L| = \frac{|V_S|}{2Z_0}\sqrt{1 + \frac{2Z_0^2}{Z_0^2+4X^2} + \frac{Z_0^2}{Z_0^2+4X^2}} = \frac{|V_S|}{2Z_0}\sqrt{1 + \frac{3Z_0^2}{Z_0^2+4X^2}} \end{cases} \tag{C.21}$$

C.0.7 Rf transformer operation

This section considers the operation of an rf transformer for the general case with a complex load (Fig. 2.18). The inductance of the primary windings of the transformer is labelled as L_1, the inductance of the secondary windings as L_2 and their mutual inductance as M. These quantities can be calculated from the known number of turns in the windings [111]. If L_0 is the inductance of a single turn in the winding then the total magnetic flux created by N_1 turns is $N_1 L_0 I_1$. In the approximation that the total magnetic flux from each turn goes through all the other turns of both coils one can write that the total flux through the second windings is $N_2 N_1 L_0 I_1$ but it is also equal to $M I_1$ (by definition), so $M = N_2 N_1 L_0$. Similarly, for self-inductances of the windings $L_1 = N_1^2 L_0$, $L_2 = N_2^2 L_0$, from which it can be written for an ideal transformer:

$$M^2 = L_1 L_2 \tag{C.22}$$

According to Eq. C.9 and Kirchhoff's law at $x = 0$:

$$\begin{cases} V_1 = V_+ e^{i\omega t} + V_- e^{i\omega t}, \\ V_1 = L_1 \frac{dI_1}{dt} + M \frac{dI_2}{dt} \end{cases} \quad \begin{cases} V_2 = I_2 Z_L, \\ V_2 = -M \frac{dI_1}{dt} - L_2 \frac{dI_2}{dt} \end{cases} \tag{C.23}$$

From Lenz's law the sign of the induced current through the secondary winding is opposite [111] and a harmonic oscillation of the current $I_2 = I_2' e^{i\omega t}$ is assumed (as before, I_2' is a complex number which includes a phase difference between the currents in the primary and the secondary windings of the transformer). Thus Eq. C.23 can be rewritten as:

$$\begin{cases} V_+ e^{i\omega t} + V_- e^{i\omega t} = L_1 \frac{dI_1}{dt} + M \frac{dI_2}{dt}, \\ I_2 Z_L = -M \frac{dI_1}{dt} - L_2 \frac{dI_2}{dt} \end{cases} <=>$$

$$\begin{cases} Z_0 e^{i\omega t}(I_+ - I_-) = L_1 \frac{d(I_+ + I_-)}{dt} + M \frac{dI_2}{dt}, \\ I_2 Z_L = -M \frac{d(I_+ + I_-)}{dt} - L_2 \frac{dI_2}{dt} \end{cases} <=>$$

$$\begin{cases} Z_0 e^{i\omega t}(I_+ - I_-) = L_1 i\omega e^{i\omega t}(I_+ + I_-) + i\omega M I_2' e^{i\omega t}, \\ I_2' e^{i\omega t} Z_L = -i\omega M e^{i\omega t}(I_+ + I_-) - i\omega L_2 I_2' e^{i\omega t} \end{cases} <=>$$

$$\begin{cases} (Z_0 + L_1 i\omega) I_- + i\omega M I_2' = (Z_0 - L_1 i\omega) I_+, \\ i\omega M I_- + (i\omega L_2 + Z_L) I_2' = (-i\omega M) I_+ \end{cases} \tag{C.24}$$

This system of equations can be solved to express I_- and I_2' through I_+:

$$\Delta = (Z_0 + L_1 i\omega)(i\omega L_2 + Z_L) - (i\omega M) i\omega M = \\ Z_0 i\omega L_2 - \omega^2 L_1 L_2 + Z_L Z_0 + Z_L L_1 i\omega + \omega^2 M^2 = Z_L Z_0 + i\omega (Z_L L_1 + Z_0 L_2) \tag{C.25}$$

where Eq. C.22 has been used for the last simplification in Eq. C.25. The solution of Eq. C.24 in matrix form is:

$$\begin{pmatrix} I_- \\ I_2' \end{pmatrix} = \frac{1}{\Delta} \begin{pmatrix} (i\omega L_2 + Z_L) & -i\omega M \\ -i\omega M & (Z_0 + L_1 i\omega) \end{pmatrix} \begin{pmatrix} (Z_0 - L_1 i\omega) I_+ \\ (-i) I_+ \end{pmatrix} \tag{C.26}$$

or for the amplitude I_2' in particular:

$$I_2' = \frac{I_+}{\Delta} \left(-i\omega M Z_0 - \omega^2 L_1 M - i\omega M Z_0 + \omega^2 L_1 M \right) = -\frac{2i\omega M Z_0}{\Delta} I_+ \tag{C.27}$$

It is easy to see that for high frequencies ω in the impedance matched case ($\frac{Z_L}{Z_0} = \frac{N_2^2}{N_1^2} = \frac{L_2}{L_1}$): $\Delta \approx i\omega(Z_L L_1 + Z_0 L_2) = 2i\omega L_0 N_2^2 Z_0$, from which $I_2' \approx I_+ \left(-\frac{2i\omega N_1 N_2 L_0 Z_0}{2i\omega L_0 N_2^2 Z_0}\right) = -I_+ \frac{N_1}{N_2}$ in full accordance with Eq. C.22.

Let us investigate which value of Z_L (in the general case it is a complex value) maximizes the amplitude of the current $|I_2'|$ in Eq. C.27 . As Z_L is present only in the denominator then the task is equivalent to minimization of $|\Delta|$. The impedance Z_L can be expressed, consisting of two parts $x + iy$, from which:

$$\begin{gathered}\Delta(Z_L) = Z_L Z_0 + i\omega(Z_L L_1 + Z_0 L_2) = (xZ_0 - yL_1\omega) + i(yZ_0 + xL_1\omega + Z_0 L_2\omega), \\ \Delta^2(x,y) = \Delta\Delta^* = x^2 Z_0^2 - 2xyZ_0 L_1\omega + y^2 L_1^2\omega^2 + \\ y^2 Z_0^2 + x^2 L_1^2\omega^2 + Z_0^2 L_2^2\omega^2 + 2xyZ_0 L_1\omega + 2xZ_0 L_1 L_2\omega^2 + 2yZ_0^2 L_2\omega = \\ (x^2+y^2)(Z_0^2 + L_1^2\omega^2) + 2xZ_0 L_1 L_2\omega^2 + 2yZ_0^2 L_2\omega + Z_0^2 L_2^2\omega^2\end{gathered} \tag{C.28}$$

where $x \geq 0$ and y are independent variables. As all coefficients in Eq. C.28 are positive then the minimum possible value of $x = 0$ minimizes the Δ which simplifies Eq. C.28 down to:

$$\Delta^2(y) = y^2(Z_0^2 + L_1^2\omega^2) + 2yZ_0^2 L_2\omega + Z_0^2 L_2^2\omega^2 \tag{C.29}$$

This is a parabolic dependence with a minimum at its vertex. To find the vertex coordinate one needs to solve the equation:

$$\begin{gathered}\left(\Delta^2(y)\right)' = 0 <=> 2y(Z_0^2 + L_1^2\omega^2) + 2Z_0^2 L_2\omega = 0, \\ y = -\frac{Z_0^2 L_2\omega}{Z_0^2 + L_1^2\omega^2}, => \\ \Delta_{min}^2 = \frac{Z_0^4 L_2^2\omega^2}{Z_0^2 + L_1^2\omega^2} - \frac{2Z_0^4 L_2^2\omega^2}{Z_0^2 + L_1^2\omega^2} + \frac{Z_0^4 L_2^2\omega^2 + Z_0^2 L_1^2 L_2^2\omega^4}{Z_0^2 + L_1^2\omega^2}\end{gathered} \tag{C.30}$$

Thus, $|I_2'|_{max}$ from Eq. C.27 can be found as:

$$\begin{gathered}|\Delta|_{min} = \sqrt{\Delta_{min}^2} = \frac{Z_0 L_1 L_2\omega^2}{\sqrt{Z_0^2 + L_1^2\omega^2}}, \\ |I_2'|_{max} = |I_+|\frac{2_0 N_1 N_2 Z_0}{Z_0 L_0^2 N_1^2 N_2^2\omega^2}\sqrt{Z_0^2 + L_0^2 N_1^4\omega^2} = \\ 2|I_+|\sqrt{\frac{Z_0^2}{L_0^2 N_1^2 N_2^2\omega^2} + \frac{N_1^2}{N_2^2}}\end{gathered} \tag{C.31}$$

It is interesting to note that if $Z_L = 0$ then:

$$I_2' = -\frac{2i_1 N_2 L_0 Z_0}{i_2^2 L_0 Z_0} I_+ = -\frac{2N_1}{N_2} I_+, => \\ |I_2'| = \frac{|V_S|}{Z_0}\frac{N_1}{N_2} \tag{C.32}$$

where in the last simplification Eq. C.15 was recalled.

Thus the rf transformer enhances the current amplitude by a factor of $\frac{N_1}{N_2}$ compared to Eq. 2.17 for the $Z_L = 0$ case without a transformer. However, in the rf transformer circuit $Z_L = 0$ does not correspond to the maximum current case as the highest current enhancement from Eq. C.31 is equal to $\sqrt{\frac{Z_0^2}{L_0^2 N_1^2 N_2^2 \omega^2} + \frac{N_1^2}{N_2^2}}$.

Our aim of rf transformer implementation is to match the load with the transmission line to minimize the reflected wave that causes instabilities during the experiment and at the same time to increase the current through the load compared with the matched case without an rf transformer. To achieve impedance matching an additional capacitor and a resistor in series with the chip-wire were implemented. For the matched circuit Z_L should minimize the amplitude of the reflected wave $|I_-|$ which from Eq. C.26 is equal to:

$$|I_-| = \left|\frac{Z_L R_0 + i\omega(R_0 L_2 - Z_L L_1)}{Z_L(R_0 + iL_1\omega) + iR_0 L_2 \omega}\right| |I_+| \approx \left|\frac{Z_L R_0 + i\omega(R_0 L_2 - Z_L L_1)}{i\omega(R_0 L_2 + Z_L L_1)}\right| |I_+| \tag{C.33}$$

where the last step can be explained as follows: from the specification for our rf transformer it is known that $L_0 = 2$ μH. Thus for frequencies of ~ 25 MHz $Z_{L_1} = L_1\omega \sim 7.5$ kΩ $>>$ $R_0 = 50$ Ω. Then the case $R_0 L_2 - Z_L L_1 = 0$ ($Z_L = \frac{L_2}{L_1} R_0$) transforms Eq. C.33 into:

$$|I_-| \approx \left|\frac{Z_L R_0}{2iZ_L L_1 \omega}\right| |I_+| = \left|\frac{R_0}{2iL_1\omega}\right| |I_+| = \frac{1}{300}|I_+| \approx 0 \tag{C.34}$$

i.e., $Z_L = \frac{L_2}{L_1} R_0$ is the solution for the matched case.

C.0.8 Tuning the rf generation circuit to a certain frequency range

As in the case for the measurement of the U-wire impedance, the 50 Ω channel of the oscilloscope is connected to the end of the BNC cable with the rf signal (parallel to the primary windings of the rf transformer (Fig. 2.19)). As before x=0 is chosen at the transformer position. For the current I_1 one can write:

$$I_+ e^{i\omega t} + I_- e^{i\omega t} = I_1 + I_3, => \\ I_1 = I_+ e^{i\omega t} + I_- e^{i\omega t} - I_3' e^{i\omega t} \tag{C.35}$$

with the voltage on the oscilloscope equal to:

$$V_3 = I_3 R_0 = I'_3 e^{i\omega t} R_0 \tag{C.36}$$

Substitution of I_1 from Eq. C.35 into Eq. C.23 gives:

$$\begin{cases} V_3 = V_+ e^{i\omega t} + V_- e^{i\omega t} = I_+ R_0 e^{i\omega t} - I_- R_0 e^{i\omega t}, \\ V_3 = L_1 \frac{dI_1}{dt} + M \frac{dI_2}{dt} = iL_1\omega \left(I_+ + I_- - I'_3\right) e^{i\omega t} + iM\omega I'_2 e^{i\omega t} \end{cases}$$
$$\begin{cases} V_2 = I_2 Z_L = I'_2 e^{i\omega t} Z_L, \\ V_2 = -M \frac{dI_1}{dt} - L_2 \frac{dI_2}{dt} = -i\omega M e^{i\omega t} \left(I_+ + I_- - I'_3\right) - i\omega L_2 I'_2 e^{i\omega t} \end{cases} \tag{C.37}$$

From Eq. C.36 and the first line of Eq. C.37 it follows:

$$I'_3 R_0 e^{i\omega t} = I'_+ R_0 e^{i\omega t} - I'_- R_0 e^{i\omega t} \iff I'_3 = I_+ - I_- \tag{C.38}$$

from which:

$$\begin{cases} I_+ R_0 e^{i\omega t} - I_- R_0 e^{i\omega t} = iL_1\omega \left(I_+ + I_- - I_+ + I_-\right) e^{i\omega t} + iM\omega I'_2 e^{i\omega t}, \\ I'_2 e^{i\omega t} Z_L = -i\omega M e^{i\omega t} \left(I_+ + I_- - I_+ + I_-\right) - i\omega L_2 I'_2 e^{i\omega t} \end{cases} \tag{C.39}$$

Similarly, as in Appendix C.0.7 the solution of the system of equations C.39 can be written in matrix form:

$$\begin{pmatrix} I_- \\ I'_2 \end{pmatrix} = \frac{1}{\Delta} \begin{pmatrix} (Z_L + iL_2\omega) & -2iM\omega \\ -iM\omega & (R_0 + 2iL_1\omega) \end{pmatrix} \begin{pmatrix} I_+ R_0 \\ 0 \end{pmatrix} \tag{C.40}$$

where the Δ is given by:

$$\Delta = Z_L R_0 + iL_2\omega R_0 + 2iL_1\omega Z_L - 2L_1 L_2 \omega^2 + 2M^2\omega^2 = Z_L R_0 + i\omega(2L_1 Z_L + L_2 R_0) \tag{C.41}$$

Now the expression for V_3 can be written using Eq. C.37:

$$V_3 = \left(I_+ - I_-\right) R_0 e^{i\omega t} = \left(1 - \frac{R_0 \left(Z_L + iL_2\omega\right)}{Z_L R_0 + i\omega(2L_1 Z_L + L_2 R_0)}\right) I_+ R_0 e^{i\omega t} = \frac{2iL_1\omega Z_L}{\Delta} I_+ R_0 e^{i\omega t} \tag{C.42}$$

Let $Z_L = x + iy$, and substituting into Eq. C.42 gives:

$$V_3 = \frac{2iL_1\omega x - 2L_1\omega y}{xR_0 - 2L_1\omega y + i(yR_0 + 2L_1\omega x + L_2\omega R_0)} I_+ R_0 e^{i\omega t}, \Rightarrow$$
$$|V_3| = \frac{|V_s|}{2} \sqrt{\frac{(2L_0 N_1^2 \omega x)^2 + (2L_0 N_1^2 \omega y)^2}{(xR_0 - 2L_0 N_1^2 \omega y)^2 + (yR_0 + 2L_0 N_1^2 \omega x + L_0 N_2^2 \omega R_0)^2}} \tag{C.43}$$

Equation C.43 is the exact solution; however to understand its physical meaning Eq. C.42 can be simplified as:

$$|V_3| = \frac{|V_s|}{2}\left|\frac{2iL_1\omega Z_L}{Z_L(R_0+2iL_1\omega)+iR_0L_2\omega)}\right| \approx \frac{|V_s|}{2}\left|\frac{2Z_LL_1}{2Z_LL_1+R_0L_2}\right| = \frac{|V_s|}{2}\sqrt{\frac{(2L_1x)^2+(2L_1y)^2}{(2L_1x+R_0L_2)^2+(2L_1y)^2}} \tag{C.44}$$

For a particular set of R, C and C_C in the circuit in Fig. 2.19, x is a constant and y is a function of ω. Let us analyze the function $f(y) = \frac{(2L_1x)^2+(2L_1y)^2}{(2L_1x+R_0L_2)^2+(2L_1y)^2}$:

$$f'(y) = \frac{2(2L_1)^2y((2L_1x+R_0L_2)^2+(2L_1y)^2)-2(2L_1)^2y((2L_1x)^2+(2L_1y)^2)}{((2L_1x+R_0L_2)^2+(2L_1y)^2)^2} = \frac{2(2L_1)^2y((2L_1x+R_0L_2)^2-(2L_1x)^2)}{((2L_1x+R_0L_2)^2+(2L_1y)^2)^2}$$
$$f'(y) = 0 \;<=>\; y = 0 \tag{C.45}$$

from which it follows that $|V_3|$ as a function of ω has one minimum where the reactive part of Z_L becomes zero.

$$|V_3|_{min} \approx \frac{|V_s|}{2}\left(\frac{2L_1x}{2L_1x+R_0L_2}\right) \tag{C.46}$$

Thus for the impedance matched case (Eq. 2.23) one can set $x = \frac{L_2}{L_1}R_0$, from which $|V_3| \approx \frac{|V_s|}{3}$.

APPENDIX D

Shape of the mw spectroscopy line

D.0.9 Effect of gravity sag on the spectroscopy line

This part of the Appendix is an addition to Section 3.1.2, which describes the mw spectroscopy line of the trapped BEC clouds. The total energy of the atoms in state $|1\rangle$, F=1, m_F=−1:

$$\begin{aligned} E_{-1}(x',y',z') &= \mu_B m_F g_f B_0 + \frac{M(\omega_x^2 x'^2 + \omega_y^2 y'^2 + \omega_z^2 z'^2)}{2} - Mgz' + \chi n(x',y',z'), \\ E_{-1}(x,y,z) &= \mu_B m_F g_f B_0 + \frac{M\omega^2(x^2+y^2+z^2)}{2} - Mg\frac{\omega}{\omega_z}z + \chi n(x,y,z) \end{aligned} \tag{D.1}$$

where B_0 is the minimum of the magnetic field, M is the mass of atoms, the $\chi n(x',y',z')$ term describes the atomic interaction energy and $n(x',y',z')$ is the number density. The energy of the untrapped state F=2, m_F=0 is raised by the hyperfine splitting E_{hf} = 6 834 682 610.9 Hz between the F=1 and F=2 without the magnetic field:

$$E_0 = E_{hf} - Mg\frac{\omega}{\omega_z}z + \chi n(x,y,z) \tag{D.2}$$

Assuming that the interaction parameter χ is the same for both internal states, the transition frequency

$$hf(r) = E_0 - E_{-1} = E_{hf} - \mu_B m_F g_f B_0 - \frac{M\omega^2 r^2}{2} \tag{D.3}$$

depends only on the modulus of the distance $r = \sqrt{x^2+y^2+z^2}$ from the minimum of the magnetic field in the new coordinate system (Eq. 3.5) (Fig. D.1).

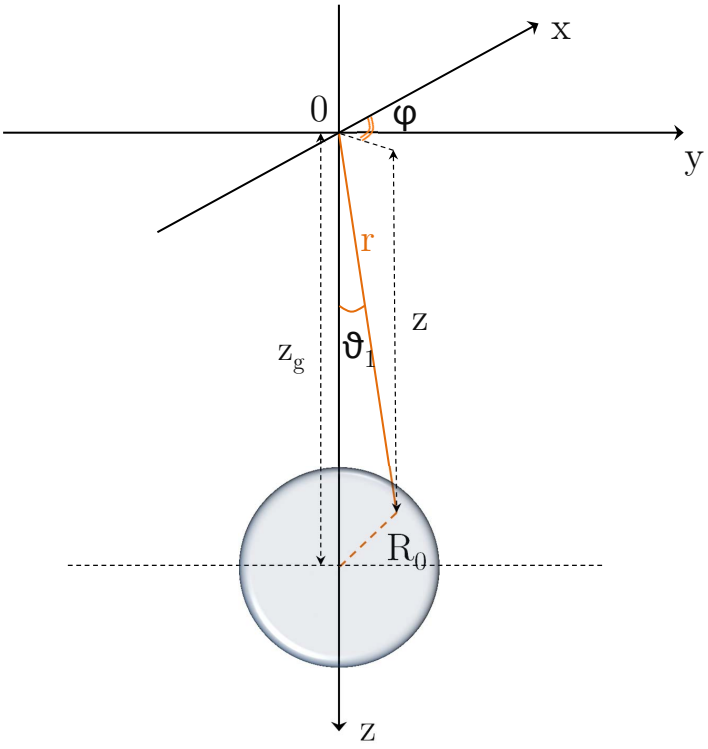

Figure D.1: Cartesian and spherical coordinate systems used for calculating the atom number resonant with a particular value of the mw frequency.

The presence of gravity does not change the Thomas-Fermi shape [76] of atoms in the harmonic trap with the same trap frequencies, shifting only the position of the cloud centre (Eq. B.20 in Appendix B.0.4).

$$\begin{aligned} n(x,y,z) &= \frac{1}{\chi}\left(\mu - \frac{M\omega^2(x^2+y^2+(z-z_g)^2)}{2}\right) => \\ n(r,\theta) &= \frac{1}{\chi}\left(\mu - \frac{M\omega^2 z_g^2}{2} - \frac{M\omega^2 r^2}{2} + M\omega^2 z_g r cos\theta\right) = C - \alpha r^2 + \beta r cos\theta \end{aligned} \tag{D.4}$$

where $C = \frac{\mu}{\chi} - \frac{M\omega^2 z_g^2}{2\chi}$, $\alpha = \frac{1}{\chi}\frac{M\omega^2}{2}$ and $\beta = \frac{1}{\chi}M\omega^2 z_g$. The number of atoms dN that are resonant at a particular frequency can be calculated as:

$$\begin{gathered} dN = \iint_{\phi\theta} n(r,\theta) r^2 sin\theta dr d\theta d\phi = 2\pi r^2 dr \int (C - \alpha r^2 + \beta r cos\theta) sin\theta d\theta = \\ 2\pi r^2 dr \left[(C - \alpha r^2)(-cos\theta)\Big|_0^{\theta_1} + \frac{1}{4}\beta r(-cos2\theta)\Big|_0^{\theta_1} \right] = \\ 2\pi r^2 dr \left[(C - \alpha r^2)(1 - cos\theta_1) + \frac{1}{4}\beta r(1 - cos2\theta_1) \right] = \\ 2\pi r^2 dr \left[(C - \alpha r^2)(1 - cos\theta_1) + \frac{1}{2}\beta r(1 - cos^2\theta_1) \right] = \\ 2\pi r^2 dr \left[(C - \alpha r^2)(1 - cos\theta_1) + \frac{1}{2}\beta r(1 - cos\theta_1)(1 + cos\theta_1) \right] = \\ 2\pi r^2 (1 - cos\theta_1) dr \left[C - \alpha r^2 + \frac{1}{2}\beta r(1 + cos\theta_1) \right] \end{gathered} \tag{D.5}$$

Equation D.5 gives the general solution to the problem; however, the result can be simplified by considering two different cases: $z_g \geq R_0$ or $z_g < R_0$. Let us start with the first case shown in Fig. D.1.

We assume that the atomic cloud maintains a Thomas-Fermi profile which leads to the bounding relation between r and θ_1: $C - \alpha r^2 + \beta r cos\theta_1 = 0$, from which:

$$\begin{gathered} dN = 2\pi r^2 (1 - cos\theta_1) dr \left[C - \alpha r^2 + \frac{1}{2}\beta r(1 + cos\theta_1) \right] = \\ 2\pi r^2 (1 - cos\theta_1) dr \left[C - \alpha r^2 + \beta r cos\theta_1 + \frac{1}{2}\beta r(1 - cos\theta_1) \right] = \\ \pi\beta r^3 (1 - cos\theta_1)^2 dr \end{gathered} \tag{D.6}$$

In the plane of the axes z, r and R_0 (Fig. D.1) one can use the law of cosines end express $cos\theta_1$ through r and R_0:

$$\begin{gathered} cos\theta_1 = \frac{z_g^2 - R_0^2 + r^2}{2 r z_g}, \; => \\ 1 - cos\theta_1 = \frac{2 r z_g - z_g^2 + R_0^2 - r^2}{2 r z_g} = \frac{R_0^2 - (r - z_g)^2}{2 r z_g} = \\ \frac{((z_g + R_0) - r)(r - (z_g - R_0))}{2 r z_g} \end{gathered} \tag{D.7}$$

from which the final dependence follows:

$$dN(r) = \frac{\pi\beta r}{4 z_g^2}((z_g + R_0) - r)^2 (r - (z_g - R_0))^2 dr \tag{D.8}$$

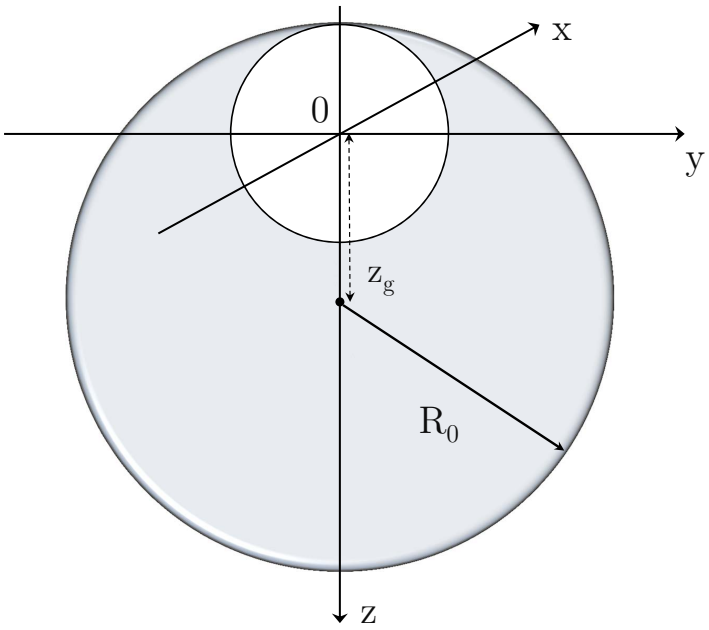

Figure D.2: In the case $z_g < R_0$ Eq. D.5 describes two different cases outlined by grey (Eq. D.8) and white (Eq. D.9) colours.

In the case $z_g < R_0$ Eq. D.8 considers only a part of the cloud (Fig. D.2). This effect can be accounted for by the calculation of the number of atoms dN for $r \in [0,\ R_0 - z_g]$ (z_g<R$_0$ case) and setting $\theta_1{=}\pi$ in Eq. D.5:

$$\begin{aligned} dN = 4\pi r^2 \left(\frac{\mu}{\chi} - \frac{M\omega^2 z_g^2}{2\chi} - \frac{1}{\chi}\frac{M\omega^2}{2} r^2 \right) dr = \\ 4\pi r^2 \left(\frac{M\omega^2 R_0^2}{2\chi} - \frac{M\omega^2 z_g^2}{2\chi} - \frac{1}{\chi}\frac{M\omega^2}{2} r^2 \right) dr \end{aligned} \tag{D.9}$$

where from Eq. D.4 it follows that $n(x, y, z) = 0$ at the border of the cloud and thus $\mu = \frac{M\omega^2 R_0^2}{2}$.

The final result for the whole range of r is a piecewise defined function:

$$\begin{cases} dN = \frac{1}{\chi} M\omega^2 2\pi r^2 \left(R_0^2 - z_g^2 - r^2 \right) dr, \ r \in [0,\ R_0 - z_g] \\ dN = \frac{1}{\chi} M\omega^2 \frac{\pi}{4 z_g} r \left(R_0^2 - (r - z_g)^2 \right)^2 dr, \ r \in [R_0 - z_g, R_0 + z_g] \end{cases} \tag{D.10}$$

Equation D.3 can be rewritten to express r as a function of f:

$$\begin{cases} r = \frac{1}{\omega\sqrt{M}}\sqrt{2(E_{hf} - \mu g_f B_0 - hf)}, \\ dr = -\frac{1}{\omega\sqrt{M}}\frac{h}{\sqrt{2(E_{hf}-\mu g_f B_0 - hf)}}df \end{cases} <=> \begin{cases} r = \frac{1}{T}\sqrt{f_m - f}, \\ rdr = -\frac{1}{2T^2}df \end{cases} \tag{D.11}$$

where $f_m = \frac{1}{h}(E_{hf} - \mu_B m_F g_f B_0)$ and $T = \frac{\sqrt{M\omega^2}}{2h}$.

The radius r changes in the range $[z_g - R_0,\ z_g + R_0]$ ($[0,\ z_g + R_0]$ in the $z_g < R_0$ case) along the size of the BEC. The corresponding resonant frequencies change according to Eq. D.3 from f_m - $\frac{M\omega^2(z_g - R_0)^2}{2h}$ (f_m in the $z_g < R_0$ case) to f_m - $\frac{M\omega^2(z_g + R_0)^2}{2h}$. So the resonant frequency decreases with the increase of r which explains the negative sign in Eq. D.11 for the differentials. The minus sign should be omitted with changing the frequency f from the minimum value to the maximum in the range [f_m - $\frac{M\omega^2(z_g+R_0)^2}{2h}$, f_m - $\frac{M\omega^2(z_g-R_0)^2}{2h}$] ([$f_m$ - $\frac{M\omega^2(z_g+R_0)^2}{2h}$, f_m] in the $z_g < R_0$ case).

It is important to remember that in Eq. D.10 the parameters z_g and R_0 are not the real gravitational sag z_g' and the BEC Thomas-Fermi radius R_0' because of the change to the new coordinate system. From Eq. 3.5 it can be written:

$$\begin{cases} z_g' = z_g\frac{\omega}{\omega_z} = z_g\frac{\omega}{\omega_r}, \\ R_y' = R_0\frac{\omega}{\omega_z} = R_0\frac{\omega}{\omega_{ax}}, \\ R_z' = R_x' = R_0\frac{\omega}{\omega_r} \end{cases} \tag{D.12}$$

The range of resonant frequencies for different parts of the condensate (the total width of the spectroscopy line) can be calculated as r changes from $z_g - R_0$ to $z_g + R_0$ (in the case $z_g \geq R_0$):

$$\Delta f = f_{max} - f_{min} = \frac{1}{h}\left[E_{hf} - \mu g_f B_0 - \frac{M\omega^2(z_g - R_0)^2}{2}\right] - \frac{1}{h}\left[E_{hf} - \mu g_f B_0 - \frac{M\omega^2(z_g + R_0)^2}{2}\right] = \frac{2}{h}M\omega^2 z_g R_0 = \frac{2}{h}MgR_z' \approx 20\ (\text{kHz}) \tag{D.13}$$

Here it is set $z_g' \sim 25\ \mu m$; $R_z' \sim 5\ \mu m$ for $\omega = 2\pi{\cdot}100$ (Hz) at 3.23 G at the trap bottom. The frequencies of the trap have been measured in a separate experiment and the Thomas-Fermi radius has been estimated from the known total number of atoms and the trap frequencies.

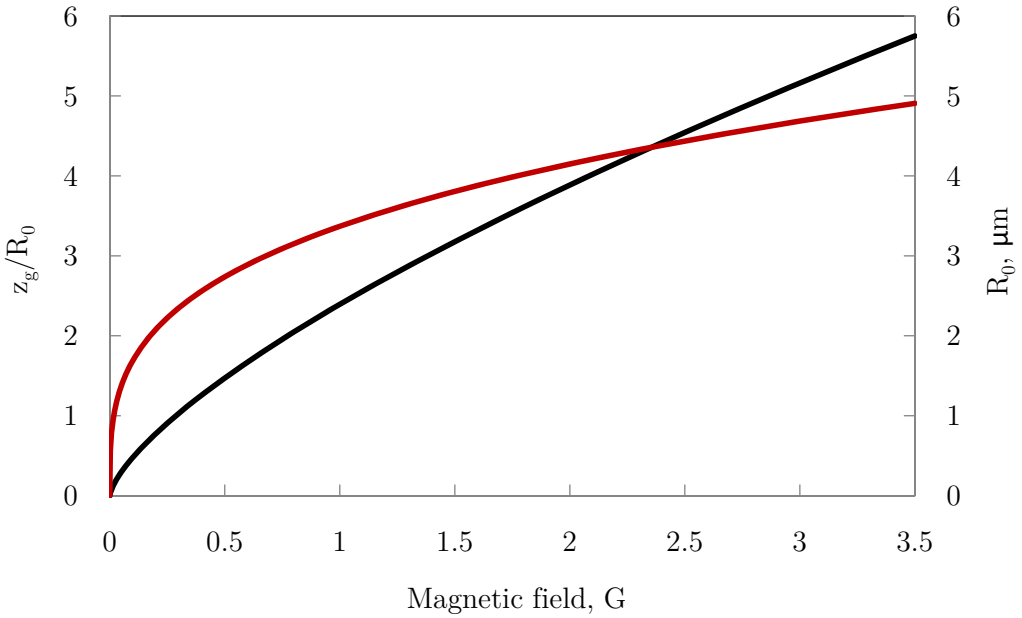

Figure D.3: The red curve shows the Thomas-Fermi radius of the BEC cloud consisting of $2{\cdot}10^5$ atoms at different magnetic trap bottoms. The black curve represents the ratio $\frac{z_g}{R_0}$ with respect to the magnetic field. In the calculations the values of the Z-wire current and B_{xLarge} are kept constant.

In the $z_g \geq R_0$ case the function $\Phi_2(f)$ in Eq. 3.6 describes the whole profile of the spectroscopy line. It is easy to find the frequency corresponding to the peak of the coupling profile:

$$\begin{aligned} y(f) &= A\left(R_0^2 - (\frac{\sqrt{f_m - f}}{T} - z_g)^2\right)^t \\ y'(f) &= At\left(R_0^2 - (\frac{\sqrt{f_m - f}}{T} - z_g)^2\right)^{t-1} \times (\frac{\sqrt{f_m - f}}{T} - z_g)\frac{1}{T\sqrt{f_m - f}} \end{aligned} \tag{D.14}$$

The derivative $y'(f)$ changes sign from positive to negative at the point where $\frac{\sqrt{f_m - f}}{T} = z_g$, from which it follows that $f_{max} = f_m - T^2 z_g^2$. Figure D.3 illustrates the dependence of the Thomas-Fermi radius R_0 and the ratio $\frac{z_g}{R_0}$ on the magnetic field. For magnetic fields larger than 0.3 G the gravity sag z_g is greater than R_0 and thus the maximum number of coupled atoms corresponds to the radius-vector which goes through the centre of the BEC cloud.

D.0.10 Uncertainty of magnetic field measurement

The standard method for computation of the uncertainties for a calculable parameter is the partial derivatives method. Equation 3.15 can be expressed in a differential form:

$$\begin{cases} df = \frac{g_I \mu_B}{h} dB + \frac{\nu_{hfs}}{2} \frac{-dx+2xdx}{2\sqrt{1-x+x^2}} + \frac{\nu_{hfs}}{2} \frac{2xdx}{2\sqrt{1+x^2}}, \\ dx = \frac{(g_J - g_I)\mu_B}{h\nu_{hfs}} dB \end{cases} \quad => \quad \Delta B = \frac{1}{\frac{g_I \mu_B}{h} + \frac{(g_J - g_I)\mu_B}{2h} \left(\frac{2x-1}{2\sqrt{1-x+x^2}} + \frac{x}{\sqrt{1+x^2}} \right)} \Delta f = C \Delta f \tag{D.15}$$

Similarly, for the computation of the resonant frequency, corresponding to the centre of the BEC cloud (Eq. 3.7):

$$\omega = \frac{A}{\sqrt{B}}, \quad => \quad f_0 = f_m - T^2 (z_g^0)^2 = f_m - \frac{Mg^2}{2hA^2} B, \qquad \Delta f_0 = \sqrt{(\Delta f_m)^2 + \left(\frac{Mg^2}{2hA^2} \Delta B \right)^2} \tag{D.16}$$

where Eq. B.17 was used to express the normalized trap frequency ω.

D.0.11 Step function and the mw spectroscopy fitting formulae

A Heaviside step function $stf(r)$ can be employed to express the total piecewise defined profile of the mw spectroscopy, Eq. 3.12, as the sum of the continuous functions. There are different analytical functions that approximate the step function and our choice is the following:

$$stf(x) = 0.5 + \frac{1}{\pi} tan^{-1}(d \times x) \tag{D.17}$$

This function is shown in Fig. D.4. In our fitting formulae the parameter d is chosen to be 10^{16} m^{-1} to make the slopes of the Heaviside function steeper. Thus Eq. 3.12 for all ranges of z_g can be written as one function:

$$dN = \sum \left(\Phi_1 \times stf(r + z_g - R_0) + \Phi_2 \times stf(R_0 - z_g - r) \right) \tag{D.18}$$

The integration over frequency (ν) in Eq. 3.12 is replaced by the sum of N summands, dividing the range of frequencies into N frequency intervals. The same step function is

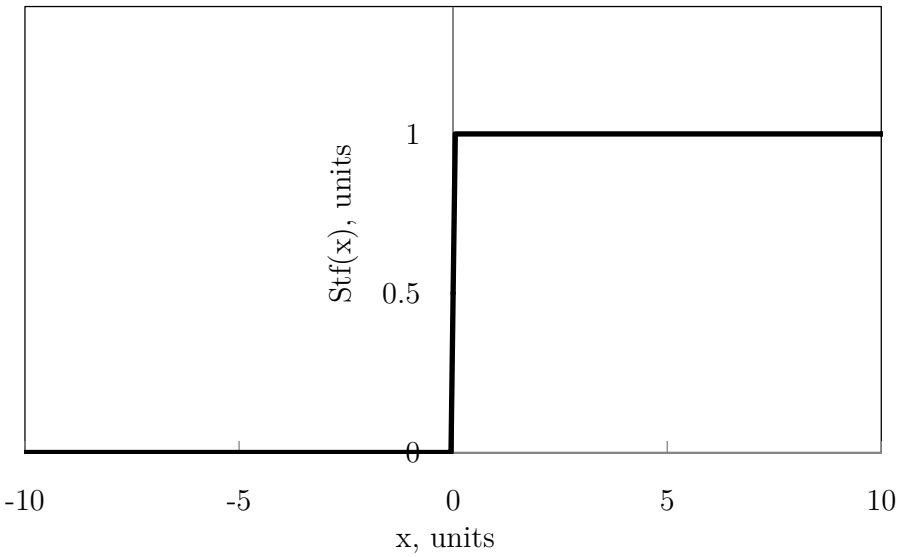

Figure D.4: Graphic representation of the step function sft(x), approximated by the Eq. D.17.

employed to combine two possible ranges of the frequencies for the cases $z_g \geq R_0$ and $z_g < R_0$:

$$\begin{cases} f_{min} = f_m - r_{max}^2 T^2 = f_m - (z_g + R_0)^2 T^2, \\ f_{max} = f_m - r_{min}^2 T^2 = f_m - stf(z_g - R_0)(z_g - R_0)^2 T^2, \\ f_k = f_m - (z_g + R_0)^2 T^2 + \dfrac{k}{N}\left[(z_g + R_0)^2 T^2 - (z_g - R_0)^2 T^2 \cdot stf(z_g - R_0)\right] \end{cases} \tag{D.19}$$

from which it can be written for r_k:

$$r_k = \frac{\sqrt{(z_g + R_0)^2 T^2 - \frac{k}{N}\left[(z_g + R_0)^2 T^2 - (z_g - R_0)^2 T^2 \cdot stf(z_g - R_0)\right]}}{T} \tag{D.20}$$

Thus Eq. D.18 becomes:

$$
\begin{aligned}
dN = \sum_{k,t} \Bigg[& 8A \times stf\Bigg(R_0 - z_g - \\
& \sqrt{(z_g+R_0)^2 - \frac{k}{N}\Big[(z_g+R_0)^2 - (z_g-R_0)^2 stf(z_g-R_0)\Big]}\Bigg) \times \\
& \sqrt{(z_g+R_0)^2 - \frac{k}{N}\Big[(z_g+R_0)^2 - (z_g-R_0)^2 stf(z_g-R_0)\Big]} \times \\
& \Bigg(\frac{k}{N}\Big[(z_g+R_0)^2 - (z_g-R_0)^2 stf(z_g-R_0)\Big] - 2z_g^2 - 2z_g R_0\Bigg) + \\
& \frac{A}{z_g} stf\Bigg(- R_0 + z_g + \\
& \sqrt{(z_g+R_0)^2 - \frac{k}{N}\Big[(z_g+R_0)^2 - (z_g-R_0)^2 stf(z_g-R_0)\Big]}\Bigg) \times \\
& \Bigg(R_0^2 - \Bigg(\sqrt{(z_g+R_0)^2 - \frac{k}{N}\Big[(z_g+R_0)^2 - (z_g-R_0)^2 stf(z_g-R_0)\Big]} - z_g\Bigg)^2\Bigg)^2\Bigg] \times \\
& \frac{df}{4\Bigg(f - f_m + (z_g+R_0)^2 T^2 - \\
& \qquad \frac{k}{N} T^2 \Big[(z_g+R_0)^2 - (z_g-R_0)^2 stf(z_g-R_0)\Big]\Bigg)^2 + \Delta^2}
\end{aligned}
\tag{D.21}
$$

where the summation over time t considers the replacement of the integral over time in Eq. 3.12 by the sum (analogous to integration over the frequency ν) and the substitution $z_g = z_g^0 + d \cdot cos(\omega t)$.

APPENDIX E

Shape of the rf induced atom loss curve during molecule associations

E.0.12 Two-body losses in a two-component BEC

All atoms in a pure BEC in a harmonic trap have the same energy. The difference of the magnetic and the gravitational potential along the BEC cloud is compensated by the mean field potential due to atomic collisional interactions. The creation of a coherent superposition of the states $|1\rangle$ and $|2\rangle$ (Section 2.5) disturbs the equilibrium state and induces collective oscillations of the different components in the BEC [90], [65] as the scattering lengths a_{11}, a_{12} and a_{22}, responsible for the atomic interactions are not equal to each other. All atoms exist in the superposition of the two states $|1\rangle$ and $|2\rangle$ but this can be treated as two different coherent BECs. Usually in the prepared superposition one cloud contains most ($\sim 80\%$) of the atoms and according to experiment it exhibits small perturbations and serves as a reservoir whereas the smaller one starts to experience non-negligible oscillations. The described collective atom dynamics of the small cloud is complex but can be approximated as a harmonic oscillation of the cloud size in the axial direction [90] for cigar-shape magnetic traps:

$$R_z(t) = \frac{R_{z0} + R_{zmin}}{2} + \frac{R_{z0} - R_{zmin}}{2} cos\omega t \tag{E.1}$$

Thus in the Thomas Fermi approximation [76] the atom number densities of pure BECs

can be calculated for both states as:

$$\begin{aligned} n_1(\rho,z) &= n_{10}\left(1-\frac{\rho^2}{R_\rho^2}-\frac{z^2}{R_{z0}^2}\right), \\ n_2(\rho,z,t) &= n_{20}\left(1-\frac{\rho^2}{R_\rho^2}-\frac{z^2}{R_z^2(t)}\right) \end{aligned} \tag{E.2}$$

where the oscillations of the bigger cloud have already been neglected.

From Eq. E.2 the atom number density $n_{1,2}$ can be easily calculated with the known values of R_ρ, R_z and the total number of atoms N after evaluation of the integral:

$$\begin{gathered} N = \int n(\rho,z)dV = n_0\int\left(1-\frac{\rho^2}{R_\rho^2}-\frac{z^2}{R_z^2}\right)\rho d\rho dz d\phi = \\ 2\pi n_0\int\left[\left(1-\frac{\rho^2}{R_\rho^2}\right)z\Big|_{-R_z\sqrt{1-\frac{\rho^2}{R_\rho^2}}}^{R_z\sqrt{1-\frac{\rho^2}{R_\rho^2}}}-\frac{z^3}{3R_z^2}\Big|_{-R_z\sqrt{1-\frac{\rho^2}{R_\rho^2}}}^{R_z\sqrt{1-\frac{\rho^2}{R_\rho^2}}}\right]\rho d\rho = \\ \frac{8\pi}{3}n_0R_z\int\left(1-\frac{\rho^2}{R_\rho^2}\right)^{\frac{3}{2}}\rho d\rho = \frac{8\pi}{3}n_0R_\rho^2R_z\left(-\frac{(1-\frac{\rho^2}{R_\rho^2})^5}{5}\right)\Big|_0^{R_\rho} = \\ \frac{8\pi}{15}n_0R_\rho^2R_z \end{gathered} \tag{E.3}$$

where during the last integration the substitution was used:

$$k=\sqrt{1-\frac{\rho^2}{R_\rho^2}} \;=>\; \rho d\rho = -R_\rho^2 k dk \tag{E.4}$$

In dilute clouds three-body collisions are unlikely and atoms are getting lost from the trap mainly due to two-body collisions. For the the second cloud the usual atom loss equation for the two-body losses can be written in a cylindrical coordinate system:

$$\frac{\partial n_2(\rho,z,t)}{\partial t} = -\gamma_{22}n_2^2(\rho,z,t)-\gamma_{12}n_1(\rho,z)n_2(\rho,z,t) \tag{E.5}$$

Here γ_{22} is the loss coefficient associated with collisions of the both atoms in the state $|2\rangle$ and γ_{12} is the loss coefficient for collisions between atoms, one in state $|1\rangle$ and the other in state $|2\rangle$. From Eq. E.5 the number of atoms in state $|2\rangle$ changes with time as

$$\frac{dN_2}{dt} = \int\frac{\partial n_2}{\partial t}\rho d\rho dz d\phi = -\gamma_{22}\int n_2^2\rho d\rho dz d\phi - \gamma_{12}\int n_1n_2\rho d\rho dz d\phi \tag{E.6}$$

which after substitution of the values for n_1 and n_2 from Eq. E.2 becomes:

$$\begin{gathered} \frac{dN_2}{dt} = -\gamma_{22}n_{20}^2\int\left(1-\frac{\rho^2}{R_\rho^2}-\frac{z^2}{R_z^2(t)}\right)^2\rho d\rho dz d\phi - \\ \gamma_{12}n_{10}n_{20}\int\left(1-\frac{\rho^2}{R_\rho^2}-\frac{z^2}{R_{z0}^2}\right)\left(1-\frac{\rho^2}{R_\rho^2}-\frac{z^2}{R_z^2(t)}\right)\rho d\rho dz d\phi \end{gathered} \tag{E.7}$$

Each integral from this equation can be evaluated with the substitution of Eq. E.4. The expression for the first integral in Eq. E.7:

$$\begin{gathered}\int\left(1-\frac{\rho^2}{R_\rho^2}-\frac{z^2}{R_z^2(t)}\right)^2\rho d\rho dz d\phi=-2\pi R_\rho^2\int\left(k^4-\frac{2k^2z^2}{R_z^2(t)}+\frac{z^4}{R_z^4(t)}\right)kdkdz=\\ -2\pi R_\rho^2\int\left[zk^4\Big|_{-R_z(t)k}^{R_z(t)k}-\frac{2z^3}{3R_z^2(t)}k^2\Big|_{-R_z(t)k}^{R_z(t)k}+\frac{z^5}{5R_z^4(t)}\Big|_{-R_z(t)k}^{R_z(t)k}\right]kdk=\\ -2\pi R_\rho^2\int\frac{16}{15}R_z(t)k^6dk=\frac{32}{105}\pi R_\rho^2R_z(t)\end{gathered}\tag{E.8}$$

and for the second one:

$$\begin{gathered}\int\left(1-\frac{\rho^2}{R_\rho^2}-\frac{z^2}{R_{z0}^2}\right)\left(1-\frac{\rho^2}{R_\rho^2}-\frac{z^2}{R_z^2(t)}\right)\rho d\rho dz d\phi=\\ -2\pi R_\rho^2\int\left(k^4-\left(\frac{k^2}{R_{z0}^2}+\frac{k^2}{R_z^2(t)}\right)z^2+\frac{z^4}{R_{z0}^2R_z^2(t)}\right)kdkdz=\\ -2\pi R_\rho^2\int\left[zk^4\Big|_{-R_z(t)k}^{R_z(t)k}-\frac{z^3}{3}\left(\frac{k^2}{R_{z0}^2}+\frac{k^2}{R_z^2(t)}\right)\Big|_{-R_z(t)k}^{R_z(t)k}+\frac{z^5}{5R_{z0}^2R_z^2(t)}\Big|_{-R_z(t)k}^{R_z(t)k}\right]kdk=\\ -4\pi R_\rho^2R_z(t)\int k^6\left[1-\frac{1}{3}\left(\frac{R_z^2(t)}{R_{z0}^2}+1\right)+\frac{R_z^2(t)}{5R_{z0}^2}\right]dk=\\ \frac{8}{105}\pi R_\rho^2R_z(t)\left(5-\frac{R_z^2(t)}{R_{z0}^2}\right)\end{gathered}\tag{E.9}$$

Thus Eq. E.7 becomes:

$$\begin{gathered}\frac{dN_2}{dt}=-\gamma_{22}n_{20}^2\frac{32}{105}\pi R_\rho^2R_z(t)-\gamma_{12}n_{10}n_{20}\frac{8}{105}\pi R_\rho^2R_z(t)\left(5-\frac{R_z^2(t)}{R_{z0}^2}\right)=\\ -\gamma_{22}\left(\frac{15N_2}{8\pi R_\rho^2R_z(t)}\right)^2\frac{32}{105}\pi R_\rho^2R_z(t)-\\ \gamma_{12}\left(\frac{15N_2}{8\pi R_\rho^2R_z(t)}\right)n_{10}\frac{8}{105}\pi R_\rho^2R_z(t)\left(5-\frac{R_z^2(t)}{R_{z0}^2}\right)<=>\\ \frac{dN_2}{dt}=-\frac{15\gamma_{22}N_2^2}{14\pi R_\rho^2R_z(t)}-\frac{\gamma_{12}n_{10}}{7}\left(5-\frac{R_z^2(t)}{R_{z0}^2}\right)N_2\end{gathered}\tag{E.10}$$

This equation can be used in an iterative calculation of the number of atoms N_2:

$$\begin{gathered}dN_{2(n+1)}=N_{2(n)}-\frac{15\gamma_{22}N_{2(n)}^2}{14\pi R_\rho^2(\frac{R_{z0}+R_{zmin}}{2}+\frac{R_{z0}-R_{zmin}}{2}cos(\omega(ndt)+\varphi_0))}dt-\\ \frac{\gamma_{12}n_{10}}{7}\left[5-\frac{(\frac{R_{z0}+R_{zmin}}{2}+\frac{R_{z0}-R_{zmin}}{2}cos(\omega(ndt)+\varphi_0))^2}{R_{z0}^2}\right]N_{2(n)}dt\end{gathered}\tag{E.11}$$

In the case when loss of atoms from state $|1\rangle$ cannot be neglected, for this state an equation should be written similar to Eq. E.6 and n_{10} in Eq. E.10 should be expressed through the number of atoms N_1 (Eq. E.3). Then the evolution of the system would be described by a system of equations: Eq. E.10 plus an analogous equation for $\frac{dN_1}{dt}$.

E.0.13 Number of collisions between atoms in different states

This part of the Appendix is an addition to Section 4.2. The number of molecules produced by rf stimulation is proportional to the number of collisions of the atoms in different internal states. The number of collisions between the atoms is proportional to the densities of the clouds, which is why the total number of created molecules is

$$\begin{gathered}
dN \sim \iint_{\phi\theta} n_1(r,\theta) n_2(r,\theta) r^2 sin\theta dr d\theta d\phi = \\
2\pi r^2 dr \int_\theta (C_1 - \alpha_1 r^2 + \beta_1 r cos\theta)^2 sin\theta d\theta = \\
2\pi r^2 dr \int_\theta \Big[(C_1 - \alpha_1 r^2)^2 + 2r cos\theta \beta_1 (C_1 - \alpha_1 r^2) + \beta_1^2 r^2 cos^2\theta \Big] sin\theta d\theta = \\
2\pi r^2 dr \Big[(C_1 - \alpha_1 r^2)^2 (-cos\theta)\Big|_0^{\theta_1} + \beta_1^2 r^2 \frac{(-cos^3\theta)}{3}\Big|_0^{\theta_1} + \\
\frac{1}{2} r\beta_1 (C_1 - \alpha_1 r^2)(-cos2\theta)\Big|_0^{\theta_1} \Big] = \\
2\pi r^2 dr \Big[(C_1 - \alpha_1 r^2)^2 (1 - cos\theta_1) + \frac{\beta_1^2 r^2}{3}(1 - cos\theta_1)(1 + cos\theta_1 + cos^2\theta_1) + \\
r\beta_1 (C_1 - \alpha_1 r^2)(1 - cos\theta_1)(1 + cos\theta_1) \Big]
\end{gathered} \tag{E.12}$$

where $n_2 = n_1$ and parameters C_1, α_1 and β_1 are defined by Eq. D.4. The visual representation of the integration is shown in Fig. D.1. As in Appendix D.0.9 for $z_g \geq R_0$ case it can be noticed that:

$$C_1 - \alpha_1 r^2 + \beta_1 r cos\theta_1 = 0 \;\; => C_1 - \alpha_1 r^2 = -\beta_1 r cos\theta_1 \tag{E.13}$$

Thus:

$$\begin{gathered}
dN \sim 2\pi r^2 dr (1 - cos\theta_1) \Big[\beta_1^2 r^2 cos^2\theta_1 + \\
\frac{\beta_1^2 r^2}{3}(1 + cos\theta_1 + cos^2\theta_1) - \beta_1^2 r^2 cos\theta_1 (1 + cos\theta_1) \Big] = \frac{2}{3}\pi\beta_1^2 r^4 (1 - cos\theta_1)^3 dr
\end{gathered} \tag{E.14}$$

With the help of the law of cosines:

$$dN(r) \sim \frac{\pi\beta_1^2 r}{12 z_g^3}(R_0^2 - (r - z_g)^2)^3 dr = \frac{\pi M^2 w^4 r}{12\chi^2 z_g}(R_0^2 - (r - z_g)^2)^3 dr \tag{E.15}$$

In the case $z_g < R_0$, θ_1 is equal to π in Eq. E.12 from which:

$$\begin{gathered} dN \sim 4\pi r^2 dr\Big[(C_1 - \alpha_1 r^2)^2 + \frac{\beta_1^2 r^2}{3}\Big] = \\ 4\pi r^2 dr\Big[\Big(\frac{Mw^2R_0^2}{2\chi} - \frac{Mw^2z_g^2}{2\chi} - \frac{Mw^2r^2}{2\chi}\Big)^2 + \frac{M^2w^4z_g^2r^2}{3\chi^2}\Big] = \\ \pi r^2 \frac{M^2w^4}{\chi^2} dr\Big[\Big(R_0^2 - z_g^2 - r^2\Big)^2 + \frac{4z_g^2r^2}{3}\Big] \end{gathered} \tag{E.16}$$

E.0.14 Rf-induced atom loss curve fitting formulae

Similar to the mw spectroscopy case, in order to fit the experimental data we employ a step function defined by Eq. D.17 to write the piecewise defined function in Eq. 4.13 as a continuous function (similar to Eq. D.18). As before, integrations over time t and frequency ν in Eq. 4.13 are replaced with approximate sums, dividing the period of the dipole oscillation into M intervals and substituting $z_g = z_g^0 + d \cdot cos(\omega_{do} t)$ and splitting the frequency range into N intervals, resulting in the total N×M summands. For the molecular state A the resonant frequencies decrease with an increase of r and Eqs. D.20 and D.19

are also valid:

$$
\begin{aligned}
dN = \sum_{k,t} \Bigg[& 12A \times stf\Bigg(R_0 - z_g - \\
& \sqrt{(z_g+R_0)^2 - \frac{k}{N}\Big[(z_g+R_0)^2 - (z_g-R_0)^2 stf(z_g-R_0)\Big]}\Bigg) \times \\
& \sqrt{(z_g+R_0)^2 - \frac{k}{N}\Big[(z_g+R_0)^2 - (z_g-R_0)^2 stf(z_g-R_0)\Big]} \times \\
& \Bigg[\Bigg(-2z_gR_0 - 2z_g^2 + \frac{k}{N}\Big[(z_g+R_0)^2 - (z_g-R_0)^2 \times stf(z_g-R_0)\Big]\Bigg)^2 + \\
& \frac{4z_g^2}{3}\Bigg((z_g+R_0)^2 - \frac{k}{N}\Big[(z_g+R_0)^2 - (z_g-R_0)^2 \times stf(z_g-R_0)\Big]\Bigg)\Bigg] + \\
& \frac{A}{z_g} stf\Bigg(-R_0 + z_g + \\
& \sqrt{(z_g+R_0)^2 - \frac{k}{N}\Big[(z_g+R_0)^2 - (z_g-R_0)^2 stf(z_g-R_0)\Big]}\Bigg) \times \\
& \Bigg[R_0^2 - \Bigg(\sqrt{(z_g+R_0)^2 - \frac{k}{N}\Big[(z_g+R_0)^2 - (z_g-R_0)^2 stf(z_g-R_0)\Big]} - |z_g|\Bigg)^2\Bigg]^3\Bigg] \times \\
& \frac{df}{4\Bigg(f - f_m + (z_g+R_0)^2T^2 - \\
& \qquad \frac{k}{N}T^2\Big[(z_g+R_0)^2 - (z_g-R_0)^2 stf(z_g-R_0)\Big]\Bigg)^2 + \Delta^2}
\end{aligned}
\tag{E.17}
$$

For the other curves B, C, D, E and F in Eq. 4.5 the range of frequencies is different: the highest rf frequency is equal to $f_m + (z_g + R_0)^2T^2$ whereas the minimum frequency is defined with the help of the step function (stf):

$$
\begin{cases}
f_{min} = f_m + stf(z_g - R_0)(z_g - R_0)^2T^2, \\
f_{max} = f_m + (z_g + R_0)^2T^2, \\
f_n = f_m + stf(z_g - R_0)(z_g - R_0)^2T^2 + \\
\qquad \frac{n}{N}\Big[(z_g+R_0)^2T^2 - stf(z_g-R_0)(z_g-R_0)^2T^2\Big]
\end{cases}
\tag{E.18}
$$

Combining Eq. E.18 with Eq. 4.10 r_n can be written:

$$
r_n = \frac{f_n - f_m}{T} = \frac{\sqrt{(z_g-R_0)^2T^2 stf(z_g-R_0) + \frac{n}{N}\Big[(z_g+R_0)^2T^2 - (z_g-R_0)^2T^2 stf(z_g-R_0)\Big]}}{T}
\tag{E.19}
$$

By using the same step function from Eq. D.17 as in Appendix D.0.11 the piecewise defined function in Eq. 4.13 can be written as one function:

$$dN \sim \sum \Big(\Phi_1 \times stf(R_0 - z_g - r) + \Phi_2 \times stf(-(R_0 - z_g - r)) \Big) \tag{E.20}$$

where the functions Φ_1 and Φ_2 refer to the first and second equations in Eq. 4.13, respectively. Thus the final fitting formula can be written as:

$$\begin{aligned} dN = \sum_{n,t} \Bigg[12kA \times stf\Bigg(R_0 - z_g - \\ \sqrt{(z_g - R_0)^2 stf(z_g - R_0) + \frac{n}{N}\Big[(z_g + R_0)^2 - (z_g - R_0)^2 stf(z_g - R_0)\Big]}\Bigg) \times \\ \sqrt{(z_g - R_0)^2 stf(z_g - R_0) + \frac{n}{N}\Big[(z_g + R_0)^2 - (z_g - R_0)^2 stf(z_g - R_0)\Big]} \times \\ \Bigg[\Bigg(R_0^2 - z_g^2 - \\ \Big((z_g - R_0)^2 stf(z_g - R_0) + \frac{n}{N}\Big[(z_g + R_0)^2 - (z_g - R_0)^2 stf(z_g - R_0)\Big]\Big)\Bigg)^2 + \\ \frac{4z_g^2}{3}\Big((z_g - R_0)^2 stf(z_g - R_0) + \frac{n}{N}\Big[(z_g + R_0)^2 - (z_g - R_0)^2 stf(z_g - R_0)\Big]\Big)\Bigg] + \\ \frac{A}{z_g} stf\Bigg(- R_0 + z_g + \\ \sqrt{(z_g - R_0)^2 stf(z_g - R_0) + \frac{n}{N}\Big[(z_g + R_0)^2 - (z_g - R_0)^2 stf(z_g - R_0)\Big]}\Bigg) \times \\ \Bigg[R_0^2 - \\ \Bigg(\sqrt{(z_g - R_0)^2 stf(z_g - R_0) + \frac{n}{N}\Big[(z_g + R_0)^2 - (z_g - R_0)^2 stf(z_g - R_0)\Big]} - \\ |z_g|\Bigg)^2\Bigg]^3\Bigg] \times \frac{df}{4\Bigg(f - f_m - (z_g - R_0)^2 T^2 stf(z_g - R_0) - \\ \frac{n}{N} T^2 \Big[(z_g + R_0)^2 - (z_g - R_0)^2 stf(z_g - R_0)\Big]\Bigg)^2 + \Delta^2} \end{aligned} \tag{E.21}$$

E.0.15 Measurement of the bound state energies at 0 G

The original task is to compare two sets of data: the set of theoretical points [113] and the experimental data. The theoretical points are the results of numerical simulations [55]

and there are no theoretical predictions about the functional dependence that describes the bound state energies approaching zero magnetic field. For this reason, in order to calculate the corrections for the energies of the molecular states at zero magnetic field, the theoretical data is fitted by the function:

$$f = A + k \cdot B + C \cdot (-2 + e^{-D \cdot B} + e^{-E \cdot \sqrt{B}}) \tag{E.22}$$

which has a similar linear asymptotic behaviour at large magnetic fields and bends at low B. The choice of the exponential function is justified by the good approximation of the theoretical data points.